BEAM-COLUMN CONNECTION FLEXURAL BEHAVIOR AND SEISMIC COLLAPSE PERFORMANCE OF CONCENTRICALLY BRACED FRAMES

BY

CHRISTOPHER D. STOAKES

DISSERTATION

Submitted in partial fulfillment of the requirements
for the degree of Doctor of Philosophy in Civil Engineering
in the Graduate College of the
University of Illinois at Urbana-Champaign, 2012

Urbana, Illinois

Doctoral Committee:

Assistant Professor Larry A. Fahnestock, Chair
Professor Daniel P. Abrams
Professor Jerome F. Hajjar
Professor of the Practice Eric M. Hines, Tufts University

ABSTRACT

This dissertation investigates the flexural behavior of beam-column connections with gusset plates and their ability to improve the seismic collapse performance of concentrically braced frames. Previous experimental and field observations demonstrated that reserve lateral force-resisting capacity due to the flexural strength of connections outside the primary lateral force-resisting system of steel frames can maintain structural stability if the primary system is damaged. Several experimental studies were conducted to quantify the flexural behavior of these connections, but there has only been limited investigation of beam-column connections with gusset plates.

Thus, the focus of this study was two-fold. First, expand existing knowledge about the flexural behavior of braced frame connections. This task was accomplished through a series of large-scale experiments of beam-column subassemblies. The braced frame connections in the experimental program were double angle and end plate details that were proportioned based on the design loads from a prototype braced frame. The results from the experiments suggested that beam-column connections with gusset plates have appreciable flexural stiffness and strength. In addition, the flexural stiffness and strength of the connections could be increased, with minimal ductility loss, by thickening the double angles and adding a supplemental seat angle. The stiffness, strength, and ductility were limited, however, by weld failure, angle fracture, and bolt fracture.

Since only one beam depth was used in the large-scale testing, it was desirable to investigate the effect of beam depth on the flexural behavior of braced frame connections using

three-dimensional finite element analyses. Three additional beam sizes were selected: W14x53, W18x46, and W21x44. Additional thicknesses for the double angles were also considered. The computational studies revealed that increasing beam depth increases the flexural stiffness and strength of beam-column connections with gusset plates. Nevertheless, the critical limit states occurred at smaller story drifts as the beam depth increased. Larger angle thicknesses were also found to increase flexural stiffness and strength. The results from the experimental and computational studies were used to develop a simplified procedure for evaluating the flexural stiffness and strength of a braced frame connection.

After completing the experimental and computational studies on the flexural behavior of braced frame connections, a series of incremental dynamic analyses were conducted on a suite of concentrically braced frames designed for a moderate seismic region to determine if beam-column connections with gusset plates can provide adequate reserve capacity to insure collapse prevention performance under maximum considered earthquake level demands. Collapse performance data were generated by analyzing the results of the incremental dynamic analyses using a reliability-based performance assessment. The results from the collapse performance assessment revealed that beam-column connections with gusset plates can function as a reserve lateral force-resisting system. The results from the incremental dynamic analyses, in conjunction with the collapse performance data, were used to synthesize recommendations for the minimum level of strength a reserve lateral force-resisting system must possess in order to insure adequate collapse prevention performance.

ACKNOWLEDGEMENTS

I am deeply indebted to my adviser, Dr. Larry A. Fahnestock, for the opportunity to study at the University of Illinois. Dr. Fahnestock continually drove me to expand the breadth of my technical knowledge, not only in the behavior of steel structures but also in finite element analysis and structural mechanics, to heights that I did not envision when I started this project.

I am also extremely grateful for the aid of our laboratory technician in the Newmark Structural Engineering Laboratory, Dr. Gregory Banas. Greg taught me everything I know about actuators and controllers, strain gages and LVDTs, data acquisition, etc. Also aiding my efforts were the guys from the Civil Engineering Machine Shop. Everyone in the shop worked on my project at some point in time, but Steve Mathine and Jamar Brown tightened most of the bolts.

I also need to mention my office mates Matt Parkolap, David Miller, and Jason Fifarek. The fellowship I shared with them over the last two years of my studies made the time pass too quickly, and is definitely one of the most enjoyable memories I will take with me from Illinois.

Of course, the testing could not have begun without the help of undergraduate students Matt Johnson, Eric Koziol, Paul Mockus, Julia Plews, and Jeff Woss. In addition, Luis Funes from San Jose State University worked with us one summer to help with the setup of individual tests. All their efforts were greatly appreciated. Dr. Matthew R. Eatherton, now an Assistant Professor at Virginia Polytechnic Institute, was also a guiding force in my doctoral studies.

I would also like to thank Dr. Jerome F. Hajjar, Northeastern Univerity, and Dr. Eric M. Hines, LeMessurier Consultants/Tufts University, for their insights into how this small study on beam-column connections fits into the broader field of earthquake structural engineering. Dr.

Robert H. Dodds, University of Illinois, also provided outstanding guidance during the finite element phase of my research.

Of course, I need to thank my parents for their influence in my life. Both have graduate degrees and were instrumental in the writing of this dissertation. More importantly, they were always willing, and are still willing, to make sacrifices for me and my family. This lesson of love is one that I hope to pass on to my boys half as well as my parents passed it on to me.

Speaking of my boys, Will and Nile are definitely the light of my life. Will makes me laugh every day and Nile is learning to do the same. A day at the office is easily forgotten when they are around.

Finally, I cannot thank my wife, Martha, enough for being my rock during my journey through graduate school. Her confidence in me never wavered. In addition, she spent many nights and weekends as a single parent. Words cannot express how thankful I am to have her in my life.

Partial funding for this research was provided by the American Institute of Steel Construction. Test specimen materials and fabrication were provided by Novel Iron Works. Inspection of the test specimens was conducted by Briggs Engineering. Professor Gian Rassati of the University of Cincinnati, Department of Civil Engineering, provided the testing equipment and data acquisition system for calibration of the bolt strain gages. The basis for the large-scale experimental study and the test specimen designs were developed in collaboration with Eric Hines (LeMessurier Consultants and Tufts University) and Peter Cheever (LeMessurier Consultants). The opinions, findings, and conclusions expressed in this dissertation are those of the author and do not necessarily reflect the views of those acknowledged here.

TABLE OF CONTENTS

CHAPTER 1

INTRODUCTION

Since the inception of seismic design codes in the United States (US), structural steel systems designed for earthquake resistance have relied exclusively on inelastic deformation to prevent collapse during large seismic events (Blume et al. 1961). The inelastic deformations are confined to specific elements, often called fuse elements, which are designed to yield at a prescribed force level. Plastic hinging in beams of moment-resisting frames (MRFs) and yielding and buckling of braces in concentrically-braced frames (CBFs) are just two examples of acceptable inelastic deformations in seismic resistant structures. Structural members connected to the fuse elements are then designed to remain elastic while the fuses deform inelastically, a process called capacity design. The principles of ductility and capacity design have been extensively researched and implemented in current US seismic design codes (ASCE 2010, AISC 2005a).

The extensive research on the seismic behavior and performance of steel structures has largely focused on structures in high seismic regions. High seismic regions are located in the familiar areas in Western North America (WNA), but also areas concentrated around New Madrid, Missouri, and Charleston, South Carolina. The thrust to improve the collapse performance of structures in these regions has increased the scope and sophistication of seismic design provisions for these regions. For example, the current edition of the American Society of Civil Engineers *Minimum Design Loads for Buildings and Other Structures* (ASCE 2010), also known as ASCE 7, contains 35 seismic force-resisting systems for steel structures. Each seismic

force-resisting system permitted in high seismic regions is accompanied by numerous design and detailing requirements to insure the assumed level of structural ductility can be realized.

The advances made in designing new building stock to resist strong earthquakes in high seismic regions, however, have not significantly influenced seismic design of steel structures in moderate seismic regions. Moderate seismic regions are defined as regions where the prevailing Seismic Design Category is B or C. This is understandable given the long history of seismic activity on the west coast, but also confusing since contemporary building codes require seismic hazard to be considered in most regions of the US (ICC 2009). Currently, only one of the basic seismic force-resisting systems recognized in ASCE 7, called the 'R = 3' system for reasons that will become apparent, is widely applied to structures in moderate seismic regions. Detailing requirements to reach a minimum level of ductility are not attached to R = 3 systems. Thus, design of structures for seismic resistance in moderate seismic regions has been insulated from the developments that have occurred for structural design in high seismic regions.

Although not explicitly stated in the buildings codes, the viability of an R = 3 system rests on the notion of reserve capacity. Reserve lateral force-resisting strength, or reserve capacity, is defined as lateral force resistance that maintains structural stability after the primary lateral force-resisting system strength has degraded. Thus, it was reasoned that adequate ductility and reserve capacity to provide collapse prevention performance exists within steel framing systems traditionally in moderate seismic regions, and the R = 3 system was born (Carter 2009).

In what follows, a thorough discussion of the conception and implementation of R = 3 systems, which is adapted from the comprehensive review provided by Carter (2009), is presented. Next, a summary of new research on the critical role of reserve capacity in preventing

collapse of CBFs during large seismic events is provided. Finally, the purpose and objectives of this study, and how they relate to reserve capacity, are defined.

1.1 A BRIEF HISTORY OF SEISMIC DESIGN IN MODERATE SEISMIC REGIONS

1.1.1 Development of National Seismic Design Provisions

Prior to the 1980s, designing structures to withstand seismic events was considered necessary only in WNA, or west of the Rocky Mountains. The Structural Engineers Association of California (SEAOC) *Recommended Lateral Force Requirements* (SEAOC 1959), or *Blue Book,* were the dominant seismic design provisions at the time, but were only applicable in the state of California. Publication of *Tentative Provisions for the Development of Seismic Regulations for Buildings* (ATC 1978), commonly referred to as ATC 3-06, by the Applied Technology Council (ATC), however, initiated the development of seismic design provisions with a national scope.

ATC 3-06 promoted the extension of seismic design provisions to Eastern North America (ENA), or east of the Rocky Mountains, by developing national seismic hazard maps and suggesting that structural systems and detailing requirements be regulated by Seismic Design Category (SDC) (Rojahn 1995). SDC is a building specific classification based on the building's occupancy classification, the building site soil profile, and the magnitude of the anticipated ground accelerations. ATC 3-06 also introduced the response modification coefficient, commonly called the '*R*-factor', which approximates the reduction in seismic base shear due to inelastic response of a structure during a seismic event. The *R*-factors prescribed in ATC 3-06

were derived from the *K*-factors published in the SEAOC *Blue Book*, although the *R*-factors were formulated as divisors, not multipliers like the *K*-factors, to better reflect their purpose of predicting the reduction in seismic base shear (Rojahn 1995). In addition to the influence of the SEAOC *Blue Book*, the *R*-factors included in ATC 3-06 were derived based on judgments which weighed the minimization of seismic risk with corresponding increases in construction cost (Carter 2009). Thus, the development of *R*-factors for seismic force-resisting systems has not historically been a purely technical exercise.

Coinciding with the publication of ATC 3-06, the National Institute of Building Sciences (NIBS) created the Building Seismic Safety Council (BSSC) with the express purpose of developing seismic design provisions with a national scope. To accomplish this task, the BSSC lobbied for development of the National Earthquake Hazard Reduction Program (NEHRP), which led to publication of the NEHRP *Recommended Provisions for Seismic Regulations for New Buildings and Other Structures* (FEMA 1997). The NEHRP recommended provisions expanded the work of ATC 3-06 by identifying additional seismic force-resisting systems and modifying some *R*-factors. In addition, publication of the NEHRP *Recommended Provisions* allowed the BSSC to lobby code agencies to adopt seismic design provisions in their building code publications. The American Institute of Steel Construction (AISC) and the American Society of Civil Engineers (ASCE), organizations with national constituencies, also supported the work of the BSSC and encouraged adoption of the NEHRP *Recommended Provisions* (Carter 2009).

In the early 1990s, two of the three primary building code agencies in the United States adopted the NEHRP *Recommended Provisions*: the Building Officials and Code Administrators

International (BOCA) in the *National Building Code* (NBC) and the Southern Building Code Congress International (SBCCI) in the *Southern Building Code* (SBC). The International Conference of Building Officials (ICBO) did not adopt the NEHRP *Recommended Provisions* because they had previously adopted the SEAOC *Blue Book* as the pre-standard for seismic design provisions in the *Uniform Building Code* (UBC). The UBC was used primarily in WNA, which accounts for the ICBO's initial resistance to the NEHRP *Recommended Provisions* (Carter 2009).

Development of seismic design provisions with a national scope added to the growing pressure for a building code publication applicable nationwide. In 1994, the three primary code agencies, BOCA, SBCCI, and ICBO, decided to consolidate into a single code agency, the International Code Council (ICC), and published the first edition of the *International Building Code* (IBC) in 1997. With publication of the 1997 IBC, which included the NEHRP *Recommended Provisions*, seismic design requirements were imposed suddenly on jurisdictions in ENA that not previously required explicit design for earthquake resistance (Carter 2009). The initial reaction from engineers and constructors in ENA was to ignore the IBC seismic design provisions, arguing that they were overly conservative or significantly increased construction cost, or to circumvent the intent of the provisions by finding loop holes in the seismic design requirements (Carter 2009).

1.1.2 Introduction of the $R = 3$ Provision

The primary code provision exploited in steel building construction was the provision exempting structures in SDC A, B, or C from seismic detailing. In this case, the design seismic

base shear was determined using a high *R*-factor, typically one large enough to ensure wind loads controlled the design of the lateral force-resisting system, but the detailing needed to generate the appropriate inelastic response was not provided (Hines et al. 2009). Clearly, this practice was not consistent with the intent of the IBC seismic design provisions.

To aid acceptance of the IBC seismic design provisions in ENA, a new basic seismic force-resisting system for steel structures was proposed by Harry W. Martin, P.E., of the American Iron and Steel Institute (AISI) (Carter 2009). The new system was identified as "structural steel systems not specifically detailed for seismic resistance" and attempted to preserve the construction practices for steel structures established in ENA while conforming to the seismic design philosophy of the new IBC. In this vein, the new system was given an *R*-factor of three and could be used without providing seismic detailing as long as the structure under consideration was in SDC A, B, or C. The value of three was selected for the new system because it was reasoned that there is adequate ductility, reserve capacity, and redundancy inherent in any steel lateral force-resisting system to provide seismic base shear reduction consistent with $R = 3$ (Carter 2009). The new $R = 3$ provision, as it is called, succeeded in resolving the problems with implementation of the seismic design provisions that arose after publication of the 1997 IBC. Until the last few years, however, there have been no experimental or computational studies to verify the amount of ductility, reserve capacity, and redundancy inherent in these systems justifies the selection of $R = 3$.

1.2 COLLAPSE PERFORMANCE OF CBFs DESIGNED USING $R = 3$

The first work on the $R = 3$ provision for seismic design of steel structures was a

computational study of concentrically-braced frames (CBFs) by Hines et al. (2009). In this study, a prototype braced frame, based on the SAC building plan geometry, was designed for 3-, 6-, 9-, and 12-story building heights using seismic forces and response modification coefficients $R = 2$, $R = 3$, and $R = 4$. The purpose for varying the R-factor was to investigate the effect of primary system strength on collapse performance. In addition, a fourth set of buildings was designed for wind forces with a moment frame reserve lateral force-resisting system, denoted wind plus reserve system (WRS). The WRS buildings were studied because the results from the nonlinear dynamic analyses of the $R = 2$, $R = 3$, and $R = 4$ buildings suggested reserve capacity, not ductility, is the primary means for preventing collapse of CBF structures subject to seismic forces. Brace connection fracture, which occurred prior to brace buckling in all frames, was modeled in the brace force-deformation relationships and the lateral load resistance provided by the gravity system, based on the results from Liu and Astaneh-Asl (2000), was included. Reliability-based performance assessment, which employed an incremental dynamic analysis (IDA) and a suite of maximum considered earthquake (MCE) level ground acceleration records developed for Boston, MA, by Sorabella (2006), was used to quantify the collapse performance of the prototype buildings.

Hines et al. (2009) concluded that adding reserve capacity uniformly improved collapse performance. In contrast, increasing primary system strength had little effect on collapse performance. The WRS frames did not collapse under any of the MCE level ground acceleration records, whereas the $R = 2$, $R = 3$, and $R = 4$ frames experienced several collapses of the 3- and 6-story building configurations. The 9-story $R = 4$ and 12-story $R = 3$ configurations also collapsed under a limited number of the unscaled ground motions. In addition, the ground

motion scale factor at collapse was significantly larger for the WRS frames than the frames designed considering seismic loads. Thus, this study demonstrated the potential for using reserve capacity to provide seismic collapse prevention for CBFs in moderate seismic regions. Hines et al. (2009) did not study local requirements for the flexural stiffness, strength, and ductility of beam-column connections expected to provide reserve capacity within a reserve lateral force-resisting system.

1.3 RESERVE CAPACITY AND BRACED FRAME CONNECTIONS

One possibility for providing the necessary reserve capacity to achieve adequate seismic collapse performance in a CBF is to employ the flexural strength and stiffness of the beam-column connections with gusset plates after the braces are no longer active. A typical braced frame connection with steel angles is shown in Figure 1.1. The brace and its connection to the gusset plate are not shown for clarity.

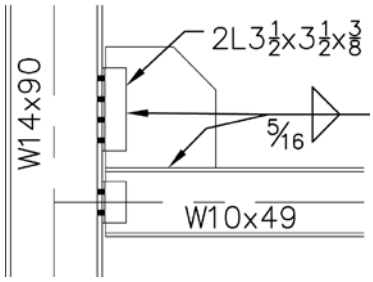

Figure 1.1 Typical braced frame connection.

Typically, these connections are assumed to possess zero flexural stiffness and strength in the design of concentrically-braced frames. The benefit of this assumption is that the frame is rendered statically determinate, which simplifies the design process. It has long been recognized, however, that beam-column connections with gusset plates have non-negligible stiffness and strength (Richard 1986, Thornton 1991), but few experimental studies corroborating

this belief have been conducted (Uriz and Mahin 2008, Kishiki et al. 2009).

Therefore, the purpose of this study was to build on existing knowledge of reserve capacity by developing design recommendations for the minimum strength of reserve capacity systems and how their strength can be quantified. In addition, procedures for assessing the flexural stiffness and strength of beam-column connections with gusset plates were developed so that their contribution to reserve capacity may be accounted for during design of reserve capacity systems. Minimum levels of strength needed in reserve capacity systems, and analytical models of the flexural stiffness and strength of braced frame connections, have not been discussed in prior research. To demonstrate the potential for using braced frame connections to provide reserve capacity, three primary tasks were identified.

1. Quantify the flexural stiffness, strength, and ductility of beam-column connections with gusset plates using full-scale experiments. It has already been stated that beam-column connections with gusset plates have appreciable flexural stiffness and strength despite the fact that they are typically designed as simple pins. A limited number of experimental studies have corroborated this belief, but the local moment vs. rotation behavior of braced frame connections is largely unexplored. A broader understanding of the flexural behavior of these connections is needed to conduct the system level collapse studies that will demonstrate the benefits of reserve capacity due to beam-column connections with gusset plates. In addition, several geometric variations for increasing the flexural stiffness, strength, and ductility of beam-column connections with gusset plates were explored.

2. Expand the database of known moment vs. rotation behaviors for beam-column connections with gusset plates using three-dimensional finite element analysis. This objective is needed since conducting an adequate number of large-scale tests investigating the range of parametric variations in a braced frame connection is cost prohibitive. In general, beam depth, double angle thickness, gusset plate thickness, and weld size all influence the flexural behavior of beam-column connections with gusset plates. It is more efficient to use computational simulations, in lieu of large-scale experiments, to study the effects of these variations. Nevertheless, the data generated during the experimental program mentioned in the first objective was required to validate the finite element models.

3. Use reliability-based performance assessment to demonstrate that beam-column connections with gusset plates can provide adequate reserve lateral force-resisting capacity to generate acceptable collapse prevention performance. This objective will demonstrate the level of collapse prevention performance that a reserve capacity system built from braced frame connections can provide. In addition, it will foster the development of design provisions for such a system.

Finally, it should be noted that this research will benefit steel structures in high seismic regions as well. It may be possible to show that the reserve capacity afforded by beam-column connections with gusset plates provides adequate collapse prevention performance for structures designed and constructed prior to the development of current seismic design provisions. In this case, reserve capacity would reduce the extent and cost of seismic retrofitting.

1.4 ORGANIZATION OF DISSERTATION

This dissertation details full-scale testing of beam-column connections with gusset plates, finite element parametric studies to simulate the behavior of a wide range of beam-column connections with gusset plates, and reliability-based collapse performance assessment of CBFs with braced frame connection behavior based on the full-scale tests and the finite element studies. It is organized as follows:

- Chapter 1 provides background information on current seismic design provisions in moderate seismic regions and introduces the concept of using reserve capacity, rather than ductility, to provide collapse prevention performance.
- Chapter 2 summarizes existing literature that discusses reserve capacity in steel structures. Reserve capacity has been noted in field observations of steel structures after large earthquakes and in large-scale experiments. Flexural strength of connections typically designed as simple pins is also demonstrated from existing literature.
- Chapter 3 discusses the cyclic, flexural testing of beam-column connections with gusset plates. Details on connection design, experimental setup, and data acquisition are provided. Normalized moment vs. story drift data that quantifies the flexural behavior and performance of the beam-column connections is presented. In addition, localized connection behaviors, including gusset plate-beam fillet weld failure, bolt fracture, and low-cycle fatigue fracture of steel angles, are examined in detail to determine their influence on flexural stiffness, strength, and ductility of the connections.
- Chapter 4 outlines the finite element modeling of beam-column connections with gusset plates. Validation of the finite element models to the experimental results is summarized and the

results of a parametric study on connection parameters are presented. A design procedure quantifying the moment vs. rotation behavior of braced frames connections is also developed.

- Chapter 5 details the nonlinear response history analyses conducted to quantify the impact of connection behavior on seismic performance of CBFs in moderate seismic regions. Recommendations for minimum strength of reserve lateral force-resisting systems composed of beam-column connections with gusset plates are detailed.
- Chapter 6 summarizes the conclusions from the current study on the reserve capacity that can be achieved using beam-column connections in braced frames. The design recommendations developed in Chapters 4 and 5 are summarized. Future research topics regarding seismic design of steel structures in moderate seismic regions are outlined.

CHAPTER 2

LITERATURE REVIEW

Currently, there is not an extensive amount of literature devoted to the seismic behavior and collapse performance of CBFs with reserve lateral force-resisting systems. A few computational studies have been completed (Hines et al. 2009, Nelson et al. 2006), but significant experimental work has not been undertaken. Nevertheless, insight into the seismic behavior and collapse performance of CBFs with reserve lateral force-resisting systems can be gained from the behavior and performance of steel structures during large seismic events and experimental studies where reserve capacity was observed during large-scale testing.

2.1 RESERVE CAPACITY OBSERVED AFTER LARGE SEISMIC EVENTS

The seismic event that heavily influenced seismic design provisions for steel structures in North America was the 1994 Northridge, California, earthquake. The 1994 Northridge earthquake had a magnitude of 6.7, an intensity of IX (MM), and a focal depth of 12 mi (USGS 2010). Tremblay et al. (1995) conducted damage surveys of several steel structures in the months following the seismic event. The authors provided extensive background information on the seismic design provisions used to engineer the damaged structures. Following the code review, Tremblay et al. (1995) compared the structural damage to the seismic design provisions used to engineer the structures to determine if the observed limit states were predicted.

Since no steel structures collapsed, initial field observations suggested steel buildings performed as expected during the 1994 Northridge earthquake. Detailed investigations of many

steel structures, however, revealed significant inelastic deformations, and in some cases failure, of connections in braced and moment-resisting frames. In the damage survey by Tremblay et al. (1995), which focused on braced frames, the most common failure was buckling of the bracing members. Typically, brace buckling led to damage of non-structural components. In severe cases, however, local buckling in hollow structural section (HSS) braces led to low-cycle fatigue fractures in the braces and out-of-plane brace buckling of the braces led to torsional failures of beam-column connections. In addition, several welded connections between braces and gusset plates failed. Tremblay et al. (1995) also observed degradation of the lateral force-resisting capacity of braced frames due to inelastic elongation of column anchor bolts and fracture of column base plates.

In addition to their discussion of braced frame damage, Tremblay et al. (1995) summarized the behavior of moment-resisting frames during the 1994 Northridge earthquake. Damage sustained by moment frames during the 1994 Northridge earthquake was studied extensively in the months following the event. Comprehensive damage reports were compiled by Bertero et al. (1994), Ghosh (1994), Ross and Mahin (1994), and Youssef et al. (1995). The discussion by Tremblay et al. (1995) is a summary of these larger works.

Tremblay et al. (1995) opened their discussion of moment frame behavior during the 1994 Northridge earthquake stating, “The brittle fracture of field welded beam-to-column connections in steel moment resisting frames is one of the most significant issue[s] of the Northridge earthquake.” Experimental studies on special moment connections with beam flanges welded to the column predicted plastic hinging of the beam would occur. Nevertheless, hundreds of moment connections experienced brittle fracture of the lower beam flange or lower

beam flange weld during the earthquake. The authors noted the connection failures were first observed in steel structures under construction at the time of the seismic event, specifically, those in which the beam-column joints were not concealed with fireproofing or architectural finishes. Tremblay et al. (1995) stated the reason the failures were not detected during initial building surveys was the structures were plumb and no significant damage to exterior building façades was observed. In addition, all steel structures maintained their stability during aftershocks. Tremblay et al. (1995) also provided detailed descriptions of failure modes in the lower beam flange, weld, and column and a thorough discussion on possible reasons for the susceptibility of the moment connections to brittle fracture.

Since steel structures sustained significant damage to their primary lateral force-resisting systems during the 1994 Northridge earthquake without collapsing, the prevailing conclusion was the structures contained reserve lateral force-resisting capacity that maintained structural stability after the primary system was damaged (Liu and Astaneh-Asl 2000). The most likely source of reserve lateral force resistance was thought to be the composite beam-column connections in the gravity framing system.

One study that quantified the flexural stiffness, strength, and ductility of gravity connections was performed by Liu and Astaneh-Asl (2000, 2004) at the University of California, Berkeley. In this study, 16 full-scale beam-column connections were subjected to cyclic loading to determine their lateral force-resisting capacity. A cruciform configuration subassembly was used for the testing. The subassembly was extracted from a prototype building by assuming inflection points at mid-height of the columns and mid-span of the beams/girders. The test setup is illustrated in Figure 2.1. Flexure in the connections was simulated by applying lateral

displacement to the top of the column with a single degree-of-freedom actuator. Gravity load on the beams was simulated with two actuators per beam/girder.

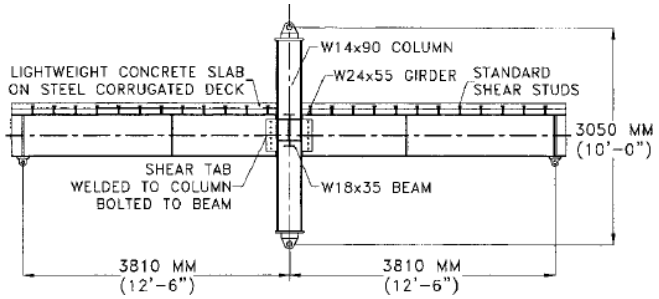

Figure 2.1 Elevation view of cruciform test setup (Liu and Astaneh-Asl 2000).

Tests on bare steel specimens were performed to establish a control group followed by specimens with partially-composite concrete slabs. All specimens were shear tab connections and tested with normal-weight and lightweight concrete. The effect of strong vs. weak axis bending of the column was also investigated. The number of bolt rows in the connections varied from 3 to 8.

Liu and Astaneh-Asl (2000, 2004) reported shear tab connections with a partially-composite concrete slab developed 30% to 45% of the beam plastic moment, M_p. In one test, the flexural strength was increased to 70% of M_p by adding a supplemental seat angle to the bottom beam flanges. Thus, the tests by Liu and Astaneh-Asl (2000, 2004) demonstrated connections in the gravity framing system of a steel structure can provide adequate stiffness and strength to act as a reserve lateral force-resisting system.

Rai and Goel (2003) also investigated the reserve capacity of CBFs by performing a computational analysis of a building from the North Hollywood area damaged during the Northridge earthquake. The building was a 4-story steel structure with six CBFs in both the North-South and East-West directions. Observations of the building's exterior after the earthquake indicated it should be 'yellow tagged', which allowed for limited entry but not

continued occupancy. Detailed inspections, however, revealed all braced frames in the second story, in the N-S direction, experienced failure of at least one brace or brace connection. Figure 2.2 summarizes the damage to the N-S braced frames.

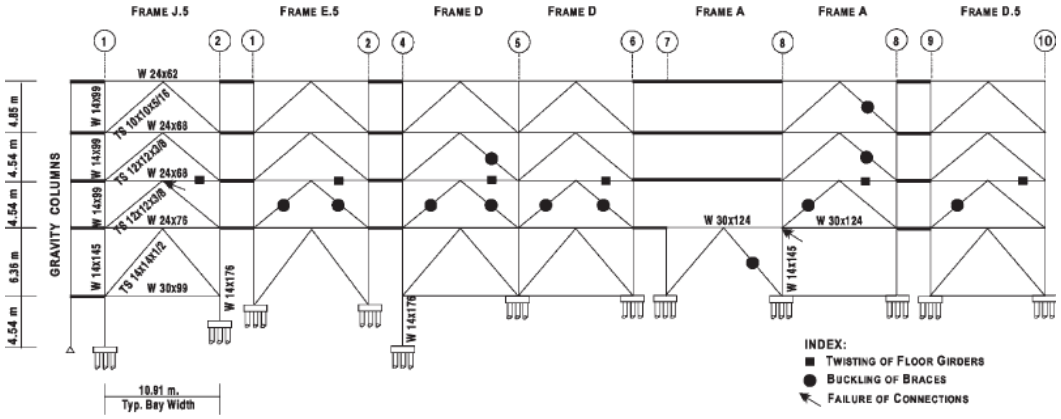

Figure 2.2 Damage to N-S braced frames (Rai and Goel 2003).

Based on the results of the damage survey, it was evident the primary lateral force-resisting capacity of the second story was significantly reduced. Yet, the structure remained stable. After performing nonlinear static pushover simulations of a two-dimensional model of the braced frames in the N-S direction, Rai and Goel (2003) concluded the continuous gravity columns provided adequate reserve lateral force-resisting strength to prevent structural collapse.

In a similar vein, Tremblay and Stiemer (1994) used analytical and computational methods to demonstrate that continuous gravity columns can provide adequate stiffness to mitigate collapse of braced frames. The authors work was based on the fact that a braced frame needs to provide adequate stiffness to resist seismic loads and to prevent sidesway buckling of the gravity columns. Once the stiffness of a braced frame degrades, which can occur through brace yielding and buckling during a seismic event, adequate stiffness to prevent sidesway of the gravity columns is not provided.

Tremblay and Stiemer (1994), however, recognized that the degradation of the stiffness in

a braced frame can lead to differential story drifts that activate the flexural stiffness of the gravity columns, if the columns are continuous across the stories. By assuming braced frame failure modes that included one or more stories, the authors developed analytical expressions for the minimum stiffness and strength of continuous gravity columns to maintain structural stability. The stiffness requirement was developed by equating the flexural stiffness of a continuous gravity column, derived from an assumed failure mode in the braced frame, with the stiffness required to prevent sidesway buckling of the gravity columns. The strength requirement was needed to guard against inelasticity in the columns that would reduce their flexural stiffness.

After formulating the minimum requirements for stiffness and strength of the continuous gravity columns, Tremblay and Stiemer (1994) used nonlinear response history analysis to determine if the computed limits were adequate to prevent structural collapse. A suite of braced frames and associated gravity systems were designed for 2-, 4-, 8-, and 12-story building heights. Gravity columns were designed solely for factored loads; they were not enhanced to satisfy the aforementioned stiffness and strength requirements. Gravity column size was varied, however, by assuming different tributary areas in gravity load calculations. Since the gravity columns were assumed to be wide flange shapes, analyses with strong axes and weak axes of the gravity columns in the plane of the braced frame were examined. Elastic-perfectly plastic force-deformation response was modeled for the axial behavior of the braces and the flexural behavior of the gravity columns. Each building design was subjected to 8 ground motions.

Prior to analyzing frames with continuous gravity columns, a control group of analyses were conducted with gravity columns pinned at each story. The lack of column continuity resulted in collapse predictions for 63% of the buildings. Subsequent analyses were conducted

with gravity columns continuous over two stories and over the entire height of the building. In all cases where the gravity columns met the proposed stiffness requirement, collapse of the structure was prevented. Nevertheless, collapse mechanisms were observed during the computational studies that were not considered during development of the stiffness and strength requirements. Thus, Tremblay and Stiemer (1994) concluded that continuous gravity columns can provide sufficient stiffness and strength to enhance collapse performance of braced frames, but additional research was needed to identify additional collapse mechanisms prior to developing design guidelines for back up stiffness of continuous gravity columns.

2.2 RESERVE CAPACITY OBSERVED DURING EXPERIMENTAL STUDIES

In addition to field observations of reserve lateral force-resisting capacity, several large-scale experiments have demonstrated the existence and benefits of reserve lateral strength. An experimental study on a seismic dual system consisting of a CBF and a ductile moment-resisting space frame (DMRSF) was undertaken by Bertero et al. (1989) as part of the US-Japan Cooperative Research Program Utilizing Large Scale Testing Facilities. The purpose of the study was to investigate the role of DMRSFs in the seismic response of a CBF/DMRSF dual system. Test results were used to assess contemporary seismic design provisions for dual systems in the US. The structure tested by Bertero et al. (1989) at the University of California, Berkeley, was a 0.3-scale model of a full-scale structure tested in the Large Size Structures Laboratory of the Building Research Institute in Tsukuba, Japan (Foutch et al. 1987).

The full-scale structure was a six story, two-bay-by-two-bay steel frame with composite concrete slab. The lateral force-resisting system parallel to the loading direction consisted of two

DMRSFs and one CBF. Plan and elevation views of the test structure are shown in Figure 2.3.

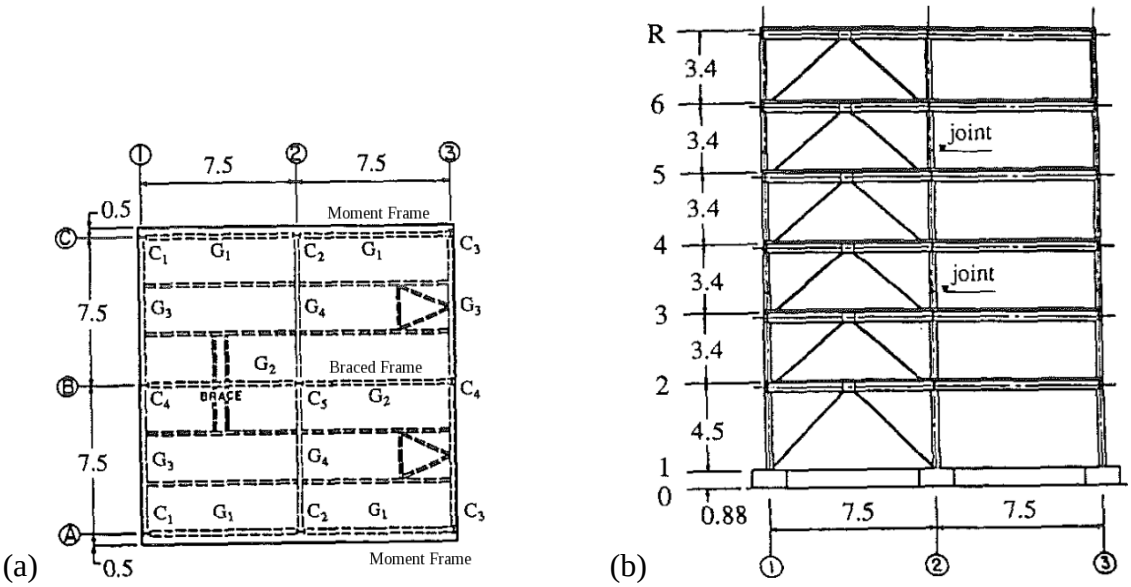

Figure 2.3 Test structure from Bertero et al. (1989): (a) plan; (b) CBF elevation.

The CBF was coincident with column line B and the DMRSFs were along column lines A and C. The frames were designed according to the contemporary Japanese seismic design code, which prescribed a larger base shear than the 1979 UBC. The DMRSFs were proportioned so their strength was greater than 50% of the design base shear; the 1979 UBC minimum strength for the DMRSF was only 25% of the design base shear. Moment connections were also provided at all beam-column connections in the CBF, which was common construction practice in Japan. In lieu of gusset plates, the braces in the CBF were welded directly to the girders, another typical Japanese practice. The beams and columns were wide-flange shapes and the braces were hollow structural sections.

To determine the similitude law for the scale model, several computational dynamic analyses were performed to determine the base shear in the scale model that matched the capacity of the earthquake simulator. The analyses showed that a scale factor of 0.3 for the geometry and loading of the scale model satisfied the experimental constraints. The N-S

component of the 1978 Miyagi-Ken-Oki earthquake record was chosen as the input ground motion. This earthquake was chosen because its frequency content centered on the fundamental frequency of the test structure. After scaling for similitude, the ground accelerations were scaled to serviceability, 0.063g, yield, 0.33g, and collapse, 0.65g, limit states.

During the collapse limit state ground motion, one brace in the 5th story ruptured at mid-length and one brace in the 4th story fractured at its lower connection. In addition, braces in the remaining stories buckled. The maximum recorded story drift was 0.019 rad in the 5th story and the seismic base shear coefficient, C_s, was computed to be 0.73.

Due to the strength of the DMRSF, the story shears in the 4th and 5th stories increased after brace fracture. The DMRSF in the 5th story remained elastic up to 0.015 rad story drift with minimal inelastic response at the maximum story drift. The DMRSF in the 4th story also exhibited minimal inelastic deformation. Thus, there was negligible ductility demand on the DMRSF. The DMRSF, however, provided sufficient reserve strength to maintain stability of the structure after the 4th and 5th story braces failed. The total story shear, CBF story shear, and DMRSF story shear are plotted against story drift in Figure 2.4, for the 4th and 5th stories.

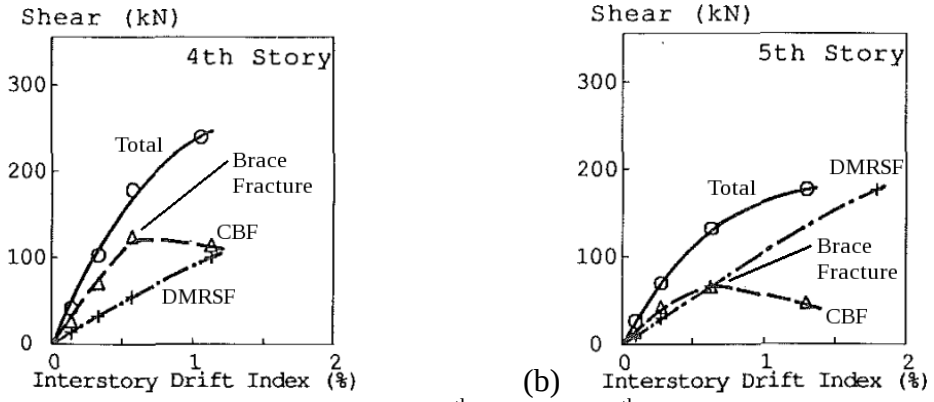

Figure 2.4 Shear vs. interstory drift: (a) 4th story; (b) 5th story (Bertero et al. 1989).

Bertero et al. (1989) concluded that existing code provisions for proportioning the

DMRSF and CBF braces were inadequate and that the *R*-factor prescribed for dual systems was unconservative. The authors recommended that the DMRSF in a dual system be designed for 50% of the design base shear and that the minimum ratio of P_{cr}/P_y for braces be increased to 0.8. For these two parameters, the 1979 UBC recommended 25% and 0.5, respectively. Bertero et al. (1989) calculated the *R*-factor from the equation $R = \Omega_d \cdot R_\mu$, where Ω_d is the inherent overstrength and R_μ is the displacement ductility, which led to an *R*-factor of 3.6 for the CBF/DMRSF dual system.

Similar shake table tests were performed on an eccentrically-braced frame (EBF), DMRSF dual steel system by Whittaker et al. (1989). The floor plan and elevation were the same as the CBF/DMRSF studied by Bertero et al. (1989). The 1952 Kern County Taft N21E earthquake record was used as the input motion in lieu of the 1978 Miyagi-Ken-Oki record. The record was again scaled to serviceability, yield, and collapse limit states.

As in the CBF/DMRSF dual system, the DMRSF in the EBF/DMRSF dual system maintained stability of the structure after damage to the primary lateral force-resisting system. Figure 2.5 shows the total story shear, EBF shear, and DMRSF shear vs. story drift for the first story in the EBF/DMRSF dual system.

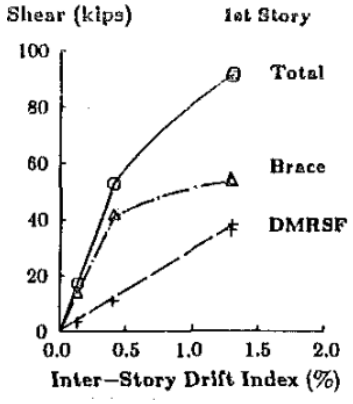

Figure 2.5 Shear vs. interstory drift (Whittaker et al. 1989).

The EBF shear vs. story drift data indicates the EBF yielded at 0.005 rad story drift and deformed plastically beyond this drift level. The total story shear, however, increased after yielding of the EBF due to reserve strength provided by the DMRSF. In addition, a significant portion of the elastic story stiffness was maintained. The EBF remained elastic in all other stories. Whittaker et al. (1989) recommended an *R*-factor of 5.2, based on calculations similar to the CBF/DMRSF dual system discussed above, for EBF/DMRSF dual systems.

Of significance to the current study is that the *R*-factors recommended by Bertero et al. (1989) and Whittaker et al. (1989) were influenced more by the inherent overstrength, Ω_D, of the systems than the displacement ductility, R_μ. The inherent overstrength was computed to be 2.4 for the CBF/DMRSF and 2.85 for the EBF/DMRSF. The displacement ductility was computed to be 1.5 for the CBF/DMRSF and 1.85 for the EBF/DMRSF. These experimental results are consistent with the conclusion that reserve lateral force-resisting capacity plays a significant role in collapse resistance of steel structures.

In addition to the results reported by Bertero et al. (1989) and Whittaker et al. (1989), large-scale tests of braced frames by Gross and Cheok (1988) and Uriz and Mahin (2008) demonstrated reserve lateral force-resisting capacity exists in braced frames due to beam-column connections with gusset plates.

Significant flexural capacity of beam-column connections with gusset plates was noted by Gross and Cheok (1988) during monotonic testing of braced frame subassemblies. The purpose of the large-scale tests was to determine how the flexibility of the beams and columns in a braced frame affects the interface forces between the gusset plate, beam, and column. Prior experiments quantifying the interface forces used isolated gusset plates with rigid boundary

conditions.

The test subassembly was extracted from a prototype building by assuming inflection points at mid-height of the columns and mid-span of the beams. The subassembly is detailed in Figure 2.6. The prototype braced frame had W10x49 columns, W16x40 beams, and W8x21 braces. All wide-flange shapes were fabricated using 50-ksi steel. The gusset plates were welded to the beam flanges and then bolted to the column with L3x3½x¼ steel angles. The beam was also bolted to the column with steel angles. The steel angles were welded to the gusset plate. ASTM A36 steel was used for the gusset plates and the bolts were ASTM A325 steel. All welds were fabricated using E70XX weld material. Back-to-back WT5x11 sections were used to bolt the braces to the gusset plates.

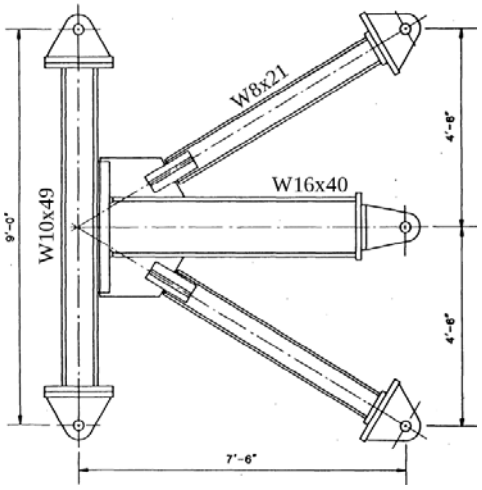

Figure 2.6 Elevation view of braced frame subassembly (Gross and Cheok 1988).

Three specimen configurations were developed: concentric connection with strong-axis column, shown in Figure 2.6; eccentric connection with strong-axis column; and eccentric connection with weak-axis column. The brace-to-gusset plate and gusset plate-to-column connections were capacity designed for the demand corresponding to gusset plate buckling. Monotonic lateral load was applied to the top of the column and the upper brace by a rigid

loading beam. The free ends of the column, beam, and lower brace were attached to reaction fixtures with pinned connections. Loading continued until gusset plate buckling occurred, typically around 0.0075 rad story drift.

The lateral load vs. lateral displacement curve for the concentric connection with strong-axis column is shown in Figure 2.7. The specimen remained elastic up to a lateral load of 90 kips, when slip in the lower brace-to-gusset connection occurred. Ultimate lateral load of 107 kips was achieved at a displacement of 0.50 in, when the lower gusset plate buckled. Close examination of Figure 2.7 reveals, however, that the subassembly possessed some stiffness after gusset plate buckling. The eccentric, strong-axis column specimen exhibited similar post-buckling behavior.

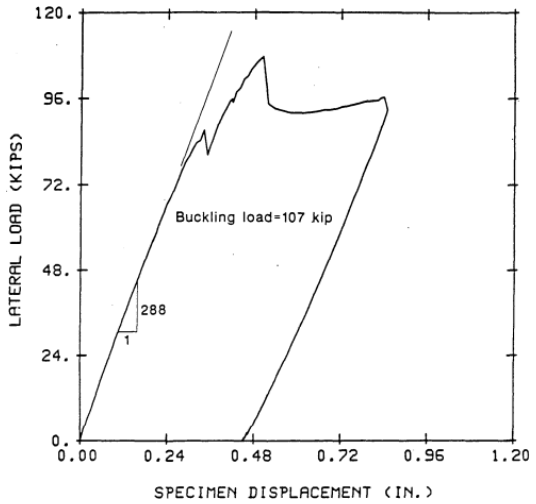

Figure 2.7 Lateral load vs. specimen displacement (Gross and Cheok 1988).

The post-buckling stiffness can be attributed to flexural strength in the beam-column connection. As part of their instrumentation scheme, Gross and Cheok (1988) recorded flange and web strains in the beam. Coupling the strain data with stress-strain curves for the beam material allowed the authors to compute the resultant shear force and moment in the beam at this location. The moment diagram for the beam, given in Figure 2.8, was then computed using

statics. For the concentric, strong-axis specimen, the maximum moment carried by the beam-column connection with gusset plate was 817 kip-in, which corresponded to 18% of the beam plastic moment.

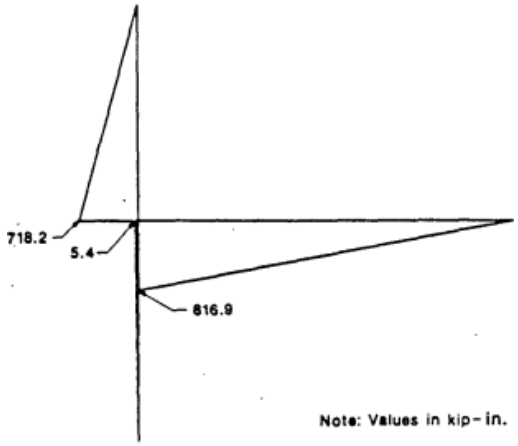

Figure 2.8 Moment diagram for concentric, strong-axis specimen (Gross and Cheok 1988).

The eccentric, strong-axis connection sustained a maximum moment equal to 22% of the beam plastic moment capacity. The beam plastic moment was computed using a yield stress equal to 63 ksi, which the authors determined from tensile coupon tests. Clearly, the test results reported by Gross and Cheok (1988) demonstrate beam-column connections with gusset plates possess appreciable flexural strength.

The flexural strength of beam-column connections with gusset plates was also evident in a full-scale test of a special concentrically braced frame (SCBF) conducted by Uriz and Mahin (2008) at the University of California, Berkeley. The test was part of a larger study that evaluated the accuracy of existing computational models for cyclic brace behavior in braced frames. The one-bay, two-story test structure is shown in Figure 2.9. The test structure had a column spacing of 20 ft and a story height of 9 ft. Wide flange sections were used for the beams and columns and HSS sections were used for the braces. The structure was designed and

detailed to meet the requirements for a SCBF per the AISC *Seismic Design Provisions* (AISC 1997). Symmetric, cyclic loading, applied to the top of the frame, was used to evaluate the behavior of the test structure.

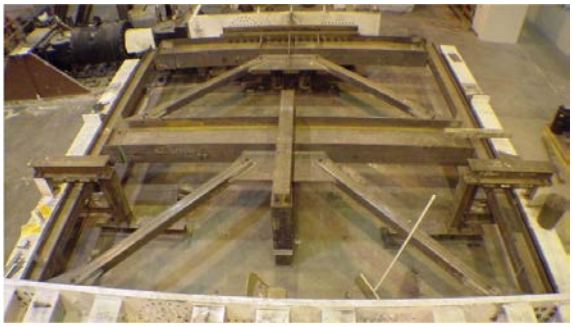

Figure 2.9 SCBF test setup (Uriz and Mahin 2008).

During the test, both braces in the first story buckled and, eventually, fractured due to local buckling. Appreciable load was still sustained by the test structure even though both braces experienced complete section loss. Uriz and Mahin (2008) concluded frame action, resulting from the braced frame gusset plate connections, was responsible for the reserve capacity of the frame. The lateral load vs. story drift data shown in Figure 2.10 summarizes the frame behavior. In this instance, 30% of the peak lateral load carried by the system was sustained through frame action.

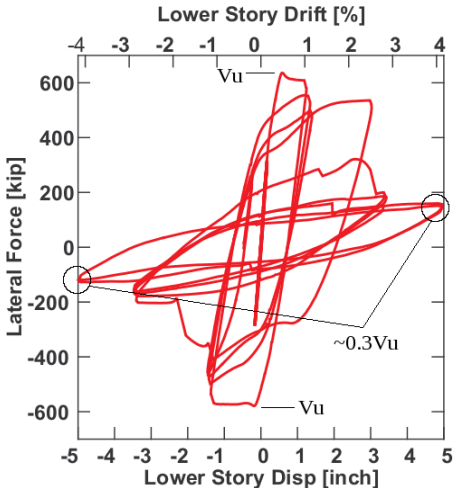

Figure 2.10 Lateral load vs. story drift (Uriz and Mahin 2008).

In addition to the tests by Gross and Cheok (1988) and Uriz and Mahin (2008), Kishiki et al. (2008) experimentally evaluated the flexural behavior of gusset plate connections for use in buckling-restrained braced frames (BRBFs). This study was initiated as a result of connection-related limit states observed in prior BRBF testing programs. Two sets of test specimens were fabricated by extracting a beam-column subassembly from a prototype BRBF by assuming inflection points at mid-height of the columns and mid-span of the beams. Representative specimens are shown in Figure 2.11. One specimen in each set was fabricated without a gusset plate so changes in flexural behavior due to the gusset plate could be evaluated.

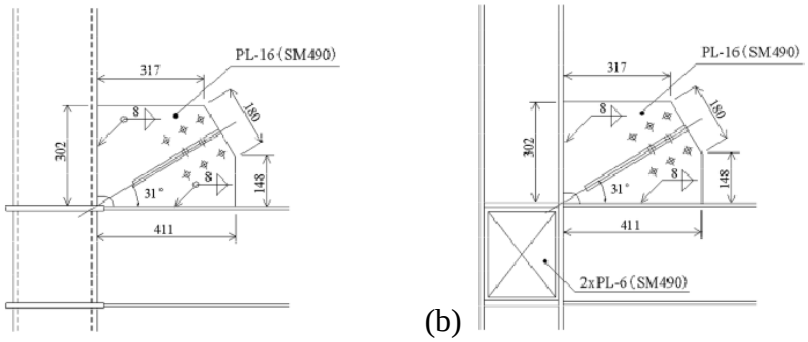

(a) (b)

Figure 2.11 Kishiki et al. (2009) test specimens: (a) HSS column; (b) Wide-flange column.

The test results revealed the gusset plate increased the flexural stiffness, strength, and ductility of the connection with the wide flange column. The flexural behavior of the connection with the tube column was unaffected. Local buckling of the beam flanges occurred at a story drift of 0.02 rad, which led to softening of the connections and, ultimately, ductile fracture of the beam flanges near the critical section of the beam, located at the toe of the gusset plate.

The experimental studies discussed above clearly show beam-column connections with gusset plates possess non-negligible flexural stiffness and strength. The studies also show the potential for using the flexural strength of braced frame connections in a CBF as a reserve lateral force-resisting system.

2.3 FLEXURAL BEHAVIOR OF SIMPLE SHEAR CONNECTIONS

In addition to recognizing that beam-column connections with gusset plates have appreciable flexural stiffness and strength, it is important to note that several other connections typically designed as simple pins possess appreciable flexural stiffness and strength. These connections are categorized as 'simple shear connections' in the current version of the AISC *Steel Construction Manual* (AISC 2005a), although they were referred to as 'Type 2' connections in previous editions. Simple shear connections are typically confined to the gravity force-resisting system in steel structures and used to transfer shear load from beams and girders to gravity columns. Double angle or single plate connections are used, although AISC also recognizes shear end plate, top and seat angle, single angle, and tee connections as simple shear connections (AISC 2005c).

Nevertheless, large-scale test results in existing literature show many simple shear connections have appreciable flexural stiffness and strength. In what follows, the flexural capacity for several types of simple shear connections is demonstrated from existing literature. The review focuses on double angle connections, top and seat angle connections, and single plate connections.

2.3.1 Flexural Behavior of Double Angle Connections

One study that investigated the flexural behavior of double angle shear connections was conducted by Astaneh et al (1989). The study was initiated to examine the influence gravity connections have on the seismic response of semi-rigid frames. In this study, six double angle connections were subjected to increasing amplitude cyclic loading to quantify their flexural

moment-rotation behavior. A tee-shaped test specimen was used in the large-scale experiments. The test setup is illustrated in Figure 2.12. The column was a W10x77 and the beam sizes were varied. Three connections with a S24x80 beam, two connections with a W16x40 beam, and one connection with a S12x31.8 beam were investigated. The column size was selected so the column would remain elastic and the beam sizes were selected based on surveys of existing steel framed buildings.

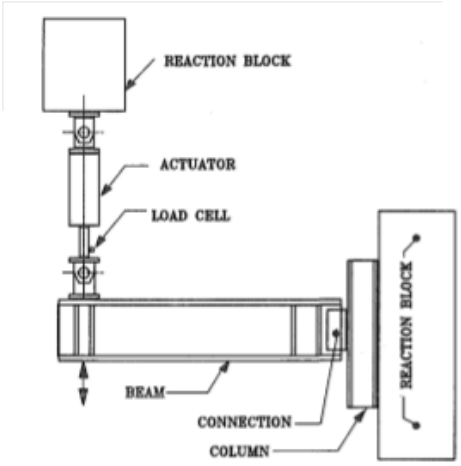

Figure 2.12 Beam-column connection test setup (Astaneh et al. 1989).

For the connection elements, five specimens used 2L3x3x3/8 and one connection used 2L3x3x5/16. The double angles were welded to the web of the beam and bolted to the column flange. Two types of 0.75-in diameter bolts were investigated: structural ribbed bolts and ASTM A325 high-strength bolts. Flexure was induced in the connection by imposing displacements at the free end of the beam with an actuator. Reaction fixtures, fixed to the testing floor, were used to anchor the actuator and column.

The results presented by Astaneh et al. (1989) show that double angle connections have appreciable flexural stiffness and strength. The connections in the study typically achieved 10% of the beam plastic moment strength and sustained rotations of 0.03 rad. The connection with a

W16x40 beam, 2L3x3x3/8, and ASTM A325 bolts realized 15% of the beam plastic moment. The moment-rotation behavior of this connection is shown in Figure 2.13.

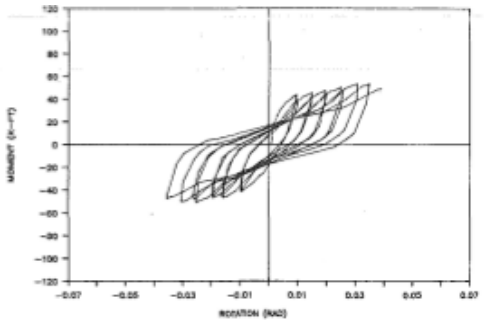

Figure 2.13 Connection moment vs. connection rotation (Astaneh et al. 1989).

Low-cycle fatigue fracture of the double angles and bolt thread failure limited the strength and ductility of the connections. The connections with structural ribbed bolts exhibited bolt thread failure and the connections with ASTM A325 bolts exhibited fracture of the steel angles. Plastic deformation concentrated along the fillet of the angles, adjacent to the web of the beam, which led to the low-cycle fatigue fractures. Astaneh et al. (1989) concluded that double angle shear connections could be used to add stiffness and strength to a semi-rigid framing system, although the authors implied that double angle connections should not be used as a primary lateral force-resisting system.

In a more recent study by Abolmaali et al. (2003), double angle connections were found to have flexural stiffness and strength exceeding that of the connections tested by Astaneh et al. (1989). Using a similar tee-shaped test setup, Abolmaali et al. (2003) examined the flexural behavior of two double angle connection configurations: angles bolted to the beam and bolted to the column (bolted-bolted), and angles welded to the beam and bolted to the column (welded-bolted). Twelve bolted-bolted and eight welded-bolted specimens were studied. Two angle sizes were used, L4x4 and L5x5, and the angle thickness varied from 0.25 in to 0.75 in. The beam

size was W16x45 and the column size was W8x67, both selected so that inelasticity would be concentrated in the double angles. The effects of bolt diameter and number of bolt rows were also considered. Bolt diameters ranged from 0.5 in to 0.875 in and the number of bolt rows varied between three and six. Flexure in the connection was simulated by applying an increasing amplitude cyclic displacement history, similar to Astaneh et al. (1989), to the free end of the beam.

Representative results for a bolted-bolted connection and a welded-bolted connection are shown in Figure 2.14. The flexural strength of the bolted-bolted connections ranged from 2.1% to 16.0% of the beam plastic moment. Rotations on the order of 0.05 rad were sustained by the bolted-bolted connections without excessive strength degradation. The bolted-bolted connections also demonstrated significant pinching due to inelasticity in the double angles and elongation of the bolt holes in the beam web.

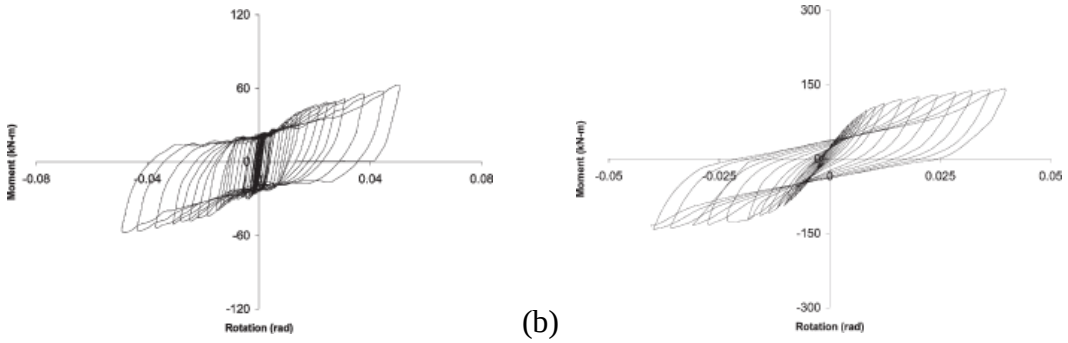

(a) (b)

Figure 2.14 Representative connection moment vs. connection rotation results: (a) Bolted-bolted connection; (b) Welded-bolted connection (Abolmaali et al. 2003).

The flexural strength of the welded-bolted connections ranged from 5.2% to 45% of the beam plastic moment, although the rotation capacity was only 0.02 rad to 0.03 rad. The larger moment capacity of the welded-bolted connections was due to thicker double angles. In addition, the elastic stiffness of the welded-bolted connections was significantly larger than the bolted-bolted

connections, due to the additional restraint the weld provided to the in-plane angle leg.

2.3.2 Flexural Behavior of Top and Seat Angle Connections

Like double angle connections, experimental evaluation of top and seat angle connections demonstrated appreciable flexural stiffness and strength in a simple shear connection. Kukreti and Abolmaali (1999) used a tee-shaped test setup and increasing amplitude cyclic loading, similar to Astaneh et al. (1989) and Abolmaali et al. (2003), to investigate the flexural behavior of top and seat angle connections. The experimental program was undertaken to develop a suite of test results that could be used to generate analytical models for the flexural behavior of top and seat angle connections. Twelve top and seat angle connections were tested. The connections had angles bolted to the beam flanges, with two rows of bolts, and bolted to the column flange, with one row of bolts. No web angles were included. The angle sizes were L6x6 and L6x4 and the angle thicknesses were 0.375 in, 0.5 in, and 0.75 in. ASTM A36 steel was selected for the angles. Two beam sizes were used, W14x43 and W16x45. A W8x67 column was selected to minimize inelasticity in the column flanges. ASTM A325 bolts were used in the connections, with diameters ranging from 0.625 in to 0.875 in. Connection rotation was recorded using a pair of LVDTs, one affixed to the top flange and the second affixed to the bottom flange of the beam. A load cell installed on the actuator recorded the applied force.

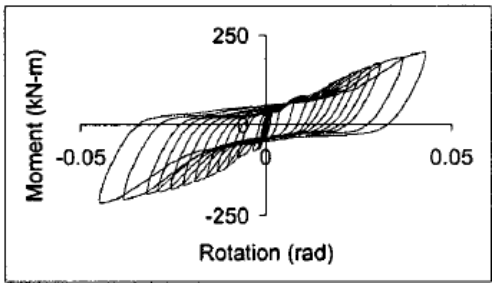

Figure 2.15 Connection moment vs. connection rotation (Kukreti and Abolmaali 1999).

Figure 2.15 illustrates the connection moment vs. connection rotation for a typical top and seat angle studied by Kukreti and Abolmaali (1999). Flexural strength values ranged from 5.2% to 36% of the beam plastic moment. The ultimate moment strength was usually realized at higher story drifts, typically 0.04 rad or larger. In addition, the connections exhibited strong pinching behavior due to inelastic deformation of the angles. The pinching effect increased with increasing story drifts. Connection stiffnesses, normalized by *EI/L* of the beam, ranged from 0.45 to 2.85.

In addition to the results presented by Kukreti and Abolmaali (1999), Azizinamini et al. (1989) also reported experimental results for top and seat angle connections with appreciable flexural stiffness and strength. The purpose of the study was to develop analytical models for the fatigue life of top and seat angle connections subject to cyclic loading. As a result, Azizinamini et al. (1999) provided little data on the flexural stiffness and strength of top and seat angle connections. The connection moment vs. rotation behavior for one connection was reported, which is reproduced in Figure 2.16.

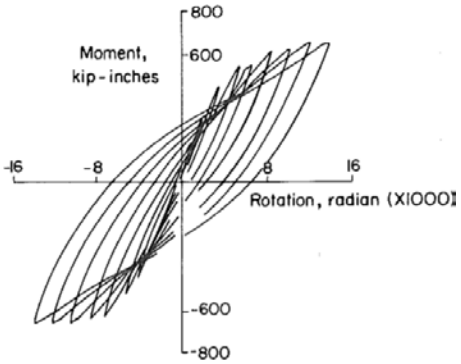

Figure 2.16 Connection moment vs. connection rotation (Azizinamini et al. 1989).

2.3.3 Flexural Behavior of Single Plate Connections

Similar to double angle and top and seat angle connections, appreciable flexural stiffness

and strength of single plate connections was observed during large-scale connection tests. The study by Liu and Astaneh-Asl (2000), mentioned previously, quantified the flexural stiffness, strength, and ductility of two single plate connections without a composite concrete slab. The flexural strength of both connections was approximately 20% of the beam plastic moment. The connections also sustained rotations of approximately 0.10 rad without significant strength degradation, but stiffness degradation was significant.

Additional tests of the flexural behavior of single plate connections were conducted by Crocker and Chambers (2004) at the University of Utah. In this study, three single plate connections were tested to study their rotation capacity. When large drifts occur during seismic events, typically in higher ductility systems undergoing inelastic deformation, the rotational demands on the gravity connections can lead to degradation of gravity load carrying capacity. The plates were 0.375-in thick, ASTM A36 steel and the number of bolt rows ranged from 3 to 6. The connection moment vs. connection rotation of a representative shear plate connection from the study by Crocker and Chambers (2004) is illustrated in Figure 2.17.

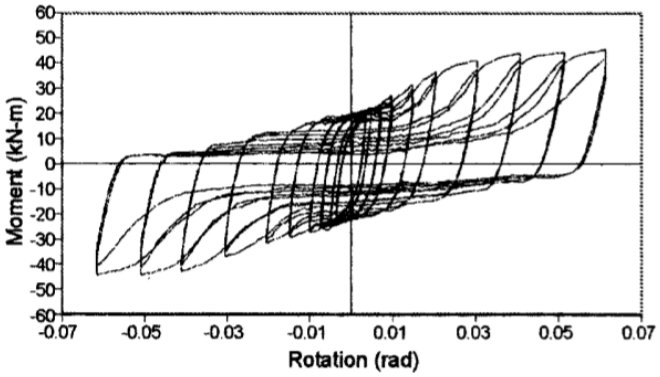

Figure 2.17 Connection moment vs. connection rotation (Crocker and Chambers 2004).

The connection stiffnesses and strengths, however, were significantly lower than the data presented by Liu and Astaneh (2000). The strength ranged from 3% to 6% of the beam plastic

moment and the connection stiffness normalized by *EI/L* of the beam ranged from 0.33 to 0.65.

2.4 SUMMARY OF LITERATURE REVIEW

Two primary conclusions were derived from the preceding literature review. First, reserve lateral force-resisting capacity exists in steel structures and plays a significant role in collapse prevention during seismic events. Reserve capacity was observed after the 1994 Northridge, California, earthquake where damage to moment resisting and braced frames was widespread, yet no collapses occurred. In addition, the stability of the damaged structures was maintained during aftershocks. Large-scale tests of braced frames (Bertero et al. 1989, Whittaker et al. 1989, Gross and Cheok 1988, Uriz and Mahin 2008) and recent computational analyses (Rai and Goel 2003, Hines et al. 2009) corroborated this observation. Second, full-scale connection tests demonstrated that connections typically designed as simple pins may possess appreciable flexural stiffness and strength. The flexural stiffness and strength of double angle, top and seat angle, and single plate shear connections were demonstrated from existing literature.

Based on the above, it is evident that beam-column connections with gusset plates are a prime candidate for inclusion in a reserve lateral force-resisting system for enhancing the collapse performance of CBFs in moderate seismic regions. The reserve capacity provided by braced frame connections has been clearly demonstrated from existing literature. In addition, the flexural capacity of braced frame connections has long been recognized even though it has not been extensively quantified or used in design. Thus, there is a foundation for this study in existing literature.

CHAPTER 3

BEAM-COLUMN CONNECTION TESTING PROGRAM

The preceding literature review demonstrated that beam-column connections with gusset plates have appreciable flexural stiffness and strength, although these characteristics are typically neglected in design. The review also demonstrated that the strength of gusset plate connections, as well as other connections that are typically designed as ideal pins, can provide adequate reserve lateral force-resisting capacity to maintain structural stability in the event of damage to the primary lateral force-resisting system in a steel structure. The flexural behavior of isolated braced frame connections, however, has only been quantified for a limited number of cases.

Thus, full-scale tests were conducted to quantify the flexural stiffness, strength, and ductility of beam-column connections with gusset plates. The large-scale tests were the first step toward demonstrating that braced frame connections can provide adequate reserve capacity to yield collapse prevention performance for steel structures in moderate seismic regions. The results from the experimental program were used to develop finite element models focused on predicting the moment-rotation response of beam-column connections with gusset plates. Ultimately, the knowledge gained from the experimental and computational studies was used to develop system models that contained varying levels of reserve capacity. These models were used to assess the impact of the flexural capacity of braced frame connections on the collapse performance of CBFs in moderate seismic regions. In what follows, the braced frame connection testing program and results are summarized. In addition, the results of tensile coupon and bolt tensile tests conducted to characterize fundamental behavior and to obtain data for the finite

element models are detailed.

3.1 PROTOTYPE CONNECTION DESIGN AND FABRICATION

To study reserve capacity in CBFs for moderate seismic regions, a set of full-scale beam-column connections with gusset plates was developed for experimental evaluation. A bracing connection with double angles joining the beam and gusset plate to the column, which is typical of current practice, was established as a baseline and subsequent connection details were variations intended to improve the flexural strength, stiffness, and ductility of the connection. This connection was extracted from a CBF designed by LeMessurier Consultants as part of a lateral force-resisting system in a building located in Boston, MA (Cheever and Hines 2009). The portion of the prototype braced frame used to develop the test specimens had a 9-ft story height and a 19-ft bay width, with W14x90 columns and W10x49 beams. The beams and columns were ASTM A992 steel, the connection plates and angles were ASTM A36 steel, the 0.75-in diameter bolts were ASTM A325 steel and E70XX weld material was used.

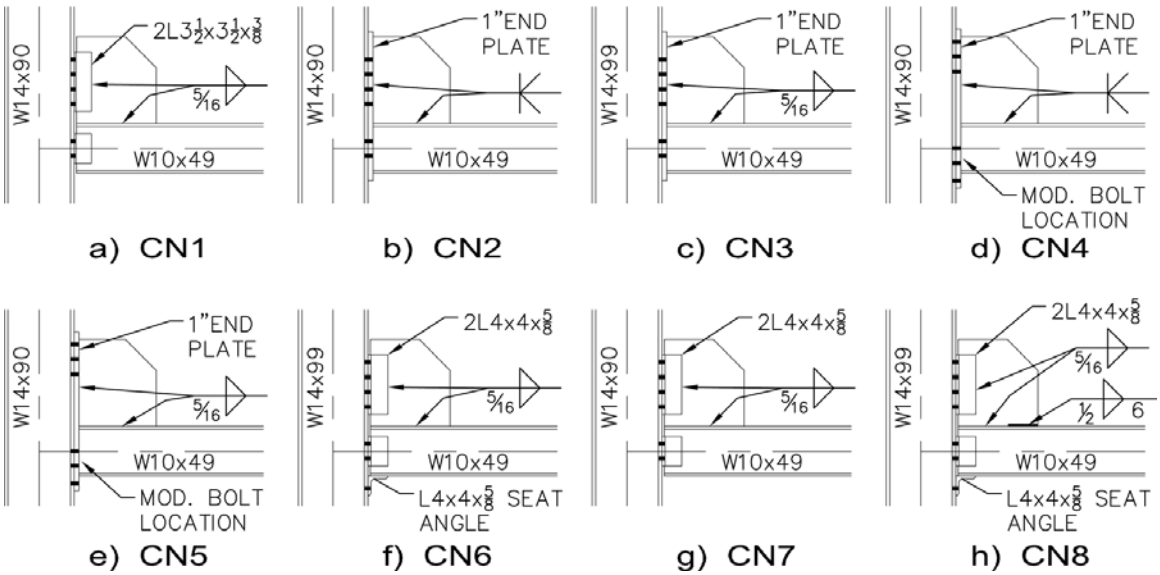

Figure 3.1 Connection details.

The baseline connection, which is named CN1 and is shown in Figure 3.1a, was designed according to the Uniform Force Method, as described in the American Institute of Steel Construction (AISC) *Steel Construction Manual* (2005c). The remaining connections, which are named CN2 – CN8, were developed by modifying various connection parameters to study potential methods for enhancing the flexural stiffness, strength, and ductility of the connection. These eight connection details are shown in Figure 3.1 and a detailed summary of the connection parameters is given in Table 3.1.

Table 3.1 Summary of connection parameters.

Specimen	Connecting Element	Gusset Plate-Beam Weld	Bolt Layout	Beam	Column
CN1	3/8" double angles	5/16" fillet	Standard	W10x49	W14x90
CN2	1" end plate	CJP	Standard	W10x49	W14x90
CN3	1" end plate	5/16" fillet	Standard	W10x49	W14x90
CN4	1" end plate	CJP	Modified	W10x49	W14x90
CN5	1" end plate	5/16" fillet	Modified	W10x49	W14x90
CN6	5/8" double angles with seat	5/16" fillet	Standard	W10x49	W14x90
CN7	5/8" double angles	5/16" fillet	Standard	W10x49	W14x90
CN8	5/8" double angles with seat	1/2" fillet*	Standard	W10x49	W14x90

*The 1/2" fillet weld started at the toe of the gusset plate and extends 6"; the remaining fillet weld was 5/16".

For connections CN2 – CN5, the baseline 0.375-in thick double angles in CN1 were replaced with a 1-in thick end plate. Figure 3.1b illustrates an end plate connection with a bolt configuration that matches the baseline connection, whereas Figure 3.1d illustrates a similar connection with modified bolt locations where the bolts have been shifted to the top and bottom of the end plate to develop greater flexural stiffness and strength. Figure 3.2 shows the geometry for the standard and modified bolt locations, as well as the annotation scheme used to reference the bolts in the discussion of test results. Figures 3.1b to 3.1e also show that within these configurations, the gusset plate-beam and gusset plate-end plate welds were varied between fillet and complete-joint-penetration (CJP). Connections CN1 – CN6 were fabricated by Novel Iron Works of Greenland, New Hampshire.

For connections CN6 – CN8 the baseline 3/8” thick double angles in CN1 were replaced with 0.625-in thick double angles. Since inelasticity in CN1 was confined to the double angles, the beam and gusset plate were reused in CN7. The gusset plate and beam web angles fillet welds were removed with a grinder, and the existing angles taken off. Then, new angles were welded to the gusset plate and beam web using the gas-metal arc welding (GMAW) process. Fabrication of CN7 was carried out by staff in the Civil Engineering Machine Shop at the University of Illinois at Urbana-Champaign. The column from CN1 was also reused in CN7.

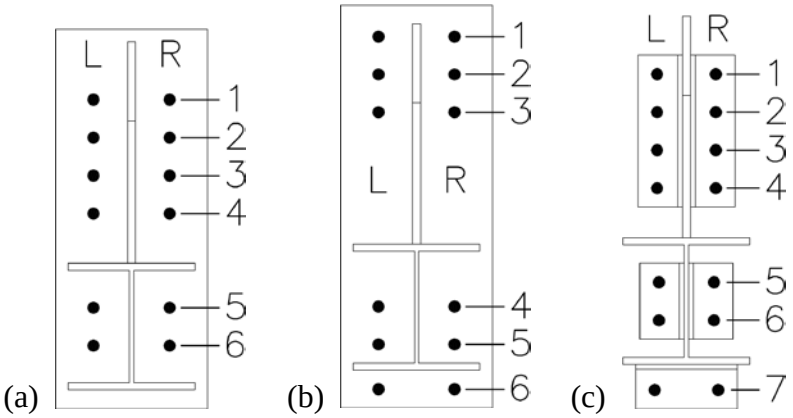

Figure 3.2 Bolt locations: (a) standard; (b) modified; (c) seat angle.

In addition to increasing the angle thickness, a 0.625-in seat angle was added to connections CN6 and CN8 to aid in transferring the beam bottom flange force to the column. A fillet weld was used to join the beam and gusset plate in CN6 and CN8. CN6 was fabricated with 0.3125-in fillet welds. As will be discussed in more detail in Section 3.5.1, failure of the gusset plate-beam fillet weld was the critical factor leading to strength loss in positive bending of CN3 and CN5 – CN8. As a result, in CN8 the leg size of the first 6 in of the welded interface, starting at the gusset plate toe, was increased to 0.5 in. The primary goal of CN8 was to prevent gusset plate-beam fillet weld failure without resorting to a CJP weld. The bolt configurations for CN6 – CN8 conformed to the baseline connection, with additional bolts required for the seat

angles in CN6 and CN8. In addition, the column from CN6 was reused for CN8 because no inelasticity was observed.

3.2 LARGE-SCALE TEST SETUP

Testing was conducted in the Newmark Structural Engineering Laboratory at the University of Illinois at Urbana-Champaign. The experimental beam-column subassembly was extracted from the prototype frame by assuming inflection points at story mid-height and beam mid-span. This assumption is based on the scenario that arises after both braces in the story have fractured. The present research did not simulate damage to the gusset plates that could occur prior to brace fracture. The T-shaped test setup for the large-scale connection subassembly, which was assembled horizontally, is illustrated in Figure 3.3.

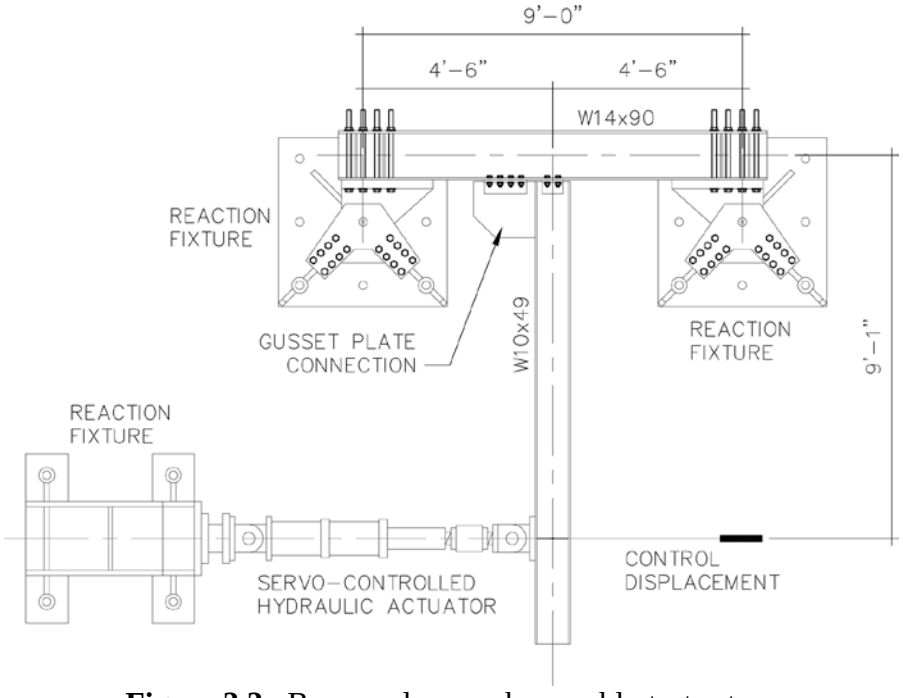

Figure 3.3 Beam-column subassembly test setup.

The column was attached to reaction fixtures, which were anchored to the strong floor

with four, 2-in diameter steel rods. Eight, 1-in diameter threaded rods were used to connect each end of the column to the reaction fixtures. Stiffeners were added to the column to prevent deformation of the column web due to tension in the threaded rods. A reaction block was also placed under the free end of the beam to support the weight of the connection subassembly. The beam was braced laterally within the span and loaded by a 100-kip, servo-controlled hydraulic actuator with a 20-in stroke. The actuator was also attached to a reaction fixture that was anchored to the strong floor in the same manner as the column reaction fixtures. Symmetric cyclic loading, based on the SAC protocol (FEMA 2000a) and described in Table 3.2, was used to evaluate connection flexural behavior and performance. Following the approach used in the SAC program, gravity loads were not simulated in the laboratory.

Table 3.2 Cyclic loading protocol.

Story Drift Angle (rad)	Load Point Displacement (in)	Number of Cycles
0.00375	0.41	6
0.005	0.55	6
0.0075	0.82	6
0.01	1.09	4
0.015	1.64	2
0.02	2.18	2
0.03	3.27	2
0.04	4.36	2
0.05	5.45	2
0.06	6.54	2

3.3 DATA ACQUISITION

Data acquisition for the large-scale experiments was conducted using National Instruments hardware in conjunction with LabView software and a series of linear variable differential transformers (LVDTs), linear potentiometers, and strain gages. The LVDTs, linear potentiometers, and strain gages were used to quantify the global and local behaviors of the connections, as well as provide insight into column behavior due to the flexural strength of the

gusset plate connections. Still-image cameras were also used to capture pictures of critical areas in the connection at a specific time interval throughout the tests. The following provides a brief overview of the data acquisition system and the displacements and strains recorded.

3.3.1 Data Acquisition System

The data acquisition system used for the large-scale tests was a National Instruments SCXI-1001, 12-slot chassis connected to a desktop computer through a PCI card. The primary means of connecting transducers to the data acquisition system is through modules that are specific to the type of transducer being used. To connect strain gages, SCXI-1520 modules were used with SCXI-1314 terminal blocks. The SCXI-1520 is an 8-channel, universal strain gage module. The SCXI-1314 terminal block was wired to breakout boxes, which were connected to the strain gages. The SCXI-1314 terminal block was attached to the strain gage module.

Since the output from the displacement transducers was analog, a National Instruments BNC-2095 terminal block, which can record 32 channels of analog input from coaxial cables with BNC connectors, was connected to the data acquisition system using an SCXI-1102 voltage input module. All displacement transducers, as well as the load cell output from the actuator and the strain output from the bolt strain gages, were connected to the BNC-2095.

LabView software, developed by National Instruments, was used to record the test data. The software was configured to work with the hardware by staff in the Newmark Structural Engineering Laboratory. Data was sampled at a rate of 0.2 Hz. This sampling rate was chosen so the resulting data would adequately characterize the observed behavior, but the data files would not be so large that the data would become difficult to process.

3.3.2 Displacement Measurements

The primary means for acquiring data about the flexural behavior of braced frame connections were displacement measurements. Measurements were made of the global movement of the subassembly as well as locally within the connection region. The displacements that were observed are shown in Figure 3.4. In addition, Table 3.3 lists the type, manufacturer, model number, and stroke for each of the transducers that were used during the full-scale tests.

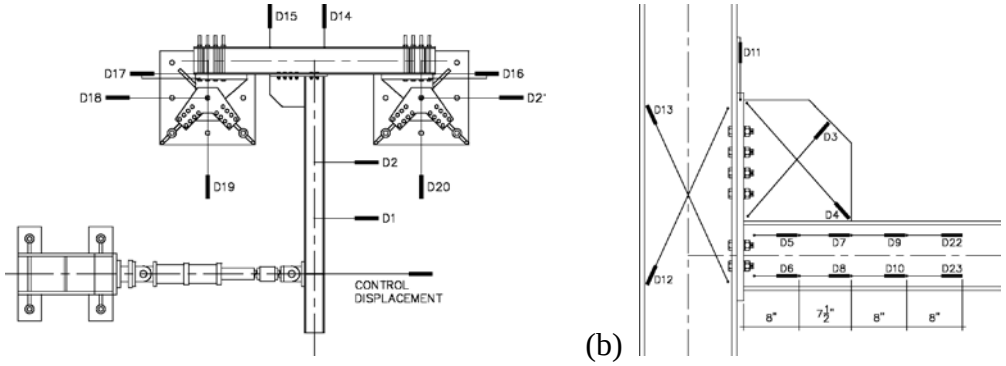

Figure 3.4 Displacement measurements: (a) global; (b) local.

The control displacement was used as feedback to the actuator controller, which was configured for displacement control. The transducer was anchored independent of the actuator and connection subassembly so an accurate control displacement could be maintained.

Displacements *D*1 and *D*2 measured elastic deflection of the connection beam. *D*3 and *D*4 were intended to quantify the shear deformation of the gusset plate, but the measurements included both in-plane and out-of-plane displacements. Thus, the shear deformation of the gusset plates could not be calculated accurately. Displacements *D*5-*D*10 and *D*22 and *D*23 were placed within the beam web and were used to calculate relative rotations of beam cross sections. The relative rotations were used to show that plastic rotation in the beam was concentrated at the toe of the gusset plate. *D*11 was needed to quantify slip between the column flange and the

gusset plate angles or end plate. Examination of the data from *D*11 revealed minimal connection slip, however. *D*12 and *D*13 were needed to calculate the panel zone shear deformation of the column and *D*14 and *D*15 were used to measure rotation of the column. Slip between the column and reaction fixtures was measured from *D*16 and *D*17. Finally, translation and rotation of the connection subassembly was computed from displacements *D*18-*D*21.

Table 3.3 Displacement transducer data.

Identifier	Type	Manufacturer	Model	Stroke (in)
Control Displacement	Temposonic	MTS	TTSRO20240AS1R	24
D1	AC LVDT	Collins	LMA-711T84	10
D2	AC LVDT	Collins	LMA-711T84	10
D3	AC LVDT	Trans Tek	0244-0000	2
D4	AC LVDT	Collins	LMA-711T42	2
D5	DC LVDT	Trans Tek	0350-0000	0.1
D6	DC LVDT	Trans Tek	0350-0000	0.1
D7	Linear Potentiometer	Celesco	CLP-25	1
D8	Linear Potentiometer	Celesco	CLP-25	1
D9	Linear Potentiometer	Celesco	CLP-25	1
D10	Linear Potentiometer	Celesco	CLP-25	1
D11	AC LVDT	Collins	LMA-711T42	2
D12	DC LVDT	Trans Tek	0351-0000	0.2
D13	DC LVDT	Trans Tek	0351-0000	0.2
D14	AC LVDT	Collins	LMA-711T42	2
D15	AC LVDT	Collins	LMA-711T42	2
D16	AC LVDT	Collins	LMA-711T42	2
D17	AC LVDT	Collins	LMA-711T42	2
D18	AC LVDT	Collins	LMA-711T42	2
D19	AC LVDT	Collins	LMA-711T42	2
D20	AC LVDT	Collins	LMA-711T42	2
D21	AC LVDT	Collins	LMA-711T42	2
D22	Linear Potentiometer	Celesco	CLP-25	1
D23	Linear Potentiometer	Celesco	CLP-25	1

AC: alternating current; DC: direct current.

All AC LDVTs were powered by a Macrosensors LPC-2000 power supply and signal conditioner. All DC LVDTs and linear potentiometers were supplied with DC power. The input

voltages for the DC LVDTs and linear potentiometers were recorded so the displacement data could be adjusted based on fluctuations in the input voltage.

Prior to use, all displacement transducers were calibrated to obtain the relationship between displacement and output voltage. The output voltage for each transducer was recorded for displacement increments equal to 10% of the transducer range. For example, *D*1 has a stroke of 10 in, which corresponds to a range of +/- 5 in. Thus, calibration points were established every 0.5 in for *D*1.

3.3.3 Strain Measurements

Strain measurements were recorded from the beam flanges and web, gusset plate, and column web using electrical resistance strain gages. The strain gages were manufactured by Tokyo Sokki Kenkyujo Co., Ltd. Locations of the strain gages are given in Figure 3.5. The linear strain gages on the beam flanges were model FLA-5-11 with a resistance of 120 ohms and a gage factor of 2.00. The '5' in the gage designation indicates the gage length was 5 mm and the '11' indicates the gage provides temperature compensation for materials with a coefficient of thermal expansion equal to $11x10^{-6}$, which is appropriate for mild steel. The strain rosettes were model FRA-5-11 with a resistance of 120 ohms and a gage factor of 2.10.

The surface of the steel was prepared to receive the strain gages by removing the mill scale and oxides with an electric grinder with an 80-grit sanding flap. Next, the surface was refined by hand sanding with 120-grit, 220-grit, and 320-grit silicon-carbide sanding paper. Then, the gage location was marked by burnishing the surface with a ball point pen. The surface was cleaned prior to application of the gage with a mild acid, which was neutralized with a basic

solution. The acid and base were manufactured by Vishay, Inc. Finally, the gage was adhered to the surface using cyanoacrylate adhesive. The resistance of all gages was verified with a multimeter.

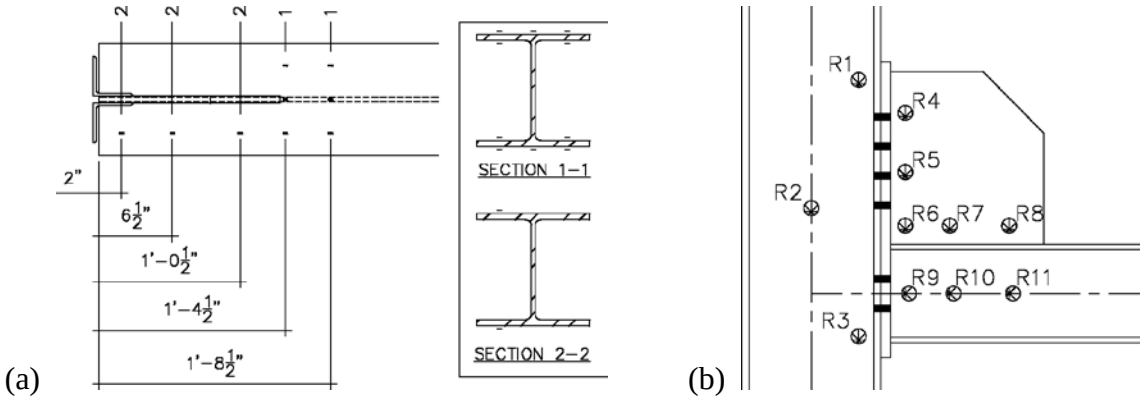

Figure 3.5 Location of strain gages: (a) linear strain gages; (b) strain rosettes.

While the strain gages are not as useful in quantifying the flexural stiffness and strength of braced frame connections, they provide valuable insight into how the components of the connection behave. The linear gages were used to determine variation of beam flange strain through the connection region. In addition, linear gages were placed on the inside and outside of the flanges at the toe of the gusset plate, as shown in Section 1-1 in Figure 3.5a, to observe local buckling of the flanges, if it occurred. Local buckling of the flanges, however, did not occur during any connection tests. The linear gages at the toe of the gusset plate were also useful in corroborating the development of a plastic hinge at the toe of the gusset plate. All the linear strain gages and strain rosettes were connected to the data acquisition system using the SCXI-1314 terminal blocks, which were connected to the SCXI-1520 universal strain gage modules.

In addition to the linear strain gages and strain rosettes, specially designed bolt strain gages were installed in the shanks of the connection bolts. A cross section of a bolt with strain gage is illustrated in Figure 3.6. The bolt strain gages, manufactured by Tokyo Sokki Kenkyujo

Co., Ltd., were model BTM-6C with a resistance of 120 ohms, a gage length of 6 mm, and a gage factor of 2.10.

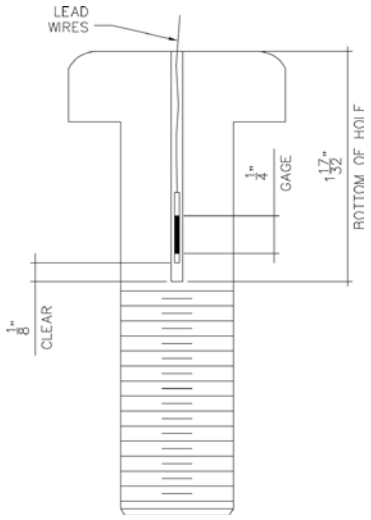

Figure 3.6 **C**ross section of bolt with strain gage.

To install the gages, a 0.078-in diameter hole was drilled approximately 1.5 in into the bolt shank. In order to prevent degradation of bolt tensile capacity, the hole was stopped outside the threaded region. In addition, the manufacturer's instructions recommended the bottom of the bolt strain gage be located 0.25 in above the bottom of the hole. This requirement was met by making a bend in the bolt gage lead wires during gage installation. After locating the bolt strain gage, residue from the drilling process was removed from the hole by a pipe cleaner dipped in acetone. Then, the strain gages were bonded to the inside of the hole with AE-10, high-strength epoxy manufactured by Vishay, Inc. The epoxy was mixed according to the manufacturer's recommendations. AE-10 epoxy requires elevated temperatures to reach maximum strength while curing, so the bolts were placed in an oven at 200 ºF for two hours after installing the bolt strain gages.

In addition to recording strain in the bolt shanks during the large-scale tests, the bolt strain gages were used to obtain accurate pretension forces in the bolts during installation. To

establish a force-per-microstrain calibration, the bolts were loaded from 0 to 14 kips while recording strain output from the bolt gages. The upper load limit for the bolt strain gage calibrations was selected as half the minimum pretension force for 0.75-in diameter, A325 bolts, which is 28 kips (AISC 2005b). Prof. Gian Rassati from the Department of Civil Engineering at the University of Cincinnati provided the testing equipment and data acquisition system for the bolt calibration.

In lieu of connecting the bolt strain gages to the strain gage modules, the bolt gages were connected to strain gage signal conditioners and the output routed to the BNC-2095 module in the data acquisition system. This was done because gages connected to the strain gage modules are balanced every time the data acquisition software was started. Since the pretension force was applied to the bolts several days in advance of a test, it was desirable to prevent balancing of the bolt strain gage bridges after bolt installation.

3.4 MOMENT-ROTATION RESPONSE OF CONNECTIONS

Normalized moment vs. story drift was used to quantify the global behavior and performance of the prototype connections. Normalized moment is the ratio of the applied moment, M, to the expected plastic moment $M_{p,exp}$. The applied moment, computed at the toe of the gusset plate, is equal to the actuator load multiplied by the moment arm of 90 in. $M_{p,exp}$ is defined based on the AISC *Seismic Provisions for Structural Steel Buildings* as:

$$M_{p,exp} = 1.1 R_y F_y Z_x \tag{3.1}$$

where R_y is the ratio of expected yield stress to the specified minimum yield stress, equal to 1.1 for ASTM A992 steel; F_y is the specified minimum yield stress; and Z_x is the plastic section

modulus (AISC 2005c). Story drift is computed as the beam tip displacement divided by the distance to the centerline of the column, equal to 109 in. The envelope of each connection response is plotted in Figure 3.7.

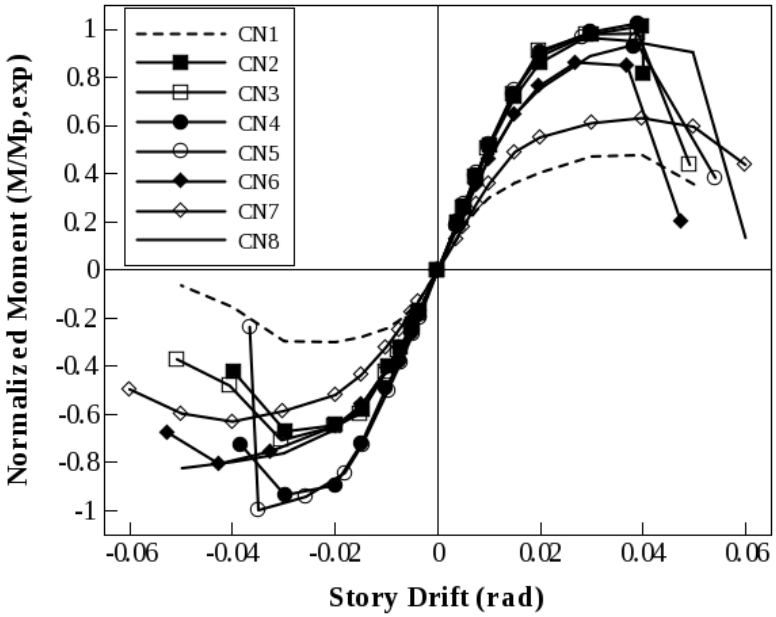

Figure 3.7 Normalized moment vs. story drift envelopes.

Table 3.4 Summary of connection behavior.

Specimen Number	Secant Stiffness $K_s \cdot (L/EI)_{beam}$ (pos/neg)	At Maximum Positive Moment		At Maximum Positive Drift		At Maximum Negative Moment		At Maximum Negative Drift	
		M / $M_{p,exp}$	Drift (rad)	M / $M_{p,exp}$	Drift (rad)	M / $M_{p,exp}$	Drift (rad)	M / $M_{p,exp}$	Drift (rad)
CN1	3.5/2.1	0.48	0.04	0.36	0.05	-0.30	-0.02	-0.06	-0.05
CN2	24.0/11.0	1.01	0.04	0.82	0.04	-0.67	-0.03	-0.42	-0.04
CN3	22.8/10.6	0.98	0.04	0.44	0.05	-0.71	-0.03	-0.37	-0.05
CN4	26.2/24.0	1.02	0.04	0.93	0.04	-0.93	-0.03	-0.73	-0.04
CN5	26.4/24.0	0.97	0.03	0.38	0.054	-1.00	-0.035	-0.24	-0.037
CN6	15.7/10.5	0.86	0.03	0.20	0.05	-0.81	-0.04	-0.67	-0.05
CN7	7.3/5.1	0.63	0.04	0.44	0.06	-0.63	-0.04	-0.49	-0.06
CN8	17.1/11.1	0.94	0.04	0.13	0.06	-0.82	-0.05	-0.82	-0.05

In addition, Table 3.4 summarizes the normalized moment and story drift for each connection at the points of initial yielding, maximum moment, and maximum story drift. Since the connection

response envelopes are not symmetrical with respect to the axis of bending, results are given for both positive moment and negative moment. Positive moment is defined as moment that induces tension in the gusset plate, which corresponds to points in the first quadrant of Figure 3.7.

The envelope connection responses plotted in Fig. 3.7 show that all connection variations increased the stiffness and strength of the connection over the stiffness and strength achieved by CN1. Connections CN2 – CN5 achieved, or nearly achieved, $M_{p,exp}$ in positive bending and connections CN4 and CN5 also nearly achieved and achieved $M_{p,exp}$ in negative bending, respectively. Connections CN6 – CN8 achieved 63% to 94% of $M_{p,exp}$ in positive and negative bending. All connections sustained at least two cycles of loading at a story drift of 0.04 rad, although the double angle connections typically sustained larger story drifts without significant strength degradation than the end plate connections. Connection performance in positive bending was typically limited by failure of the gusset plate-beam fillet weld and connection performance in negative bending was limited by bolt fracture. The critical limit states that were observed during each test are summarized in Figure 3.8 and details of critical angle and weld limit states for CN1 and CN5, respectively, are shown in Figure 3.9.

The results from CN1 are discussed first and compared to typical design assumptions related to connection strength and stiffness. After establishing the baseline behavior, the results from the end plate connections, CN2 – CN5, are presented and their behavior compared to the behavior of CN1. Next, the results from the modified angle connections, CN6 – CN8, are presented along with comparisons to the baseline and end plate connections. Finally, the energy dissipated vs. cycle is plotted for each connection and compared to results from connections used in high seismic regions.

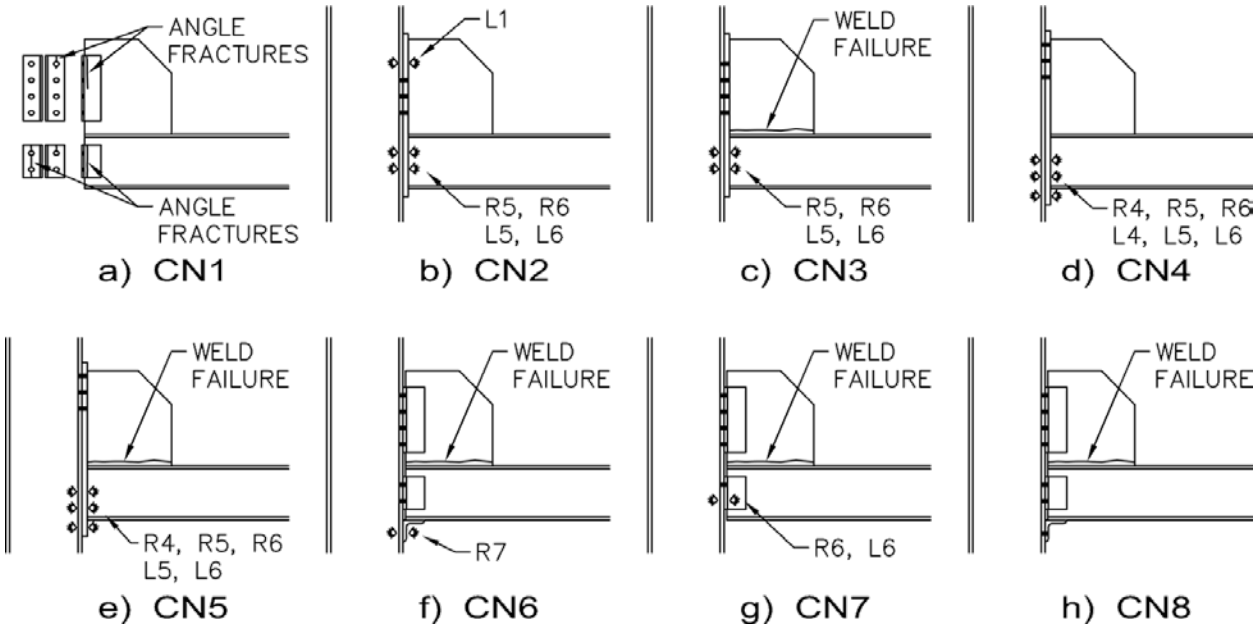

Figure 3.8 Summary of failure limit states (column CN1 removed for clarity; bolt fractures denoted by bolt name, e.g. L1).

(a) (b)

(c) (d)

Figure 3.9 Photographs of connection limit states: (a) CN1 gusset plate angle; (b) CN1 beam web angle; (c) CN5 fillet weld at maximum moment; (d) CN5 fillet weld at maximum story drift.

3.4.1 Behavior of Baseline Connection (CN1)

Current design practice assumes vertical bracing connections composed of double angles have negligible flexural strength and stiffness. The results from CN1, however, show that double angle braced frame connections have flexural strength and stiffness that could aid the collapse resistance of structures designed using R = 3. The cyclic normalized moment vs. story drift history for CN1 is illustrated in Figure 3.10, which shows the peak positive and negative moments for CN1 are 48% and 30% of $M_{p,exp}$, respectively, and that the connection sustained story drift between 0.03 and 0.04 rad without significant strength degradation.

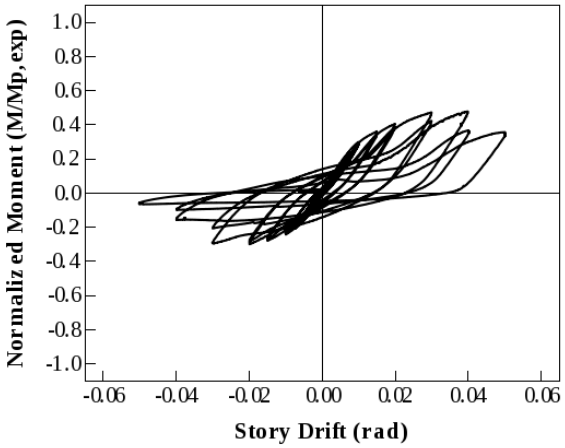

Figure 3.10 Normalized moment vs. story drift for CN1.

The normalized secant stiffness, $K_S \cdot (L/EI)_{beam}$, computed from data for connection moment vs. connection rotation, which is shown in Figure 3.11 for CN1, is 3.5 in positive bending and 2.1 in negative bending. The commentary to Chapter B of the AISC *Specification* defines the boundary between simple and partially-restrained connections as $K_S \cdot (L/EI)_{beam}$ = 2, where the normalized secant stiffness is calculated using service loads. Since the service loads in the prototype building for the present research were very small and the resulting connection secant stiffness was close to the initial stiffness, the normalized secant stiffness was quantified by

finding the intersection of the connection moment vs. connection rotation curve with the beam line for a uniformly loaded W10x49.

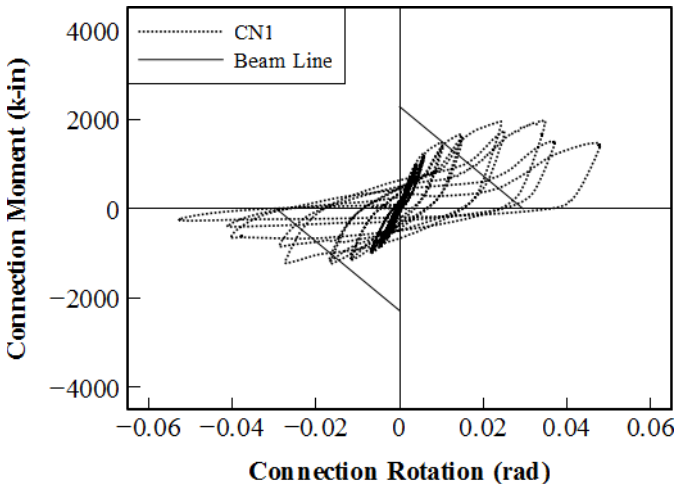

Figure 3.11 Connection moment vs. connection rotation for CN1.

The moment-axis intercept for the beam line was found by dividing $M_{p,exp}$ by 1.6, which is the scale factor used in Chapter C of the AISC *Specification* to approximately convert from a service load level to an ultimate strength level. To compute the rotation axis intercept, an equivalent uniform load, w, for the beam was computed from $M_{p,exp}/1.6 = wL^2/12$, which is based on the end moment for a uniformly-loaded, fixed-end beam, and then the rotation axis intercept was computed from $\theta = wL^3/24EI$, which is the end rotation for a uniformly-loaded, simply-supported beam. This procedure assumes the connecting beam was designed with a plastic moment capacity nearly equal to the expected ultimate load, M_u.

Connection moment was computed as the actuator load multiplied by the distance to the face of the column, which was 102 in. Since connection rotation was not directly measured during testing, it was computed from data for column rotation, beam plastic hinge rotation, and beam elastic rotation. The first step in computing connection rotation was to determine the portion of the beam tip displacement due to connection rotation, which is found from

$$\Delta_{Tip} = \Delta_{Column} + \Delta_{Conn} + \Delta_{PH} + \Delta_{Beam} \tag{3.2}$$

where Δ_{Tip} is the beam tip displacement, Δ_{Column} is the tip displacement due to column rotation, Δ_{Conn} is the tip displacement due to connection rotation, Δ_{PH} is the tip displacement due to beam plastic hinging at the toe of the gusset plate, and Δ_{Beam} is the tip displacement due to elastic deformation of the beam. The contributions of Δ_{Column} and Δ_{PH} to beam tip displacement were found by multiplying data for θ_{Column} and θ_{PH} by the distance from their centers of rotation to the applied load. The distances were 109 in for θ_{Column} and 90 in for θ_{PH}. Data for θ_{Column} and θ_{PH} was generated from displacement measurements using the equations

$$\theta_{Column} = \frac{D15 - D14}{27.5"} \tag{3.3}$$

$$\theta_{PH} = \theta_{B1} - \frac{P}{K^{e}_{B1}} \tag{3.4}$$

and

$$\theta_{B1} = \frac{D9 - D10}{5.88"} \tag{3.5}$$

where $D9$, $D10$, $D14$, and $D15$ are displacement measurements shown in Figure 3.4; 27.5 in is the perpendicular distance between $D14$ and $D15$; θ_{B1} is the relative rotation between the beam sections defined by $D9$ and $D10$; P is the applied actuator load; K^{e}_{B1} is the elastic slope of the applied load vs. θ_{B1} data; and 5.88 in is the perpendicular distance between $D9$ and $D10$.

Next, Δ_{Beam} was computed using elastic beam theory accounting for flexural and shear deformation with

$$\Delta_{Beam} = \frac{Pl^3}{3EI} + \frac{Pl}{GA_S} \tag{3.6}$$

where l is the distance from the applied load to the toe of the gusset plate, equal to 90 in; E is the steel elastic modulus, equal to 29000 ksi; I is the strong-axis moment-of-inertia for the beam, equal to 272 in^4 for the W10x49 beams used in the experimental program; G is the steel shear modulus, equal to 11200 ksi; and A_S is the shear area of the beam, equal to 3.4 in^2 for W10x49 beams.

Finally, after computing Δ_{Conn} from Equation 3.2, θ_{Conn} was computed by dividing Δ_{Conn} by the distance from the applied load to the face of the column. Defining θ_{Conn} in this manner simplified implementation of braced frame connection behavior in the system studies, discussed in Chapter 5, since all inelastic deformation in the connection region, including double angle yielding and gusset plate yielding and buckling, is included in θ_{Conn}.

The commentary to the AISC *Specification* also states that connections that transmit less than 20% of the plastic moment of the beam at a rotation of 0.02 rad may be considered to have no flexural strength in design. Since CN1 transmitted 40% of $M_{p,exp}$ in positive bending and 30% of $M_{p,exp}$ in negative bending at 0.02 rad, the stiffness and strength of CN1 warrant consideration in the design of a CBF.

The stiffness and strength of CN1 were limited by the 0.375-in thick double angles. All yielding observed during the test was located in the double angles and no yielding was observed in the gusset plate, beam, or column. Yielding initiated at the bolt lines in the outstanding legs of the angles and propagated toward the fillet of the angles. There was also yielding of the in-plane angle legs where the angles were bent around the edge of the gusset plate or beam web. Since the yielding was concentrated in these areas, low cycle fatigue fractures of the double angles occurred, which led to strength loss at story drifts greater than 0.02 rad. The left beam web angle

fractured along its length at the bolt line and at the edge of the beam web, as shown in Figure 3.9b, and the right beam web angle fractured along its length at the edge of the beam web. In addition, the left gusset plate angle had a fracture of 6 in along the edge of the gusset plate, as shown in Figure 3.9a.

3.4.2 Effect of End Plate and Bolt Location (CN3 and CN5)

The first variation from the baseline connection was to use a 1 in end plate instead of double angles. As shown in Figure 3.2, two bolt configurations were investigated: in CN3 the bolts were located in the same configuration as the CN1 bolts and in CN5 the bolts were moved closer to the top and bottom of the end plate. This modified bolt configuration was intended to increase the flexural strength of the connection. The welds joining the gusset plate, beam, and end plate were all 0.3125-in fillet welds, which is the same size as the gusset plate-beam weld in CN1. The end plate thickness was chosen to minimize prying forces induced in the bolts when the beam reached its expected plastic moment strength. The cyclic normalized moment vs. story drift histories for specimens CN3 and CN5 are given in Figure 3.12.

As stated previously, replacing the 0.375-in double angles with a 1-in end plate significantly increased the flexural strength of the connections. In positive bending, CN3 and CN5 achieved $M_{p,exp}$ with CN5 also reaching $M_{p,exp}$ in negative bending. CN3 reached 71% of $M_{p,exp}$ in negative bending. As noted in Table 3.4, the end plate connections also had secant stiffnesses that were significantly larger than CN1. The larger capacity of the end plate connections, however, led to increased tensile demand on the bolts, which resulted in bolt fractures during negative bending of CN3 and CN5. Strength losses due to the bolt fractures are

shown in Figure 3.12.

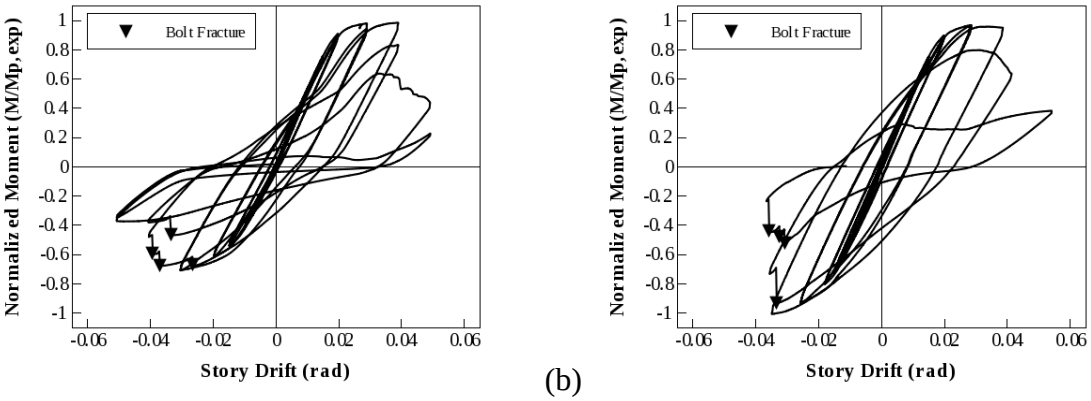

Figure 3.12 Normalized moment vs. story drift: (a) CN3; (b) CN5.

Fracture of bolts R6, L6, and R5 in specimen CN3 occurred during the first cycle at a story drift of 0.04 rad, followed by fracture of bolt L5 during the second cycle at 0.04 rad. For CN5, bolts R6 and L6 fractured simultaneously during the second cycle at a story drift of 0.04 rad, and bolts L5, R5 and R4 fractured during the first cycle at a story drift of 0.05 rad. Both connections experienced strength degradation in positive bending due to failure of the gusset plate-beam fillet weld. The failures initiated at the toe of the gusset plate, at a story drift of approximately 0.03 rad, and propagated along the length of the weld. For CN5, Figure 3.9c illustrates the weld crack that was present at maximum positive moment and Figure 3.9d illustrates the extensive propagation that occurred by the end of the test.

3.4.3 Effect of Weld Type (CN2 and CN4)

For CN2 and CN4, CJP welds were used to join the beam, end plate, and gusset plate. The cyclic normalized moment vs. story drift histories for CN2 and CN4 are plotted in Figure 3.13. The peak strengths in positive and negative bending, and the story drifts at which they occur, are nearly equal for CN2 and CN3 and for CN4 and CN5. The secant stiffnesses in

positive and negative bending were also nearly equal for CN2 and CN3 and for CN4 and CN5. CN2 and CN4 experienced bolt fractures beginning at a story drift of 0.04 rad in negative bending, similar to CN3 and CN5.

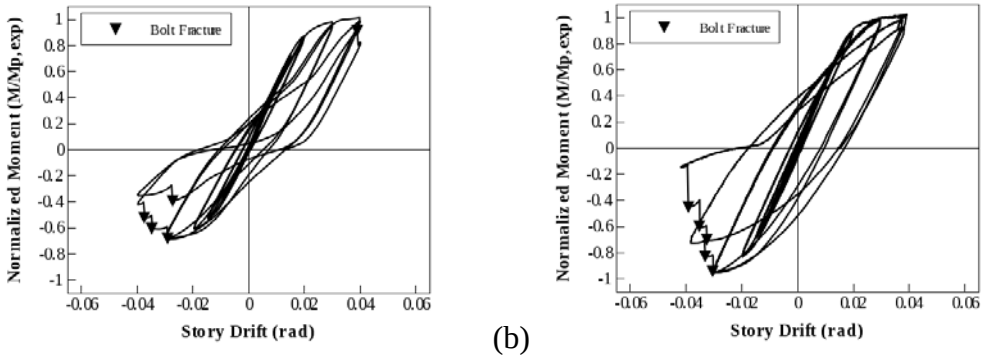

(a) (b)

Figure 3.13 Normalized moment vs. story drift: (a) CN2; (b) CN4.

In addition, the strength of the CJP weld increased the demand on bolts R1 and L1 at higher drift levels. In CN2, bolt R1 fractured during the first excursion towards 0.05 rad story drift and similar concerns about the bolts in CN4 led to the decision to end the test after two cycles at a story drift of 0.04 rad. Both CN3 and CN5 sustained at least a partial loading cycle of 0.05 rad drift, which was possible due to lower bolt tensile demand that resulted from the gusset plate-beam fillet weld failures.

3.4.4 Effect of Angle Thickness and Seat Angle (CN6 and CN7)

The connection variations for CN6 and CN7 aimed to increase the strength of the brace connection through thicker angles and a supplemental seat angle. CN7, tested before CN6, was a replica of the CN1 configuration, but the 0.375-in double angle thickness in CN1 was increased to 0.625 in in CN7. For CN6, the 0.625-in double angle thickness was maintained and a supplemental 0.625-in thick seat angle was welded to the bottom flange of the beam and bolted to the column. The length of the seat angle was determined by the workable gage of the column

and the minimum bolt edge distance from the AISC *Steel Construction Manual* (2005c). The cyclic normalized moment vs. story drift histories for CN6 and CN7 are given in Figure 3.14.

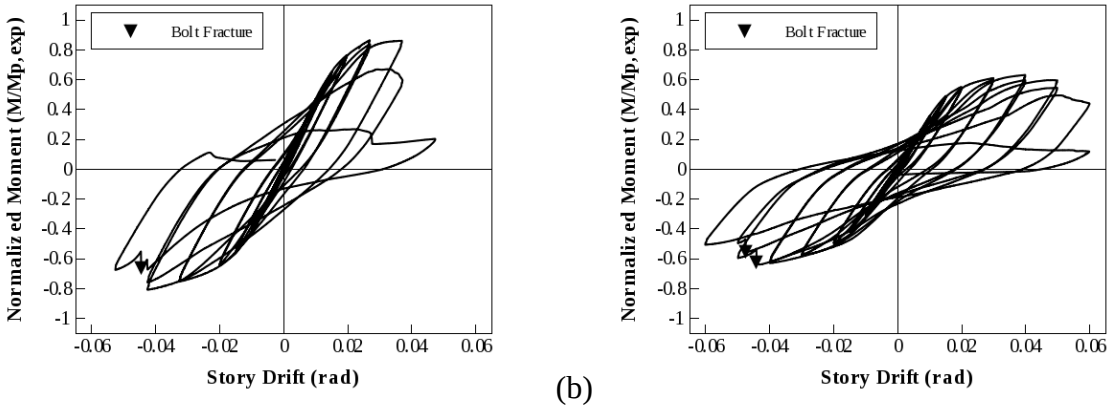

(a) (b)

Figure 3.14 Normalized moment vs. story drift: (a) CN6; (b) CN7.

Figures 3.10 and 3.14 illustrate that increasing the thickness of the double angles, from CN1 to CN7, significantly increased the flexural strength of the connection and the addition of the seat angle, in CN6, increased the flexural strength beyond the capacity reached in CN7. It is also apparent from Figure 3.7 that the increase in angle thickness had a greater impact on the negative moment strength and addition of a seat angle had a greater impact on positive moment strength. Nevertheless, neither connection reached load levels achieved by the end plate connections. CN7 reached 63% of $M_{p,exp}$ in positive and negative bending while CN6 reached 86% and 81% of $M_{p,exp}$ in positive and negative bending, respectively, although the negative moment strength of CN6 was greater than CN2 or CN3.

The seat angle also had a larger influence on the secant stiffness of the connection. CN6 was two times stiffer, in positive and negative bending, than CN7, which was two times stiffer than CN1. Both CN6 and CN7 sustained at least one cycle of loading at a story drift of 0.05 rad, with CN7 sustaining two cycles of 0.06 rad story drift.

Bolt R7 of CN6 and bolts R6 and L6 of CN7 fractured in negative bending during the

first excursion to a story drift of 0.05 rad. The drift level at which the fractures occurred was comparable to the end plate tests, but the load level was lower due to prying forces in the bolts induced by the flexibility of the angles. Both CN6 and CN7 also experienced failure of the gusset plate-beam fillet weld. The failures initiated at story drifts of 0.03 rad in CN6 and 0.02 rad in CN7, similar to the weld failures in CN3 and CN5.

3.4.5 Effect of Gusset Plate-Beam Fillet Weld Size (CN8)

In an attempt to prevent the initiation of the gusset plate-beam fillet weld failure, CN8 was fabricated as a replica of the CN6 configuration, but the fillet weld size was increased to 0.5 in for a distance of 6 in starting at the toe of the gusset plate. The cyclic normalized moment vs. story drift history for CN8 is shown in Figure 3.15.

CN8 reached 94% of $M_{p,exp}$ in positive bending and 82% of $M_{p,exp}$ in negative bending. Table 3.4 shows that the positive moment strength of CN8 was greater than the positive moment strength of CN6, but the negative moment strengths of CN6 and CN8 were equal, although both had negative moment strengths greater than CN2 and CN3. In addition, the positive and negative secant stiffnesses of CN8 were nearly equal to CN6. CN8 sustained higher positive moment strength through larger story drifts. Figures 3.14 and 3.15 illustrate that CN6 experienced a small strength loss between the first and second cycles at a story drift of 0.04 rad whereas CN8 experienced minimal strength loss during the same cycles. CN6 also experienced a significant strength loss during the first excursion to a story drift of 0.05 rad. CN8 did not experience a similar magnitude of strength degradation until the first excursion to a story drift of 0.06 rad. No bolt fractures occurred during testing of CN8.

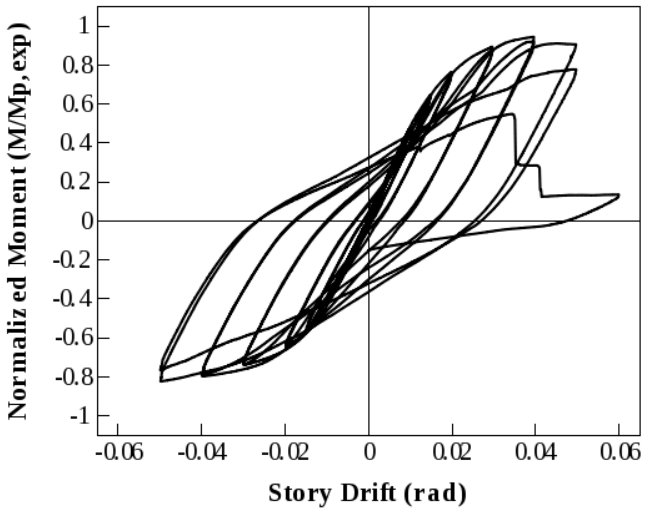

Figure 3.15 Normalized moment vs. story drift for CN8.

CN8 also experienced failure of the gusset plate-beam fillet weld. The weld failure did not initiate, however, until a story drift of 0.04 rad was reached. Prior failures of the 0.3125-in fillet weld initiated at story drifts of 0.03 rad or less. In addition to delaying the onset of weld failure, the larger weld size led to smaller strength losses at higher rotation demands, as discussed above. Nevertheless, once the weld failure propagated from the 0.5-in weld region to the 0.3125-in weld region, CN8 experienced sudden, significant strength loss. Thus, it appears that using the 0.5-in weld size for the full gusset plate-beam interface would have led to even better performance.

3.4.6 Cyclic Flexural Energy Dissipation

Cumulative energy dissipation vs. cumulative story drift for all connections is plotted in Figure 3.16. The energy dissipation was computed from total moment vs. story drift data, where the total moment, computed at the centerline of the column, is equal to the actuator load multiplied by the moment arm of 109 in.

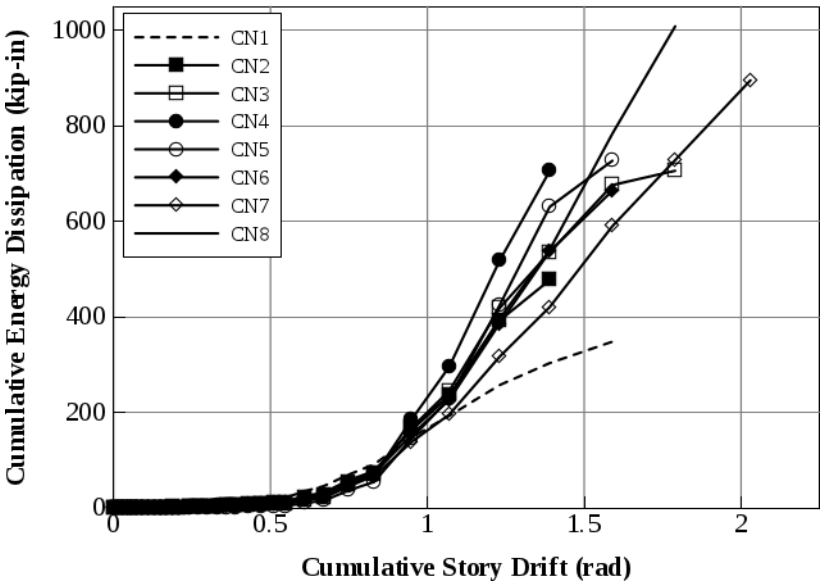

Figure 3.16 Energy dissipation vs. cumulative story drift for CN1 – CN8.

Figure 3.16 illustrates that the energy dissipation was approximately the same for all connections up to a cumulative story drift of 0.8 rad. Figure 3.16 also shows that all connections sustained a cumulative story drift of at least 1.4 rad, and that CN4 and CN5 had the largest energy dissipation at that cumulative story drift. CN2, CN3, and CN6 – CN8 dissipated approximately the same amount of energy up to a cumulative story drift of 1.4 rad, but less than CN4 or CN5. CN1 demonstrated very little energy dissipation capacity. Beyond a cumulative story drift of 1.4 rad, the bolt fractures in CN2 – CN5 decreased the rate of energy dissipation, while the rate of energy dissipation in CN6 – CN8 remained essentially constant. CN8 had the largest cumulative energy dissipation, equal to 1009 kip-in.

The energy dissipation exhibited by the flexural response of the connections tested in this research was relatively small compared to the energy dissipation provided through the flexural response of connections that are typically used in high seismic regions. For example, Lee et al. (2003) observed approximately 5310 kip-in of cumulative energy dissipation in moment connections reinforced with a welded straight haunch over the same cumulative story drift using

the SAC protocol. Recent computational studies (Hines et al. 2009), however, have shown that the collapse performance of CBFs designed using $R = 3$ may be significantly improved by the addition of reserve lateral-load resisting strength without relying on the ductility of the reserve system. Thus, the extensive detailing required to achieve ductility in high seismic systems is not necessary for connections that are being relied upon for reserve capacity. The connections evaluated in this experimental program demonstrate the ability to provide reserve lateral-load resisting capacity that contributes to seismic collapse prevention in CBFs.

3.5 LOCAL CONNECTION LIMIT STATES

In the discussion of normalized moment vs. story drift behavior of the braced frame connections, the limit states of weld failure, low cycle fatigue fracture of steel angles, and bolt fracture were identified as the cause of stiffness and strength degradation of the connections. The mechanisms that cause these failures, however, are not readily understood from normalized moment vs. story drift data. In addition, there are other localized connection behaviors not represented in the plots of $M/M_{p,exp}$ vs. story drift that influence how the connections behave and need to be addressed in the braced frame connection analysis procedure that is developed in Chapter 4. These behaviors include the location of the plastic hinge in the beam, out-of-plane deformation of the gusset plate, and flexural and panel zone shear yielding of the column. Thus, the purpose of this section is to characterize the behavior of the aforementioned limit states so they can be included in the finite element model. This analysis will also help identify limit states that should be avoided when developing the connection analysis procedure. Details about the fillet weld failures, angle fractures, and bolt fractures are presented, followed by brief

discussions of the beam plastic hinge location, gusset plate deformation, and column behavior.

3.5.1 Failure of Gusset Plate-Beam Fillet Weld

All connections with a fillet weld between the gusset plate and beam, except CN1, experienced failure of the weld. Fillet weld failure was not observed for CN1 because the connection angles were not strong enough to elevate weld demands to a critical level. For CN3 and CN5 – CN8, the failures initiated at the gusset plate toe and propagated along the gusset plate-beam interface. The failure path and rate of crack propagation significantly affected the connection strength and ductility in positive bending. Figures 3.17 – 3.21 show the fillet weld failures and moment-story drift response for connections CN5 – CN8. The results from CN3 are not presented because they are similar to CN5. To corroborate the visual observations of the weld failures, inspection was made of cross sections of the weld failures by polishing and etching the surface. To polish the surface of the weld cross section, silicon-carbide sandpaper ranging from 120 grit to 1000 grit was first used to flatten the surface, and then abrasive compounds up to 5000 grit were used to polish the surface. After polishing was complete, the surface was etched with a mild acid so the boundaries between the base metal, heat affected zone (HAZ), and fusion zone could be identified. In the photographs that follow, the fusion zone appears with a light gray color while the base metal of the gusset plate and beam flange has a darker gray color. The HAZ is located at the interface between the fusion zone and the base metal.

Visual inspection indicated that the weld failure in CN5, which was an end plate connection with modified bolt layout, occurred through the weld throat. This observation was corroborated by weld cross section inspection. These observations are shown in Figure 3.17. As

a result, the connection exhibited minimal strength loss until the second cycle at a story drift of 0.04 rad. Strength loss during the first cycle at a story drift of 0.05 rad was approximately equal to the strength loss during the previous cycle.

(a)  (b) 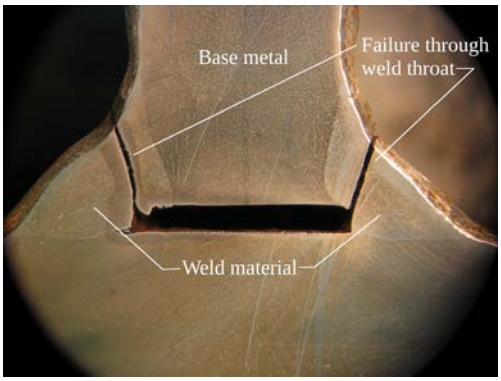

Figure 3.17 CN5 weld failure: (a) side view; (b) cross-section.

(a)  (b) 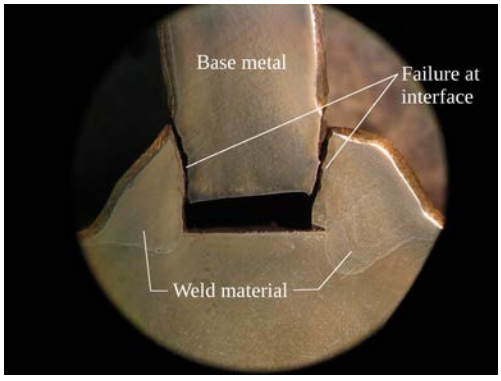

Figure 3.18 CN6 weld failure: (a) side view; (b) cross-section.

(a) 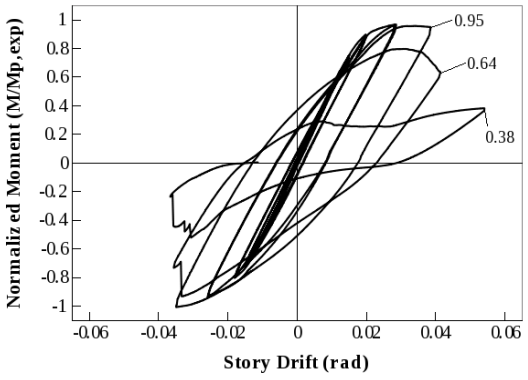

(b) 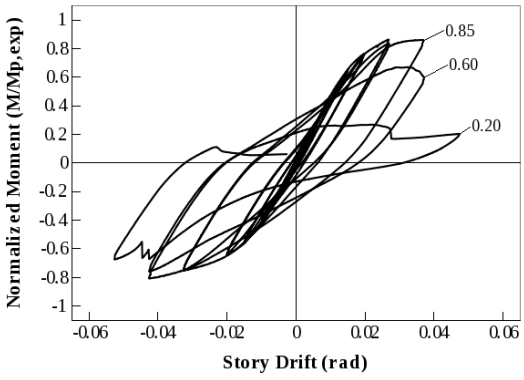

Figure 3.19 Normalized moment vs. story drift: (a) CN5; (b) CN6.

In contrast, visual observation and weld cross section inspection revealed the weld failure in CN6 occurred at the interface between the leg of the weld and the gusset plate. These observations are detailed in Figure 3.18. The CN6 weld failure propagated rapidly, which led to significant strength loss between the second cycle at a story drift of 0.04 rad and the first cycle at a story drift of 0.05 rad. The magnitudes of normalized moment are shown in Figure 3.19 at the points noted above.

The weld failure in CN7 initiated like the failure in CN6, at the interface between the weld material and the gusset plate. The failure transitioned, however, into the weld throat approximately half-way across the width of the gusset plate. Figure 3.20 shows the weld cross sections at these two locations in CN7. The transition into the weld throat slowed the crack propagation and prevented significant strength loss up to the first cycle at a story drift of 0.06 rad, which was shown previously in Figure 3.14b.

(a) 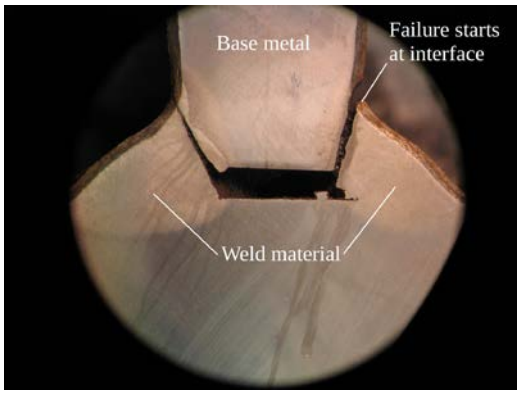

(b) 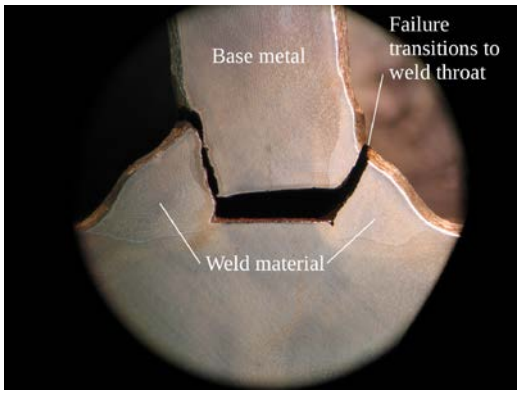

Figure 3.20 CN7 weld cross-sections: (a) toe of gusset plate; (b) middle of gusset plate.

In CN8, the weld failure propagated through the weld throat. Photographs of the weld failure and weld cross section in CN8 are given in Figure 3.21. Figure 3.21 shows that on the left side of the gusset plate, the weld failure initiated in the flange base metal. The failure transitioned to the weld throat after 1 in of propagation. On the right side of the gusset plate,

however, weld failure initiated in the weld throat. The larger weld at the toe of the gusset plate delayed the initiation of weld failure, as well as slowed the rate of crack propagation. Nevertheless, Figure 3.15 shows once the weld failure propagated through the enlarged weld region and into the region with smaller weld, significant strength loss occurred suddenly. The strength loss initiated during the first cycle at a story drift of 0.06 rad.

(a)  (b) 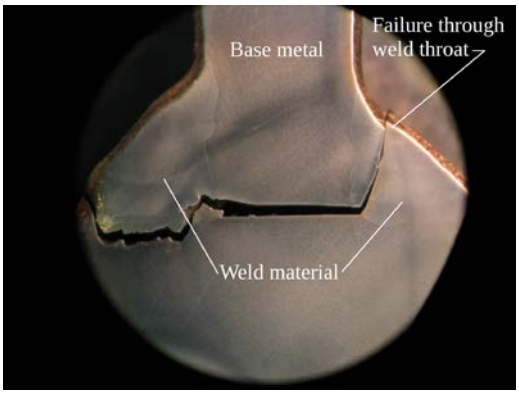

Figure 3.21 CN8 response: (a) weld failure; (b) weld cross-section.

Thus, for braced frame connections to function properly within a reserve lateral force-resisting system, fillet weld behavior and performance is critical and should be examined in greater detail, both with respect to design approaches and fabrication practices.

3.5.2 Low-Cycle Fatigue Fracture of Steel Angles

In CN1, low cycle fatigue fracture of the steel angles was the primary cause of stiffness and strength degradation of the connection. Therefore, capturing this limit state in finite element models of beam-column connections with gusset plates is paramount in accurately predicting behavior of connections that were not examined experimentally. Existing damage models for structural steel (Kanvinde and Deierlein 2007) are based on void growth and coalescence driven fractures, since this is the typical failure mechanism for fracture of ductile metals (Anderson

2004). Visual inspection of the fracture surface of the angles in CN1, however, cast doubt on the validity of this assumption for the present study. Thus, a more rigorous examination of the failure surfaces was undertaken using scanning electron microscopy (SEM).

One of the web angles from CN1 is shown in Figure 3.22. The leg with the bolt holes will be referred to as the out-of-plane leg and the leg that was removed due to fracture will be referred to as the in-plane leg. Micrographs of two different fracture surfaces were considered, the fracture surface through the in-plane leg and the fracture surface through the bolt holes. Three small pieces, outlined in Figure 3.22, were removed from this angle for SEM examination.

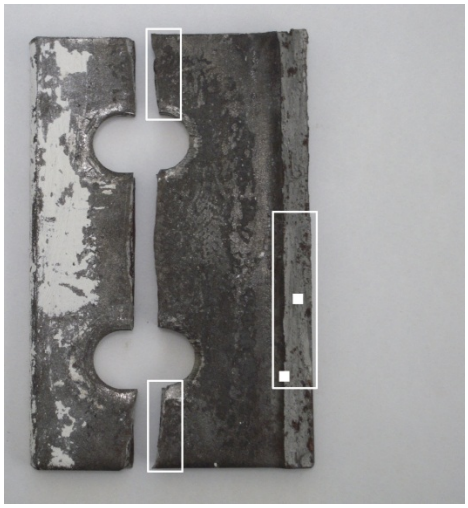

Figure 3.22 Location of fracture surface examinations.

It was necessary to examine both fracture surfaces in detail because they exhibited different failure rates. The fracture through the in-plane leg was slow and gradual, while the fracture through the out-of-plane leg occurred rapidly. The SEM work and photographs were completed by James Mabon, a technician at the Frederick Seitz Materials Research Laboratory on the campus of the University of Illinois at Urbana-Champaign.

Figure 3.23 shows micrographs of the in-plane leg fracture surface at two locations. Figure 3.23a is a micrograph taken along the centerline of the in-plane leg and Figure 3.23b is a

micrograph taken along the edge of the in-plane leg. The locations of the micrographs are denoted by solid squares in Figure 3.22 for clarity.

(a) 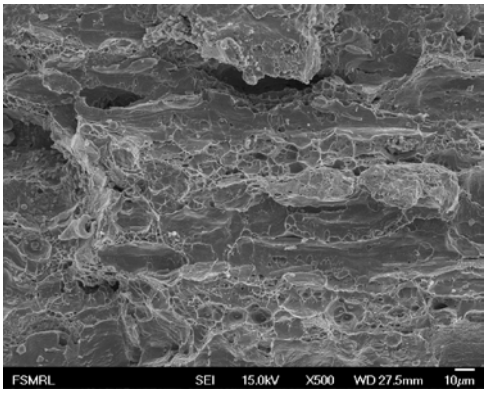

(b) 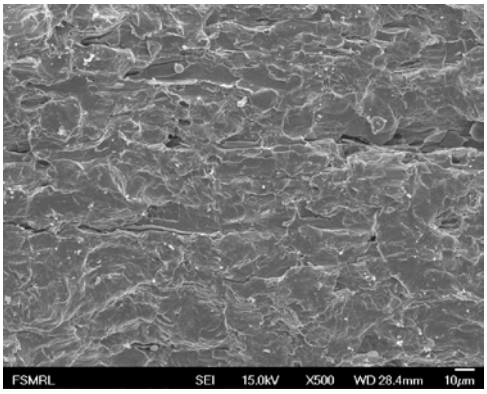

Figure 3.23 Micrographs of low-cycle fatigue fracture of steel angles in CN1: (a) micrograph at center of in-plane leg; (b) micrograph at edge of in-plane leg.

The primary observation from Figure 3.23 is that void growth and coalescence was not the sole cause of fracture in the steel angles from CN1. In Figure 3.23a, there are a number of areas where void growth fracture occurred, which are characterized by a "honeycomb" structure, but there are also significant areas of cleavage fracture, which are characterized by a smooth fracture surface. Thus, the fracture mechanism should be characterized as "quasi-cleavage." In addition, Figure 3.23b reveals that the fracture mechanism at the edge of the in-plane leg was almost entirely cleavage fracture. This observation suggests that the initial fractures in the gusset and web angles were caused by cleavage fracture, and that the quasi-cleavage fracture behavior ensued after the initial fractures at the edge of the in-plane leg. Quasi-cleavage fracture was possible due to yield stress increases in the steel angles that resulted from cyclic loading.

Therefore, computational models for ductile fracture of metals based on void growth and coalescence are not applicable to this type of fracture. Instead, a simplified damage model based on accumulated plastic strain was developed to approximate low cycle fatigue fracture of steel angles in the present study. The damage model is outlined in Chapter 4. Prof. Robert H. Dodds

from the University of Illinois at Urbana-Champaign, Department of Civil and Environmental Engineering, was instrumental in developing the conclusions from these micrographs.

3.5.3 Bolt Fracture

In addition to weld failure and low-cycle fatigue fracture of steel angles, the flexural strength of the braced frame connections was limited by bolt fracture. Typically, the bolts in rows five through seven, as identified in Figure 3.2, were susceptible to fracture, although bolts in rows one through four in CN2 and CN4 would have fractured if the tests had not been stopped. The bolt fractures were summarized in Figure 3.8. Figure 3.8 shows that all connections with an end plate, CN2 – CN5, and two connections with double angles, CN6 and CN7, experienced bolt fractures. The number of bolt fractures in the end plate connections was significantly larger than in the double angle connections. Representative bolt fractures from the experimental program are illustrated in Figure 3.24.

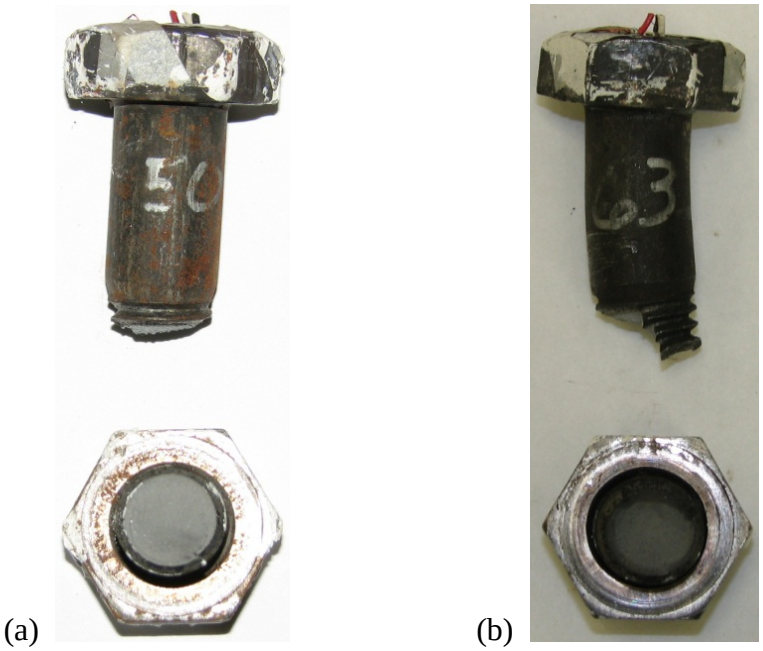

Figure 3.24 Representative bolt fractures: (a) CN5, bolt R4; (b) CN7, bolt R6.

The majority of the bolt fractures are represented by Figure 3.24b, where the failure occurs along a diagonal plane through the threads of the bolt. Figure 3.24b correlates well with the typical failure path for bolts in direct tension that is recognized in existing literature (Kulak et al. 2001). Figure 3.24a, however, corresponds to failure of a bolt subjected to torqued tension, i.e. applying tension to the bolt through increasing torque (Kulak et al. 2001). This failure pattern surfaced in four cases and may indicate that those bolts experienced yielding due to shear stress during installation. Based on the normalized moment vs. story drift results shown previously, however, it does not appear that shear yielding diminished the tensile capacity of the bolts. It should also be noted that the bolt in Figure 3.24b exhibits bending in the shank which was due to the deformation of the double angles in CN6. Flexural deformation of the double angles decreased the tensile load on the bolts, which partially accounts for their larger ductility capacity when compared to the end plate connections.

Visual inspection of the failure surface of both bolts in Figure 3.24 indicated that fracture was probably caused by void growth and coalescence. Since bolts can only be loaded in tension, not compression, cyclic hardening of the bolt material did not occur, which nullified the possibility of quasi-cleavage fracture in the bolts. This observation was not corroborated with microscopic methods like the double angle fractures, however. Again, Prof. Robert Dodds was instrumental in developing conclusions about the fracture mechanisms.

In addition to visual observations, bolt tensile strain vs. normalized moment data was used to understand the behavior of the connection bolts. Figure 3.25 illustrates bolt tensile strain vs. normalized moment data for bolts R1 and R6 in CN2. The strain data originate at the bolt pretension strain, approximately 2500 με for both bolts, which is denoted in Figure 3.25. The

strain in bolt R1, CN2, increased due to positive moment and plateaued when subject to negative moment. The converse was true for bolt R6, CN2. As the pretension pressure between the end plate and column flange decreased, the plateau strain decreased in both bolts. In addition, bolt R6, CN2, experienced plastic elongation, which caused the strain plateaus to occur at progressively larger tensile strains after plastic elongation initiated. Eventually, fracture of bolt R6, CN2, occurred. Tensile strain at bolt fracture varied significantly between tests, ranging from 0.004 to 0.012 in/in, so the bolt tensile strain data collected during the experimental program were not suitable for establishing a damage index for simulating bolt fracture in the finite element models, which are discussed in Chapter 4.

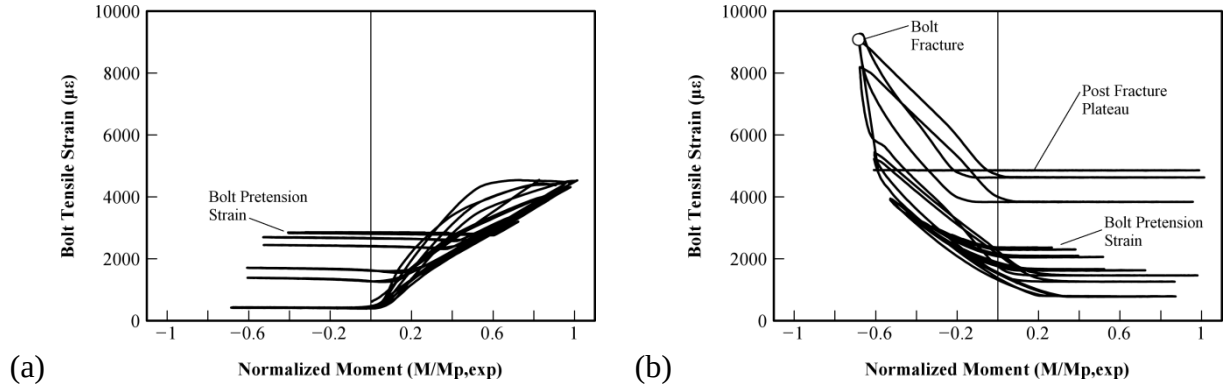

Figure 3.25 Bolt tensile strain vs. normalized moment: (a) CN2, bolt R1; (b) CN2, bolt R6.

3.5.4 Beam Plastic Hinge Location

As stated previously, the normalized moment vs. story drift results show that plastic hinging occurred in tests CN2 – CN5. The location of the plastic hinges, however, is not evident from these results. Visual observations during the experimental program indicated plastic hinging of the beam occurred at the toe of the gusset plate. Figure 3.26 shows photographs, taken during test CN4, that demonstrate flaking of the whitewash in the beam flanges at the toe

of the gusset plate.

(a) 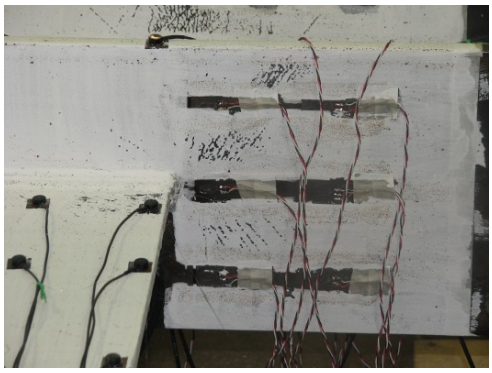 (b) 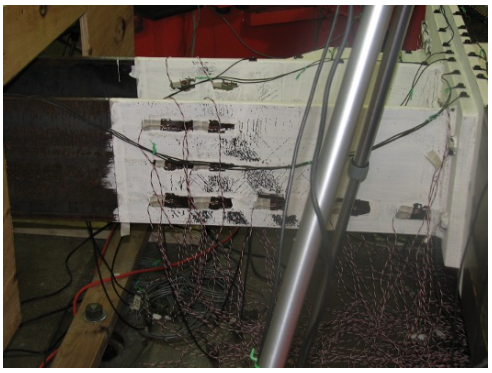

Figure 3.26 Flaking of whitewash in CN4: (a) top beam flange; (b) bottom beam flange.

Whitewash flaking occurs along slip lines in the beam flanges, which are rotated 45° with respect to the principal stress directions (Lubliner 2008). Since the slip lines are oriented approximately 45° with respect to the axis of the beam, the maximum principal stress direction is parallel to the beam flange. This indicates that flexural normal stresses are predominant in the region at the toe of the gusset plate. Thus, significant yielding due to flexural normal stresses occurred in CN4.

Observations of plastic hinging in the beams of CN2 – CN5 were corroborated with data from LVDTs in the beam web. Plotted in Figure 3.27 are data for normalized moment vs. beam relative rotation data computed from displacement measurements *D*9 and *D*10, and *D*22 and *D*23 in test CN4. Beam relative rotation 1, θ_{B1}, was computed using Equation 3.5, presented earlier, and beam relative rotation 2, θ_{B2}, was computed using the same equation, but displacement *D*22 was substituted for *D*9 and displacement *D*23 was substituted for *D*10. The location of the displacement measurements was shown in Figure 3.4.

From Figure 3.27, it is evident that significant inelastic rotation occurs in the beam at the toe of the gusset plate, which corresponds to θ_{B1}, but outside this region the rotation demand is essentially elastic, which corresponds to θ_{B2}. Results for the other end plate connections are

similar to those shown here. In addition, the elastic slope of both curves correlates well with the slope predicted by the 'moment-area' method for computing beam rotations. This indicates that the beam outside the gusset plate region behaves according to Euler-Bernoulli beam theory, and that the connection behavior is actually comprised of several components, including gusset plate yielding and/or buckling, shear yielding of the beam web, and deformation of the double angles or end plate. This observation played a critical role in the development of connection models for the system studies, which will be discussed in Chapters 4 and 5.

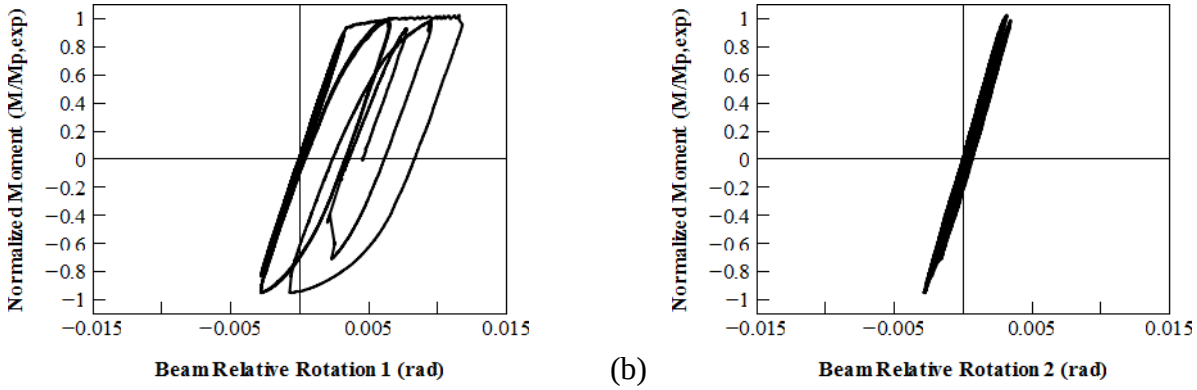

(a) (b)

Figure 3.27 Normalized moment vs. beam relative rotation in CN4: (a) θ_{B1}; (b) θ_{B2}.

3.5.5 Out-of-Plane Gusset Plate Deformation

While severe strength degradation due to gusset plate buckling was not evident in the normalized moment vs. story drift data, the gusset plates in the end plate tests experienced visible out-of-plane deformation. Gusset plate deformation at maximum negative moment in CN4 is depicted in Figure 3.28. Out-of-plane gusset plate deformation in the double angle tests did not reach the magnitude observed in the end plate tests. The absence of out-of-plane deformation of the gusset plate in the double angle tests was due to the flexibility of the web/seat angles. As the web/seat angles deformed under applied load, the beam flanges were allowed to

move away from the column face, which reduced demands on the gusset plate. Nevertheless, the possibility of gusset plate buckling needs to be acknowledged since a single gusset plate thickness, which was relatively stocky, was used in the large-scale experiments. The gusset plates in the experimental study had a b/t radio equal to 28, with the width b taken as the dimension of the gusset plate perpendicular to the beam. This possibility was investigated for a limited number of cases in the connection finite element analyses, as well the braced frame connection flexural behavior analysis procedure, both detailed in Chapter 4.

Figure 3.28 Out-of-plane deformation of gusset plate.

3.5.6 Column Flexural and Panel Zone Behavior

While the previous discussion focused exclusively on beam and connection behavior, column behavior also needs to be examined. Three potential limit states in the column are yielding due to flexure, yielding due to panel zone shear force, and yielding due to local bending of the beam flanges. These limit states were identified from visual observations during the large-scale tests and from analysis of displacement measurements.

Figure 3.29 illustrates column moment vs. column rotation data for tests CN1 and CN4.

The results from CN1, Figure 3.29a, are representative of all connections with double angles and the results from CN4, Figure 3.29b, are representative of all connections with end plates.

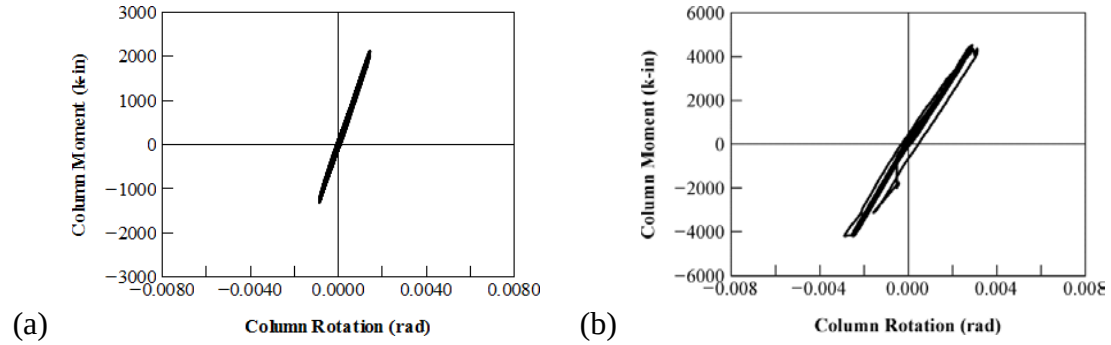

Figure 3.29 Column moment vs. column rotation: (a) CN1; (b) CN4.

Column moment was computed as the actuator load multiplied by the distance to the centerline of the column, equal to 109 in. Column rotation was computed from displacement measurements using Equation 3.3. Figure 3.29 shows that the columns remained elastic during the connection tests. This was verified by computing the yield moment of the W14x90 columns, which was equal to 7800 kip-in for a yield stress of 54.6 ksi, which was the average yield stress calculated from the results of tensile tests of the column material. The column moment vs. column rotation data in Figure 3.29b was corrected to eliminate apparent inelastic behavior due to drifting of one of the displacement measurements used in the column rotation calculation.

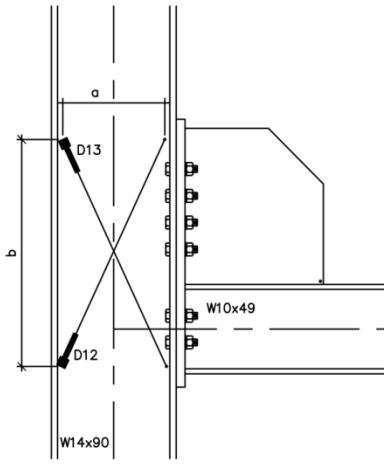

Figure 3.30 Column panel zone displacement measurements.

In addition to column flexure, using the flexural capacity of the braced frame connections in a CBF to provide reserve capacity induces panel zone shear deformation in the column web. Displacement measurements were used to quantify panel zone shear deformation. A close-up view of the column panel zone displacement measurements is shown in Figure 3.30.

To compute the panel zone shear deformation, the displacements *D*12 and *D*13 are used in the equation

$$\gamma = \frac{\left(a^2 + b^2\right)\left(D12 - D13\right)}{2ab} \tag{3.7}$$

where γ is the column panel zone shear deformation, and *a* and *b* are the width and height of the panel zone. The panel zone dimensions were 9.58 in and 30 in for the connections considered herein. Panel zone shear force is computed from

$$V_u = \frac{M_{Conn}}{b} \tag{3.8}$$

where M_{conn} is the connection moment, equal to the actuator load multiplied by 102 in, which was the distance from the actuator to the face of the column. Panel zone shear force vs. panel zone shear deformation data are illustrated for CN1 and CN4 in Figure 3.31. As with the column moment vs. column rotation results, the data for CN1 is representative of the double angle connections and the data for CN4 is representative of the end plate connections. In addition, the panel zone shear deformation data in Figure 3.31b was corrected to erroneous inelastic behavior.

Figure 3.31 demonstrates that the panel zone response in CN1 and CN4 was essentially elastic. This can also be verified by computing the panel zone shear capacity according to Equation J10-9 of the AISC *Specification* (2005b). Taking the yield stress to be 54.6 ksi, as before, the panel zone shear strength for a W14x90 is 202 kips, which is significantly greater

than the panel zone shear force demand of 145 kips in CN4.

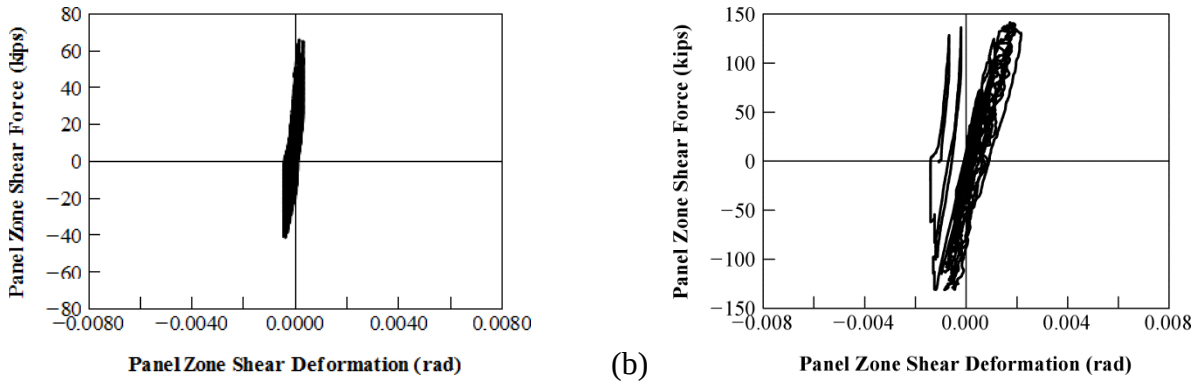

Figure 3.31 Panel zone shear force vs. panel zone shear deformation: (a) CN1; (b) CN4.

Nevertheless, visual observations from tests CN2 and CN3 are in conflict with these numerical results. Figure 3.32a shows significant whitewash flaking in the column panel zone of CN2, which indicated that panel zone shear yielding occurred. The area in which the yielding concentrated, however, was much smaller than the area bounded by displacements *D*12 and *D*13, which were used to compute the column panel zone shear deformation.

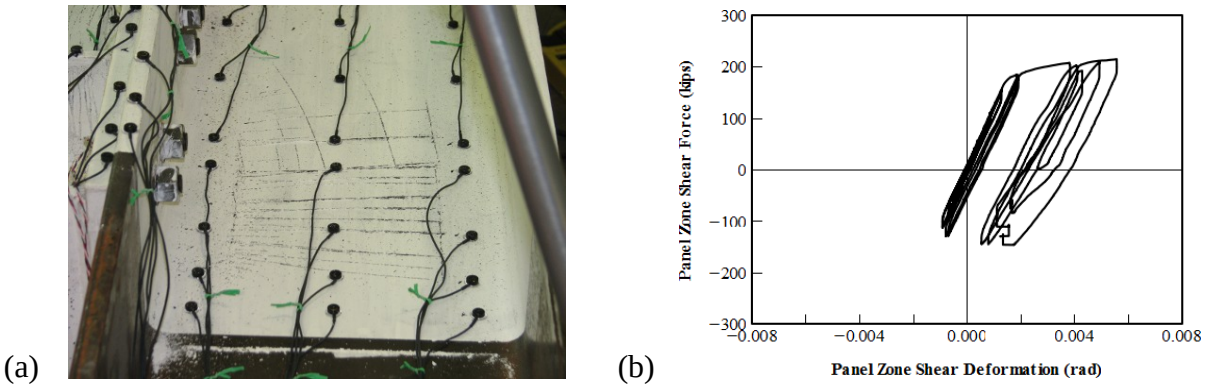

Figure 3.32 Column panel zone yielding during test CN2.

Thus, the column panel zone shear force data computed for the connections in the experimental program was too low, owing to the fact that the *b* dimension assumed for the panel zone was too large. Based on the observations from CN2, shown in Figure 3.32a, the correct panel zone height, *b*, should be the distance between the outer bolts in the connection bolt group. This

yields *b* equal to 19.5 in for the connections with the standard bolt location. The panel zone shear force vs. panel zone shear deformation data for CN2 shown in Figure 3.32b was updated to reflect the smaller *b* dimension, although the panel zone shear deformation was not changed. It is evident from Figure 3.32b that yielding due to panel zone shear deformation occurred in CN2, since the maximum panel zone shear force is approximately 210 kips, which exceeded the panel zone shear force capacity.

Finally, flaking of the whitewash on the outer face of the column flange was observed during the end plate tests. One example of this behavior is illustrated in Figure 3.33. The whitewash flaking around the centerline of the column flange was due to local bending of the column flange. The tensile forces in the bolts act as a pair of concentrated forces that induce flexural stresses in the column flange. This phenomenon is present in all tests, but was only readily visible in test CN4 and CN5 because the modified bolt location was used for those tests.

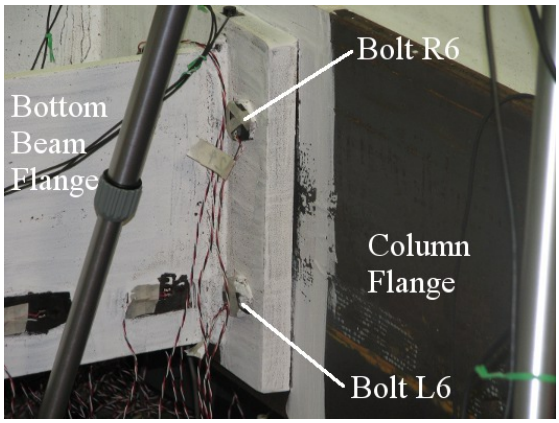

Figure 3.33 Flaking of column whitewash during test CN4.

3.6 ANCILLARY TESTS

After the large-scale tests were complete, ancillary small-scale tests were performed to generate data for the finite element study of braced frame connection flexural behavior. The

primary information desired from the ancillary tests was stress-strain relationships for the beams, columns, angles, plates, and bolts used in the large-scale experiments. The desired constitutive relationships were derived from tensile tests of coupons taken from unstressed material in the experimental program. In addition, tensile testing of 0.75-in diameter, ASTM A325 high-strength bolts was used to quantify the failure elongation of the bolts so that a simplified damage model for bolt fracture could be implemented in the finite element analyses. In what follows, the methods used for each set of small-scale tests are outlined, and then representative results from each set are presented and discussed.

3.6.1 Tensile Coupon Tests

The tensile coupon tests were conducted according to the requirements of *ASTM A370-09a: Standard Test Methods and Definitions for Mechanical Testing of Steel Products* (ASTM 2009). In addition, the tensile coupons were fabricated based on recommendations in this specification. Rectangular specimens having a 1.5 in x 9 in gage section were used for the beam and column specimens. The beam specimens were taken from the portion of the beam that extended beyond the actuator, and the column specimens were taken from the portion of the column between the attachment to the reaction fixture and the connection region. Three specimens were taken from the flanges and three from the webs. A schematic drawing of a rectangular specimen is illustrated in Figure 3.34.

For the plates and angles, subsize rectangular specimens were used since it was not possible to fabricate standard size specimens. The gage section of the subsize specimens was 0.25 in x 2.25 in and the thickness was required to be 0.25 in. The thickness of the standard size

specimens did not need to be reduced per ASTM A370. The plate specimens were taken from the end plate material that was removed from CN6 when it was converted from an end plate test to a double angle test. The angle specimens were taken from the in-plane leg of the angle that was welded to the gusset plate. It was reasoned this portion of the angle remained essentially elastic during testing. A schematic drawing of the subsize rectangular specimens is shown in Figure 3.35. Three specimens were taken from the CN6 plate and three were taken from the double angles in CN1, CN6, and CN8, respectively.

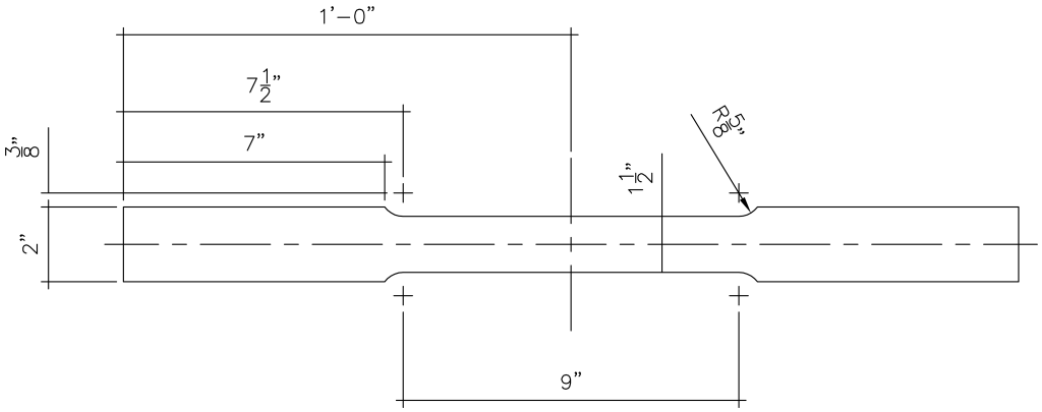

Figure 3.34 Schematic drawing of rectangular tensile coupon specimen.

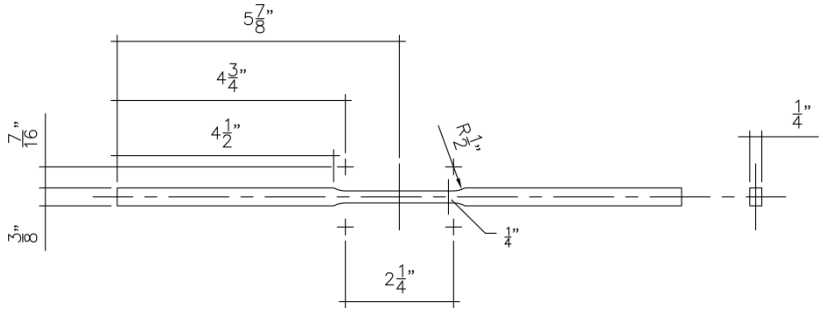

Figure 3.35 Schematic drawing of subsize rectangular tensile coupon specimen.

Finally, tensile coupons derived from 0.75-in diameter, ASTM A325 bolts that were 6 in long were fabricated to quantify the constitutive behavior of the bolt material. The remnant bolts from the large-scale tests were too short for this application. The bolts used to fabricate the bolt tensile coupons, however, were manufactured by the same company that provided the majority of

the bolts used in the connection tests. The bolt manufacturer was Delta Screw Company of Chicago, Illinois. The bolt tensile coupons were fabricated by machining a 0.5-in diameter x 2.25 in gage section into the shank of the bolts. Three bolt tensile coupon specimens were fabricated in this manner. Figure 3.36 illustrates a schematic drawing of the bolt tensile coupon specimens.

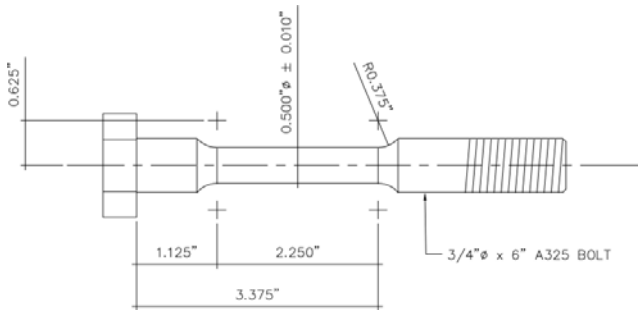

Figure 3.36 Schematic drawing of bolt tensile coupon specimen.

All specimens were fabricated by the staff of the Civil Engineering Machine Shop in the Newmark Structural Engineering Laboratory. A summary of all tensile coupons is included in Table 3.5. Each specimen was given a designation based on the part of the connection it was extracted from. For instance B2-F1 would be a flange specimen taken from the beam from test CN2. Other abbreviations in the specimen designation include 'C' for column, 'A' for angle, and 'P' for plate.

Table 3.5 Tensile coupon specimen list.

Specimen Origin	Size	Specimen Designation
CN1: angles	Subsize	CN1-A1, CN1-A2, CN1-A3
CN2: beam	Regular	B2-F1, B2-F2, B2-F3 / B2-W1, B2-W2, B2-W3
CN2: column	Regular	C2-F1, C2-F2, C2-F3 / C2-W1, C2-W2, C2-W3
CN3-beam	Regular	B3-F1, B3-F2, B3-F3 / B3-W1, B3-W2, B3-W3
CN6-angles	Subsize	CN6-A1, CN6-A2, CN6-A3
CN6-plate	Subsize	CN6-P1, CN6-P2, CN6-P3
CN8-angles	Subsize	CN8-A1, CN8-A2, CN8-A3
CN8-beam	Regular	B8-F1, B8-F2, B8-F3 / B8-W1, B8-W2, B8-W3
CN8-column	Regular	C8-F1, C8-F2, C8-F3 / C8-W1, C8-W2, C8-W3
Bolts	Bolt	Bolt 1, Bolt 2, Bolt 3

All tensile coupon tests were conducted using MTS uniaxial testing frames in the Newmark Structural Engineering Laboratory. The standard size rectangular and bolt tensile coupon specimens were tested on a frame with 100-kips force capacity, and the subsize rectangular specimens were tested on a frame with 50-kips force capacity. The tests were conducted using displacement control and ASTM recommendations for loading rates were followed. Prior to testing, the cross-section dimensions of all specimens were measured using a digital caliper to increase the accuracy of the cross-sectional areas used in computing engineering stresses from the tensile coupon data.

Figure 3.37 Test setup for rectangular specimens.

Figure 3.37 illustrates the test setup for the rectangular tensile specimens. Two extensometers were used during testing, one with a 2-in gage length and 0.4-in stroke to record data in the elastic region and one with an 8-in gage length and 1.6-in stroke to record data in the inelastic region. The large extensometer was manufactured by Epsilon Technology, Inc., and the small extensometer was manufactured by MTS, Inc. Rubber bands were used to connect the

extensometers to the tensile specimens. Representative stress-strain curves from the beam and column tensile specimens are shown in Figures 3.38 and 3.39. One curve from each set of three flange specimens was chosen for inclusion in Figure 3.38 and one curve from each set of three web specimens was chosen for inclusion in Figure 3.39.

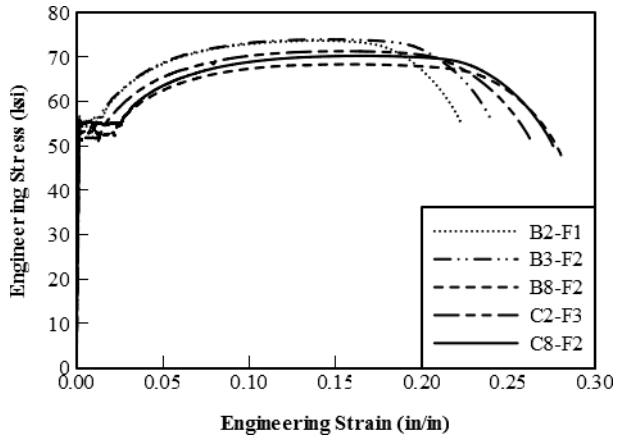

Figure 3.38 Representative stress-strain curves for ASTM A992 beam and column flanges.

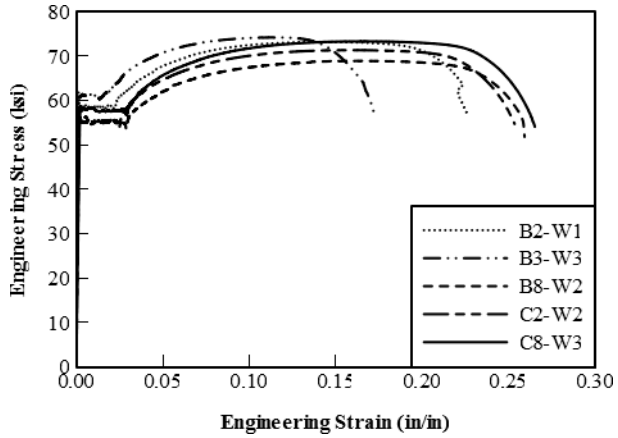

Figure 3.39 Representative stress-strain curves for ASTM A992 beam and column webs.

Figures 3.38 and 3.39 illustrate that the yield stress ranged from 50 to 55 ksi for the beam and column flanges, and 55 to 60 ksi for the beam and column webs. The failure elongations for all specimens were also consistent except for specimen B3-W3, which had a significantly lower elongation at failure.

Figure 3.40 illustrates the test setup for the bolt tensile coupons. A single extensometer with a 2-in gage length and 0.4-in stroke was used to measure elongation of the bolt specimens. In addition, the bolts were gripped with specially designed fixtures that engaged the bolt head and threads, similar to a bolt proof load test. Three specimens were fabricated and tested. The stress-strain results for the bolt tensile coupon tests are plotted in Figure 3.41.

Figure 3.40 Test setup for bolt tensile coupon testing.

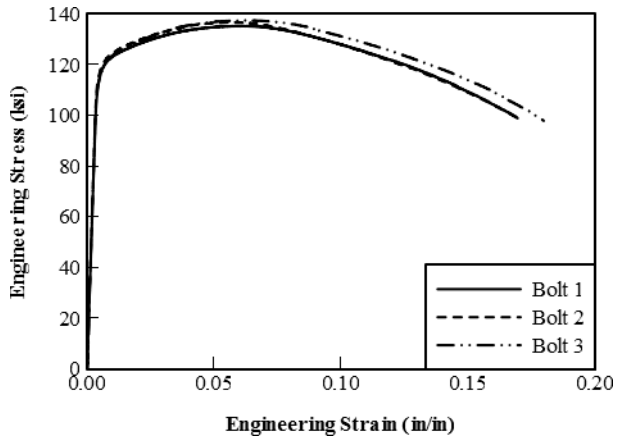

Figure 3.41 Stress-strain curves for ASTM A325 bolt material.

The stress-strain data for the three bolt specimens are nearly identical. ASTM A325 material is quenched and tempered when it is manufactured, which yields stress-strain behavior that is less variable than materials used for rolled shapes. In addition, the material does not

exhibit a yield plateau that is characteristic of low-carbon steels. This is also due to heat treatment of the material, which generates a more uniform distribution of the dislocations that cause yielding in structural steels.

Finally, Figure 3.42 illustrates the test setup for the subsize rectangular tensile specimens. A single extensometer with a 2-in gage length and a 0.4-in stroke was used to measure elongation of the gage section. Since the material under consideration, ASTM A36 steel, has a very large elongation at failure, the extensometer was compressed during installation so the entire 0.4-in stroke could be used in collecting data. Subsize specimens for the end plate material from CN6 and steel angle material from CN1, CN6, and CN8 were tested using the setup in Figure 3.42.

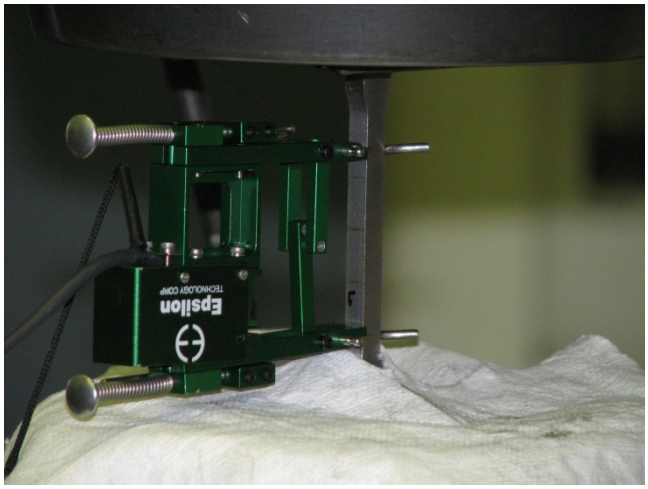

Figure 3.42 Test setup for subsize rectangular specimens.

Representative stress-strain curves for the steel plate and angle materials are shown in Figure 3.43. In general, the ASTM A36 steel demonstrated a wider range of yield stresses than the ASTM A992 steel used for the beams and columns. The yield stresses for the plate specimens ranged from 38 to 46 ksi, and the yield stresses for the angle specimens ranged from 50 to 58 ksi. Figure 3.43 also shows that compressing the extensometer prior to loading allowed

elongation at ultimate load to be observed, but the extensometer did not have adequate stroke to measure elongation at failure. The data for CN6-P2 is highly truncated since the extensometer was not compressed prior to testing of the specimen. In addition, data for CN6-P1 was lost due to an extensometer malfunction.

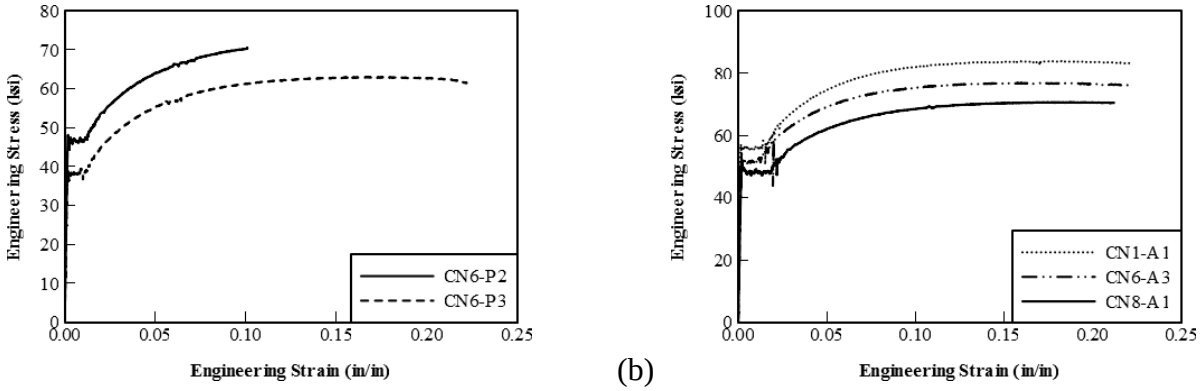

Figure 3.43 Representative stress-strain curves for ASTM A36 steel: (a) plate; (b) angles.

3.6.2 Bolt Failure Testing

In addition to the tensile coupon tests, force vs. elongation behavior of steel bolts was examined experimentally to determine a rational method for quantifying initiation of bolt fracture in the connection finite element models. The experimental setup for the bolt tests is shown in Figure 3.44. An MTS uniaxial testing frame with 100-kips capacity actuator was used for the bolt testing. Specially designed fixtures were used to connect the bolt to the grips of the uniaxial testing frame. The ASTM A370 procedure for proof load testing of high strength bolts was followed except for inclusion of a wedge washer under the bolt head (ASTM 2009). The wedge washer simulates localized bending of the bolt that may occur in a connection. This deformation, however, was not consistent with the bolt demands in the large-scale tests. One spring-loaded LVDT was used to measure elongation of the bolts. The LVDT was calibrated and

then attached to the bolt grips with hose clamps. Bolt force data was recorded from the internal load cell of the test frame actuator.

Figure 3.44 Test setup for bolt failure testing.

Two groups of six bolts each were examined to determine their bolt force vs. bolt elongation behavior. The first group was manufactured by Delta Screw Company, of Chicago, Illinois, and the second group was manufactured by St. Louis Screw Company, of St. Louis, Missouri. The bolt manufacturer was determined from markings on the bolt heads. Bolts from each manufacturer were used in the connection experiments. Bolt force vs. bolt elongation data for each group is illustrated in Figure 3.45. The ultimate strength of the bolts in each group was very consistent, ranging from 46 to 48 kips. The elastic behavior of the Delta bolts, however, demonstrated less variability than the St. Louis bolts. In addition, the failure elongation of the Delta bolts was significantly larger than the failure elongation of the St. Louis bolts. The fracture plane occurred in the threaded region of all the bolts and was similar to the fracture pattern illustrated in Figure 3.24b.

The bolt force vs. bolt elongation results from the bolt testing demonstrated that bolt elongation could be used as a rational method for predicting initiation of bolt fracture. The failure elongation of the bolts within a group was very consistent. For the Delta bolts, the failure elongation was approximately 0.18 in, and the failure elongation for the St. Louis bolts was approximately 0.11 in. Since bolts from both groups were used during the large-scale tests, the failure elongation of the St. Louis bolts was adopted for the connection finite element modeling.

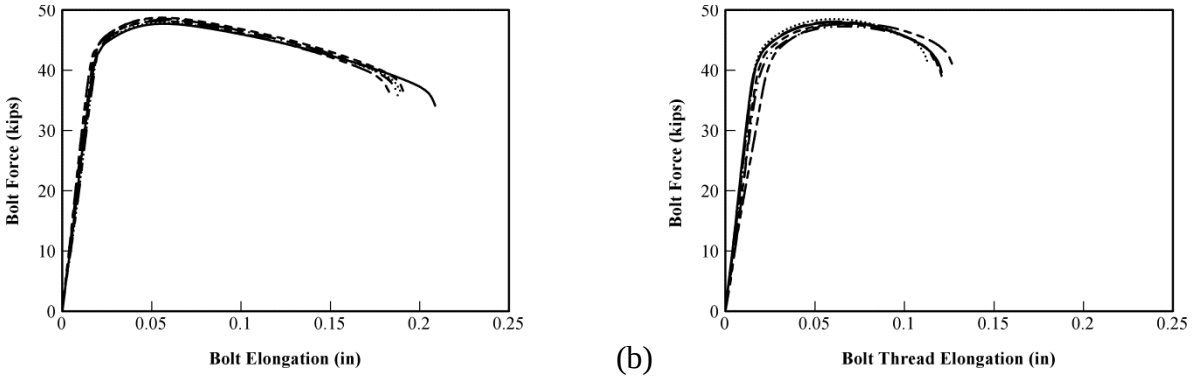

(a) (b)

Figure 3.45 Bolt force vs. bolt elongation: (a) Chicago bolts; (b) St. Louis bolts.

3.7 CONCLUSIONS FROM EXPERIMENTAL PROGRAM

Full-scale tests were used to study the cyclic flexural behavior and performance of beam-column connections with gusset plates. The following conclusions were drawn from the global and local response of the test specimens.

- The baseline brace connection, CN1, which was a typical double angle detail, had more stiffness and strength than has traditionally been considered in design of concentrically-braced frames. CN1 exceeded the strength and stiffness thresholds commonly used as upper bounds to classify pinned connections, and instead behaved as a partially-restrained connection.

- The end plate connections demonstrated greater strength than the double angle connections. In addition, the end plate connections with a modified bolt location demonstrated greater negative moment strength than the end plate connections with the standard bolt location. All end plate connections achieved or nearly achieved positive moment equal to the expected plastic moment of the beam. The modified end plate connections achieved or nearly achieved negative moment equal to the expected plastic moment of the beam and the standard end plate connections had negative moment strength equal to 60 to 70% of the expected plastic moment of the beam.
- The modified angle connections, CN6 – CN8, exhibited more deformation capacity than the end plate connections. None of the modified angle connections, however, achieved the expected plastic moment of the beam in positive or negative bending. Increasing angle thickness had a greater impact on the negative moment strength and adding a seat angle had a greater impact on positive moment strength. Bolt fractures occurred in CN6 and CN7 due to prying forces induced by flexibility of the double angles. The larger weld size in CN8 delayed the initiation of gusset plate-beam fillet weld failure as well as the onset of strength degradation.
- The double angle connection configuration with a supplemental seat angle provided the best balance of strength and deformation capacity.
- The path and propagation rate of the fillet weld failures in CN3 and CN5 – CN8 significantly affected the strength and ductility of the connections in positive bending. Weld failure paths that developed through the weld throat propagated slowly and the global loss of strength due to this event was gradual. In contrast, the weld failure path in CN6 was along the interface

between the leg of the weld and the gusset plate, resulting in more rapid global strength loss. In addition, increasing the fillet weld size significantly improved the cyclic response in CN8. For braced frame connections to provide reserve lateral force-resisting capacity, fillet weld behavior and performance is critical and should be examined in greater detail, both with respect to design approaches and fabrication practices.

- Low cycle fatigue fracture of the steel angles in CN1 was driven by a combination of void growth and coalescence and cleavage fracture. In addition, the initial fractures along the face of the angle showed almost no evidence of void growth and coalescence.
- Significant out-of-plane deformation of the gusset plate was not observed during the large-scale test, but should be investigated during the computational studies.
- Displacement data and visual observations indicated that flexural yielding, panel zone shear yielding, and local flange flexural yielding may occur in a braced frame column if the flexural capacity of the beam-column connection with gusset plate is used in a reserve capacity system. Although energy dissipation is not the primary mechanism a reserve capacity system uses to maintain structural stability, energy dissipation due to the aforementioned column limit states would aid collapse performance.
- Tensile testing of ASTM A325 bolts demonstrated that bolt elongation may be used in a finite element model to predict initiation of bolt fracture during cyclic flexural loading of beam-column connections with gusset plates.

CHAPTER 4

FINITE ELEMENT MODELING OF BRACED FRAME CONNECTIONS

The primary goal of the proposed research is an assessment of the role played by the flexural capacity of beam-column connections with gusset plates in preventing seismic collapse of CBFs in moderate seismic regions. The experimental program detailed in the previous chapter demonstrated that braced frame connections possess appreciable flexural stiffness and strength. It was also shown that double angle braced frame connections provided the best combination of flexural stiffness, strength, and ductility. In addition, the large-scale experiments revealed that the flexural stiffness and strength of these connections can be enhanced by increasing the double angle thickness and/or adding a supplemental seat angle to the bottom beam flange. Nevertheless, the usefulness of the results from the large-scale testing program is limited since only one beam depth was used during the tests and several of the connection limit states were not adequately investigated.

Therefore, a computational study of the flexural behavior and performance of double angle beam-column connections was undertaken to examine the flexural stiffness and strength of braced frame connections across a broader range of connection parameters. Three-dimensional nonlinear finite element models were developed and validated against the experiments from Chapter 3 with focus on the limit states of failure of the fillet weld between the gusset plate and beam, low-cycle fatigue fracture of the steel angles joining the beam and gusset plate to the column, and bolt fracture. These models were used to evaluate the flexural stiffness and strength of braced frame connections with primary attention on the effects of beam depth, angle

thickness, and a supplemental seat angle. A simplified procedure was also developed for estimating connection parameters that can be used in design and assessment of CBFs. The new knowledge gained from the computational studies discussed in this chapter is essential for understanding the role that reserve capacity plays in the seismic behavior and performance of low-ductility CBFs, which are currently constructed in moderate seismic regions and comprise a significant portion of existing building stock in high seismic regions.

4.1 DEVELOPMENT AND VALIDATION OF FINITE ELEMENT MODEL

To extend the results from the experimental program summarized in Chapter 3, three-dimensional models were created using the *Abaqus FEA* software (Simulia 2011) to study CBF beam-column connection behavior across a wide range of parametric variations. As noted above, double angle connections were chosen for this study since they are a common connection configuration and provided the best combination of stiffness, strength, and ductility in the beam-column connection testing program. Damage indices were identified to predict the initiation of stiffness and strength degradation due to fillet weld failure, bolt fracture, and low-cycle fatigue failure of steel angles. The damage indices were calibrated using data from the experimental program and existing literature. The finite element model and damage indices were validated using experimental results from specimens CN1, CN6, and CN7.

4.1.1 Three-Dimensional Finite Element Model

Figure 4.1 illustrates the three-dimensional finite element model, which replicated the test setup from the experimental program discussed in Chapter 3. Displacement control of the node

at the free end of the beam was used to simulate the cyclic loading protocol. The beam, column, gusset plate, and angles in the connection region were modeled with four-node shell elements with full integration. The typical shell element size in the connection region was approximately 0.25-in square. The results of the convergence study used to determine the element size are shown in Figure 4.1b. The convergence study was conducted by applying an 18-kip concentrated force to the control node of the finite element model and observing the corresponding tip displacement for various mesh sizes.

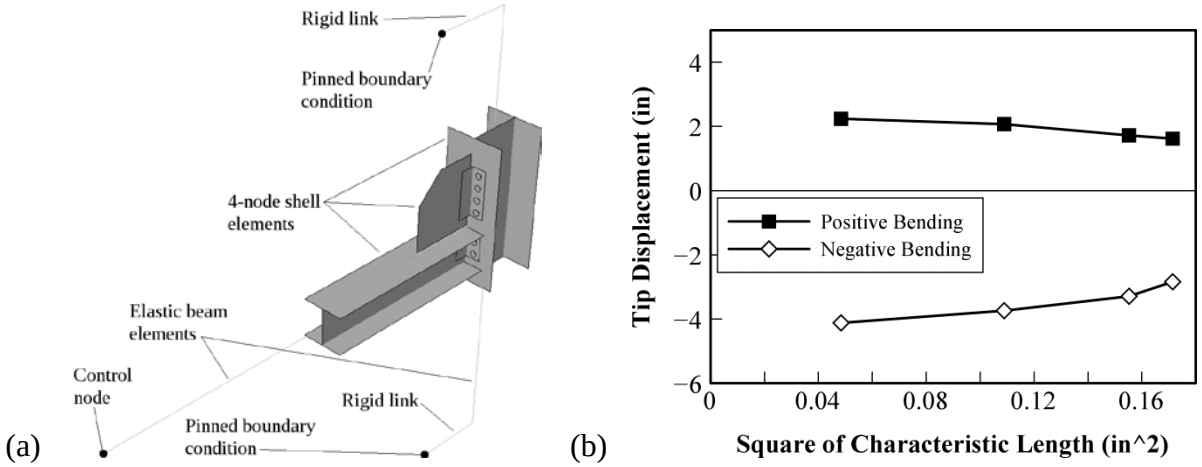

Figure 4.1 Finite element model: (a) model schematic; (b) convergence study results.

The beam and column outside the connection region were modeled with two-node elastic beam elements to reduce computational cost. Normal and frictional contact between the angles and column flange were simulated with a node-to-surface contact formulation. Contact constraints were enforced with the penalty method and the frictional slip coefficient was taken to be 0.35 (AISC 2005b). The widths and thicknesses of the flanges, webs, gusset plates, and angles in the finite element models used for validation were based on measured dimensions. Rigid links, shown in Figure 4.1a, were used to represent the column reaction fixtures used in the full-scale tests. The boundary conditions at the reaction fixtures were modeled as pins based on

the experimental setup. All translational degrees-of-freedom and the two out-of-plane rotational degrees-of-freedom were constrained at the free ends of the beam elements representing the reaction fixtures.

Material nonlinearities were incorporated through the von Mises yield criterion with associated flow rule and isotropic strain hardening. The beam and column were ASTM A992 steel and the gusset plate and angles were ASTM A36 steel. Constitutive relationships for the beam, column, angle and gusset plate materials were based on uniaxial tension tests conforming to the requirements of ASTM A370 (ASTM 2009). Representative stress-strain curves are shown in Figure 4.2a, where the legend labels refer to the ASTM designations for the materials. Geometric nonlinearities were incorporated through the use of large-displacement analysis and element formulations.

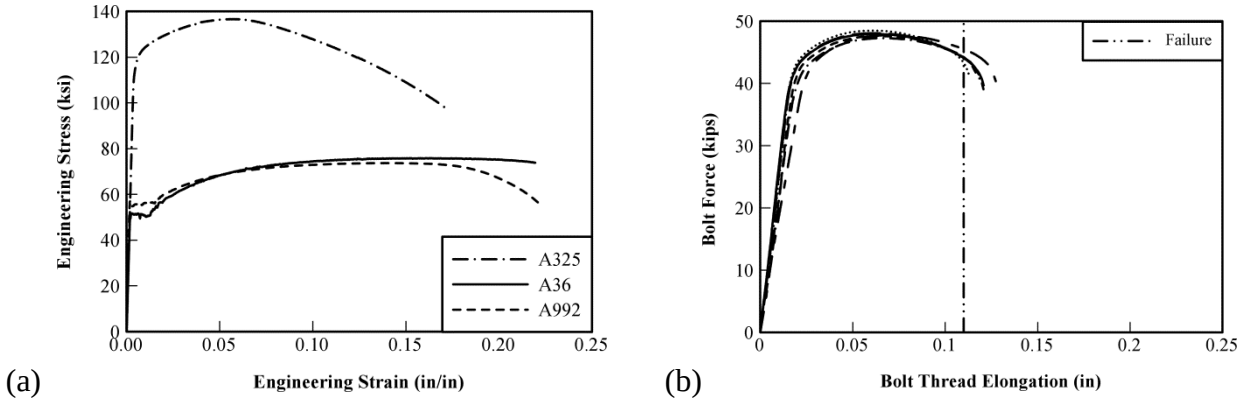

Figure 4.2 Component behavior: (a) representative material stress-strain; (b) A325 bolt force-elongation.

The 0.75-in diameter A325 bolts were modeled with two-node beam elements that account for axial, shear, and bending deformations. Stress-strain behavior for the A325 material is shown in Figure 4.2a and force-deformation behavior is shown in Figure 4.2b. An enlarged view of the bolt model is shown in Figure 4.3. Elements in the shank region had a circular cross-section defined by the nominal bolt diameter and elements in the threaded region had a smaller

diameter. The diameter change was necessary since the smaller threaded area limits the maximum load the bolt can sustain. The reduced diameter was equivalent to the net tensile area for high strength bolts defined by the AISC *Specification* (2005b). The bolt head and nut were modeled with three-node shell elements. Different stiffnesses were assigned to the inner and outer regions of the bolt head and nut since the beam elements simulating the bolt shank connect to the bolt head and nut shell elements at only one node on the center axis of the bolt.

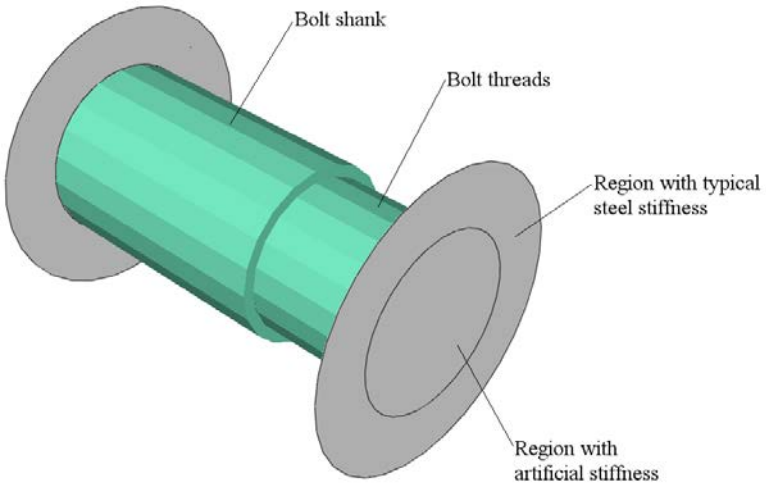

Figure 4.3 Bolt model – shank and threads rendered for clarity.

Elements in the inner region of the bolt head and nut were assigned an artificially large elastic modulus to account for the stiffness provided by the bolt shank. Elements in the outer region of the head and nut were assigned the typical steel elastic modulus, 29000 ksi. The specified pretension force, 28 kips for 0.75-in diameter A325 bolts (AISC 2005b), was applied to the bolt shanks using a temperature change. The required temperature change was computed from

$$\Delta T = \frac{\alpha E A_B}{T_P} \tag{4.1}$$

where ΔT is the temperature change; α is the coefficient of thermal expansion, equal to 6.5×10^{-6} in/in/°F for structural steel; E is the elastic modulus of the bolt material; A_B is the nominal bolt

diameter; and T_P is the specified bolt pretension force.

The interaction between the bolt nuts and angles was modeled with normal and frictional contact. The contact was formulated with a node-to-surface discretization and enforced with the penalty method. In contrast, the bolt head translational degrees-of-freedom were tied to the column flange elements. Modeling the interactions in this manner allowed the bolts to undergo plastic straining in tension, but the bolts were not loaded in compression.

The gusset plate-beam fillet weld was explicitly modeled so initiation of fillet weld failure could be predicted. As shown in Figure 4.4, the fillet weld was modeled as a series of two-node connector elements, where each short fillet weld segment was represented by three connector elements in parallel. Figure 4.4 illustrates the behaviors of the connector elements, which represent (a) the weld, (b) contact between the gusset plate and beam flange, and (c) a flexible elastic spring for numerical stability.

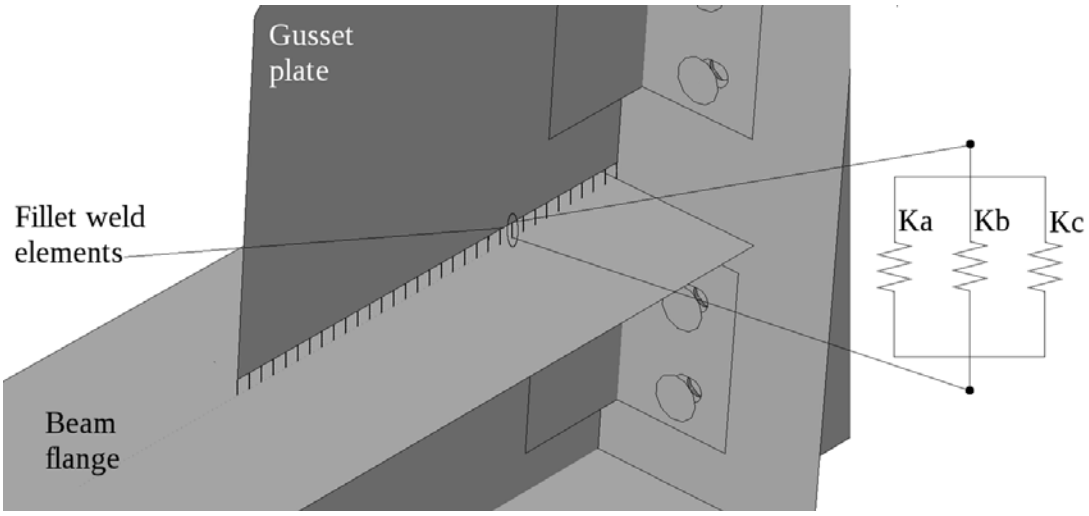

Figure 4.4 Schematic configuration of fillet weld model.

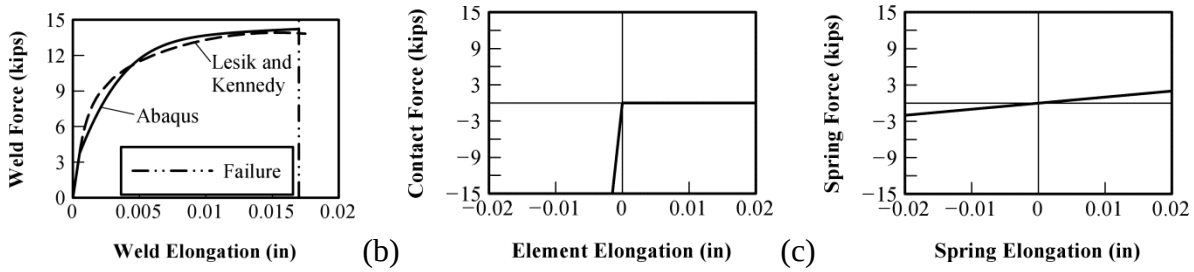

Figure 4.5 Fillet weld components: (a) weld behavior; (b) contact behavior; (c) flexible spring.

The connector modeling the inelastic weld force-deformation behavior was assumed to act as a fillet weld loaded at 90° to the weld axis. The inelastic behavior of the weld was based on the model developed by Lesik and Kennedy (1990), which is characterized by

$$P = P_0\left(1.00 + 0.5\sin^{1.5}\theta\right) f\left(\rho\right) \tag{4.1}$$

for $0 \le \rho \le 0.0325$,

$$f\left(\rho\right) = 8.234\rho \tag{4.2a}$$

for $\rho > 0.0325$,

$$f\left(\rho\right) = -13.29\rho + 457.32\rho^{\frac{1}{2}} - 3385.9\rho^{\frac{1}{3}} + 9054.29\rho^{\frac{1}{4}} - 9952.13\rho^{\frac{1}{5}} + 3840.71\rho^{\frac{1}{6}} \tag{4.2b}$$

and

$$\rho = \frac{\Delta}{0.209d\left(\theta + 2\right)^{-0.32}} \tag{4.3}$$

where P_0 is the weld strength for $\theta = 0°$, θ is the angle in degrees between the axis of the weld and the applied load, Δ is the weld elongation, and d is the weld size. For design according to the AISC *Specification* (2005b):

$$P_0 = \phi_w\left(0.6F_{EXX}\right)\left(\frac{d}{\sqrt{2}}l_w\right) \tag{4.4}$$

where ϕ_w is the strength reduction factor, equal to 0.75, F_{EXX} is the weld material tensile strength,

and l_w is the length of the weld. The Lesik and Kennedy (1990) model is shown in Figure 4.5a along with the *Abaqus FEA* implementation used in the present research.

Contact between the gusset plate and the beam flange was modeled with a no-tension connector that is quasi-rigid in compression, shown in Figure 4.5b. Finally, a flexible elastic spring, represented in Figure 4.5c, was used to maintain numerical stability of the weld model since the stiffness of the weld connector approaches zero at large deformations.

4.1.2 Damage Identification

Since the stiffness, strength, and ductility of CN1, CN6, CN7, and CN8 were limited by bolt fracture, weld failure, and ductile angle fracture, damage indices were defined for each limit state to predict the initiation of damage. Propagation of damage and associated strength degradation were not captured by the models, however. Critical values of the damage indices were calibrated using results from the experimental program and data from existing literature. The damage models were validated based on observations from the large-scale tests.

For low cycle fatigue fracture of the steel angles, the damage index was termed the damaged plastic strain, ε^p_{dam}, and was calculated using equivalent plastic strain data. To compute ε^p_{dam}, equivalent plastic strain increments and mean stresses were recorded for critical elements in the finite element models. Since shell elements were used to represent the steel angles, the necessary data were recorded for the top and bottom surfaces of the elements. ε^p_{dam} was monitored at the critical regions for fracture initiation in the angles that were identified in the reference experimental program, namely the extreme top and bottom fibers of the angles within the in-plane angle legs at the edge of the gusset plate or beam web. Figure 4.6 shows

photographs of the critical regions in CN1.

(a) 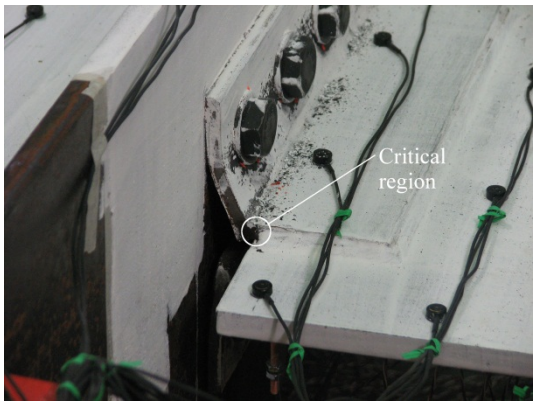

(b) 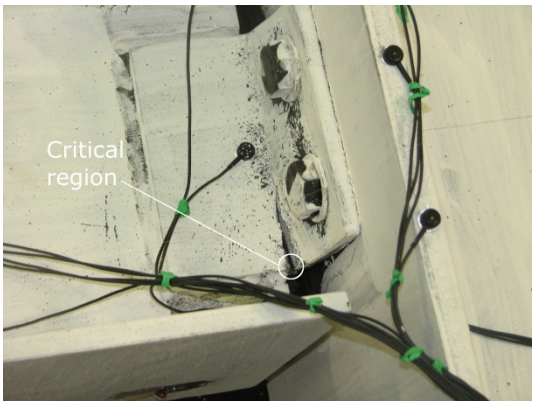

Figure 4.6 Critical angle fracture region: (a) gusset angles; (b) web angles.

Next, the equivalent plastic strain increments for which the mean stress was compressive were discarded. The summation of the remaining equivalent plastic strain increments was the damaged plastic strain. This approach is based on the concept that ductile fracture initiation in mild steel is driven by void growth and coalescence that occurs when mean stress is tensile (Kanvinde and Deierlein 2007).

The critical value of ε^{p}_{dam} was determined using the computational and experimental results for CN1, which are shown in Figure 4.7. In positive bending, which is defined to be when the gusset plate is in tension, the experimental results show CN1 gained strength between the second cycle to 0.02 rad story drift and the first cycle to 0.03 rad story drift. Between the first and second cycles to 0.03 rad story drift, however, a significant amount of strength was lost. In addition, the finite element results for CN1 match the experimental data well up to 0.03 rad story drift, but predict higher strengths than were realized in the test past this point. Thus, it was concluded that fracture of the gusset angles in CN1 initiated during the first cycle to 0.03 rad story drift.

Similarly, in negative bending, CN1 exhibited a significant strength loss between the first

and second cycles to 0.02 rad story drift. Again, the finite element results matched the experimental data up to this story drift. Thus, it was concluded that the web angle fractures initiated during the second cycle to 0.02 rad story drift. . The value of ε^{p}_{dam} corresponding to the fracture initiations in the gusset and web angles at these drift levels was 0.091 for both positive and negative bending.

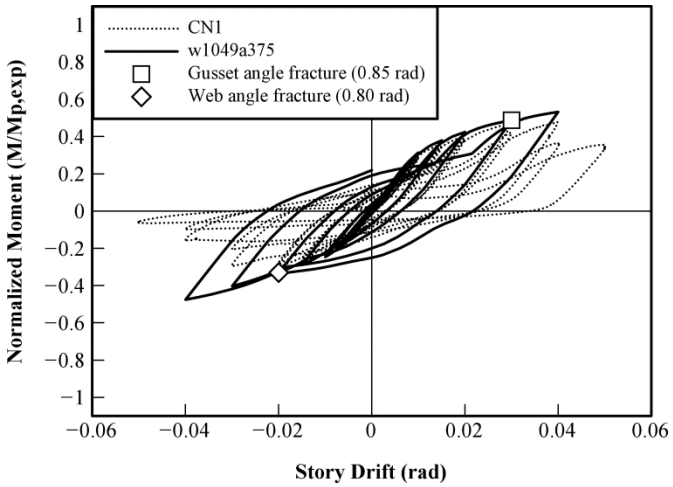

Figure 4.7 Validation of model for CN1.

To evaluate failure of the gusset-plate beam fillet weld, elongation of the fillet weld was chosen as the damage index. The critical elongation was calculated as

$$\Delta_f = 1.087d\left(\theta + 6\right)^{-0.65} \tag{4.5}$$

where Δ_f is the failure elongation, d is the weld size, and θ is the angle in degrees between the applied load and the axis of the weld (Lesik and Kennedy 1990). For CN1, CN6 and CN7, d was 0.3125 in, and θ was 90°, which yielded Δ_f = 0.016". The critical weld elongation is shown in Figure 4.5a.

Similarly, the damage index selected for bolt fracture was elongation of the bolt threads. The critical bolt thread elongation was determined from uniaxial bolt tension tests conducted in the Newmark Structural Engineering Laboratory. The bolt tests were summarized in Chapter 3.

The force vs. elongation curves for the St. Louis bolts, as well as the critical bolt thread elongation, are shown in Figure 4.2b. Based on these tests, the critical bolt thread elongation was taken as 0.11 in.

4.1.3 Finite Element Model and Damage Index Validation

The finite element model was validated using the experimental results from CN1, CN6, and CN7. Experimental and computational results for CN1, CN6, and CN7 are shown in Figures 4.7 – 4.9. As illustrated, the initial stiffness and ultimate strength of the finite element models correlate well with the experimental results. Unloading stiffnesses and pinching behavior are also well represented up to the initiation of weld failure or angle fracture.

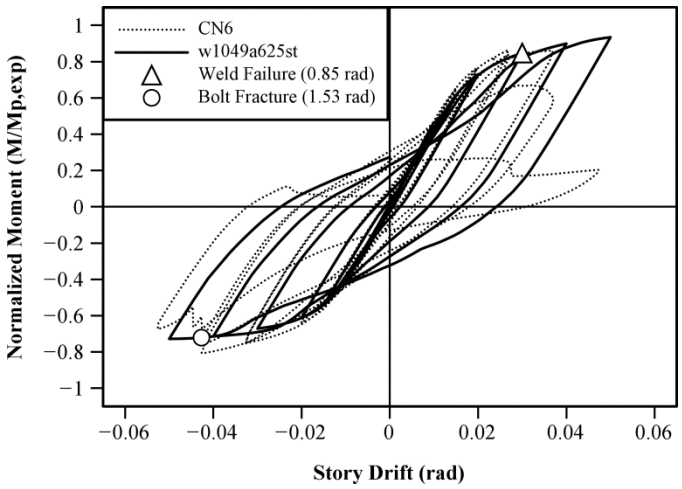

Figure 4.8 Validation of model for CN6.

The angle fracture damage index was confirmed based on observations of the angles from test CN1. Photographs of the critical regions were taken at peak story drifts to monitor the spread of inelasticity in these regions. The photographs also show the propagation of the low-cycle fatigue failures in the angles and indicate that macroscopic cracks initiated in the beam web angles during the second cycle to 0.02 rad story drift and in the gusset plate angles during

the first cycle to 0.03 rad story drift. These observations are consistent with the strength drops discussed above.

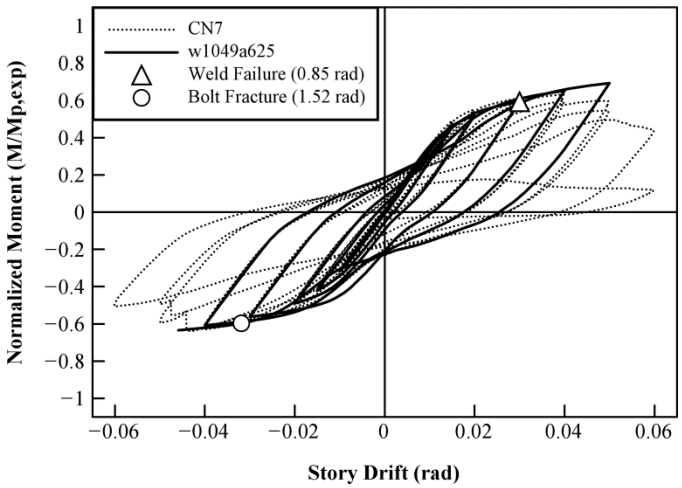

Figure 4.9 Validation of model for CN7.

The weld failure damage index was validated by comparing the elongation of the connector elements representing the fillet weld in the finite element model to observed failures of the fillet weld. Figure 4.10a illustrates the initiation of the fillet weld failure in CN6 and Figure 4.10b plots weld elongation vs. story drift for the connector elements near the toe of the gusset plate in the finite element model of CN6. Figure 4.10a shows that the weld failure propagated approximately 1 in beyond the toe of the gusset plate at 0.02 rad story drift. The finite element results in Figure 4.10b show that the first three connector elements had reached the critical failure elongation at this story drift. Since the elements are spaced 0.25 in apart, the finite element model predicted a weld propagation of 0.5 in. Since weld connector elements are not being removed from the model when they reach the critical elongation, prediction of weld failure propagation is expected to lag the experimental observations. Thus, the calibration of the fillet weld damage index was deemed satisfactory for predicting weld crack initiation.

(a)  (b) 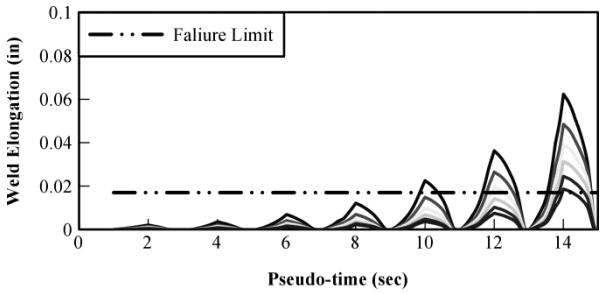

Figure 4.10 Validation of weld failure model: (a) CN6 at weld failure at 0.02 rad story drift; (b) finite element results predicting weld failure at 0.02 rad story drift.

The bolt fracture damage index was validated by comparing the bolt elongation of the connector elements representing the bolt threads in the finite element model to observed bolt fractures. In Figure 4.8 and 4.9, a filled circle is used to denote a bolt fracture prediction. Bolt fractures observed experimentally are identified by a sudden loss of strength in the third quadrant of the figures. As shown in Figures 4.8 and 4.9, the calibration of the bolt fracture damage index was deemed satisfactory for predicting bolt fracture.

4.2 PARAMETRIC STUDY

Using the validated finite element model, a parametric study was conducted to determine how changes in the connection components affect the flexural behavior of the connection and the initiation of damage. Focus was placed on beam depth, angle thickness and supplemental seat angle. The beam sizes considered in this study were W10x49, W14x53, W18x46, and W21x44. This set of beam depths covers the range that is typical for CBFs. The angle thicknesses considered in this study were 0.375 in, 0.5 in, 0.625 in, and 0.75 in. The two thinner angle sizes have 3.5-in legs and the two thicker angle sizes have 4-in legs. Supplementary seat angles were also

considered to evaluate their impact in connections with various beam depths and angle thicknesses.

Several assumptions were made in developing the parametric study connections. First, the gusset plate dimensions and thickness did not vary. The effect of gusset plate thickness was studied for a select group of connections, but this was considered a secondary variation in the connection geometry. As a result, the number of bolt rows in the gusset plate angles did not change. Second, the beam web connection was a full depth connection. Thus, the W14x53 beams had three rows of bolts in the web angles, the W18x46 beams had five rows of bolts in the web angles, and the W21x44 beams had six rows of bolts in the web angles. The web angles were centered on the beam web. Third, the column size did not change. Fourth, all weld sizes remained the same. The size of the gusset plate-beam fillet weld was considered a secondary variation and was investigated for a select group of connections.

In the results that follow, each connection simulation is assigned a name based on the connection geometry. For example, the designation w1453a500st refers to a connection with a W14x53 beam with 0.5-in steel angles connecting the gusset plate and beam to the column and a supplemental seat angle. The angle size is given in thousandths of an inch and the 'st' abbreviation is dropped if a seat angle is not present. Using this notation, CN1 is represented by w1049a375, CN6 is represented by w1049a625st, and CN7 is represented by w1049a625.

4.2.1 Summary of Parametric Study Results

Table 4.1 provides a summary of the parametric study results. The positive moment strengths ranged from 41% to 99% of $M_{p,exp}$ while the negative moment strengths ranged from

29% to 93% of $M_{p,exp}$. In general, the magnitude of the maximum positive moment was greater than the magnitude of the negative moment, although for some seat angle connections the two were nearly equal.

Table 4.1 Summary of parametric study results.

Specimen Name	Max positive normalized moment ($M/M_{p,exp}$)	Max positive story drift (rad)	Positive moment limit state*	Cumulative drift (rad)	Max negative normalized moment ($M/M_{p,exp}$)	Max negative story drift (rad)	Negative moment limit state*	Cumulative drift (rad)
w1049a375	0.49	0.03	GAF	0.85	-0.33	-0.02	WAF	0.80
w1049a375st	0.65	0.03	GAF	0.84	-0.45	-0.02	SAF	0.71
w1049a500	0.57	0.03	WLD	0.85	-0.54	-0.03	WAF	0.91
w1049a500st	0.83	0.03	WLD	0.85	-0.66	-0.03	SAF	0.91
w1049a625	0.60	0.03	WLD	0.85	-0.62	-0.04	BLT R6/L6	1.52
w1049a625st	0.85	0.03	WLD	0.85	-0.72	-0.04	BLT R7/L7	1.53
w1049a750	0.62	0.03	WLD	0.85	-0.64	-0.03	BLT R6/L6	1.18
w1049a750st	0.91	0.03	WLD	0.84	-0.80	-0.03	BLT R7/L7	1.18
w1453a375	0.41	0.02	GAF	0.67	-0.29	-0.015	WAF	0.65
w1453a375st	0.47	0.015	GAF	0.63	-0.40	-0.015	SAF	0.59
w1453a500	0.52	0.02	WLD	0.69	-0.47	-0.02	WAF	0.71
w1453a500st	0.70	0.02	WLD	0.69	-0.60	-0.02	SAF	0.73
w1453a625	0.53	0.02	WLD	0.69	-0.53	-0.03	BLT R7/L7	1.18
w1453a625st	0.71	0.02	WLD	0.69	-0.59	-0.02	BLT R8/L8	1.17
w1453a750	0.58	0.02	WLD	0.68	-0.59	-0.03	BLT R7/L7	1.17
w1453a750st	0.79	0.02	WLD	0.68	-0.74	-0.03	BLT R8/L8	0.92
w1846a375	0.51	0.015	GAF	0.62	-0.44	-0.015	WAF	0.60
w1846a375st	0.61	0.015	GAF	0.57	-0.63	-0.02	SAF	0.73
w1846a500	0.73	0.02	WLD	0.69	-0.59	-0.015	WAF	0.65
w1846a500st	0.87	0.02	WLD	0.69	-0.88	-0.03	BLT R10/L10	0.92
w1846a625	0.74	0.02	WLD	0.69	-0.77	-0.03	BLT R9/L9	1.18
w1846a625st	0.96	0.03	WLD	0.84	-0.87	-0.03	BLT R10/L10	1.17
w1846a750	0.80	0.02	WLD	0.68	-0.80	-0.03	BLT R9/L9	0.92
w1846a750st	0.94	0.02	WLD	0.68	-0.93	-0.03	BLT R10/L10	0.92
w2144a375	0.58	0.01	GAF	0.57	-0.51	-0.015	WAF	0.59
w2144a375st	0.66	0.01	GAF	0.57	-0.68	-0.02	SAF	0.73
w2144a500	0.81	0.01	GAF	0.76	-0.64	-0.015	WAF	0.65
w2144a500st	0.92	0.01	GAF	0.76	-0.88	-0.02	BLT R11/L11	0.92
w2144a625	0.90	0.02	WLD	0.85	-0.80	-0.03	BLT R10/L10	0.92
w2144a625st	0.99	0.01	WLD	0.85	-0.88	-0.02	BLT R11/L11	0.91
w2144a750	0.87	0.02	WLD	0.84	-0.84	-0.02	BLT R10/L10	0.92

*GAF = Gusset angle fracture; WAF = Web angle fracture; SAF = Seat angle fracture; WLD = Weld failure; BLT = Bolt fracture

The story drift at maximum positive moment ranged from 0.01 rad to 0.04 rad and the story drift at maximum negative moment ranged from 0.015 rad to 0.04 rad. The story drift at maximum moment in both positive and negative flexure typically decreased with increasing beam depth. Gusset angle fracture and weld failure limited the moment strength in positive bending, and web or seat angle fracture and bolt fracture limited the moment strength in negative bending.

4.2.2 Effect of Beam Depth

Normalized moment vs. story drift is plotted for each beam depth with 0.375-in angles in Figure 4.11. The cumulative story drift at gusset/web angle fracture initiation is given in parentheses after each beam name. The results are presented up to 0.03 rad story drift since all limit states were observed within this range.

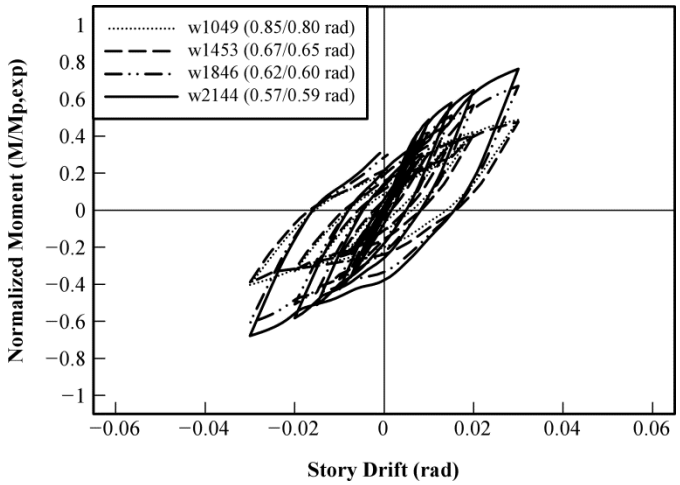

Figure 4.11 Normalized moment vs. story drift for various beam depths with 0.375-in thick angles.

As expected, the flexural strength increased with beam depth, due to the larger moment arm between the tension and compression components of the force couple. There was minimal strength gain between w1049a375 and w1453a375 since only one additional bolt row was added

to the web angle in w1453a375. Adding two bolt rows to the web angles resulted in a significant strength increase between w1453a375 (3 bolts) and w1846a375 (5 bolts). Adding another bolt row to reach w2144a375 (6 bolts) produced a small gain in moment strength, but less than the increment between w1453a375 and w1846a375. In addition, the initial stiffnesses of w1846a375 and w2144a375 were significantly larger than the initial stiffnesses of w1049a375 and w1453a375. Nevertheless, the cumulative story drifts at angle fracture initiation show that low-cycle fatigue fractures in the web and gusset angles occurred earlier as the beam depth increased. This trend was expected since increasing the beam depth results in larger strain demands in the critical regions of the gusset plate and web angles for the same connection rotation.

4.2.3 Effect of Angle Thickness

Normalized moment vs. story drift for the W14x53 beam with different angle thicknesses are given in Figure 4.12. The results are typical of the response of the other beam depths as angle thickness increased. Increasing the angle thickness from 0.375 in to 0.5 in generated a significant increase in flexural strength. But, when the angle thickness was increased from 0.5 in to 0.625 in, minimal stiffness and strength increase were realized. This is due to the larger angle leg size for the 0.625-in angles. Since the leg size increased to 4 in, the gage distance for the bolt holes increased from 1.5 in to 2 in. The larger gage distance resulted in more flexibility in the angles, which caused the minimal stiffness and strength increase between w1453a500 and w1453a625. Increasing the angle thickness to 0.75 in provided additional strength, but the increase was smaller than the strength increase generated by the 0.5 in angles.

In addition to the strength increases, increasing the angle thickness changed the limiting

damage state in positive bending from gusset angle fracture to fillet weld failure. Increasing the angle thickness also delayed the onset of web angle fracture. The cumulative story drifts for the strength limiting failure modes are given in parentheses in the legend of Figure 4.12. A 'w' in front of a cumulative story drift indicates a weld failure initiation. Bolt fractures were not predicted for the W14x53 beams, although the W18x46 and W21x44 beams with 0.625-in and 0.75-in angles were susceptible to bolt fractures as indicated in Table 4.1.

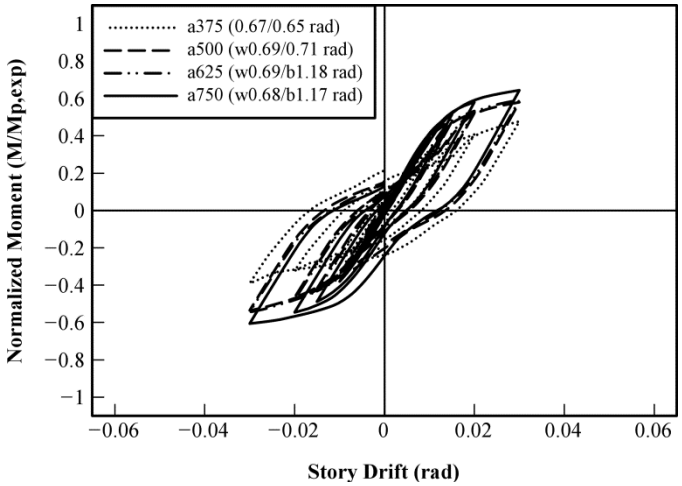

Figure 4.12 Normalized moment vs. story drift for W14x53 beam with various angle thicknesses.

4.2.4 Effect of Seat Angle

Figure 4.13 illustrates the normalized moment vs. story drift for connections w1453a500 and w1453a500st. The seat angle was found to increase the connection stiffness and strength, which was consistent with the results presented in Chapter 3. In addition, the strength gain in positive bending was larger than the strength gain in negative bending. These results are representative of all beam depths and angle thicknesses. The length of the seat angle was determined by the workable gage of the column and the minimum bolt edge distance from the

AISC *Steel Construction Manual* (2005c).

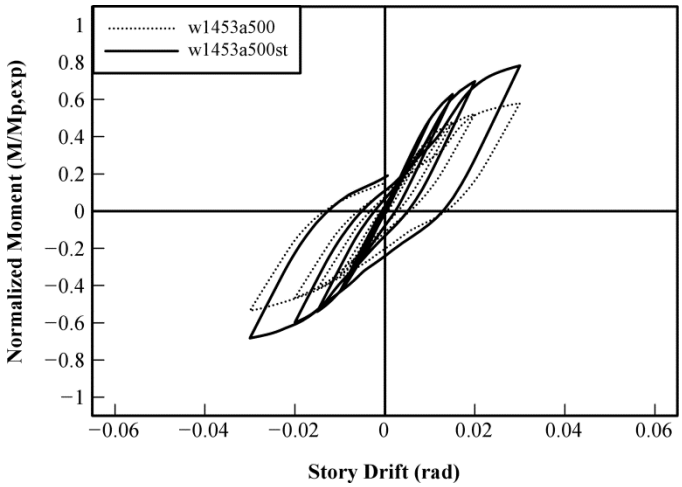

Figure 4.13 Normalized moment vs. story drift for W14x53 with 0.5-in angles, with and without supplemental seat angle.

For seat angle connections with 0.375-in angles, the negative moment strength was limited by fracture of the seat angle, as opposed to fracture of the web angle in connections without the supplemental seat angle. As indicated in Table 1, seat angle fractures were predicted at smaller cumulative story drifts for w1049a375st and w1453a375st than the web angle fractures in w1049a375 and w1453a375. For w1846a375st and w2144a375st, however, the seat angle fractures were predicted at larger cumulative story drifts than the corresponding web angle fractures in w1846a375 and w2144a375. This is the result of the beam flange width being significantly smaller than the seat angle width in w1846a375st and w2144a375st. Since the beam flange was narrower than the seat angle, the strain demands in the seat angle were lower due to increased seat angle flexibility. In positive bending, the gusset angle fractures occurred at equal or smaller story drifts than in the seat angle connections.

As shown in Table 1, for seat angle connections with 0.5-in thick angles, the strength in negative bending was limited by seat angle fracture in w1049a500st and w1453a500st instead of

the web angle fracture observed for the corresponding connections without seat angles (w1049a500 and w1453a500). The cumulative story drifts at fracture initiation were unchanged, however. For w1846a500st and w2144a500st, the negative moment strength was limited by fracture of the seat angle bolts. In positive bending, the strength limit state and cumulative story drift at initiation remained the same between connections with and without a supplemental seat angle.

For seat angle connections with 0.625-in and 0.75-in angles, the negative moment strength was limited by fracture of the bolts in the seat angle instead of the web angles. The cumulative story drift at bolt fracture remained constant between connections with and without a supplemental seat angle. The lone exception was w1453a750st, where fracture of the seat angle bolts occurred at a lower cumulative story drift than fracture of the web angle bolts in w1453a750. Again, in positive bending, the strength limit state and cumulative story drift at initiation remained constant between connections with and without a supplemental seat angle.

4.2.5 Effect of Weld Size and Gusset Plate Thickness

As mentioned previously, the effects of weld size and gusset plate thickness on connection flexural behavior were investigated for a limited number of cases. Connections w1049a500, w1453a500, and w1846a500 were selected for the weld size study since the finite element results indicated that gusset angle fracture was likely to initiate soon after weld failure in these models. The weld sizes selected for the study were 0.375 in, 0.4375 in, and 0.5 in. The baseline weld size used in the other portions of the parametric study was 0.3125 in. This set spans the range of weld sizes investigated in the reference experimental program.

Connections w1049a375 and w1846a375 were chosen for the gusset plate thickness study since the 0.375-in angles were deemed to provide the least resistance to gusset plate buckling. In addition, it was desirable to investigate the effect of gusset plate thickness on connections with different beam depths. The gusset plate thicknesses selected were 0.375 in, 0.5 in, and 0.75 in, which are typical for CBFs (Carter 2009). The gusset plate thickness from the experimental program was 0.625 in. In the results presented thus far, geometric imperfections in the connection region were not considered since analyses including imperfections demonstrated no appreciable differences in stiffness, strength, or damage initiation when compared to connections with unperturbed geometry. In addition, buckling of the gusset plate and beam flanges were not observed during the large-scale tests. Nevertheless, geometric imperfections were included for models with 0.375-in and 0.5-in gusset plates. The imperfection geometry was based on an eigenvalue buckling analysis of the connection model, and the imperfection magnitude was based on values measured in the reference experimental program. In the results that follow, additional information is added to the connection name. For the weld size study, an 'fw' followed by the fillet weld size in thousandths of an inch is added (e.g. w1049a500fw375). And, for the gusset plate study, a 'gp' followed by the gusset plate thickness in thousandths of an inch is added (e.g. w1846a375gp750).

Figure 4.14 shows cumulative story drift at weld failure vs. weld size data for w1453a500 with various weld sizes. The cumulative story drift at initiation of gusset angle fracture is also shown. It is evident from Figure 4.14 that increasing the weld size delays the onset of weld failure, even to the point that weld failure is no longer the controlling strength limit state in positive bending. For the cases studied, a weld size of 0.4375 in prevented weld failure. Results

are not shown for the 0.5-in weld since weld failure was not predicted for that weld size. In addition, normalized moment vs. story drift data suggested that weld size has no effect on the flexural stiffness and strength of beam-column connections with gusset plates. The trends for w1049a500 and w1846a500 are similar. Thus, the conclusions about weld size developed in Chapter 3 were corroborated with finite element analyses.

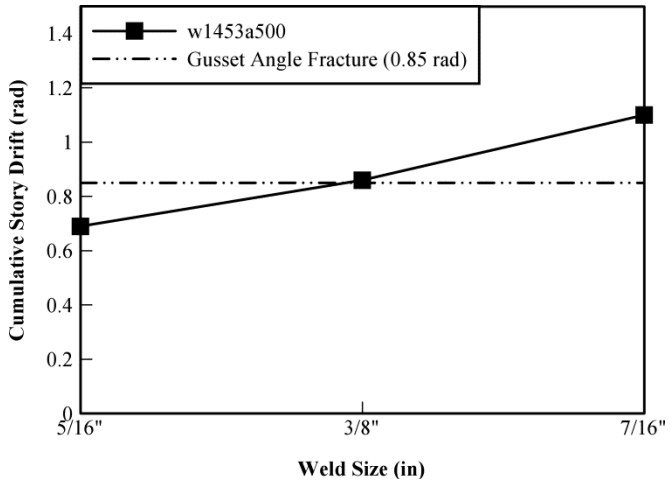

Figure 4.14 Cumulative story drift at weld failure vs. weld size.

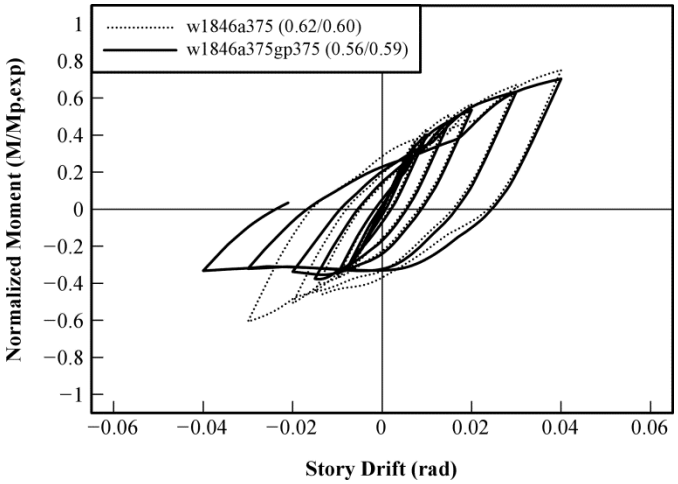

Figure 4.15 Normalized moment vs. story drift for w1846a375 and w1846a375gp375.

Figure 4.15 shows normalized moment vs. story drift for w1846a375 and w1846a375gp375. Examination of the third quadrant of Figure 4.15 reveals that the thinner gusset plate buckled, which degraded the flexural strength of the connection in negative bending.

In addition, the cumulative story drift at gusset angle fracture was significantly lower due to the out-of-plane deformation of the angles caused by gusset plate buckling. It can be surmised that bolt fracture in the web angles would also occur at lower story drifts due to gusset plate buckling, although this hypothesis was not tested in this study. Thus, gusset plate buckling should be prevented in braced frame connections used within a reserve lateral force-resisting system. This issue is addressed in the braced frame connection analysis procedure that follows.

Flexural strength in positive bending and both positive and negative stiffnesses were relatively unaffected by gusset plate thickness. Gusset plate buckling, and associated strength loss, was not as pronounced when the gusset plate thickness was increased to 0.5 in, and nonexistent for the 0.625-in and 0.75-in gusset plates. Similar results were obtained for w1049a375 with the various gusset plate thicknesses.

4.3 ANALYTICAL MODELS OF CONNECTION FLEXURAL RESPONSE

Although current seismic design procedures for CBFs do not explicitly consider the flexural behavior of beam-column connections with gusset plates, employing reserve capacity to achieve seismic collapse prevention is a promising design approach (Hines and Fahnestock 2010). In addition, seismic evaluation of existing low-ductility CBFs in high seismic regions is another context where reserve capacity is potentially beneficial (Callister and Pekelnicky 2011). Thus, a simplified procedure for quantifying the flexural stiffness and strength of beam-column connections with gusset plates was developed from the present numerical simulations and experimental results. This type of beam-column connection with gusset plate, which is considered to be part of a low-ductility CBF, is typically designed using the Uniform Force

Method (AISC 2005c) and is not detailed for seismic. Thus, detailing requirements as defined in the AISC *Seismic Provisions* (2005a) for ductile systems are not employed. The procedure described below is primarily viewed as a tool to determine the flexural stiffness and strength for a connection that has already been proportioned as part of the braced frame system design. Additionally, if there is a need to increase reserve capacity in a braced frame system, this procedure can be used to assess potential braced frame connection variations to achieve this goal. Thus, it is not suitable to be the primary design approach for braced frame connections since it does not consider axial force effects, but only quantifies flexural properties.

The procedure predicts elastic stiffnesses and ultimate strengths for positive and negative bending. Estimated moment-rotation behavior and associated experimental/numerical data are shown for CN1 and w1846a500 in Figure 4.16.

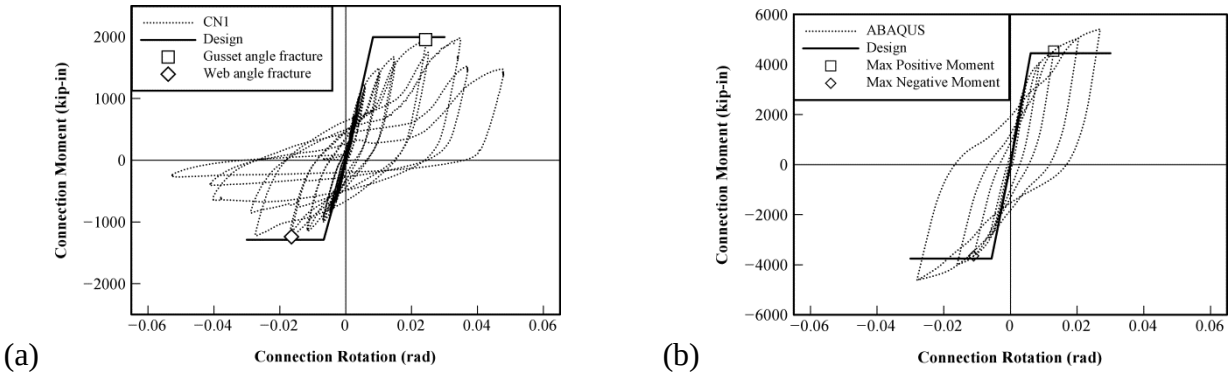

Figure 4.16 Simplified connection moment vs. connection rotation: (a) CN1; (b) w1846a500.

It is envisioned that this backbone behavior could be established for the braced frame connections in a CBF and then implemented, via rotational springs at the beam-column joints, within a static pushover or nonlinear response history analysis. The design procedure consists of three parts: estimation of initial connection stiffness, estimation of ultimate moment strength, and capacity design of other connection elements. The initial connection stiffness and ultimate

moment strength are based on the geometry and material properties of the steel angles. Capacity design of other connection elements is carried out using existing design procedures.

4.3.1 Initial Connection Stiffness

Initial connection stiffness is approximated by dividing the gusset plate and beam web angles into segments based on the spacing of the connection bolts. The seat angle, if present, should be considered similarly as one segment with a width, *b*, equal to the width of the seat angle. Each segment is assumed to act as a linear spring. The stiffness of each segment is determined by assuming that the out-of-plane legs of the gusset plate and beam web angles, or vertical leg of the seat angle, act as cantilever beams subjected to a point load at the free end. Figure 4.17 shows the angle geometry and Figure 4.18 shows the connection geometry used in the initial stiffness calculations.

In Figures 4.17 and 4.18, *g* is the gage distance from the heel of the angle to the centerline of the bolt hole, L_{eff} is the effective length of the cantilever beam model of the out-of-plane angle leg, *t* is the angle thickness, and P_i is the point load applied to the free end of the cantilever.

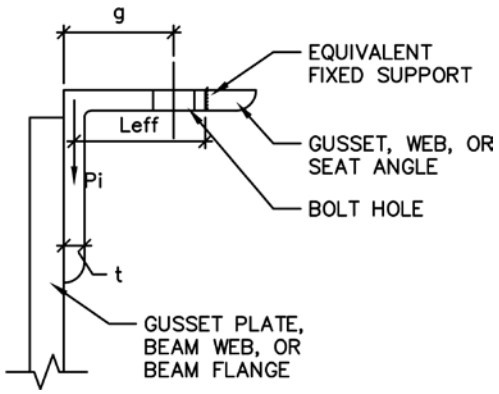

Figure 4.17 Angle cross-section for estimation of connection stiffness.

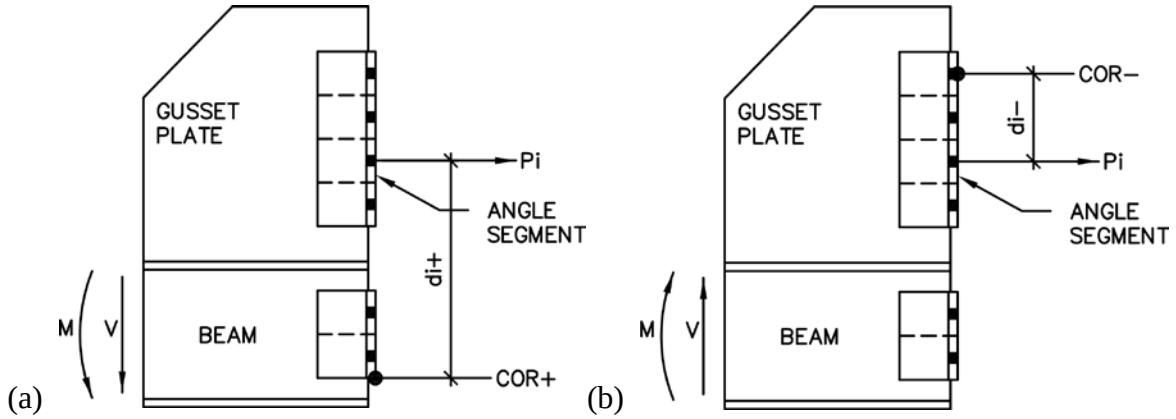

Figure 4.18 Connection geometry for estimation of connection stiffness: (a) positive bending; (b) negative bending.

Considering flexural and shear deformations, the stiffness of each segment is determined from

$$k_i = \frac{P_i}{\Delta_i} = \left(\frac{L_{eff}^3}{3EI} + \frac{L_{eff}}{GA_s} \right)^{-1} \tag{4.6}$$

where E is the elastic modulus, I is the moment of inertia, G is the shear modulus, A_s is the shear area, and Δ_i is the displacement corresponding to P_i. The section properties, I and A_s, should be based on a rectangular section having thickness t and width b_{net} which is computed from

$$b_{net} = b - d_b \tag{4.7}$$

where b is the width of the angle segment and d_b is the nominal bolt diameter. For seat angles, $2d_b$ is subtracted from b to compute b_{net}. Since the critical section is rectangular, A_s should be taken as 5/6 of the gross area $A = b_{net}t$. Based on the experimental and numerical results, L_{eff} is computed as

$$L_{eff} = 4t + \frac{g}{4} \tag{4.8}$$

The initial stiffness of the simplified connection moment vs. connection rotation response can now be expressed as

$$K_{conn} = \sum_{1}^{N_b} k_i d_i^2 \tag{4.9}$$

where d_i is the distance from the centroid of the angle segment, or centerline of the bolts in the seat angle, to the center of rotation, and N_b is the number of bolts. The center of rotation, shown in Figure 4.18, is the bottom of the beam web angles for positive bending and the top bolt row for negative bending. For connections with a seat angle, the center of rotation for positive bending is located at the heel of the seat angle. In addition, k_i of the seat angle should only be included in calculating the initial stiffness in negative bending. It should be noted that d_i for positive bending will, typically, be different than d_i for negative bending.

4.3.2 Ultimate Moment Strength

To compute the ultimate moment strength of braced frame connections, the angles are again divided into segments based on the bolt spacing, with the seat angle, if present, being considered as one segment. In the moment strength calculation, however, plastic hinges are assumed to form in both legs of the angles. Figures 4.19 and 4.20 show the angle and connection geometry used in the moment strength calculations.

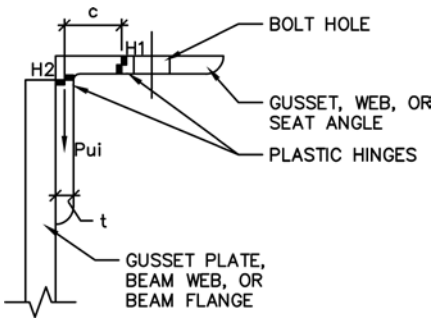

Figure 4.19 Angle cross-section for estimation of connection strength.

In Figure 4.19, H_1 and H_2 denote the plastic hinges in the out-of-plane leg and the in-

plane leg, respectively; c is the distance between the plastic hinges; and P_{ui} is the applied load corresponding to formation of H_1 and H_2. Taking a free body diagram of the angle between the two plastic hinges yields an expression for P_{ui}

$$P_{ui} = \frac{M_{p1} + M_{p2}}{c} \tag{4.10}$$

in terms of the plastic moment strength M_{p1}, of H_1, and M_{p2}, of H_2. M_{p1} and M_{p2} are calculated from

$$M_{p\alpha} = F_u Z_{x\alpha} \tag{4.11}$$

where F_u is the ultimate tensile strength of the angles and $Z_{x\alpha}$ is the plastic section modulus that corresponds to plastic hinge H_α. Z_{x1} is computed using b_{net} and Z_{x2} is computed using b, which were defined in the previous section. The tensile strength is used in the plastic hinge calculation to recognize that strain hardening of the angle material results in higher moment strengths for cyclic loading than would be realized under monotonic loading. In addition, the ultimate moment strength corresponds to fracture initiation in the gusset plate and web angles. Fracture limit states are typically approximated using F_u in the AISC *Specification* (2005b). The distance between the plastic hinges, c, is computed using:

$$c = L_{eff} - \frac{t}{2} - \frac{W}{2} \tag{4.12}$$

where t is the angle thickness, W is the width of the head of the bolt corresponding to the angle segment, which can be found in the AISC *Steel Construction Manual* (2005c). L_{eff} was defined in the previous section. Once P_{ui} is known for each angle segment, the connection moment strength M_{conn} is found from

$$M_{conn} = \sum_{1}^{N_b} P_{ui} d_{ui} \tag{4.13}$$

where d_{ui} is the distance from the centroid of the angle segment, or centerline of the bolts in the seat angle, to the location of the contact force F_c.

Figure 4.20a shows d_{ui} and the location of F_c for positive bending and Figure 4.20b shows d_{ui} and the location of F_c for negative bending. Like d_i for the initial stiffness calculation, d_{ui} is different for positive and negative bending. Similar to the initial stiffness calculation, P_{ui} from the seat angle should only be included for calculating M_{conn} in negative bending. F_c is located at the bottom of the web angle, or heel of the seat angle when it is present, for positive bending.

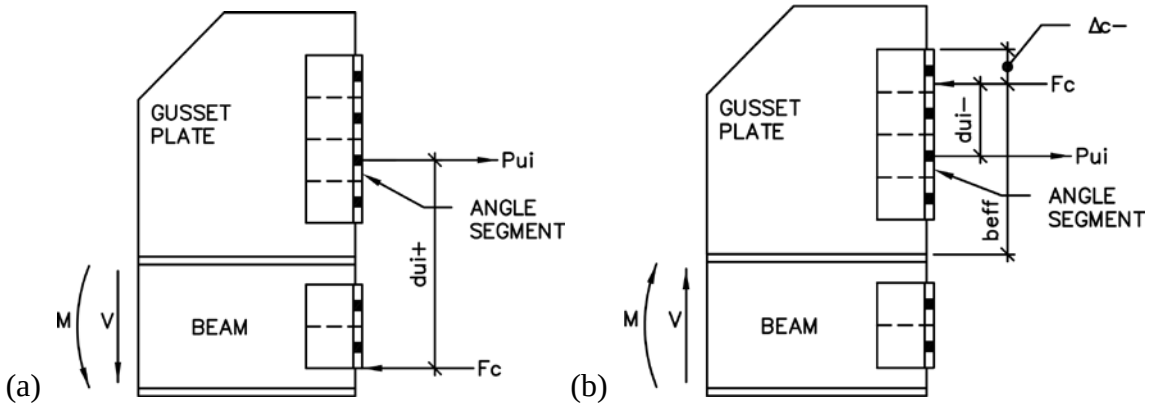

Figure 4.20 Connection geometry for estimation of connection strength: (a) positive bending; (b) negative bending.

In negative bending, however, the location of F_c varies with angle thickness and beam depth according to

$$\Delta_c^- = 0.5 d_{beam} - 28t + 8 \tag{4.14}$$

where Δ^-_c is the distance, in inches, from the top of the gusset plate angle to F_c for negative bending, shown in Figure 4.20b, and d is the beam depth. The minimum value of Δ^-_c is 0 in and the maximum value is 4.5 in, which are based on the experimental and computational results. In

addition, if Δ_c^- is greater than or equal to the edge distance to the first bolt row, P_{ui}, all bolts in this row should be excluded when calculating M_{conn}.

It should also be noted that a limit needs to be placed on the rotation capacity of braced frame connections used for reserve capacity. Since the experimental program considered only one beam depth, and the finite element models did not model propagation of damage, there is insufficient data to make a recommendation based on the results presented in this study. Thus, based on the recommendations of the commentary to Chapter B of the AISC *Specification* (2005b), the rotation capacity for braced frame connections used in reserve LFRSs should be limited to 0.03 rad.

4.3.3 Capacity Design of Other Connection Elements

Since low-cycle fatigue fracture of steel angles was the most ductile limit state observed in the reference experimental program, the gusset plate, gusset plate-beam fillet weld, gusset plate/beam web to angles fillet welds, bolts, and column must be capacity designed to develop the full strength of the gusset plate and beam web angles. Adequate guidance for designing these connection elements can be found in existing literature. Design guidelines for the gusset plate and gusset plate-beam fillet weld are presented by Salmon et al. (2009), and design guidelines for the gusset plate/beam web to angles fillet welds, bolts, and column are presented in the AISC *Steel Construction Manual* (2005c) and *Specification* (2005b). What follows is a summary of these design procedures and how they apply to design of braced frame connections for flexure.

In designing the gusset plate, the thickness needs to be selected so buckling of the gusset plate is prevented. The complexity of the stress distribution within the gusset plate makes it

difficult to develop a rational method for computing the compressive capacity and demand of the gusset plate. Instead, a width-thickness requirement is specified for the gusset plate, based on prior experimental work, to provide a conservative estimate for the gusset plate thickness. Salmon et al. (2009) recommend the following width-thickness ratios to develop the full plastic strength of triangular bracket plates in compression. The notation has been specialized for the present application as

$$\frac{b_{eff}}{t_p} \leq 0.73\sqrt{\frac{E}{F_y}} \tag{4.15a}$$

for $0.5 \leq b_{eff}/a \leq 1.0$, and

$$\frac{b_{eff}}{a} \leq 0.73\left(\frac{b_{eff}}{t_p}\right)\sqrt{\frac{E}{F_y}} \tag{4.15b}$$

for $1.0 \leq b_{eff}/a \leq 2.0$, where a is the dimension of the gusset plate parallel to the beam, b_{eff} is the distance between the heel of the gusset plate and F_c in negative bending, shown in Figure 4.20b, t_p is the thickness of the gusset plate, and F_y is the yield stress of the gusset plate.

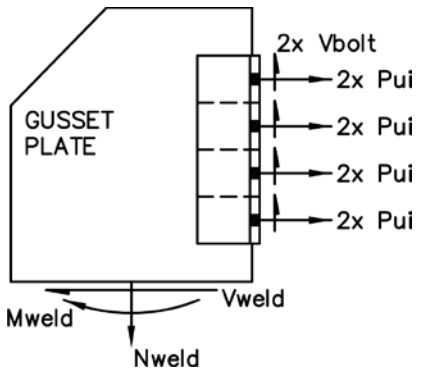

Figure 4.21 Free-body diagram for computing weld demand.

To design the gusset plate-beam fillet weld, elastic vector analysis should be used. One possibility for conducting this analysis is presented by Salmon et al. (2009). For the present case of flexure in beam-column connections with gusset plates, the gusset plate-beam fillet weld is

subjected to direct normal, shear, and flexural stresses. To compute the demand on the fillet weld, the free-body diagram in Figure 4.21 should be used. The direct normal, shear, and flexural forces are denoted N_{weld}, V_{weld}, and M_{weld} in Figure 4.21. V_{bolt} in Figure 4.21 is calculated as

$$V_{bolt} = \frac{M_{conn}}{\left(L/2\right) N_b} \tag{4.16}$$

where L is the span of the beam under consideration. M_{conn} and N_b were defined previously. Essentially, V_{bolt} in Equation (4.16) is the tip load on a cantilever beam, similar to the large-scale test setup, required to produce M_{conn} divided equally between all connection bolts. Once the weld demand is known, the procedures in Salmon et al. (2009) should be followed to determine the gusset plate-beam fillet weld size.

To compute the required weld size for the fillet welds connecting the angles to the gusset plate and beam web, a free-body diagram should be created with P_{ui} and V_{bolt} applied to each bolt to determine the weld demand. V_{bolt} may be neglected if it is significantly smaller than P_{ui}. Design methods for fillet welds, such as found in the AISC *Specification* (2005b), should then be used to proportion the welds.

In addition, the tensile strength of the connection bolts should be designed to resist the applied load at ultimate moment, P_{ui}, plus the prying force induced by deformation of the angles. One version of the prying force calculation is provided in the AISC *Steel Construction Manual* (2005c). In lieu of calculating t_{min} to prevent prying action, the authors recommend calculating q, the prying force per bolt, and proportioning the bolts to resist $P_{ui} + q$. Finally, the column should be designed considering the combined effects of axial force, due to gravity load, and

M_{conn}. The rational for using only the gravity load in the strength interaction check is discussed thoroughly in Chapter 5.

4.4 SUMMARY OF FINITE ELEMENT ANALYSIS

This chapter presented the results of numerical simulations studying the flexural behavior of beam-column connections with gusset plates. This flexural behavior can provide reserve capacity to low-ductility braced frames after failure of brace-gusset plate welded connections. This reserve capacity is critical for preventing seismic collapse in low-ductility braced frames (Hines et al. 2009). Since the experimental work detailed in Chapter 3 focused on a small number of variations in the connection parameters, the parametric study discussed herein was undertaken to expand the range of known flexural behaviors for braced frame connections. This parametric study provides a valuable database of connection response that covers a broad range of typical configurations. The following conclusions were drawn from the numerical simulations:

- Beam-column connections with gusset plates have appreciable flexural stiffness and strength. The stiffness and strength were increased, without loss of ductility, by using thicker double angles in the connection and adding a supplemental seat angle to the bottom beam flange.
- Flexural strengths of double angle connections ranged from 41% to 99% of the beam plastic moment strength in positive bending and from 29% to 93% of the beam plastic moment strength in negative bending.
- The story drift at maximum positive moment ranged from 0.01 rad to 0.04 rad and the story drift at maximum negative moment ranged from 0.015 rad to 0.04 rad. The story drift at

maximum moment in both positive and negative flexure typically decreased with increasing beam depth. Gusset angle fracture and weld failure limited the moment strength in positive bending, and web or seat angle fracture and bolt fracture limited the moment strength in negative bending.

- Thicker double angles delayed the onset of fatigue fracture in the beam web angles and changed the strength limit state in positive bending to weld failure, not gusset angle fracture. Bolt fracture, instead of web angle failure, was observed for negative bending in most cases with 0.625-in and 0.75-in angles.
- The flexural stiffness and strength of the double angle connections studied increased with increasing beam depth. Initiation of fatigue fractures in the angles, however, occurred at smaller story drifts for deeper beams.
- The addition of a supplemental seat angle was found to increase flexural stiffness and strength for the range of beam depths considered in the parametric study, 14 in to 21 in, just as observed in the experimental program for a single beam depth, 10 in. The seat angle did not affect, or only slightly decreased, the cumulative drift at which the critical limit states occurred.
- Increasing the gusset plate-beam fillet weld size delayed the initiation of weld failure, but did not provide additional flexural stiffness or strength.

Finally, a simplified analysis procedure was developed to describe the flexural behavior of braced frame double angle connections. This procedure estimates connection initial stiffness and peak strength for both positive and negative bending, and it is valuable for analyzing concentrically braced frames as part of seismic design or assessment methods that employ

reserve capacity. Defining connection flexural behavior allows for quantification of overall reserve system strength and stiffness, which can then be evaluated against requirements for seismic collapse prevention. Ongoing numerical simulations of concentrically braced frame system earthquake response will establish appropriate reserve system requirements.

CHAPTER 5

COLLAPSE PERFORMANCE EVALUATION

In the preceding chapters, the flexural stiffness and strength of beam-column connections with gusset plates were extensively explored using full-scale experiments and computational simulation. Nevertheless, the primary question this dissertation seeks to answer remains: "How much reserve lateral force-resisting strength is needed to achieve acceptable collapse prevention performance of CBFs in moderate seismic regions?" As a first step toward answering this question, the collapse performance of a suite of CBFs designed using the R = 3 provision for Boston, Massachusetts, was studied using reliability-based performance assessment. The baseline CBF designs were augmented with reserve lateral systems comprised of braced frame connections with flexural behavior consistent with the results from Chapters 3 and 4 of this dissertation.

In addition to a thorough investigation of the collapse behavior of chevron configuration CBFs, static pushover (SPO) analyses were used to quantify the strength and stiffness of the reserve systems of the case study buildings. The results from the collapse performance assessment were compared to the data from the SPO analyses in order to determine the minimum level of reserve lateral-force resisting strength that leads to acceptable collapse performance under MCE level seismic hazard. Combining the results from both types of analyses satisfactorily answers the primary question of this dissertation. In what follows, a detailed description of the design and computational modeling of the case study buildings is presented first. Then, the results from the SPO analyses are presented. The basic framework of the reliability-based performance assessment used to quantify collapse performance is outlined and

the results from the assessment are presented. Finally, recommendations for the minimum level of reserve lateral force-resisting capacity needed to achieve acceptable collapse performance in moderate seismic regions are presented and a simplified model for estimating the strength of a reserve LFRS composed of braced frame connections is developed.

5.1 CASE STUDY BUILDING DESIGN AND MODELING

5.1.1 Case Study Building Design

The case study buildings for the present investigation were based on the structures studied by Hines et al. (2009), which were derived from the SAC building floor plan geometry (FEMA 2000b). The geometry for the case study buildings is illustrated in Figure 5.1.

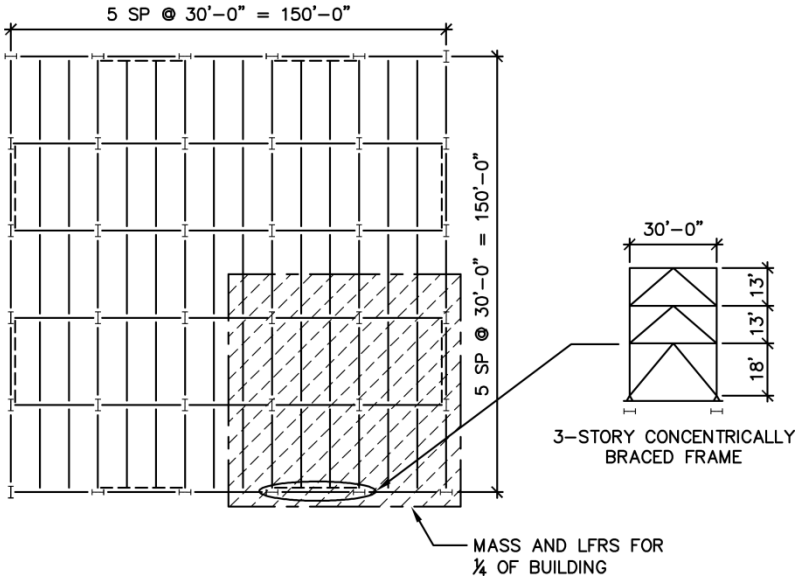

Figure 5.1 Case study building geometry (Hines et al. 2009).

Hines et al. (2009) designed the buildings represented by Figure 5.1 for the Boston, Massachusetts, moderate seismic region using a response modification coefficient, *R*, of three. In addition, site soil class D was assumed, which resulted in Seismic Design Category (SDC) C for the structures. Seismic detailing was not carried out since it is not required for steel

structures in SDC A, B, or C designed with the R = 3 provision. The above assumptions resulted in code prescribed maximum considered earthquake spectral accelerations S_{MS} = 0.52g and S_{M1} = 0.216g for the short duration and one-second periods, respectively. ASCE 7 (ASCE 2002) was used to determine the design gravity loads and response spectrum. The member sizes for the CBFs designed by Hines et al. (2009) are given in Table 5.1 and the design loads are given in Table 5.2.

Table 5.1 Member sizes for case study buildings (after Hines et al. 2009).

Height	Story	Brace	Girder	Column	Interior Gravity Column	Corner Column
3 Story	R		W21x44			
	3	HSS 6x6x1/4	W21x44	W12x40	W12x40	W12x40
	2	HSS 7x7x1/4	W21x44	W12x40	W12x40	W12x40
	1	HSS 8x8x1/4		W12x53	W12x53	W12x53
6 Story	R		W21x44			
	6	HSS 6x6x1/4	W21x44	W12x40	W12x40	W12x40
	5	HSS 6x6x1/4	W21x44	W12x40	W12x40	W12x40
	4	HSS 7x7x1/4	W21x44	W12x53	W12x53	W12x40
	3	HSS 8x8x1/4	W21x44	W12x53	W12x53	W12x40
	2	HSS 8x8x1/4	W21x44	W12x87	W12x87	W12x53
	1	HSS 8x8x5/16		W12x87	W12x87	W12x53

Table 5.2 Design loads for case study buildings (after Hines et al. 2009).

Height	Floor	Seismic Weight (kips)	Dead Load (kips)	Live Load (kips)	$1.0DL + 1.25LL$ (kips)
3 Story	R	2268	2268	1158	2560
	3	2184	2415	1158	2704
	2	2224	2454	1158	2744
6 Story	R	2268	2268	1158	2560
	6	2184	2415	1158	2704
	5	2184	2415	1158	2704
	4	2184	2415	1158	2704
	3	2184	2415	1158	2704
	2	2224	2454	1158	2744

The seismic weights listed in Table 5.2 differ from the given dead loads because only ½ the dead load due to partition walls was included in the seismic weight calculations. Additional details

about the design of the case study buildings may be found in Hines et al. (2009) and Appel (2008).

The collapse results from Hines et al. (2009) suggested that 3-story and 6-story chevron configuration CBFs were more susceptible to seismic collapse than taller structures in moderate seismic regions. In light of this fact, the present study focused exclusively on 3-story and 6-story structures. A key distinction between the present investigation and the study by Hines et al. (2009) is the braced frame connection flexural behavior used to create the reserve LFRS. Hines et al. (2009) analytically created reserve capacity by assuming rigid connections between the beams and columns in the braced frame. The connections were assumed to have no degradation under cyclic loading. In contrast, the focus of the current study is creating reserve capacity systems using the realistic flexural behavior of beam-column connections with gusset plates, including stiffness and strength degradation under cyclic loading. Thus, the present study is needed to determine if adequate collapse prevention performance can be achieved by harnessing the flexural behavior of braced frame connections. The general conclusion by Hines et al. (2009) that increasing reserve capacity enhances collapse performance of CBFs designed using $R = 3$ is reinforced by the findings presented here, and the critical framework for how this may be realistically accomplished within the CBF is established by this research.

To vary the stiffness and strength of the reserve LFRS in the case study buildings, the beam depth and double angle thickness were varied in the braced frame connections. The data presented in Chapter 4 demonstrated that increasing beam depth and/or angle thickness increases the flexural strength of braced frame connections, which increases reserve capacity. In addition to the W21x44 used in the original building design by Hines et al. (2009), W18x86 and W14x53 beams were considered. These beams were selected because they represent typical beam depths

for CBFs and have plastic moment capacities similar to the W21x44. In addition to the baseline 0.375-in thick double angles, 0.5-in, 0.625-in, and 0.75-in angle thicknesses were selected since this range of angle thicknesses is typical for CBFs in moderate seismic regions. Seat angle connections were excluded from the system studies since they introduce additional complexity into the fabrication and erection of braced frame connections that increasing angle thickness does not. However, the addition of seat angles is still considered to be a simple and effective means for increasing reserve capacity. All CBFs considered in this study are listed in Table 5.3.

Table 5.3 Matrix of case study buildings.

Building Height	Beam		
	W14x53	W18x46	W21x44
3 story	3storyR3w14a000	3storyR3w18a000	3storyR3w21a000
	3storyR3w14a375	3storyR3w18a375	3storyR3w21a375
	3storyR3w14a500	3storyR3w18a500	3storyR3w21a500
	3storyR3w14a625	3storyR3w18a625	3storyR3w21a625
	3storyR3w14a750	3storyR3w18a750	3storyR3w21a750
6 story	6storyR3w14a000	6storyR3w18a000	6storyR3w21a000
	6storyR3w14a375	6storyR3w18a375	6storyR3w21a375
	6storyR3w14a500	6storyR3w18a500	6storyR3w21a500
	6storyR3w14a625	6storyR3w18a625	6storyR3w21a625
	6storyR3w14a750	6storyR3w18a750	6storyR3w21a750

Each case study building was designated by a name with four components: the first component indicates the building height, ‘3story’ or ‘6story’; the second component indicates the building was designed using the R = 3 provision, ‘R3’; the third component indicates the beam used in the braced frame, ‘w14’ for W14x53 beams, ‘w18’ for W18x46 beams, and ‘w21’ for W21x44 beams; and the fourth component indicates the double angle thickness of the braced frame connections, ‘a000’ for a simple pin connection, ‘a375’ for 0.375-in angles, ‘a500’ for 0.5-in angles, ‘a625’ for 0.625-in angles, and ‘a750’ for 0.75-in angles. Each combination of beam depth and angle thickness represents the flexural behavior of a beam-column connection with

gusset plate investigated in Chapter 4. Buildings with the angle thickness designation 'a000' should be considered to have zero flexural strength in the braced frame connections.

5.1.2 Case Study Building Modeling

Computational models of the case study buildings were built using the *OpenSees* nonlinear analysis software package (Mazzoni et al. 2009). To reduce computational cost, ¼ of the building was modeled as a planar frame in *OpenSees*, which was indicated in Figure 5.1. The computational model for the 3-story building is illustrated in Figure 5.2. Masses and gravity loads were lumped at the beam-column intersections, which are denoted by the dashed circles in Figure 5.2. The flexural axis orientation for all the columns is also shown.

In addition to the braced frame, all gravity columns were explicitly modeled to account for P-Δ effects. The columns were assumed to be continuous over the height of the building for both 3-story and 6-story configurations. Modeling continuous gravity columns recognizes that gravity columns can provide reserve system strength after damage to the braced frame. This fact has been documented in several previous studies (Tremblay and Stiemer 1994, Tremblay et al. 1995, and Rai and Goel 2003). In Figure 5.2, column stacks 2, 3, 6, and 7 represent interior gravity columns, column stacks 1 and 8 represent braced frame columns perpendicular to the loading direction, and column stack 9 represents the corner column. Column stacks 4 and 5 are part of the braced frame resisting seismic loading. The leaning columns were placed on both sides of the braced frame so inertial forces would be applied approximately equally. The columns were connected to the braced frame with rigid links at each floor, assuming ideal pin connections. All column base supports were also assumed to be ideal pins.

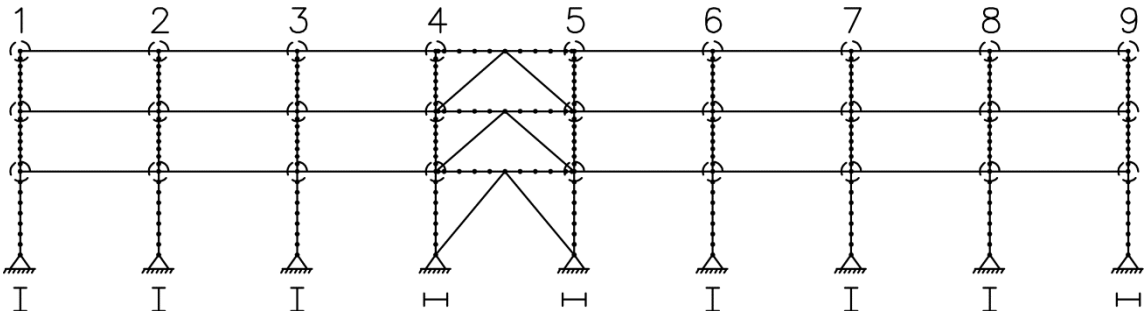

Figure 5.2 *OpenSees* model of 3-story case study building.

All beams and columns were modeled with the 'forceBeamColumn' element from the *OpenSees* element library (Mazzoni et al. 2009). This element is a force-based element that accounts for large-deformations and spread of inelasticity along the length of the element. The stiffness matrix for the element was formulated from a fiber discretization of the cross-section in conjunction with specified stress-strain behavior for the steel material. By using a fiber discretization, the interaction of axial and flexural forces is accounted for in the element integration. In addition, elastic shear deformation was modeled in the beams and columns.

The constitutive model 'Steel02' was chosen from the *OpenSees* material library to represent the ASTM A992 steel of the beams and columns. The 'Steel02' material seeks to simulate the cyclic behavior of structural steel by accounting for kinematic and isotropic hardening through the Giuffre-Menegotto-Pinto hardening law (Mazzoni et al. 2009). The cyclic hardening parameters were calibrated in a previous study by Ariyaratana (2009), which used results from experimental investigations of the cyclic behavior of various low-carbon steels by Kauffman and Pense (1999). The Kauffman and Pense (1999) data is shown with a dashed line, and the 'Steel02' calibration used in this study is shown with a solid line, in Figure 5.3.

To account for P-δ effects, the beams and columns were modeled with eight elements per member. This discretization was used since it was found to provide the best combination of

computational efficiency and solution accuracy (Lamarche and Tremblay 2008). The finite element mesh is shown in Figure 5.2, where a small, filled circle represents a node.

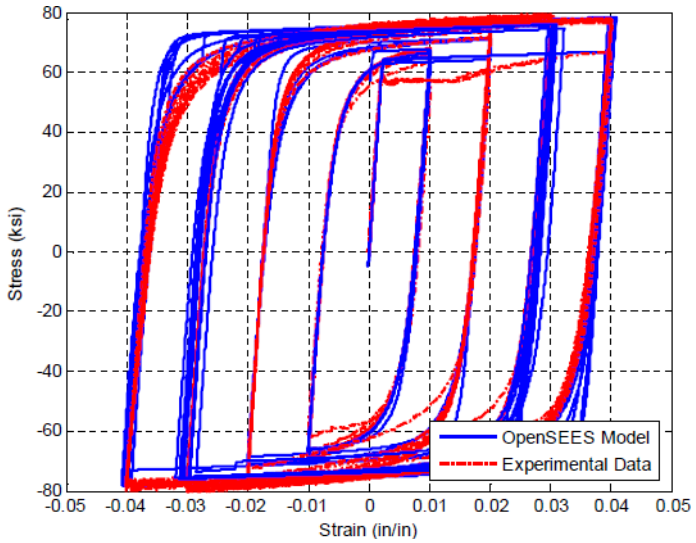

Figure 5.3 Stress-strain behavior for beams and columns (Ariyaratana 2009).

Table 5.4 Brace size and brace connection strengths (after Hines et al. 2009).

Height	Story	Design Load (kips)	Brace	Expected Strength (kips)	Weld (x4)	Weld Capacity (kips)
3 Story	3	81	HSS6x6x1/4	201	3/16”x6”	134
	2	121	HSS7x7x1/4	268	1/4”x7”	208
	1	158	HSS8x8x1/4	302	1/4”x8”	238
6 Story	6	63	HSS6x6x1/4	201	3/16”x6”	134
	5	99	HSS6x6x1/4	201	3/16”x6”	134
	4	125	HSS7x7x1/4	268	1/4”x7”	208
	3	153	HSS8x8x1/4	332	1/4”x8”	238
	2	167	HSS8x8x1/4	332	1/4”x8”	238
	1	197	HSS8x8x5/16	371	1/4”x9”	267

The braces were modeled as elastic truss elements since it was assumed that the brace connections to the gusset plates would fracture prior to brace buckling. Hines et al. (2009) also made this assumption based on calculations that demonstrated that brace buckling strength, accounting for expected yield stress, was greater than the strength of the welded brace-to-gusset plate connections. These calculations are summarized in Table 5.4.

To simulate fracture of the brace-to-gusset plate connections in *OpenSees*, the force in each of the braces was monitored during the analysis and compared to the appropriate weld capacity given in Table 5.4. Once the brace force exceeded the weld capacity, the brace was removed from the analysis. Thus, braces were allowed to fail in tension or compression. Sudden removal of a brace resulted in large discontinuities in stiffness and strength that hindered numerical convergence. To circumvent this problem, the analysis convergence tolerance was relaxed, if convergence failed after removal of a brace, until convergence was gained. The convergence tolerance was then reset to the desired value before proceeding to the next step in the analysis. Since the time step used in the nonlinear response history analyses was very small, 0.0025 sec, locally relaxing the convergence tolerance for a small number of steps around the discontinuity does not severely distort the results.

Finally, the damping matrix for the case study buildings was constructed in the *OpenSees* model by using Rayleigh damping, which is defined by the equations

$$C = a_0 M + a_1 K \tag{5.1}$$

where C is the damping matrix, M is the mass matrix, and K is the stiffness matrix. The constants a_0 and a_1 are defined by

$$a_0 = \xi \frac{2\omega_i \omega_j}{\omega_i + \omega_j} \tag{5.2}$$

and

$$a_1 = \xi \frac{2}{\omega_i + \omega_j} \tag{5.3}$$

where ξ is the desired damping ratio, and ω_i and ω_j are the natural frequencies of the structure at modes i and j. For the present study, a damping ratio of 2% was enforced at the 1st and 3rd modes of each structure. *OpenSees* contains internal functions for computing the natural

frequencies of a structure, so the Rayleigh damping calculations were automated and the constants a_0 and a_1 updated for each structure. The natural periods used for design and those calculated by *OpenSees* are presented in Table 5.5. The natural periods used for design were calculated from

$$T_a = C_t h_n^x \tag{5.4}$$

where T_a is the approximate fundamental period in sec, h_n is the height of the structure, and C_t and x are coefficients based on the type of structure under consideration. For CBFs, $C_t = 0.02$ and $x = 0.75$ (ASCE 2002) when h_n is expressed in ft.

Table 5.5 Natural periods of case study buildings.

Height	Building	1st Natural Period (sec)	Height	Building	1st Natural Period (sec)
3 Story	Design	0.342	6 Story	Design	0.550
	w14a000	0.723		w14a000	1.37
	w14a375	0.723		w14a375	1.36
	w14a500	0.723		w14a500	1.36
	w14a625	0.723		w14a625	1.36
	w14a750	0.723		w14a750	1.36
	w18a000	0.729		w18a000	1.38
	w18a375	0.723		w18a375	1.37
	w18a500	0.723		w18a500	1.37
	w18a625	0.723		w18a625	1.37
	w18a750	0.723		w18a750	1.37
	w21a000	0.729		w21a000	1.38
	w21a375	0.729		w21a375	1.38
	w21a500	0.729		w21a500	1.38
	w21a625	0.729		w21a625	1.38
	w21a750	0.729		w21a750	1.38

5.1.3 Braced Frame Connection Model

The braced frame connection model used in the system studies was critical for an accurate assessment of the seismic behavior and collapse performance of CBFs in moderate seismic regions. The flexural behavior implemented in the connection models must match the stiffness, strength and hysteretic characteristics (strength loss and pinching) of the connection

moment-rotation relationships observed experimentally and generated in the finite element parametric study. The connection model for the system studies is illustrated in Figure 5.4. The connection model components are overlaid on a schematic drawing of a beam-column joint to aid in understanding their functions.

The key element in the connection model is the rotational spring. The moment-rotation behavior of the rotational spring was defined using the results of the finite element parametric study of braced frame connection flexural behavior presented in Chapter 4. As mentioned previously, changing the braced frame connection flexural behavior was the primary mechanism for varying the reserve lateral force-resisting capacity of the structures in this study. All connection deformations, including shear and bending deformations, deformation of the steel angles, and out-of-plane distortion of the gusset plate, are contained in the moment-rotation relationship of the rotational spring.

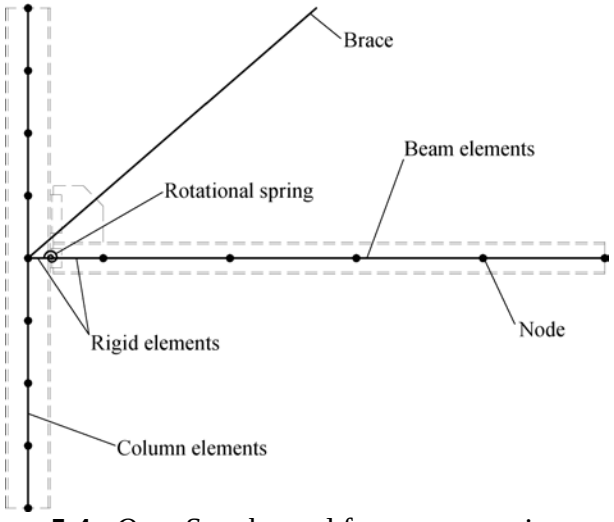

Figure 5.4 *OpenSees* braced frame connection model.

The moment-rotation behavior of the rotational spring was modeled with the 'hysteretic' material from the *OpenSees* material library (Mazzoni et al. 2009). The 'hysteretic' material simulates the force-deformation behavior of an element using a trilinear curve, which is illustrated for finite element models w14x53a375, w1846a375, and w2144a375 in Figure 5.5.

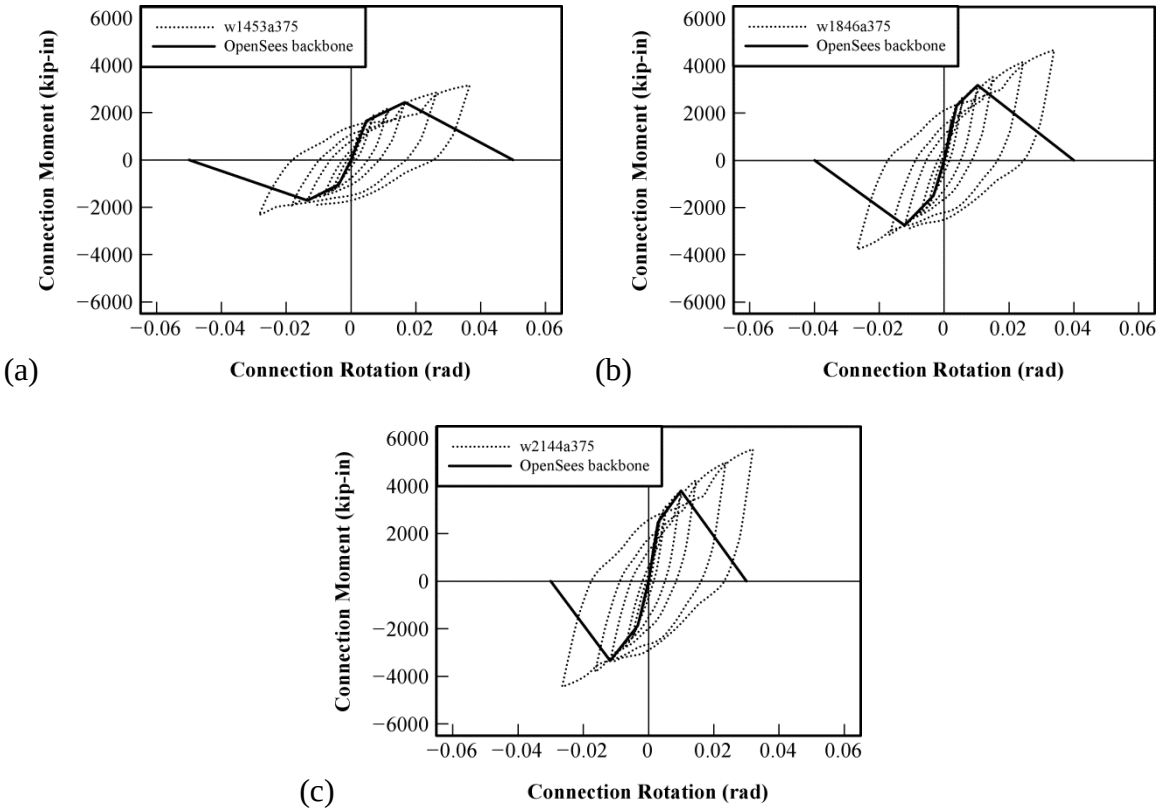

Figure 5.5 Connection moment vs. connection rotation OpenSees model: (a) w1453a375; (b) w1846a375; (c) w2144a375.

The pivot points of the backbone curve illustrated in Figure 5.5 were chosen to approximate the yield moment, ultimate moment, and failure rotation of the connection moment vs. connection rotation data taken from the finite element parametric study outlined in Chapter 4. The yield moment point was chosen by determining where the moment-rotation data of each connection deviated from its initial elastic slope. The elastic stiffness was determined from the analytical model developed in Chapter 4. The ultimate moment point was chosen based on the limiting damage state identified during the finite element parametric study. In positive bending, the ultimate moment point corresponded to initiation of gusset angle fracture or weld failure. In negative bending, the ultimate moment point corresponded to web or seat angle fracture, or bolt fracture. The yield moment and rotation and ultimate moment and rotation for all connections are summarized in Table 5.6.

Table 5.6 Summary of braced frame connection behavior.

Connection	Positive M_y (k-in)	Positive θ_y (rad)	Positive M_u (k-in)	Positive θ_u (rad)	Negative M_y (k-in)	Negative θ_y (rad)	Negative M_u (k-in)	Negative θ_u (rad)
w14a000	-	-	-	-	-	-	-	-
w14a375	1650	0.00472	2435	0.0166	1039	0.00381	1714	0.0134
w14a500	1930	0.00422	3121	0.0154	1687	0.00544	2780	0.0173
w14a625	2348	0.00599	3184	0.0151	2015	0.00650	3148	0.0245
w14a750	1987	0.00407	3466	0.0147	3139	0.00900	3617	0.0275
w18a000	-	-	-	-	-	-	-	-
w18a375	2324	0.00387	3180	0.0103	1489	0.00330	2755	0.0122
w18a500	3316	0.00482	4538	0.0130	2389	0.00459	3646	0.0110
w18a625	3308	0.00478	4630	0.0125	2851	0.00550	4799	0.0313
w18a750	3474	0.00452	4990	0.0113	3322	0.00602	4997	0.0298
w21a000	-	-	-	-	-	-	-	-
w21a375	2470	0.00289	3798	0.00993	1863	0.0033	3344	0.0118
w21a500	3169	0.00305	5300	0.0118	2805	0.00433	4202	0.0107
w21a625	4355	0.00500	5910	0.0167	3544	0.00550	5235	0.0252
w21a750	4084	0.00421	5716	0.0101	3779	0.00564	5465	0.0206

The connection failure rotations were estimated based on experimental observations and fundamental connection behavior, since propagation of damage to full degradation, which would have quantified the rotation at zero flexural strength, is difficult to implement in finite element models and was not included in the finite element parametric study. Observations from the experimental program indicated that the connections with 10-in deep beams reached zero flexural strength at approximately 0.06-rad rotation. Since a deeper beam experiences higher strain demands on the extreme fibers of the connection angles and the outer connection bolts, when compared to a shallower beam at a given rotation level, the failure rotation should decrease with increasing beam depth. Thus, the failure rotation was chosen as 0.05 rad for the W14x53 beams, 0.04 rad for the W18x46 beams, and 0.03 rad for the W21x44 beams.

The 'hysteretic' material used to model the braced frame connection flexural behavior also simulates pinching and stiffness degradation behaviors. To calibrate the pinching and stiffness degradation parameters, a beam-column connection model, similar to Figure 5.4, was

developed and a cyclic displacement history applied to the free end of the beam to simulate flexure in the connection. Connection moment vs. connection rotation data for the rotational spring was recorded and compared to the results from CN1. The results from the pinching and stiffness degradation calibration study are shown in Figure 5.6. The results in Figure 5.6 were determined by varying the pinching and stiffness degradation parameters of the 'hysteretic' material until satisfactory agreement between the experimental and computational results was obtained. Although the numerical hysteretic model is a fairly rough approximation of the experimental behavior, the results presented in Figure 5.6 were deemed acceptable for the present study and the pinching and stiffness degradation parameters from this connection were used for all the connections in the nonlinear response history analyses. Figure 5.6(b) illustrates a model for CN7 and shows that the chosen parameters are reasonable for connections beyond CN1.

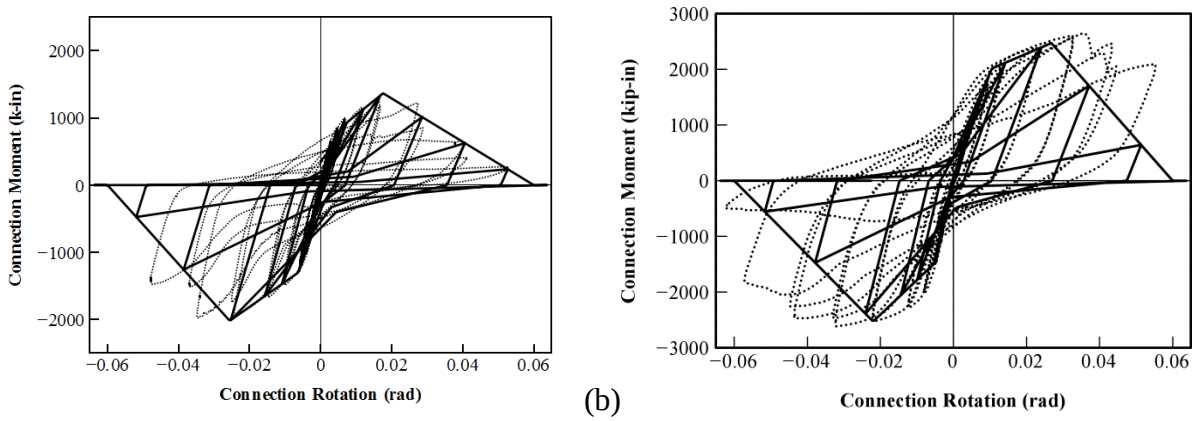

Figure 5.6 Connection moment vs. connection rotation model with pinching: (a) CN1; (b) CN7.

5.2 QUANTIFICATION OF RESERVE SYSTEM STIFFNESS AND STRENGTH

Since the primary goal of this study was to determine the amount of reserve capacity needed to generate adequate collapse performance, the reserve lateral force-resisting strength of the case study buildings was quantified with static pushover (SPO) analysis. The results from

the SPO analyses were then used in conjunction with collapse performance to establish a link between the magnitude of reserve strength and acceptable collapse performance. In addition, the SPO analyses were vital in understanding the mechanisms that generate reserve capacity in chevron configuration CBFs.

5.2.1 Static Pushover Analyses

Static pushover analyses were used to quantify the reserve lateral force-resisting capacity of the case study buildings. The computational model that was outlined above was employed to conduct a displacement-controlled simulation based on roof displacement. An inverted triangular distribution of lateral forces was assumed for the SPO analyses. Figure 5.7 shows the SPO curves for all the case study buildings. Base shear vs. first story drift is illustrated in Figure 5.7 to recognize that the first story controlled the behavior and strength of the reserve capacity system.

The SPO data demonstrated that all the case study buildings behaved in a similar manner. The buildings responded linearly up to the peak base shear, approximately 300 kips for the 3-story buildings and 325 kips for the 6-story buildings. At this point, a large, sudden drop in base shear occurred when the force in one of the first story braces reached its connection strength and the connection failed. Loss of a brace changed the lateral resistance mechanism from a concentrically braced frame, governed by axial forces in the members, to an eccentrically braced frame, governed by flexural response of the beams and columns in the first story. After loss of a brace, the sequence of limit states leading to the reserve system strength was somewhat different between buildings with and without flexural strength in the braced frame connections.

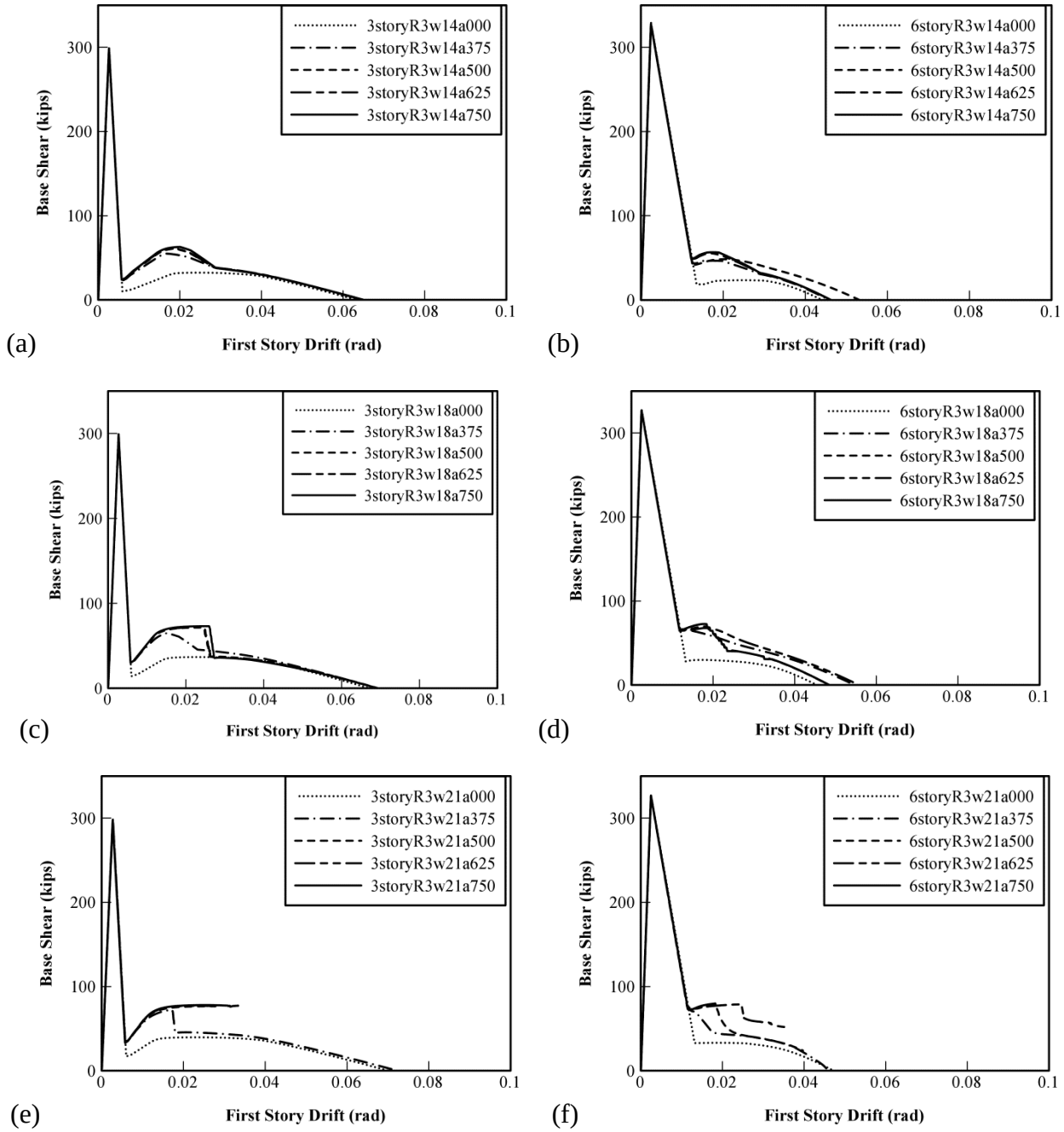

Figure 5.7 Static pushover curves for all case study buildings: (a) 3storyR3w14; (b) 6storyR3w14; (c) 3storyR3w18; (d) 6storyR3w18; (e) 3storyR3w21; (f) 6storyR3w21.

In buildings without flexural strength in the braced frame beam-column connections, a000 cases, the reserve system strength was due to the plastic moment capacity of the second floor braced frame beam and the plastic moment capacity of the braced frame columns. After loss of a first story brace, base shear increased due to flexural response in the second floor braced

frame beam. The beam eventually developed its plastic moment capacity and a secondary base shear peak was reached shortly thereafter. After the base shear began to degrade due to P-Δ effects, plastic hinges developed in the braced frame columns that led to collapse of the structure.

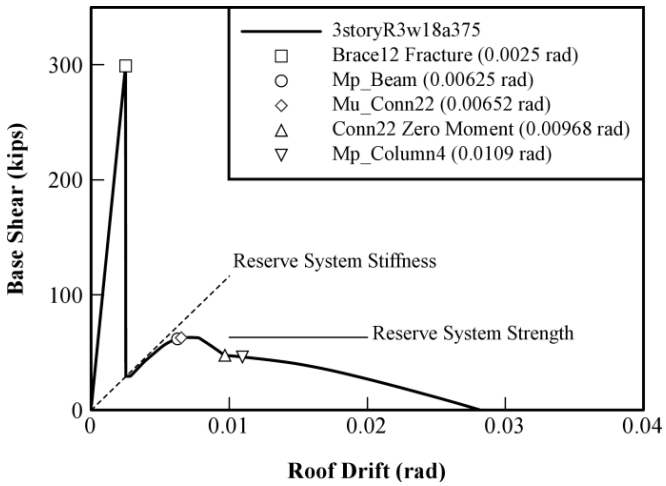

Figure 5.8 Roof drift vs. base shear for 3storyR3w18a375 building with annotations.

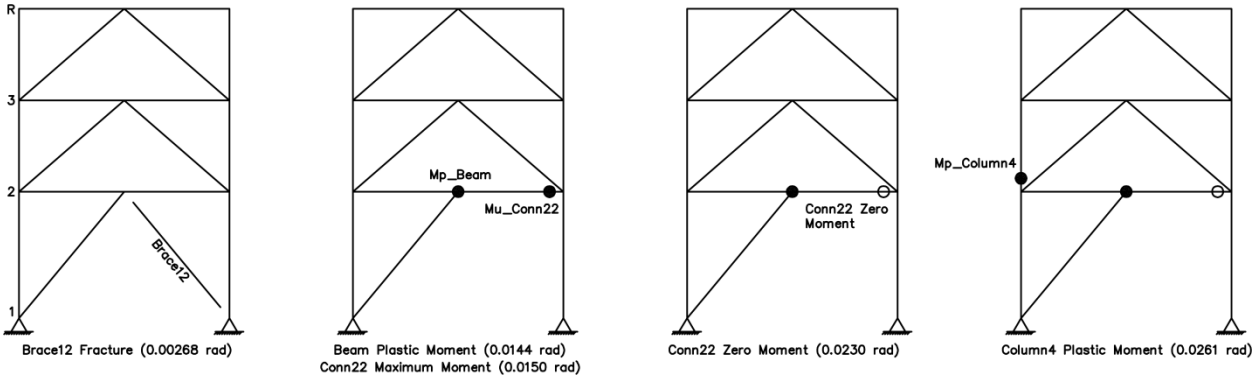

Figure 5.9 Damage sequence for 3storyR3w18a375 SPO analysis.

In buildings with flexural strength in the braced frame beams, the reserve system strength was due to the flexural strength in the braced frame connections as well as the elements discussed previously. After loss of a first story brace, base shear increased due to flexural response in the second story braced frame beam and braced frame connections. A secondary base shear peak was reached when the braced frame connection adjacent to the failed brace reached its ultimate moment strength. Prior to this connection reaching its ultimate moment strength, the second story braced frame beam reached its plastic moment strength. After the

secondary peak was observed, the strength of the braced frame connection adjacent to the failed brace decreased, which led to another rapid loss of base shear. After this braced frame connection reached zero moment strength, additional lateral displacement caused a plastic hinge to form in the braced frame column adjacent to the remaining brace, which initiated collapse of the structure. The sequence of events that led to collapse in the SPO analyses is annotated in the base shear vs. roof drift data for the 3storyR3w18a375 case study building in Figure 5.8. In addition, elevation views of the 3storyR3w18a375 building and the associated damage are shown in Figure 5.9. The results for the remaining buildings were similar.

The base shear realized at the secondary peak was taken as the reserve system strength, V_r. Table 5.7 lists the reserve system strengths for all the case study buildings. The reserve system stiffness, K_r, was calculated based on the slope of the line between the origin and the point immediately after failure of one of the first story braces. Table 5.8 lists the reserve system stiffnesses for all the case study buildings. The reserve system stiffness and strength are denoted in Figure 5.8.

Table 5.7 Reserve system strength for case study buildings.

Building	Reserve System Base Shear (kips)	
	3 Story	6 Story
w14a000	32.3	24.4
w14a375	54.9	47.8
w14a500	60.9	51.0
w14a625	61.2	56.0
w14a750	62.9	57.9
w18a000	36.8	29.9
w18a375	64.9	63.4
w18a500	71.5	70.9
w18a625	71.8	70.3
w18a750	73.1	74.0
w21a000	39.7	33.5
w21a375	72.5	69.8
w21a500	76.5	79.5
w21a625	77.1	79.3
w21a750	78	81.2

Since development of a plastic hinge in the second story braced frame beam played a crucial role in developing reserve system strength, the rotation demand in the hinge corresponding to reserve system strength was examined. Table 5.9 shows plastic hinge rotation that corresponds with reserve system strength for each of the case study buildings. The beam plastic hinge rotation of buildings that were found to exhibit acceptable collapse prevention performance are shown in bold in Table 5.9.

Table 5.8 Reserve system stiffness for case study buildings.

Building	Reserve System Stiffness (k/in)	
	3 Story	6 Story
w14a000	7.55	5.9
w14a375	17.3	14
w14a500	18.1	13.2
w14a625	17.7	15.7
w14a750	18.3	16
w18a000	10.6	8.87
w18a375	22	21.5
w18a500	22.3	20.8
w18a625	22.4	20.6
w18a750	22.6	21.1
w21a000	12.6	10.3
w21a375	24.8	23.7
w21a500	25.2	24.4
w21a625	25	23.4
w21a750	25.1	23.1

To calculate plastic hinge rotation, the moment and curvature at the element integration points in the elements on both sides of the plastic hinge were recorded. The total rotation across this region was calculated by finding the area under the curvature distribution across the region. The elastic rotation was found by integrating the elastic curvature distribution, which was found by dividing the beam moment at each integration point by EI of the beam. The plastic rotation was calculated by subtracting the elastic rotation from the total rotation. The region used for the integration was larger than the plastic region to insure that all plastic rotation was accounted for.

Table 5.9 Beam plastic hinge rotation at reserve system strength.

Building	Plastic Hinge Rotation (rad)	
	3 Story	6 Story
w14a000	0.013	0.003
w14a375	0.003	0.001
w14a500	0.008	0.003
w14a625	0.008	0.003
w14a750	0.011	0.005
w18a000	0.015	0.005
w18a375	**0.005**	0.001
w18a500	**0.025**	0.013
w18a625	**0.025**	0.013
w18a750	**0.027**	**0.014**
w21a000	0.019	0.005
w21a375	**0.012**	**0.005**
w21a500	**0.031**	0.011
w21a625	**0.025**	**0.027**
w21a750	**0.029**	**0.018**

It is clear from Table 5.9 that significant plastic rotations are needed in the braced frame beam to develop the reserve system strength of a majority of the case study buildings. In addition, if the case study buildings are assumed to behave like EBFs with long links, which are links with a length greater than $2.6M_p/V_p$ (AISC 2005a), after loss of a first story brace, the AISC *Seismic Provisions* limit their plastic rotation to 0.02 rad (AISC 2005a). Several buildings exceeded this limit, with the 3storyR3w21a500 building exceeding the limit by 50%. In the buildings where rotations less than 0.02 rad were realized in the beam and acceptable collapse prevention performance was not achieved, P-Δ effects typically limited the reserve system strength, so the plastic moment in the beam was not realized until after the reserve system strength occurred. All beams used in this study were seismically compact, however. The maximum b/t ratio for flexure in flanges was 7.22 (AISC 2005a), and the $b_f/2t_f$ ratios for the W14x53, W18x46, and W21x44 beams were 6.1, 5.0, and 7.2, respectively.

The plastic hinge rotation demands summarized in Table 5.9 indicate that the plastic moment capacity of the beam may degrade prior to the reserve capacity system reaching its maximum strength. The CBF behavior after fracture of one brace is similar to the behavior of long-link EBFs, but the CBF was not designed or detailed to conform to the requirements for EBFs in the *AISC Seismic Provision* (AISC 2005a). Thus, inferences about potential degradation of the flexural strength of the braced frame beam are approximate. Nevertheless, the collapse performance results presented herein are predicated on minimal degradation of the plastic moment strength of the braced frame, since degradation was not modeled in this study.

5.3 RELIABILITY-BASED COLLAPSE PERFORMANCE ASSESSMENT

After completing the SPO analyses, the case study buildings were used as part of a reliability-based performance assessment of the collapse behavior of CBFs in moderate seismic regions. The framework for the collapse performance assessment used in this study is detailed in FEMA P695: *Quantification of Building Seismic Performance Factors* (FEMA 2009). There are two primary components for a collapse assessment according to FEMA P695: nonlinear response history (NLRH) analysis of the buildings in the study and evaluation of the performance through probabilistic analysis of the NLRH results. The NLRH analysis required by FEMA P695 is a specific computational technique termed an incremental dynamic analysis (IDA), which was proposed by Vamvatsikos and Cornell (2002). In the following sections, the results of the IDA performed on the case study buildings with reserve capacity will be presented. A summary of the probabilistic analyses used to quantify the collapse performance of the case study buildings is also provided.

5.3.1 Incremental Dynamic Analysis

In the IDA procedures outlined by Vamvatsikos and Cornell (2002), a computational model of a building is subjected to a suite of ground acceleration time histories to determine the structures ability to resist collapse. The magnitudes of the ground accelerations are then scaled up in small increments until all the ground acceleration records in the suite initiated collapse of the model building. Collapse is defined based on a chosen damage measure (DM) that indicates when the structure is likely to collapse. For a scale factor of unity, the ground acceleration time histories approximate MCE level seismic hazard for the structure under consideration. Scaling of the ground acceleration records is usually defined based on the first natural period of the structure because the IDA approach was developed for collapse modeling of ductile seismic force-resisting systems in high-seismic regions.

For the present study, the suite of ground acceleration time histories was taken from a study of the Boston, Massachusetts, moderate seismic region by Sorabella (2006). In this study, 14 synthetic motions were created based on soil column analyses and the 2002 USGS seismic hazard maps. Another motion was also created that was matched to the design spectral acceleration curve for the buildings designed by Hines et al. (2009). Figure 5.10 illustrates the 15 motions, the average of the 14 synthetic motions, and the design spectral acceleration curve from Hines et al. (2009).

The damage measure selected for detecting structural collapse was the maximum story drift. Story drifts were recorded for each story in the case study buildings and the maximum story drift compared to the collapse story drift, which was chosen to be 0.10 rad based on the recommendation of Vamvatsikos and Cornell (2002). When the maximum story drift exceeded this value, the building was considered to have collapsed.

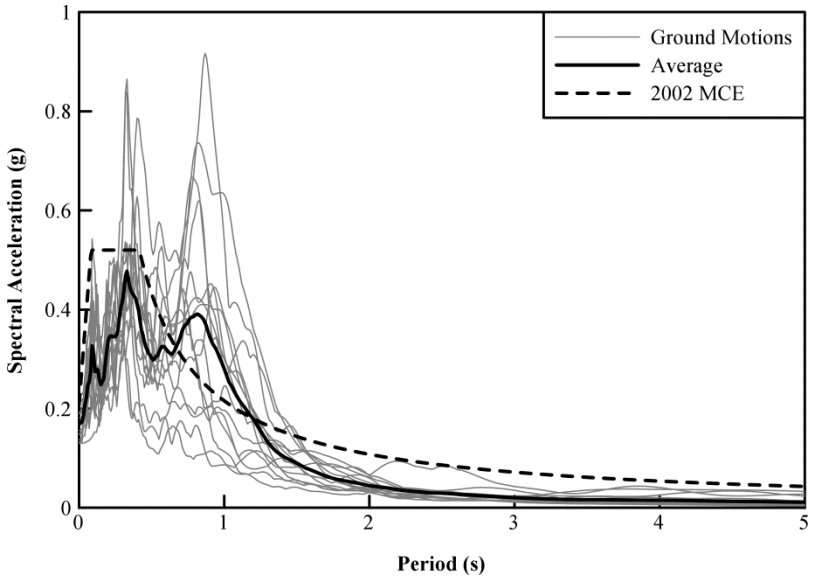

Figure 5.10 Ground acceleration time history suite for IDA.

In contrast to Vamvatsikos and Cornell (2002) and FEMA P695 (FEMA 2009), scaling of the ground acceleration time histories in the present study was not centered around the fundamental period of the case study buildings. Instead, the accelerations from the MCE level motions from Sorabella (2006) were scaled without matching them to the first fundamental period of each structure. Since brace connection fracture was likely to occur during the early stages of the nonlinear response history analyses, the fundamental mode of the case study CBFs does not dominate the seismic behavior in the same way that it dominates the behavior of more ductile systems, particularly moment-resisting frames. This methodology was also used in the analyses by Hines et al. (2009). In the discussion that follows, the letters 'gm' followed by an integer from 1 – 15 are added to the building designations listed in Table 5.3 to indicate the building and ground motion that generated a particular set of results.

Figures 5.11 and 5.12 illustrate IDA curves for case study buildings 3storyR3w18a000 and 3storyR3w18a375 for all ground acceleration time histories considered in this study. The IDA curves were generated by recording the maximum story drift for each of the case study buildings, subject to each ground acceleration intensity. Then, ground acceleration intensity,

which is represented by the 'scale factor' used to generate the intensity, is plotted against maximum story drift. The curves were truncated at the lowest scale factor that caused collapse. The results presented here are representative of the majority of the IDA data.

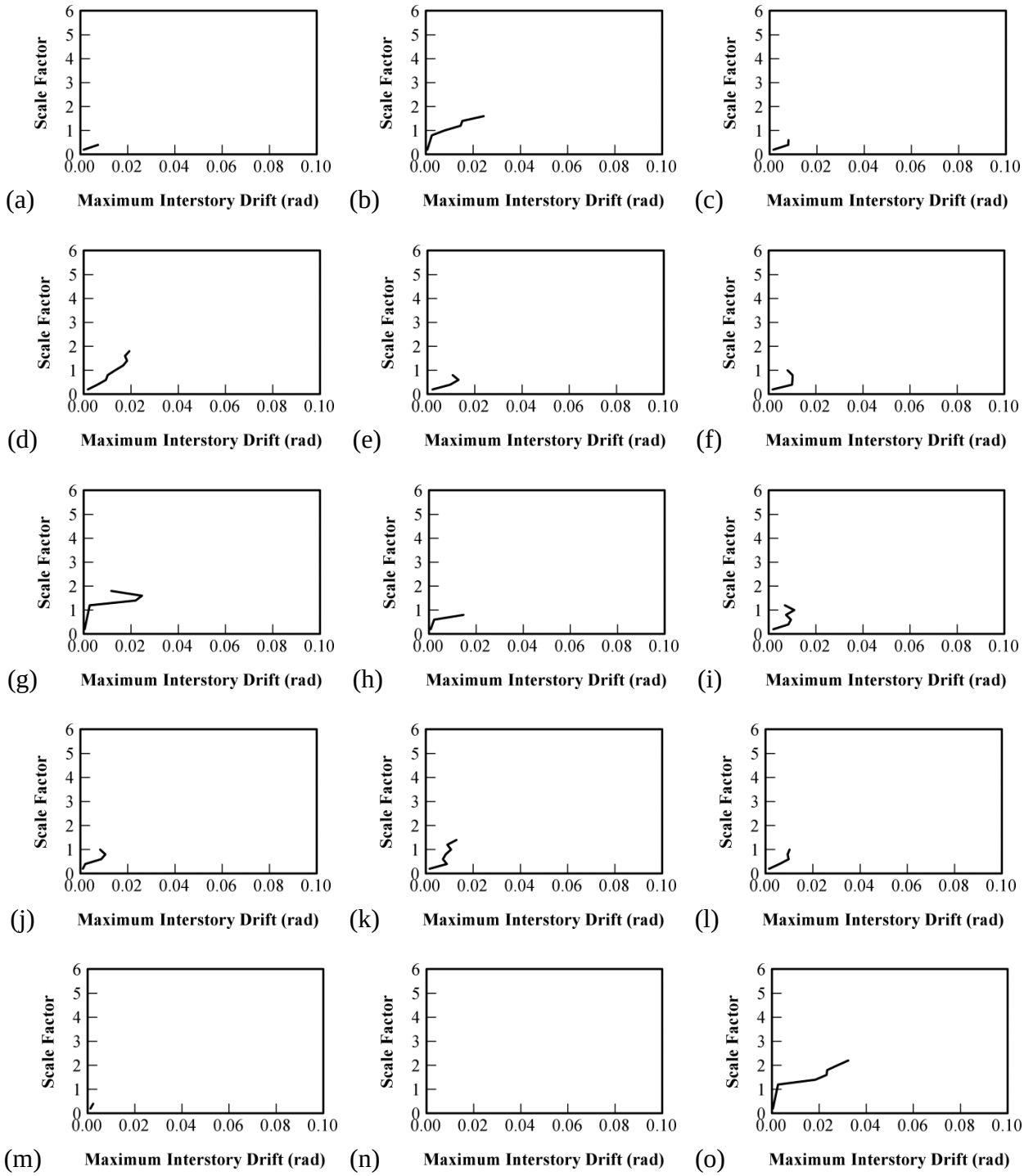

Figure 5.11 IDA curves for 3storyR3w18a000: (a) gm1 – (o) gm15.

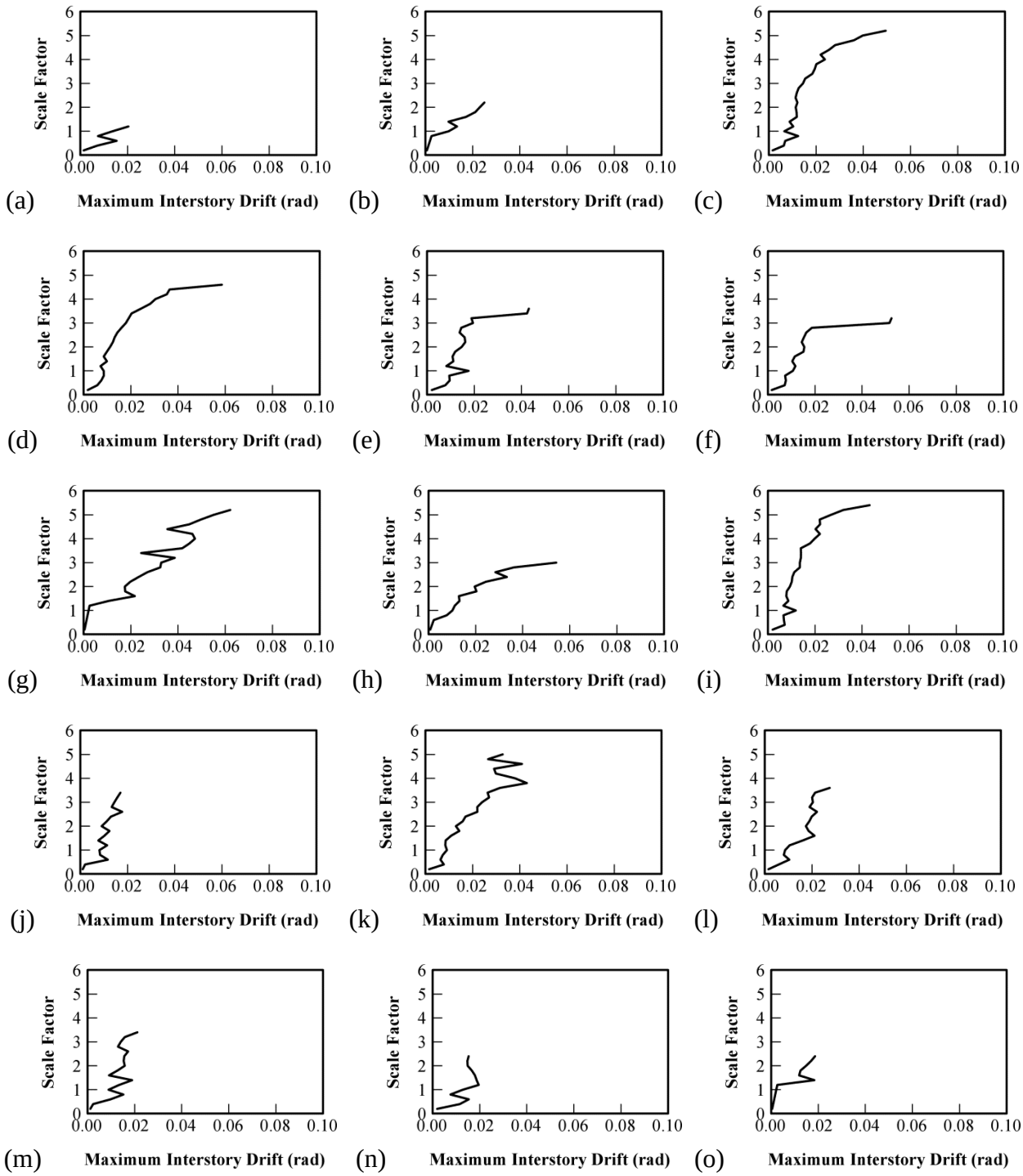

Figure 5.12 IDA curves for 3storyR3w18a375: (a) gm1 – (o) gm15.

The IDA curves shown in Figures 5.11 and 5.12 exhibit some of the basic traits of IDA curves identified by Vamvatsikos and Cornell (2002). The most prominent feature of the IDA curves in this study was weaving behavior, which is demonstrated by Figures 5.12g and 5.12l for

case study buildings 3storyR3w18a375gm7 and 3storyR3w18a375gm12, respectively. This behavior is characterized by the maximum story drift oscillating between small and large drifts, rather than monotonically increasing, as earthquake intensity increases. In addition, some of the IDA curves, in particular 3storyR3w18a375gm3, gm4, and gm9, demonstrate appreciable softening behavior as earthquake intensity increases.

Finally, it should be noted that some IDA curves, most notably those for buildings without flexural strength in the braced frame connections, experienced several discontinuities in the IDA curve, i.e. the case study building would collapse at a specific scale factor but would survive when the earthquake intensity increased. This behavior, called "resurrection", was also noted by Vamvatsikos and Cornell (2002) and is the result of the larger intensity earthquake initiating structural damage earlier in the ground acceleration record, which leads to period elongation and lower base shear demands. When discontinuities were encountered within an IDA, the lowest scale factor that caused collapse was taken as the collapse point.

Two primary conclusions can be drawn from Figures 5.11 and 5.12. First, the scale factor at collapse is significantly larger for the building with braced frame connection flexural strength, 3storyR3w18a375. The second conclusion taken from Figures 5.11 and 5.12 is that collapse occurs suddenly for chevron configuration CBFs. In general, the maximum story drifts do not gradually increase as the ground acceleration intensity increases. Instead, maximum story drifts of 0.02 rad to 0.04 rad were realized and then the structure collapsed with a small increment in ground acceleration intensity. This is in stark contrast to the example IDA curves presented by Vamvatsikos and Cornell (2002) that show story drifts steadily approaching collapse level drifts in moment-resisting frames. In light of this fact, however, IDA still appears to be an effective tool for assessing the collapse performance of CBFs.

The conclusion that reserve lateral force-resisting systems allow CBFs to withstand larger intensity ground accelerations is reinforced by examining collapse data from all the case study buildings. Tables 5.10 – 5.15 provide a summary of the collapse data from this study. For each case study building, Tables 5.10 – 5.15 provide the scale factor at collapse, story that collapsed, and maximum story drift achieved prior to collapse.

Tables 5.10 – 5.15 also show that collapse resistance does not continue to increase with increasing angle thickness, for a given beam depth, in the braced frame connections. For example, the scale factor at collapse for each ground acceleration time history is approximately equal for 3storyR3w18a375, 3storyR3w18a500, 3storyR3w18a625, and 3storyR3w18a750. In addition, it appears that beam depth within the braced frame has an impact on collapse resistance, since the scale factor at collapse was significantly higher for 3-story and 6-story buildings with W18x46 and W21x44 beams.

Table 5.10 IDA results for 3-story buildings with W14x53 beams.

		Ground Motion														
		1	2	3	4	5	6	7	8	9	10	11	12	13	14	15
w14a000	SF	0.8	2	0.8	1	1.4	1.2	2.2	1.4	1	0.8	2.4	0.8	0.6	0.6	1.4
	Story	1	1	1	1	1	1	1	1	1	1	1	1	1	1	1
	Drift	.015	.025	.010	.016	.014	.017	.025	.022	.011	.013	.014	.009	.002	.014	.003
w14a375	SF	1.4	1.8	1.2	2.6	2	4	3.8	1.4	5	1.2	1.6	1.6	0.6	2.4	2
	Story	1	1	1	1	1	1	1	1	1	1	1	1	1	1	1
	Drift	.021	.017	.009	.021	.014	.050	.024	.015	.022	.010	.013	.017	.002	.018	.031
w14a500	SF	4.4	1.8	1.4	2.6	2	3.8	4.6	1.4	5	1.2	1.6	1.6	1.8	2.2	2
	Story	1	1	1	1	1	1	1	1	1	1	1	1	1	1	1
	Drift	.034	.017	.011	.020	.012	.041	.032	.013	.027	.010	.015	.017	.016	.017	.033
w14a625	SF	4.4	1.8	1.4	2.6	2	3.8	4.6	1.4	5	1.2	1.6	1.6	1.8	2.2	2
	Story	1	1	1	1	1	1	1	1	1	1	1	1	1	1	1
	Drift	.027	.017	.011	.020	.015	.038	.038	.012	.026	.010	.015	.017	.016	.018	.028
w14a750	SF	4.4	1.8	5.2	2.6	2	4.6	5.2	3.4	1	1.2	1.6	1.6	1.8	2.4	2
	Story	1	1	1	1	1	1	1	1	1	1	1	1	1	1	1
	Drift	.027	.017	.032	.019	.012	.054	.051	.061	.011	.011	.015	.017	.016	.018	.025

Table 5.11 IDA results for 3-story buildings with W18x46 beams.

		Ground Motion														
		1	2	3	4	5	6	7	8	9	10	11	12	13	14	15
w18a000	SF	0.6	1.8	0.8	2	1	1.2	2	1	1.4	1.2	1.6	1.2	0.6	0.4	2.4
	Story	1	1	1	1	1	1	1	1	1	1	1	1	1	1	1
	Drift	.007	.025	.008	.019	.013	.010	.025	.015	.011	.011	.013	.010	.002	.002	.032
w18a375	SF	1.4	2.4	5.4	4.8	3.8	3.4	5.4	3.2	5.6	3.6	5.2	3.8	3.6	2.6	2.6
	Story	1	1	1	1	1	1	1	1	1	1	1	1	1	1	1
	Drift	.020	.025	.049	.059	.043	.052	.062	.054	.043	.018	.043	.028	.021	.020	.019
w18a500	SF	3.4	2.4	5.4	4.8	3.8	3.2	5.4	3.2	5.8	3.6	4.6	4.8	4	2.6	1.8
	Story	1	1	1	1	1	1	1	1	1	1	1	1	1	1	1
	Drift	.026	.025	.038	.050	.049	.041	.065	.033	.047	.017	.061	.050	.028	.021	.027
w18a625	SF	3.4	2.4	5.4	4.6	3.8	4	4.6	3.2	6	3.6	5.4	5.4	4	2.6	1.8
	Story	1	1	1	1	1	1	1	1	1	1	1	1	1	1	1
	Drift	.026	.025	.028	.034	.046	.043	.064	.028	.028	.017	.059	.029	.028	.020	.026
w18a750	SF	3.4	2.4	5.8	4.8	3.4	4	4.4	3.2	6	3.6	4	5.4	1.4	2.6	1.8
	Story	1	1	1	1	1	1	1	1	1	1	1	1	1	1	1
	Drift	.031	.025	.052	.014	.032	.071	.063	.031	.009	.018	.065	.022	.028	.032	.021

Table 5.12 IDA results for 3-story buildings with W21x44 beams.

		Ground Motion														
		1	2	3	4	5	6	7	8	9	10	11	12	13	14	15
w21a000	SF	0.6	2.4	0.8	1.8	1	2	3.6	2.6	1.6	1.8	1.6	1.4	1.6	0.4	1.8
	Story	1	1	1	1	1	1	1	1	1	1	1	1	1	1	1
	Drift	.006	.023	.008	.017	.015	.015	.025	.037	.014	.013	.012	.013	.021	.002	.019
w21a375	SF	3.6	2.2	0.8	3	3.2	3	5.2	3.6	5.6	5.2	4.4	4.6	4	0.6	2.4
	Story	1	1	1	1	1	1	1	1	1	1	1	1	1	1	1
	Drift	.034	.023	.007	.014	.024	.019	.055	.061	.046	.047	.060	.050	.026	.011	.019
w21a500	SF	4.4	2.2	0.8	3	3.2	3.2	5	4.6	5.6	5.2	4.2	4.8	4	0.6	1.8
	Story	1	1	1	1	1	1	1	1	1	1	1	1	1	1	1
	Drift	.031	.022	.007	.014	.023	.020	.060	.061	.025	.027	.043	.056	.024	.011	.030
w21a625	SF	4.4	2.2	0.8	3	3.2	6	4.8	5.6	6	6	5	5.2	4	0.6	1.8
	Story	1	1	1	1	1	1	1	1	1	1	1	1	1	1	1
	Drift	.031	.023	.007	.013	.024	.035	.062	.037	.031	.031	.034	.030	.024	.011	.027
w21a750	SF	4.4	2.2	0.8	3	3.2	5.8	5	5.4	5.8	6	4.2	5.2	4	3.6	1.8
	Story	1	1	1	1	1	1	1	1	1	1	1	1	1	1	1
	Drift	.031	.030	.007	.010	.022	.060	.041	.038	.012	.017	.044	.025	.018	.015	.027

Table 5.13 IDA results for 6-story buildings with W14x53 beams.

		Ground Motion														
		1	2	3	4	5	6	7	8	9	10	11	12	13	14	15
w14a000	SF	0.8	1.2	1	1.4	1	0.6	2.6	1.4	1	1.6	1.4	1	1.2	0.8	2.4
	Story	1	1	1	1	1	1	1	1	1	1	1	1	1	1	1
	Drift	.003	.004	.003	.026	.030	.003	.018	.033	.013	.014	.019	.003	.016	.007	.021
w14a375	SF	1	2.2	2.4	2.4	1.6	2.2	3.2	1.8	1	2.6	1.6	1.2	1.4	1.6	2
	Story	1	1	1	1	1	1	1	1	1	1	1	1	1	1	1
	Drift	.013	.020	.020	.035	.021	.020	.020	.054	.009	.017	.018	.017	.015	.022	.023
w14a500	SF	1	4.4	1.4	2.2	1.6	3.2	1.8	1.4	1.4	2	1.8	1.2	1.4	1.4	2
	Story	1	1	1	1	1	1	1	1	1	1	1	1	1	1	1
	Drift	.012	.031	.008	.030	.028	.037	.014	.032	.016	.014	.019	.017	.014	.016	.027
w14a625	SF	1	2.2	1.4	2	1.4	3.2	1.8	1.8	4.6	3	1.8	1.4	1.4	1.4	2
	Story	1	1	1	1	1	1	1	1	1	1	1	1	1	1	1
	Drift	.012	.020	.008	.030	.017	.037	.013	.062	.023	.017	.019	.017	.014	.016	.027
w14a750	SF	1	2.2	1.2	2.2	1.6	3.2	1.8	1.8	4.6	2.8	1.8	1.2	2.2	1.4	2
	Story	1	1	1	1	1	1	1	1	1	1	1	1	1	1	1
	Drift	.012	.019	.008	.040	.027	.035	.015	.064	.021	.017	.019	.017	.017	.015	.026

Table 5.14 IDA results for 6-story buildings with W18x46 beams.

		Ground Motion														
		1	2	3	4	5	6	7	8	9	10	11	12	13	14	15
w18a000	SF	1	1.4	1.2	2	1.2	1.2	3	1.6	1	1.2	1.6	1.4	1	0.8	1.8
	Story	1	1	1	1	1	1	1	1	1	1	1	1	1	1	1
	Drift	.013	.013	.008	.035	.026	.021	.026	.033	.004	.013	.014	.023	.013	.015	.015
w18a375	SF	2	3	1.6	2.2	3.2	4.2	3.6	1.4	4.6	3.4	3.6	2.6	1	3.6	2
	Story	1	1	1	1	1	1	1	1	1	1	1	1	1	1	1
	Drift	.014	.023	.014	.033	.031	.043	.025	.021	.030	.021	.024	.040	.005	.027	.032
w18a500	SF	2	2.2	4	2	3.4	4.2	3.2	1.4	4.6	2.4	3.8	2.6	1	3.6	2
	Story	1	1	1	1	1	1	1	1	1	1	1	1	1	1	1
	Drift	.014	.021	.030	.024	.064	.034	.016	.019	.025	.015	.038	.037	.005	.036	.031
w18a625	SF	2	2.2	1.4	2	3.6	4	3.2	1.8	4.6	2.4	3.8	2.6	1	3.4	2
	Story	1	1	1	1	1	1	1	1	1	1	1	1	1	1	1
	Drift	.014	.021	.009	.020	.056	.033	.016	.027	.022	.015	.037	.027	.005	.032	.027
w18a750	SF	2.2	2.4	2.4	2.4	3.8	4.4	3.4	1.8	4.6	3	3.8	2.6	2.4	3.2	2
	Story	1	1	1	1	1	1	1	1	1	1	1	1	1	1	1
	Drift	.012	.021	.028	.034	.024	.032	.017	.029	.030	.023	.013	.027	.019	.028	.031

Table 5.15 IDA results for 6-story buildings with W21x44 beams.

		Ground Motion														
		1	2	3	4	5	6	7	8	9	10	11	12	13	14	15
w21a000	SF	2	1.8	1.6	1	1.8	1.2	2.2	1.6	1	1.6	1.6	1.4	2.2	0.8	2.8
	Story	1	1	1	1	1	1	1	1	1	1	1	1	1	1	1
	Drift	.019	.022	.015	.003	.025	.016	.019	.029	.004	.016	.015	.023	.016	.013	.038
w21a375	SF	2.6	3.4	1.4	2.2	3.8	3.6	4.6	1.8	4.2	3.4	3.8	3	4.6	3	2.2
	Story	1	1	1	1	1	1	1	1	1	1	1	1	1	1	1
	Drift	.023	.022	.008	.032	.034	.036	.031	.041	.022	.019	.038	.033	.034	.030	.038
w21a500	SF	5	2.4	1.4	2.4	3	3.6	3.2	2.2	1.2	5	4	2.8	1.6	3	2.2
	Story	1	1	1	1	1	1	1	1	1	1	1	1	1	1	1
	Drift	.039	.021	.008	.026	.024	.032	.021	.043	.014	.027	.042	.045	.013	.034	.038
w21a625	SF	5	3.4	1.4	2.8	4.2	4.2	3.2	2	1.2	3.2	1.8	2.8	4.8	3.2	2.8
	Story	1	1	1	1	1	1	1	1	1	1	1	1	1	1	1
	Drift	.039	.022	.008	.042	.060	.034	.020	.033	.015	.015	.012	.039	.039	.039	.035
w21a750	SF	5	3.4	2.4	2.8	4	3.8	3.2	2	1.2	3.2	4	3.4	4.6	3	2.8
	Story	1	1	1	1	1	1	1	1	1	1	1	1	1	1	1
	Drift	.039	.020	.011	.025	.031	.033	.017	.035	.004	.015	.026	.013	.020	.016	.042

The data in Tables 5.10 – 5.15 is also notable because the first story initiated collapse in every case study building under every ground acceleration record. The results from Hines et al. (2009) were similar, although a few cases were observed in which the first story did not initiate collapse.

The conclusions derived from Figures 5.11 and 5.12, as well as Tables 5.10 – 5.15, are also evident in the median IDA curves that are illustrated in Figure 5.13. The median IDA curves were developed by calculating the median story drift of the story drifts achieved by a case study building for all ground motions at a specific scale factor. Resurrections of the IDA curves were neglected in these calculations, i.e. after a case study building reached collapse under a ground acceleration record it was assumed to remain collapsed for scale factors larger than the collapse scale factor. Thus, the collapse scale factors shown in the median IDA curves of Figure 5.13 represent the scale factor at which each case study building collapsed under ½ the ground

acceleration records used in the IDA. In Figure 5.13, a dotted line represents a case study building that does not have flexural strength in the braced frame connections, and all other line types represent buildings with flexural strength in the braced frame connections.

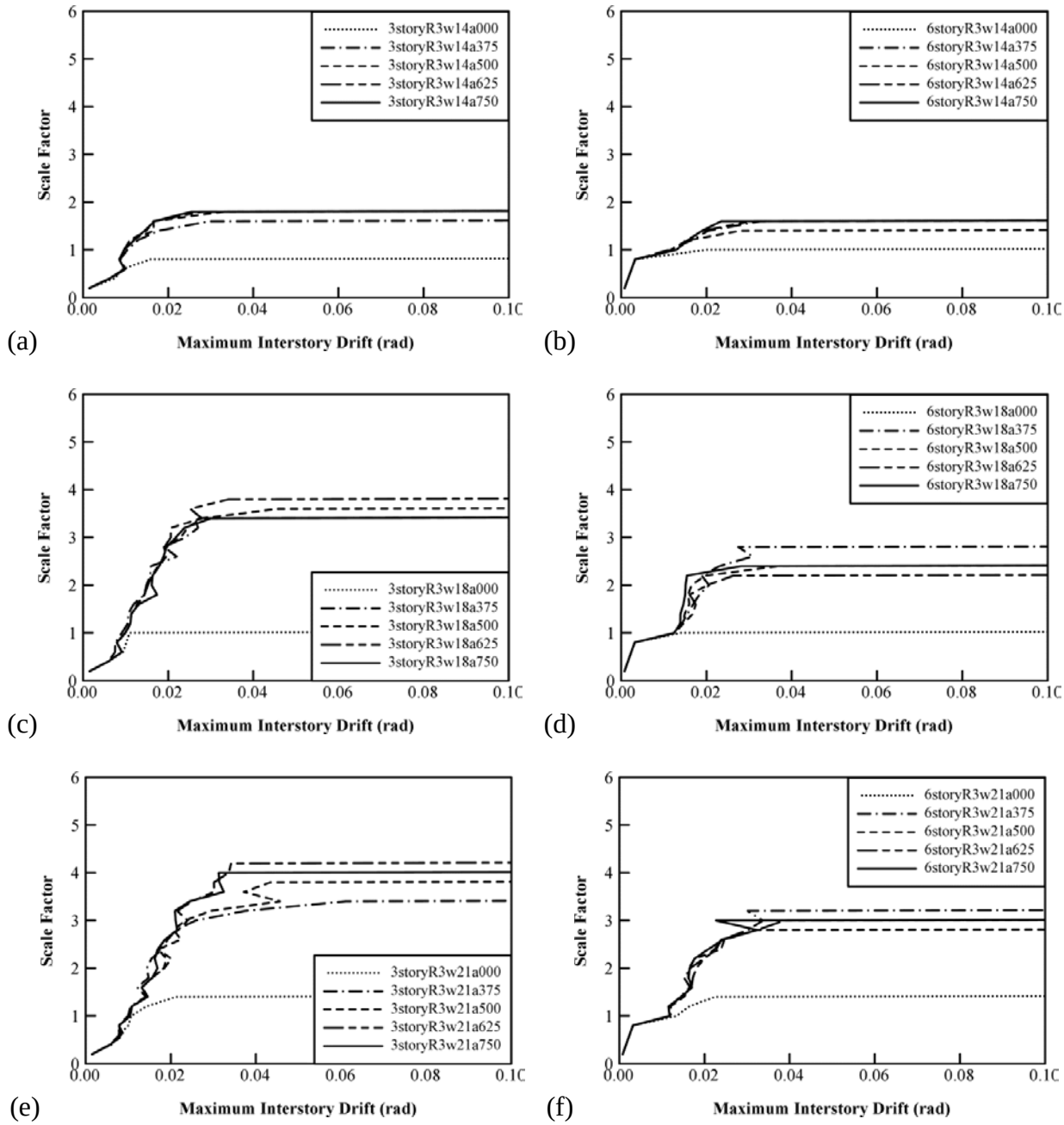

Figure 5.13 Median IDA curves for all case study buildings: (a) 3storyR3w14; (b) 6storyR3w14; (c) 3storyR3w18; (d) 6storyR3w18; (e) 3storyR3w21; (f) 6storyR3w21.

Clearly, the buildings with flexural strength in the braced frame connections were able to withstand larger ground acceleration intensities prior to collapse. In addition, the median IDA curves seem to indicate that increasing angle thickness for a given beam depth in the braced frame connections does not necessarily lead to enhanced collapse performance. This is due to the fact that increasing angle thickness does not increase reserve capacity, as was demonstrated with the SPO analyses outlined earlier. However, the reason that increasing angle thickness did not lead to increased reserve capacity was the flexural strength of the braced frame connections in positive bending was limited by weld failure. As shown in Table 5.6, the ultimate moment strength of the connections in positive bending was approximately constant for a given beam depth. Thus, the present study does not fully capture the potential impact of increasing angle thickness since the connections were not capacity designed to prevent weld failure prior to angle fracture.

Figure 5.13 also demonstrates differences in collapse behavior between the 3-story and 6-story buildings. In the IDA curves for the 6-story case study buildings; Figures 5.13b, 5.13d, and 5.13f; a linear, elastic response is observed up to a scale factor of 0.8. Beyond this ground acceleration intensity, damage to the primary LFRS leads to softening of the structure, which is represented by larger story drifts. In the 3-story case study buildings; Figures 5.13a, 5.13c, and 5.13e; no such linear, elastic region is present. In these cases, damage to the primary LFRS occurs at extremely low ground acceleration intensities, and the response of the structures is governed by this more flexible structural configuration.

In both groups of case study buildings, after the initial damage occurs, the buildings respond in an approximately linear manner up to collapse. Thus, collapse of these structures occurs suddenly, prior to significant inelastic drifting that is often observed in ductile systems.

The effect of reserve system strength on collapse behavior can also be seen in roof drift time history results. In addition, the flexural response history of the braced frame connections used to create the reserve LFRS needs to be examined. These issues are summarized in the discussion that follows. Figure 5.14 is included to show the designations used to refer to components of the braced frame in the discussion. The results and discussion presented here are confined to 3-story structures, but the results for 6-story structures are similar.

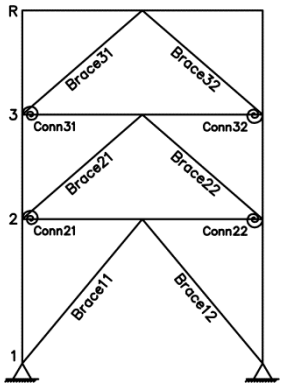

Figure 5.14 Component abbreviations used in discussion.

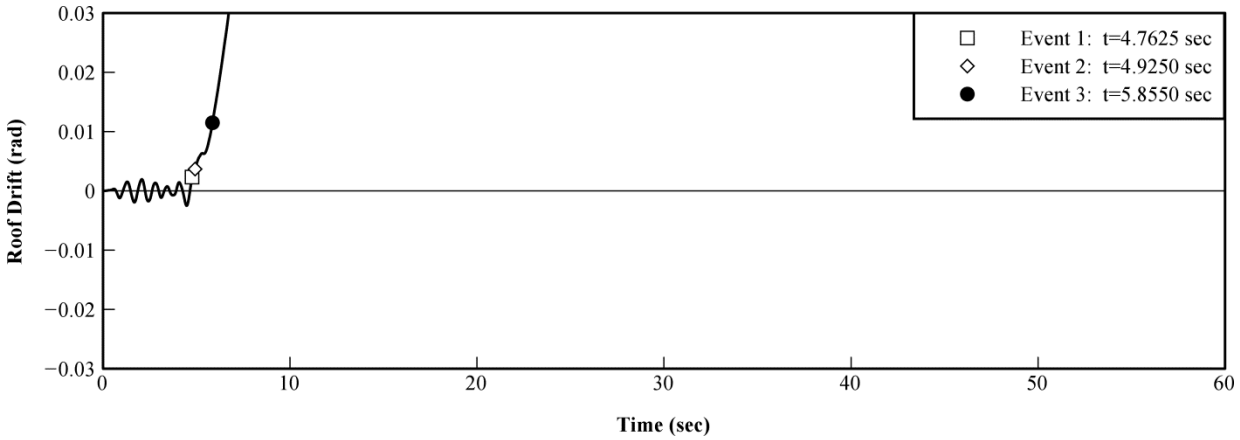

Figure 5.15 Roof drift vs. time for 3storyR3w18a000gm5 at SF = 1.0.

Figure 5.15 shows roof drift vs. time data and Figure 5.16 illustrates the damage accumulation for the 3storyR3w18a000 case study building under gm5, at a scale factor of 1.0. For this building, which does not have flexural strength in the braced frame connections, both braces in the first story lost their load carrying capacity at 4.7625 sec and both braces in the third

story were lost at 4.9250 sec. Flexural hinges developed in both first story columns at 5.8550 sec and the building collapsed shortly thereafter.

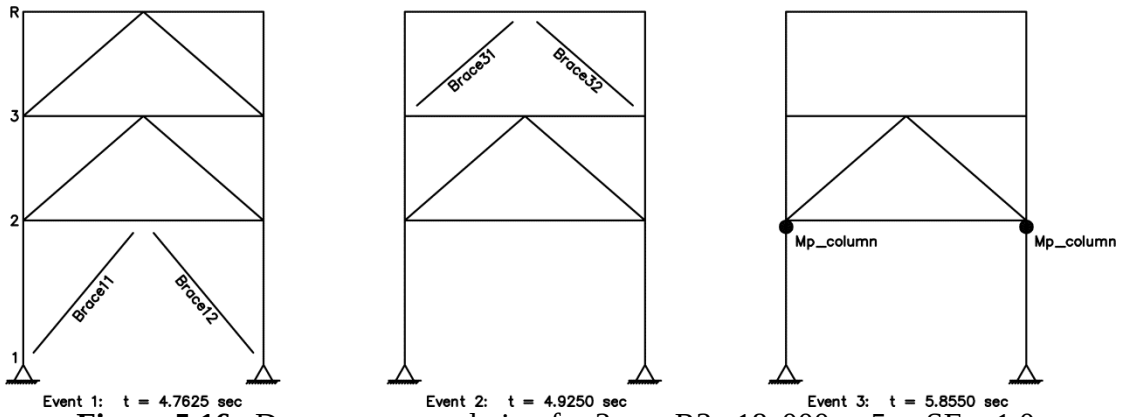

Figure 5.16 Damage accumulation for 3storyR3w18a000gm5 at SF = 1.0.

Figures 5.17 and 5.18 show the same data for the 3storyR3w18a375 case study building under the same ground motion, at the same scale factor. In this case, only Brace12 was lost in the first story and the building did not collapse.

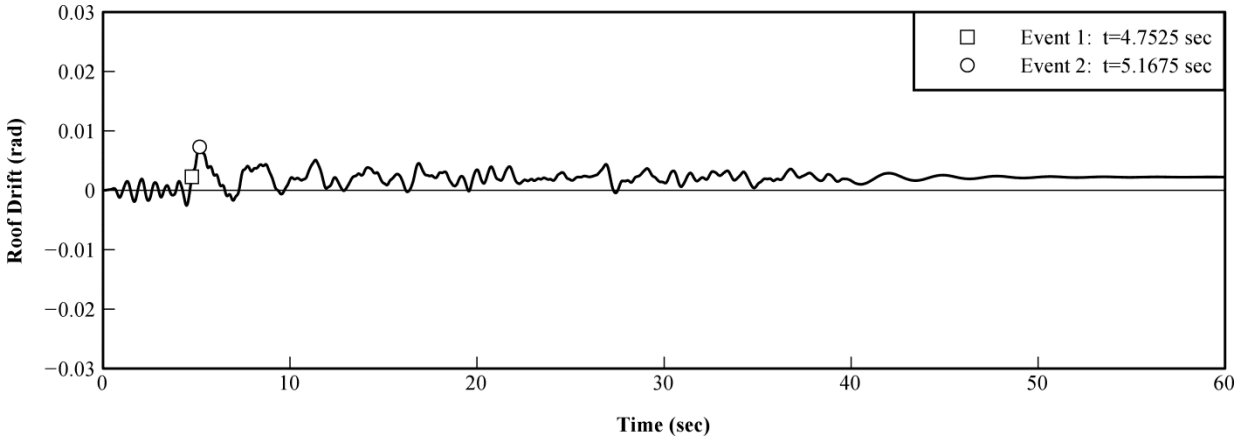

Figure 5.17 Roof drift vs. time for 3storyR3w18a375gm5 at SF = 1.0.

After Brace12 is no longer active, the first story behaves as a knee-braced frame by inducing flexure in the braced frame beam. The braced frame beam plastic moment and the ultimate moment strength of Conn22 were achieved at 5.1675 sec due to the eccentrically-braced frame behavior. These results demonstrate that a reserve LFRS composed of beam-column connections with gusset plates performs two functions. First, it aids in preventing additional

brace fractures by stiffening the braced frame beam. Second, it enhances the stiffness and strength of the knee-braced frame system that evolves after the initial brace fracture.

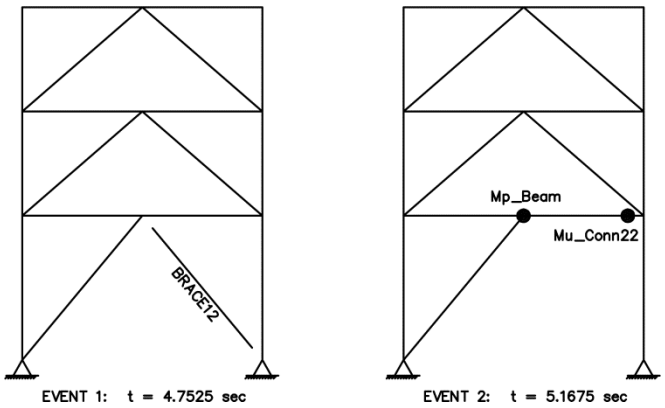

Figure 5.18 Damage accumulation for 3storyR3w18a375gm5 at SF = 1.0.

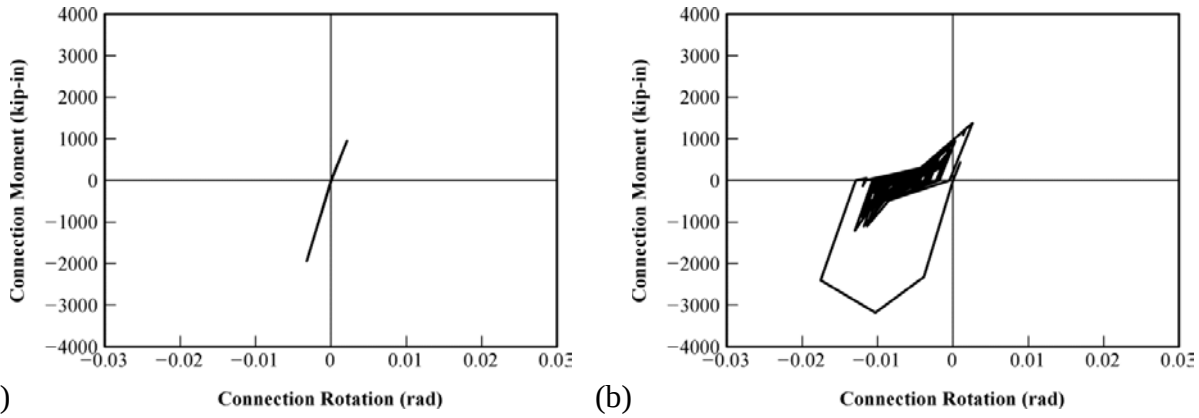

Figure 5.19 Connection moment vs. connection rotation for 3storyR3w18a375gm5 at SF = 1.0: (a) Conn21; (b) Conn22.

Figure 5.19 shows the connection moment vs. connection rotation for Conn21 and Conn22 for the 3storyR3w18a375 building. Conn21 remains essentially elastic, although moment demand reaches approximately ½ the yield moment in both positive and negative bending. This indicates that the portion of the first story bounded by the beam, column, and brace behaves like a rigid triangular truss. In contrast, flexural demand in Conn22 is adequate to induce the ultimate moment capacity of the connection, and the rotation demand reaches approximately 0.02 rad. Therefore, the flexural capacity of the beam and connection provide the reserve system strength to prevent collapse.

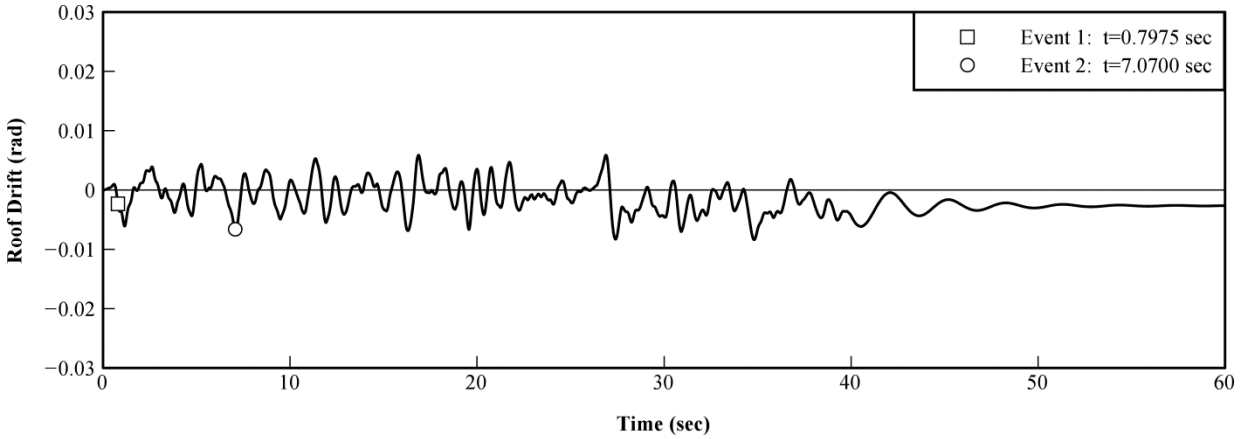

Figure 5.20 Roof drift vs. time for 3storyR3w18a375gm5 at SF = 3.0.

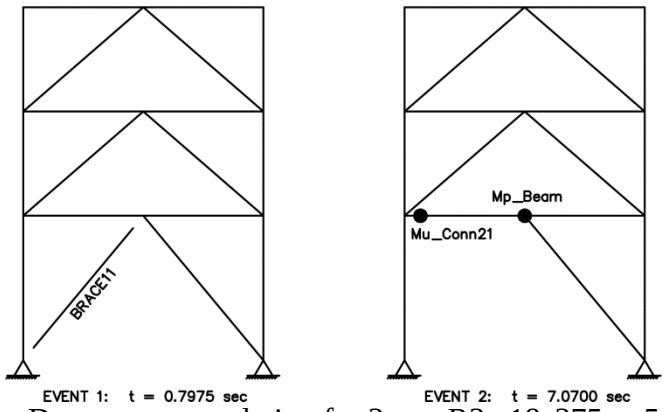

Figure 5.21 Damage accumulation for 3storyR3w18a375gm5 at SF = 3.0.

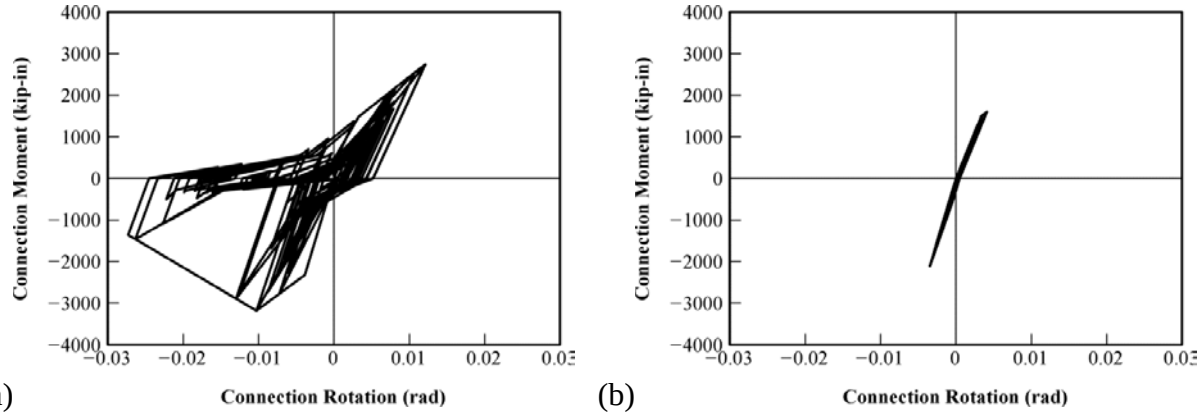

Figure 5.22 Connection moment vs. connection rotation for 3storyR3w18a375gm5 at SF = 3.0: (a) Conn21; (b) Conn22

Figures 5.20 – 5.22 show data for the same case study building, under the same ground motion, but the scale factor was increased to 3.0. In this case, Brace11 fractures early in the ground acceleration record, 0.7975 sec, which causes Conn21 and the braced frame beam to

form the reserve LFRS. Again, collapse is avoided, although larger roof drifts are realized than at a scale factor of 1.0. The rotation demand on Conn21 is significantly larger, approximately 0.03 rad, than Conn22 at a scale factor of 1.0.

In order to develop a more thorough understanding of the flexural rotation demands in the braced frame connections, connection rotation demand (CRD) data for the 3storyR3w18 buildings with various angle thicknesses in the braced frame connections was compiled. The CRD data is presented in Table 5.16. CRD data was obtained by finding the absolute maximum connection rotation achieved by any connection in each building, for each ground motion, at the scale factor prior to collapse. For instance, building 3storyR3w18a375gm5 collapsed at SF = 3.8, so the CRD was taken from connection rotation data at SF = 3.6.

The data in Table 5.16 suggest that CRD decreases with increasing angle thickness. In addition to the data presented in Table 5.16, mean values of CRD were calculated for all the case study buildings. The mean CRD values are presented in Figure 5.23. Shapes that are filled in Figure 5.23 represent case study buildings that exhibited acceptable collapse performance, which is quantified in section 5.2.2.

Table 5.16 Connection rotation demand for 3storyR3w18 buildings.

		Ground Motion														
		1	2	3	4	5	6	7	8	9	10	11	12	13	14	15
w18a375	SF	1.4	2.4	5.4	4.8	3.8	3.4	5.4	3.2	5.6	3.6	5.2	3.8	3.6	2.6	2.6
	CRD	.029	.044	.092	.110	.074	.094	.100	.100	.070	.023	.058	.047	.034	.017	.023
w18a500	SF	3.4	2.4	5.4	4.8	3.8	3.2	5.4	3.2	5.8	3.6	4.6	4.8	4	2.6	1.8
	CRD	.027	.025	.066	.081	.017	.065	.102	.060	.086	.011	.032	.090	.043	.011	.048
w18a625	SF	3.4	2.4	5.4	4.6	3.8	4	4.6	3.2	6	3.6	5.4	5.4	4	2.6	1.8
	CRD	.016	.022	.024	.047	.014	.021	.107	.030	.019	.012	.031	.046	.042	.012	.024
w18a750	SF	3.4	2.4	5.8	4.8	3.4	4	4.4	3.2	6	3.6	4	5.4	1.4	2.6	1.8
	CRD	.016	.013	.086	.098	.012	.019	.056	.016	.017	.010	.015	.024	.005	.010	.022

Figure 5.23 shows that mean CRD values generally range from 0.02 to 0.04 rad. This range is denoted by the light gray horizontal lines in Figure 5.23. The exceptions to this observation were the 3storyR3w18a375, 3storyR3w18a500, and 3storyR3w21a375 case study buildings. In addition, Figure 5.23 shows that the observation that CRD decreases with increasing angle thickness is only valid for the 3storyR3w18 and 3storyR3w21 case study buildings. Nevertheless, it is reasonable to conclude that the minimum connection rotation capacity of braced frame connections used in a reserve capacity system should be 0.03 to 0.04 rad without significant strength degradation.

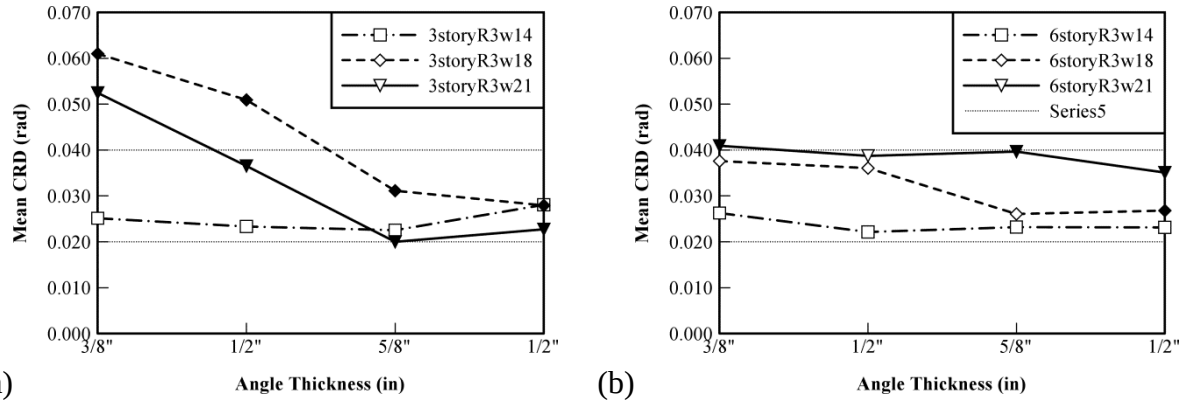

Figure 5.23 Mean connection rotation demand: (a) 3-story buildings; (b) 6-story buildings.

It should also be noted that after both braces in the first story fractured for any case study building, under any ground acceleration intensity, collapse ensued. Thus, it appears that the inherent redundancy of the chevron bracing configuration is crucial in developing the reserve system strength of the buildings in this study. This was also demonstrated in the SPO analyses where failure of one brace in the first story induced flexure in the second story braced frame beam, which led to reserve capacity. Bracing configurations without this benefit, single diagonal braced frames for example, may be prone to seismic collapse even if the flexural strength of the braced frame connections are considered in design.

5.3.2 Collapse Performance Evaluation

To evaluate the collapse performance of the case study buildings, the procedures in FEMA P695 (FEMA 2009) were used. The FEMA P695 procedure has four parts: construct fragility curves from the IDA data, evaluate the uncertainty in the IDA results, adjust the fragility curves based on the uncertainty, and determine acceptable collapse performance based on the uncertainty and the adjusted fragility curves.

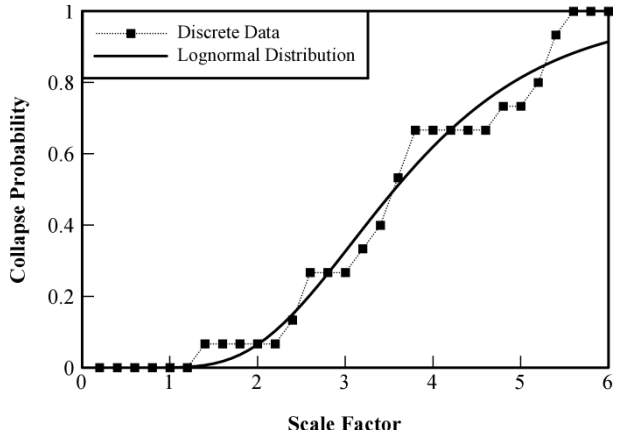

Figure 5.24 Fragility curve for 3storyR3w18a375.

Figure 5.24 illustrates the fragility curve for the 3storyR3w18a375 case study building, which is representative of the fragility curves for the other buildings in this study. The fragility curves were constructed by determining the probability of collapse of each case study building at a given ground acceleration intensity, which is represented by scale factor in this study. The scale factor at collapse was recorded for the 3storyR3w18a375 building for all 15 ground motions. The probability of collapse at each scale factor was found by counting the number of buildings to collapse for that scale factor and then dividing by the number of ground acceleration records. The discrete data points in Figure 5.24 represent this procedure. A lognormal distribution was then fit to the discrete data by finding the mean and standard deviation of the natural logarithm of the collapse scale factors. The lognormal distribution is shown as a solid line in Figure 5.24.

After fragility curves were developed for all the case study buildings, the collapse margin ratio (CMR) for each building was calculated. CMR is, essentially, a measure of a structure's collapse resistance. Coupled with the uncertainty of the IDA, CMR is used to determine if a case study building demonstrates acceptable collapse performance. CMR is calculated from

$$CMR = \frac{\hat{S}_{CT}}{S_{MT}} \tag{5.5}$$

where $\hat{S}_{CT}$ is the median collapse intensity and S_{MT} is the MCE level collapse intensity. $\hat{S}_{CT}$ is found from the fragility curves, and represents the collapse intensity that causes a case study building to collapse under ½ the ground motions in the IDA. S_{MT} is equal to 1 for the present study, since a scale factor of 1.0 represents an MCE level ground acceleration. Thus, $CMR = \hat{S}_{CT}$ for this study. Table 5.17 lists CMR for all the case study buildings.

Table 5.17 Collapse margin ratio for case study buildings.

Building	3 Story	6 Story
w14a000	1.115131579	1.1986494
w14a375	1.89680505	1.7808371
w14a500	2.233449625	1.7424946
w14a625	2.233449625	1.8723971
w14a750	2.38594518	1.9106719
w18a000	1.145827387	1.3497365
w18a375	3.561944482	2.5816137
w18a500	3.734701176	2.6091987
w18a625	3.818352489	2.4658995
w18a750	3.480050047	2.8462394
w21a000	1.458841987	1.557987
w21a375	2.957711824	3.0121062
w21a500	2.993312108	2.6454731
w21a625	3.253657086	2.8386704
w21a750	3.60882936	3.0906508

The next step in evaluating the collapse performance of the case study buildings was quantifying the uncertainty in the IDA. According to FEMA P695, there are four sources of uncertainty: record-to-record uncertainty, design requirements uncertainty, test data uncertainty, and computational modeling uncertainty. Record-to-record uncertainty, β_{RTR}, is due to

variability in the response of a case study building to various ground acceleration records (FEMA 2009). FEMA P695 recommends β_{RTR} = 0.4 for structures with period elongation. Since brace fracture, which leads to period elongation, is a significant factor in the seismic response of braced frames, this value was used for the present study.

The remaining sources of uncertainty are quantified in FEMA P695 based on qualitative assessments of the reliability of the design requirements, test data, and computational modeling. Uncertainty values range from 0.1 to 0.5. For design requirement uncertainty, β_{DR} was taken as 0.5 since the buildings in this study were designed using the R = 3 provision, and this design provision is not thoroughly understood. A value of 0.35 was chosen for test data uncertainty, β_{TD}, and modeling uncertainty, β_{MDL}. The total uncertainty is then calculated from

$$\beta_{TOT} = \sqrt{\beta_{RTR}^2 + \beta_{DR}^2 + \beta_{TD}^2 + \beta_{MDL}^2} \tag{5.6}$$

which yielded β_{TOT}= 0.8. This was the same uncertainty value used by Hines et al. (2009) in the development of their fragility curves. Table 5.18 summarizes the uncertainty values.

Table 5.18 Summary of IDA uncertainty.

β_{RTR}	β_{DR}	β_{TD}	β_{MDL}	β_{TOT}
0.4	0.5	0.35	0.35	0.8

After quantifying the uncertainty in the IDA results, the fragility curves were adjusted to reflect this uncertainty. To adjust the curves, the standard deviation that was calculated from the IDA data is replaced by the uncertainty calculated from Equation (5.6). Figure 5.22 shows the adjusted fragility curves for all the case study buildings. One measure of acceptable collapse performance according to FEMA P695 is a 10% probability of collapse under MCE level seismic hazard. This condition is represented by the horizontal line through 10% collapse probability and the vertical line through a scale factor of 1.0 in Figure 5.25. Thus, any fragility curve that

intersects the vertical line at SF = 1.0 below the horizontal line representing 10% collapse probability indicates a case study building that exhibits acceptable collapse performance.

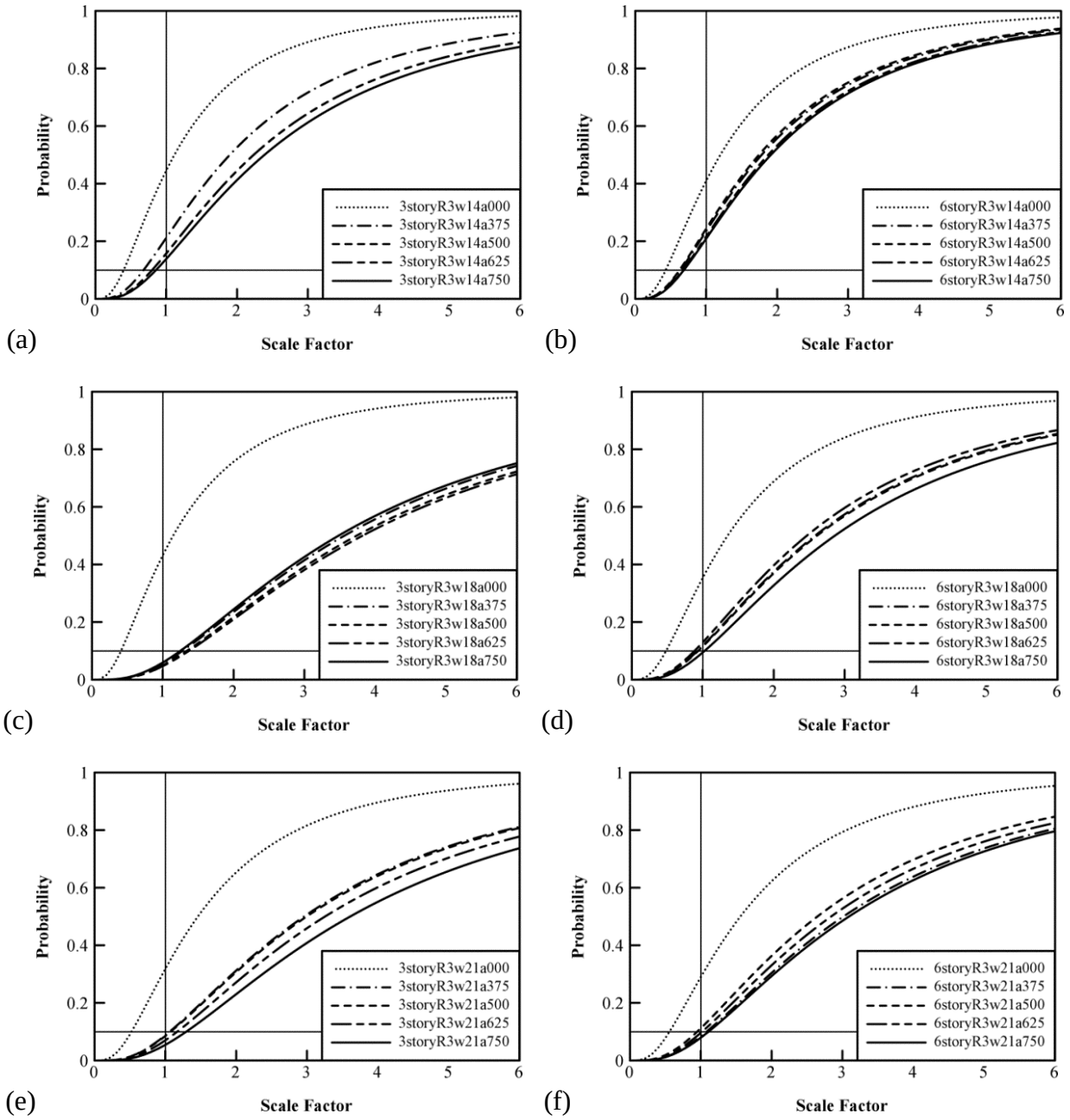

Figure 5.25 Fragility curves adjusted for uncertainty: (a) 3storyR3w14; (b) 6storyR3w14; (c) 3storyR3w18; (d) 6storyR3w18; (e) 3storyR3w21; (f) 6storyR3w21.

Based on the performance criteria of 10% probability of collapse under an MCE level seismic event, Figure 5.25 reveals that all 3storyR3w18 and 3storyR3w21 structures with reserve

capacity exhibited acceptable collapse performance. One of the 6storyR3w18 structures and three of the 6storyR3w21 structures demonstrated acceptable collapse performance as well.

All structures that had zero flexural strength in the braced frame connections, in addition to all the structures with W14x53 beams in the braced frame, exhibited poor collapse performance. Thus, it appears that beam flexural stiffness and strength also plays a role in the collapse performance of chevron configuration CBFs with reserve LFRSs.

To simplify evaluation of collapse performance, FEMA P695 recommends calculating adjusted collapse margin ratio (ACMR) for each case study building. ACMR is then compared to the 'Acceptable Value of ACMR' from FEMA P695, which is based on the uncertainty of the IDA data, to determine if collapse performance is acceptable. The 'Acceptable Value of ACMR' is denoted $ACMR_{10\%}$, to indicate that this is the value of ACMR a case study building must exceed in order to realize collapse probability of 10%, or better, for an MCE level seismic event. ACMR is calculated with the equation

$$ACMR = CMR \cdot SSF \tag{5.7}$$

where SSF is the spectral shape factor. The SSF accounts for the influence that the frequency content of the ground acceleration suite has on collapse capacity. Since the ground acceleration records used in this study were derived from the USGS uniform hazard spectrum (UHS), deviation from the UHS is negligible and the SSF can be taken as unity (Sorabella 2006). Thus, ACMR is equal to CMR for the case study buildings in this investigation, and the CMR values given in Table 5.17 can be taken as the ACMR values. In addition, $ACMR_{10\%} = 2.79$ based on $\beta_{TOT} = 0.8$ from FEMA P695. Therefore, any case study building that has an ACMR greater than 2.79 exhibited acceptable collapse prevention performance.

5.4 DESIGN OF RESERVE CAPACITY SYSTEMS

5.4.1 Relationship between Collapse Performance and Reserve System Strength

In order to develop design recommendations for reserve LFRSs, the relationship between collapse performance and reserve system behavior was established. This was accomplished by plotting ACMR against reserve system strength and ACMR against reserve system stiffness. Figures 5.26 and 5.27 illustrate this data. In Figure 5.26, the reserve system strength, V_r, was normalized to the code design base shear for the building, V_{code}. V_{code} was calculated from ASCE 7 (ASCE 2002) since the ground acceleration records used in the IDA were based on the 2002 USGS uniform hazard maps.

Figure 5.26 shows that the reserve system strength needed to generate adequate collapse prevention performance was significantly higher for the 3-story buildings than for the 6-story buildings. This corroborates the observation by Hines et al. (2009) that taller structures are not as susceptible to seismic collapse in moderate seismic regions. Figure 5.26 also demonstrates that a minimum level of reserve strength is needed to achieve acceptable collapse prevention performance. For the 3-story structures this threshold appeared to be $V_r/V_{code} = 0.33$, and for the 6-story structures this threshold appeared to be $V_r/V_{code} = 0.2$. Thus, a conservative recommendation for the minimum value of V_r/V_{code} needed to provide acceptable collapse prevention performance for low-rise chevron configuration CBFs is 0.35.

Figure 5.27 illustrates the reserve system stiffness of the case study buildings. In Figure 5.27, the reserve system stiffness, K_r, was normalized by the roof displacement stiffness of the undamaged braced frame, K_{bf}. Figure 5.27 reveals that the 3-story structures were significantly more flexible than the 6-story structures. The reserve system stiffness for buildings that exhibited acceptable collapse prevention performance was only 10% of the braced frame

stiffness in the 3-story structures and 27% in the 6-story structures. Since the required stiffness to generate adequate collapse prevention performance is so low, however, it appears that strength should be the primary consideration in design of reserve lateral force-resisting systems.

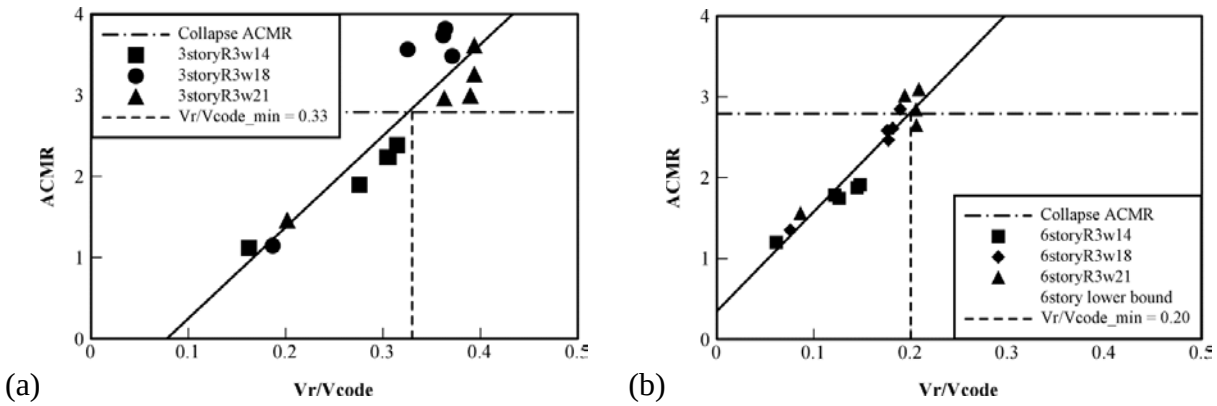

Figure 5.26 ACMR vs. V_r/V_{code}: (a) 3-story buildings; (b) 6-story buildings.

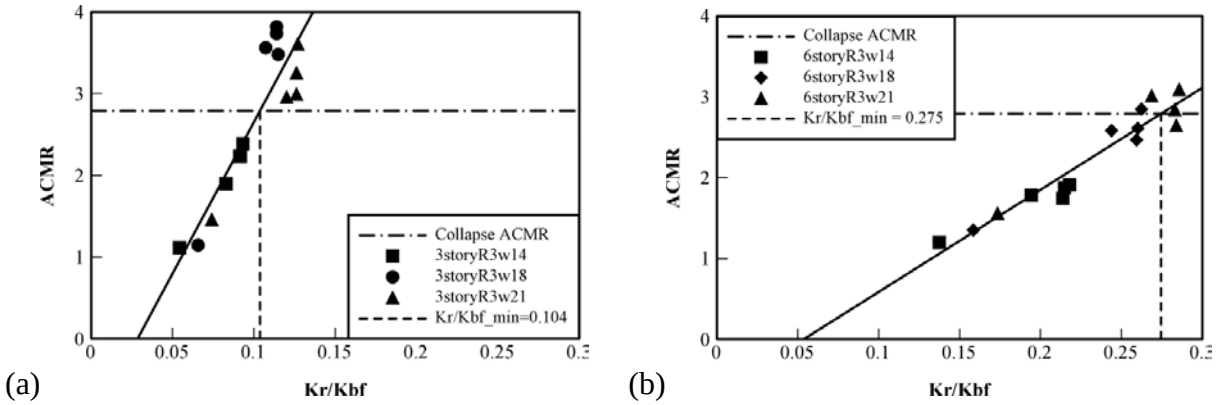

Figure 5.27 ACMR vs. K_r/K_{bf}: (a) 3-story buildings; (b) 6-story buildings.

5.4.2 Reserve System Design Procedure

In order to facilitate implementation of reserve lateral force-resisting systems in seismic design practice for CBFs in moderate seismic regions, a design procedure quantifying the reserve lateral force-resisting strength of a chevron CBF was developed from the results of the IDA and SPO analyses. Since it appears that reserve system strength is the critical link in achieving

acceptable collapse performance in CBFs, the design procedure focuses on this aspect of reserve system performance.

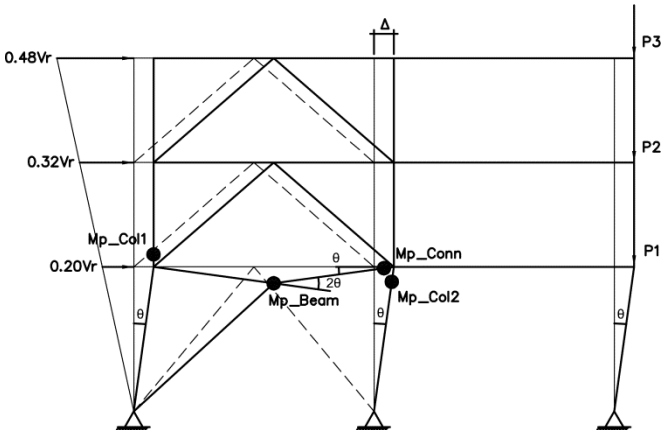

Figure 5.28 Collapse mechanism for determining reserve system strength.

To quantify reserve system strength, a collapse mechanism consistent with the SPO analyses was identified. The collapse mechanism for a 3-story building is shown in Figure 5.28. In this mechanism, one brace is assumed to have lost its load-carrying capacity due to brace-to-gusset plate connection failure, and plastic moment in the beam, $M_{p,Beam}$, one of the braced frame connections, $M_{p,Conn}$, and both of the braced frame columns, $M_{p,Col1}$ and $M_{p,Col2}$, have been reached. $M_{p,Conn}$ can be determined from the braced frame connection flexural strength procedure outlined in Chapter 4, or a rigorous finite element analysis of the braced frame beam-column connection under consideration. The beam is assumed to have experienced a rotation of 2θ and the connection and both columns are assumed to have experienced a rotation of θ. A leaning column, assumed pinned at each story level, is included to account for P-Δ effects. Although continuous gravity columns also contribute to reserve system strength, they are not included in this analysis since the focus of this study is on reserve capacity available within braced frames. The lateral force distribution is based on the equivalent lateral force procedure outlined in ASCE 7 (ASCE 2002). The upper stories are considered to move as a rigid body above the first story.

Applying the method of virtual velocities to the mechanism of Figure 5.28 results in the following equation for reserve system strength, V_r,

$$V_r = \frac{2M_{p,Beam} + 0.7M_{p,Conn} + M_{p,Col1} + M_{p,Col2}}{h_1} - P\theta \tag{5.8}$$

where h_1 is the height of the first story, P is the sum of all gravity loads acting on the leaning column, and θ is the first story drift that coincides with V_r. The 0.7 reduction factor on the $M_{p,conn}$ term in Equation 5.8 was included to recognize the fact that the ultimate moment strength of the connections is not sustained while additional hinges are developing. As shown previously in Figure 5.5, the moment strength of the braced frame connections degrades after the ultimate moment strength is achieved. The 0.7 reduction factor was calculated by taking the average of the ratio M_y/M_u for each connection in Table 5.6. Thus, the braced frame connection moment that is sustained during formation of additional plastic hinges is the yield moment of the connection, which is approximately $0.7M_{p,conn}$.

In addition, $M_{p,Col1}$ and $M_{p,Col2}$ need to be adjusted to account for the interaction of axial and flexural load. Salmon et al. (2009) provide the following equation to approximate the reduced strong-axis flexural strength of a wide flange shape due to the presence of axial force

$$M_p^{Adj} = 1.18M_p\left(1 - \frac{P_u}{P_y}\right) \le M_p \tag{5.9}$$

where M_p^{Adj} is the adjusted moment strength, M_p is the plastic moment strength, P_u is the gravity load applied to the column under consideration, and P_y is the squash load. Axial forces due to overturning are neglected in Equation 5.9 since they are small in comparison to the gravity load. The value of θ in Equation 5.8 should be taken as the connection rotation when the braced frame connection reaches its ultimate strength, which was shown in Table 5.6 for the connections in this study. This is due to the observation that the reserve system strength from the SPO analyses

occurred when the maximum moment in the braced frame beam-column connection occurred. If the analysis procedure from Chapter 4 is used to construct the moment-rotation behavior of the braced frame connections, θ in Equation 5.8 may be approximated as $2 \cdot \theta_y$, where $\theta_y = M_{conn}/K_{conn}$. In addition, the contribution of gravity columns to reserve lateral force-resisting strength was not included since plastic hinges in the gravity columns were not observed in the SPO analyses until drifts significantly higher than the drift at V_r.

Table 5.19 compares the reserve system strengths taken from the SPO analyses with strengths calculated from Equation 5.8 assuming θ equal to the braced frame connection rotation when connection ultimate moment strength is reached. For buildings without flexural strength in the braced frame connections, θ was taken as 0.02 rad, which was consistent with the results from the SPO analyses. The percent difference in reserve system strength between the SPO analyses and Equation 5.9 are also provided in Table 5.19. Positive percent differences correspond to unconservative predictions of reserve system strength. Table 5.19 demonstrates that the reserve system strengths predicted by Equation 5.8 provide reasonable agreement with the SPO results.

To achieve acceptable collapse prevention performance, the value of V_r calculated from Equation 5.8 needs to be greater than or equal to $0.35V_{code}$. After the reserve strength of the first story satisfies this requirement, the upper stories would need to be checked using a collapse mechanism similar to the one shown in Figure 5.28 to ensure that they also provide adequate reserve system strength. For collapse mechanisms involving roof beams, $M_{p,Conn}$ would be excluded from the calculation for V_r since the connections between the roof beam and the column do not include gusset plates.

Table 5.19 Comparison of computational and analytical reserve system base shear results.

Building	Reserve System Strength (kips)					
	3 Story SPO	3 Story Equation 5.7	Percent Difference	6 Story SPO	6 Story Equation 5.7	Percent Difference
w14a000	32.3	36.9	14.3%	24.4	24.3	-0.247%
w14a375	54.9	51.6	-6.00%	47.8	45.9	-3.91%
w14a500	60.9	56.2	-7.67%	51.0	53.0	3.91%
w14a625	61.2	57.0	-6.80%	56.0	54.4	-2.85%
w14a750	62.9	58.7	-6.60%	57.9	56.9	-1.67%
w18a000	36.8	38.8	5.35%	29.9	26.2	-12.4%
w18a375	64.9	68.5	5.55%	63.4	75.6	19.2%
w18a500	71.5	67.5	-5.62%	70.9	69.1	-2.53%
w18a625	71.8	68.8	-4.22%	70.3	71.4	1.60%
w18a750	73.1	72.3	-1.04%	74.0	77.4	4.63%
w21a000	39.7	41.1	3.65%	33.5	28.6	-14.7%
w21a375	72.5	73.6	1.51%	69.8	81.5	16.7%
w21a500	76.5	74.7	-2.32%	79.5	78.8	-0.889%
w21a625	77.1	66.9	-13.2%	79.3	61.0	-23.0%
w21a750	78	79.5	1.89%	81.2	87.0	7.13%

Even though good agreement was demonstrated between Equation 5.8 and the results of the SPO analyses, there are several aspects of frame behavior that are not considered in Equation 5.8. The first aspect that is lacking is modification of the $M_{p,col}$ terms due to variations in the column flexibility. The braced frame beam-column connection flexural behavior acts as a rotational restraint to the braced frame columns, which allows the braced frame columns to reach their plastic moment strength at lower story drifts than the gravity columns. If the braced frame columns are sufficiently flexible, or the rotational restraint due to the connection sufficiently small, the columns may not reach their plastic moment strength until after the reserve system strength is realized. Thus, inclusion of the plastic flexural strength of the braced frame columns may be unconservative in some cases.

A second aspect of frame behavior not explicitly captured by Equation 5.9 is the elastic strength of the continuous gravity columns. Even though their plastic moment strength was not developed in the SPO analyses, previous studies (Tremblay and Stiemer 1994, Rai and Goel 2003) demonstrated that the elastic strength of continuous gravity columns can substantially

increase reserve capacity. Hence, Equation 5.8 may severely underestimate reserve system strength if the number of gravity columns is much larger than the number of braced bays.

Finally, one of the fundamental assumptions underlying the plastic mechanism analysis procedure used to derive Equation 5.9 is that all plastic hinges have adequate rotation capacity to allow the formation of all hinges in the mechanism. As was stated previously, the braced frame connection flexural behavior does not satisfy this assumption, owing to the fact that the connection strength begins degrading immediately after reaching its ultimate strength. In addition, the rotation of the plastic hinge developed in the braced frame beam was shown to exceed the 0.02 rad rotation limit for EBF links prescribed in the AISC *Seismic Provisions for Structural Steel Buildings* (2005a). Both of these issues involving rotational capacity of elements in the reserve lateral force-resisting system need to be addressed in order to refine the methods for quantifying reserve system strength presented here.

5.5 SUMMARY OF COLLAPSE PERFORMANCE EVALUATION

In this chapter, the collapse performance of chevron configuration CBFs was evaluated using reliability-based performance assessment. A series of case study buildings were subjected to a suite of ground acceleration records developed for the Boston, Massachusetts, moderate seismic region. The ground acceleration records were used to conduct an incremental dynamic analysis of the case study buildings by scaling the ground accelerations until they caused collapse of each building. Collapse was defined to be achieving a story drift of 0.10 rad in any story within a structure. The results from the IDA were used to generate fragility curves for each of the case study buildings, which were used to evaluate their collapse performance. After completing the collapse performance evaluation, a relationship between the collapse

performance and reserve system strength of each structure was established. The reserve system strength was quantified using static pushover analyses of the case study buildings. Finally, a simplified design procedure for calculating reserve system strength for chevron CBFs was derived from the results of the collapse performance evaluation and static pushover analyses. The following conclusions were drawn from the results of the computational system analyses.

- Increasing the strength of the reserve lateral force-resisting system increased the collapse resistance of chevron configuration CBFs located in a moderate seismic region. It was found that the reserve capacity provided by all angle thicknesses for a given beam depth was approximately the same since the flexural strength of the connections in positive bending was limited by failure of the weld between the beam and gusset plate. It was also noted that braced frame beam depth is closely tied to collapse resistance.
- The 6-story structures required less reserve strength to demonstrate acceptable collapse prevention performance than the 3-story structures because of their inherent flexibility.
- The rotation demand of the braced frame connections in this study was large enough to push the connection beyond its ultimate moment capacity and into the descending branch of the connection moment vs. connection rotation behavior. Thus, it appears that the connections in the reserve system need to possess some ductility to allow the reserve system to generate adequate collapse prevention performance. A minimum flexural rotation capacity of 0.03 to 0.04 rad is reasonable based on the results of this study.
- The plastic moment strength of the braced frame beams was found to play a critical role in developing the reserve system strength. Flexure in the braced frame beam was induced when one of the braces in the first story would fracture, which caused the remaining structure to behave like a long-link EBF. Data summarizing the rotation demand on the beam in the SPO

analyses indicated that plastic rotations larger than 0.02 rad may be experienced in the beam as the reserve system strength is developed. Rotations of this magnitude may lead to flexural strength degradation in the braced frame beam, although this phenomenon was not included in the computational models used for this study.

- The reserve system strength can be evaluated for each story in a structure assuming a plastic-hinge collapse mechanism involving the braced frame beam, one of the braced frame connections, and the braced frame columns. One of the braces in the story under consideration is removed to simulate the behavior observed in the static pushover analyses. If desired, the reserve system strength can be quantified with static pushover analyses following the procedure described in this chapter.

CHAPTER 6

CONCLUSIONS AND ENGINEERING RECOMMENDATIONS

This dissertation investigated the flexural behavior of beam-column connections with gusset plates and their ability to improve the seismic collapse performance of concentrically braced frames. Previous experimental and field observations demonstrated that reserve lateral force-resisting capacity due to the flexural strength of connections outside the primary lateral force-resisting system of steel frames can maintain structural stability if the primary system is damaged. Several experimental studies were conducted to quantify the flexural behavior of these connections, but minimal work was completed involving isolated beam-column connections with gusset plates.

6.1 RESEARCH MOTIVATION, OBJECTIVES, AND TASKS

This research was motivated by the need to rigorously study the seismic collapse performance of CBFs in moderate seismic regions and to evaluate the influence of reserve lateral force-resisting capacity. Several previous studies (Tremblay et al. 1995, Rai and Goel 2003, Uriz and Mahin 2008, Hines et al. 2009) demonstrated that reserve capacity positively benefits the seismic collapse resistance of steel braced frames after the primary lateral force-resisting system has been damaged. In general, these studies did not investigate global quantification of reserve capacity or local requirements for the flexural stiffness and strength of the connections comprising the reserve capacity system, although several potential sources of reserve capacity were identified: connections in the gravity framing system, continuous gravity columns, and braced frame connections with gusset plates. Additional studies (Gross and Cheok 1988, Kishiki et al. 2007) corroborated the observation that braced frame connections with gusset plates

possess appreciable flexural stiffness and strength, but the flexural behavior of isolated braced frame connections has not been extensively quantified in existing literature.

Therefore, two objectives were defined for this study. First, expand existing knowledge about the flexural behavior of braced frame connections using experimental and computational methods. Second, use reliability-based performance assessment to demonstrate that braced frame connections with gusset plates can enhance reserve capacity to levels that generate acceptable collapse prevention performance.

The first objective was accomplished through a series of full-scale experiments and finite element analyses of beam-column subassemblies. The braced frame connections in the experimental program were double angle and end plate details that were proportioned based on the design loads from a prototype braced frame. The results from the experiments suggested that beam-column connections with gusset plates have appreciable flexural stiffness and strength. In addition, the flexural stiffness and strength of the connections could be increased, with minimal ductility loss, by thickening the double angles and adding a supplemental seat angle. The stiffness, strength, and ductility were limited, however, by weld failure, angle fracture, and bolt fracture.

Since only one beam depth was used in the large-scale testing, it was desirable to investigate the effect of beam depth on the flexural behavior of braced frame connections using three-dimensional finite element analysis. Three additional beam sizes were selected: W14x53, W18x46, and W21x44. Various double angle thicknesses were also considered. The computational studies revealed that increasing beam depth increases the flexural stiffness and strength of beam-column connections with gusset plates. But, the limit states observed in the full-scale tests occurred at smaller story drifts as the beam depth increased. Larger angle

thicknesses were also found to increase flexural stiffness and strength. The results from the experimental and finite element studies were used to develop a simplified procedure for evaluating the flexural stiffness and strength of a braced frame connection.

After completing the experimental and computational studies on the flexural behavior of braced frame connections, the second objective was accomplished through a series of incremental dynamic analyses on a suite of concentrically braced frames in a moderate seismic region to determine if beam-column connections with gusset plates can provide adequate reserve capacity to insure collapse prevention performance. Collapse performance data was generated by analyzing the results of the incremental dynamic analyses using a reliability-based performance assessment. The results from the collapse performance assessment revealed that beam-column connections with gusset plates can function as a reserve lateral force-resisting system. The results from the incremental dynamic analyses, in conjunction with the collapse performance data, were used to synthesize recommendations for the minimum level of strength a reserve lateral force-resisting system must possess in order to insure adequate collapse prevention performance.

6.2 CONCLUSIONS FROM FULL-SCALE EXPERIMENTS

The following conclusions were drawn from the large-scale testing program.

- The baseline brace connection, CN1, which was a typical double angle detail, had more stiffness and strength than has traditionally been considered in design of concentrically-braced frames. CN1 exceeded the strength and stiffness thresholds commonly used as upper bounds to classify pinned connections, and instead behaved as a partially-restrained connection.

- The modified angle connections, CN6 – CN8, exhibited more deformation capacity than the end plate connections. None of the modified angle connections, however, achieved the expected plastic moment of the beam in positive or negative bending. Increasing angle thickness had a greater impact on the negative moment strength and adding a seat angle had a greater impact on positive moment strength. Bolt fractures occurred in CN6 and CN7 due to prying forces induced by flexibility of the double angles. The larger weld size in CN8 delayed the initiation of gusset plate-beam fillet weld failure as well as the onset of strength degradation.
- The double angle connection configuration with a supplemental seat angle provided the best balance of strength and deformation capacity.
- The path and propagation rate of the fillet weld failures in CN3 and CN5 – CN8 significantly affected the strength and ductility of the connections in positive bending. Weld failure paths that developed through the weld throat propagated slowly and the global loss of strength due to this event was gradual. In contrast, the weld failure path in CN6 was along the interface between the leg of the weld and the gusset plate, resulting in more rapid global strength loss. In addition, increasing the fillet weld size significantly improved the cyclic response in CN8.
- Low cycle fatigue fracture of the steel angles in CN1 was driven by a combination of void growth and coalescence and cleavage fracture. In addition, the initial fractures along the face of the angle showed almost no evidence of void growth and coalescence.
- Displacement data and visual observations indicated that flexural yielding, panel zone shear yielding, and local flange flexural yielding may occur in a braced frame column if the flexural capacity of the beam-column connection with gusset plate is used in a reserve capacity system. Although energy dissipation is not the primary mechanism a reserve

capacity system uses to maintain structural stability, energy dissipation due to the aforementioned column limit states would aid collapse performance.

6.3 CONCLUSIONS FROM FINITE ELEMENT MODELING OF CONNECTIONS

The following conclusions were drawn from the finite element analyses detailed in Chapter 4.

- Flexural strengths of double angle connections ranged from 41% to 99% of the beam plastic moment strength in positive bending and from 29% to 93% of the beam plastic moment strength in negative bending.
- The story drift at maximum positive moment ranged from 0.01 rad to 0.04 rad and the story drift at maximum negative moment ranged from 0.015 rad to 0.04 rad. The story drift at maximum moment in both positive and negative flexure typically decreased with increasing beam depth. Gusset angle fracture and weld failure limited the moment strength in positive bending, and web or seat angle fracture and bolt fracture limited the moment strength in negative bending.
- Thicker double angles delayed the onset of fatigue fracture in the beam web angles and changed the strength limit state in positive bending to weld failure, not gusset angle fracture. Bolt fracture, instead of web angle failure, was observed for negative bending in most cases with 0.625-in and 0.75-in angles.
- The flexural stiffness and strength of the double angle connections studied increased with increasing beam depth. Initiation of fatigue fractures in the angles, however, occurred at smaller story drifts for deeper beams.
- The addition of a supplemental seat angle was found to increase flexural stiffness and

strength for the range of beam depths considered in the parametric study, 14 in to 21 in, just as observed in the experimental program for a single beam depth, 10 in. The seat angle did not affect, or only slightly decreased, the cumulative drift at which the critical limit states occurred.

- Increasing the gusset plate-beam fillet weld size delayed the initiation of weld failure, but did not provide additional flexural stiffness or strength.

6.4 CONCLUSIONS FROM COLLAPSE PERFORMANCE EVALUATION

The following conclusions were drawn from the collapse performance evaluation of CBFs with reserve lateral force-resisting systems.

- Increasing the strength of the reserve lateral force-resisting system increased the collapse resistance of chevron configuration CBFs located in moderate seismic regions. It was found that the reserve capacity provided by all angle thicknesses for a given beam depth was approximately the same since the flexural strength of the connections in positive bending was limited by failure of the weld between the beam and gusset plate. It was also noted that braced frame beam depth is closely tied to collapse resistance.
- The 6-story structures required less reserve strength to demonstrate acceptable collapse prevention performance than the 3-story structures because of their inherent flexibility.
- The rotation demand of the braced frame connections in this study was large enough to push the connection beyond its ultimate moment capacity and into the descending branch of the connection moment vs. connection rotation behavior. Thus, it appears that the connections in the reserve system need to possess some ductility to allow the reserve system to generate adequate collapse prevention performance. A minimum flexural rotation capacity of 0.03 to

0.04 rad is reasonable based on the results of this study.

- The plastic moment strength of the braced frame beams was found to play a critical role in the developing the reserve system strength. Flexure in the braced frame beam was induced when one of the braces in the first story would fracture, which caused the remaining structure to behave like a long-link EBF. Data summarizing the rotation demand on the beam in the SPO analyses indicated that plastic rotations larger than 0.02 rad may be experienced in the beam as the reserve system strength is developed. Rotations of this magnitude may lead to flexural strength degradation in the braced frame beam, although this phenomenon was not included in the computational models used for this study.
- The reserve system strength can be evaluated for each story in a structure assuming a plastic-hinge collapse mechanism involving the braced frame beam, one of the braced frame connections, and the braced frame columns. One of the braces in the story under consideration is removed to simulate the behavior observed in the static pushover analyses. If desired, the reserve system strength can be quantified with static pushover analyses following the procedure described in Chapter 5.

6.5 ENGINEERING RECOMMENDATIONS

Two analysis/ design procedures were developed during this study. The first was the analysis procedure for beam-column connections with gusset plates outlined in Chapter 4. The procedure quantifies the flexural stiffness and strength of a braced frame connection given the geometry and material properties of the connection elements. The desired limit state is ductile fracture of the steel angles in the connection. All other connection components are capacity designed to insure that the angles fail. Flexural stiffness and strength equations for beam-column

connections with gusset plates were developed and guidelines for capacity design of the connection elements, based on established methods of structural steel design, were assembled.

The second set of design recommendations were derived from the collapse performance evaluation of the case study buildings, which was presented in Chapter 5. Procedures for quantifying the reserve lateral force-resisting strength of chevron configuration CBFs were outlined, and a minimum level of reserve strength necessary to achieve acceptable collapse prevention performance was recommended. It is worth repeating that the procedures should only be used for chevron configuration CBFs. The collapse mechanism identified relies heavily on the existence of one of the braces in a story to achieve an acceptable level of reserve system strength. Braced frame configurations without the natural redundancy of a chevron configuration may not achieve adequate collapse prevention performance even though the recommendations developed in Chapter 5 were followed.

6.6 DIRECTIONS FOR FUTURE RESEARCH

The following research topics were identified for future study during the course of the present investigation.

- Additional beam-column connection tests should be conducted to validate the results from the parametric study conducted in Chapter 4. Future tests will also provide more data for calibrating the damage initiation criteria for ductile angle fracture. In addition, further testing is needed to quantify the rotation capacity of connections with deeper beams.
- It is also desirable to test connections with a composite concrete slab and connections with a gusset plate that has been distorted by brace buckling.

- To extend the results from the connection finite element simulations to include comprehensive stiffness and strength degradation, the finite element models should be refined to include damage propagation. Recent advances in constitutive models for damage of steel may be implemented for this refinement.
- Collapse performance evaluations of other bracing configurations need to be conducted. As was mentioned previously, the recommendations for the minimum strength of a reserve capacity system should only be used for chevron configuration CBFs. In addition, it is desirable to include other sources of reserve capacity, e.g. flexural strength of gravity connections and/or column base connections, in the analyses.
- The procedures developed for quantifying the strength of reserve lateral force-resisting systems need to be refined to indicate when the plastic moment strength of the braced frame columns should be included in the strength calculations. In addition, the rotational capacity of braced frame beam-column connections needs to be investigated so inclusion of their moment strength in a plastic analysis of collapse can be justified quantitatively.
- Since failure of the welded connection between brace and gusset plate plays such a prominent role in the collapse performance, wider variations in connection strengths should be considered. In the present study, the weld strength was treated as deterministic, but in reality it is highly variable. Refining the system models to include a probabilistic distribution of welded connection strengths would add credence to the argument for allowing these connections to fracture.
- Consideration of varying weld strength in the brace-to-gusset plate connection raises the issue of brace buckling and its influence on the performance of reserve capacity systems. If the weld strength is increased sufficiently, brace buckling would occur, not fracture of the

connection as was assumed in the present study. This behavior, and associated brace strength degradation, should be included in future computational models. Another braced frame behavior that should be examined in future studies is the possibility of braces that fracture their connections in compression and then bear upon the gusset plate, thus allowing the brace to become active in compression, but not in tension.

- Validation of the present, and future work, should be accomplished through large-scale testing. The interaction between the braces, beam, columns, and connections is highly complex. Subassembly testing has proven useful for quantifying the behavior of isolated elements, but the interaction of the braces, beams, columns, and connections can only be accurately observed through large-scale simulations.

REFERENCES

Abolmaali, A., Kukreti, A.R., and Razavi, H. (2003). "Hysteresis behavior of semi-rigid double web angle steel connections." *J. Const. Steel Res.*, 59, 1057-1082.

American Institute of Steel Construction. (1997). *Seismic Provisions for Structural Steel Buildings*, Chicago, Illinois,

American Institute of Steel Construction. (2005a). *Seismic Provisions for Structural Steel Buildings*, ANSI/AISC 341-05, Chicago, Illinois, 330 pp.

American Institute of Steel Construction. (2005b). *Specification for Structural Steel Buildings*, ANSI/AISC 360-05, Chicago, Illinois, 256 pp.

American Institute of Steel Construction. (2005c). *Steel Construction Manual*, Chicago, Illinois.

American Society of Civil Engineers (2010). *Minimum Design Loads for Buildings and Other Structures*, ASCE 7-10, Reston, Virginia.

American Society of Civil Engineers (2002). *Minimum Design Loads for Buildings and Other Structures*, ASCE 7-02, Reston, Virginia.

Anderson, T.L. (2004). *Fracture Mechanics: Fundamentals and Applications, 3rd Ed*. CRC Press, Boca Raton, Florida.

Appel, M.E. (2008). *Design and Performance of Low-Ductility Chevron Braced Frames under Moderate Seismic Demands*, Masters Thesis, Department of Civil and Environmental Engineering, Tufts University, Medford, Massachusetts.

Applied Technology Council. (1978). *Tentative Recommended Provisions for the Development of Seismic Regulations for Buildings*, ATC 3-06, Redwood City, California.

Ariyaratana, C. (2009). *Performance Assessment of Buckling-Restrained Braced Frame Dual Systems*, Masters Thesis, Department of Civil and Environmental Engineering, University of Illinois, Urbana, Illinois.

Astaneh, A., Nader, M.N., and Malik, L. (1989). "Cyclic behavior of double angle connections." *J. Struct. Eng.*, 115(5), 1101-1118.

ASTM International. (2009). *ASTM A 370 – 09a: Standard Test Methods and Definitions for Mechanical Testing of Steel Products.* West Conshohocken, PA.

Azizinamini, A. and Radziminski, J.B. (1989). "Static and cyclic performance of semirigid steel beam-to-column connections." *J. Struct. Eng*., 115(12), 2979-2999.

Bertero, V.V., Anderson, J.C., and Krawinkler, H. (1994). “Performance of steel building structures during the Northridge earthquake.” UCB/PEER-1994/09, University of California, Berkeley, California.

Bertero, V.V., Uang, C.M., Llopiz, C.R., and Igarashi, K. (1989). “Earthquake simulator testing of concentric braced dual system.” *J. Struct. Eng.*, 115(8), 1877-1894.

Blume, J.A., Newmark, N.M., and Corning, L.H. (1961). *Design of Multistory Reinforced Concrete Buildings for Earthquake Motions*, published by the Portland Cement Association, Chicago, Illinois.

Callister, J.T. and Pekelnicky, R.G. (2011). “Seismic evaluation of an existing low ductility braced frame building in California,” *Proceedings, ASCE Structures Congress 2011*, Las Vegas, Nevada.

Carter, C.J. (2009). *Connections and Collapse Resistance in R = 3 Braced Frames*, Doctoral Dissertation, Department of Civil and Environmental Engineering, Illinois Institute of Technology, Chicago, Illinois.

Cheever, P.J. and Hines, E.M. (2009). “Building design for moderate seismic regions.” *Proceedings, ASCE Structures Congress*, Austin, Texas.

Crocker, J.P. and Chambers, J.J. (2004). “Single plate shear connection response to rotation demands imposed by frames undergoing cyclic lateral displacements.” *J. Struct. Eng*. 130(6), 934-941.

Federal Emergency Management Agency. (1997). *Recommended Provisions for Seismic Regulations for New Buildings and Other Structures*, FEMA 302, prepared by the SAC Joint Venture, 335 pp.

Federal Emergency Management Agency. (2000a). *Recommended Seismic Design Criteria for new Steel Moment-Frame Buildings*, FEMA 350, prepared by the SAC Joint Venture, July, 342 pp.

Federal Emergency Management Agency (2000b). *State of the Art Report on Systems Performance of Steel Moment Frames subject to Earthquake Ground Shaking*, FEMA 355C, prepared by the SAC Joint Venture.

Federal Emergency Management Agency. (2009). *Quantification of Building Seismic Performance Factors*, FEMA P695, prepared by the Applied Technology Council, June, 421 pp.

Foutch, D.A., Goel, S.C., and Roeder, C.W. (1987). “Seismic testing of full-scale steel building – Part I.” *J. Struct. Eng.*, 113(11), 2111-2129.

Ghosh, S.K. (1994). "Code implications of the Northridge earthquake of January 17, 1994." *Proceedings, 6th U.S. - Japan Workshop on the Improvement of Building Structural Design and Construction Practices,* ATC 15-5, prepared by the Applied Technology Council, August.

Gross, J. and Cheok, G. (1988). *Experimental Study of Gusseted Connections for Laterally Braced Steel Buildings,* National Institute of Science and Technology, Gaithersburg, Maryland.

Hines, E.M., Appel, M.E., and Cheever, P.J. (2009). "Collapse performance of low-ductility chevron braced steel frames in moderate seismic regions." *AISC Eng. J.,* 3rd quarter, 149-180.

Hines, E.M. and Fahnestock, L.A. (2010). "Design philosophy for steel structures in moderate seismic regions." *Proceedings, 9th US National and 10th Canadian Conference on Earthquake Engineering,* July 25-29.

International Code Council. (2009). *International Building Code*, Country Club Hills, Illinois, 668 pp.

Kanvinde, A.M. and Deierlein, G.G. (2007). "Cyclic void growth model to assess ductile fracture initiation in structural steels due to ultra low cycle fatigue." *J. Eng. Mech.,* 133(6), 701-712.

Kauffman, E.J. and Pense, A.W. (1999). *Characterization of Cyclic Inelastic Strain Behavior on Properties of A572 Gr. 50 and A913 Rolled Sections,* AISC-PITA Project Progress Report, ATLSS Research Center, Lehigh University, Bethlehem, Pennsylvania.

Kishiki, S., Yamada, S., and Wade, A. (2008). "Experimental evaluation of structural behavior of gusset plate connections in BRB frame system." *Proceedings, 14th World Conference on Earthquake Engineering*, October 12-17.

Kukreti, A.R. and Abolmaali, A.S. (1999). "Moment-rotation hysteresis behavior of top and seat angle steel frame connections." *J. Struct. Eng.*, 125(8), 810-820.

Kulak, G.L., Fisher, J.W., and Struik, J.H.A. (2001). *Guide to Design Criteria for Bolted and Riveted Joints, 2nd Ed.* American Institute of Steel Construction, Chicago, IL.

Lamarche, C.P. and Tremblay, R. (2008). "Accounting for residual stresses in the seismic stability of nonlinear beam-column elements with cross-section fiber discretization." *Proceedings, 2008 SSRC Annual Stability Conference*, Structural Stability Research Council, April 2-5.

Lee, C.H., Jung, J.H., Oh, M.H., and Koo, E.S. (2003). "Cyclic seismic testing of steel moment connections reinforced with welded straight haunch." *Eng. Struct.*, 25(14), 1743-1753.

Lesik, D.F. and Kennedy, D.J.L. (1990). “Ultimate strength of fillet welded connections loaded in plane.” *Can. J. Civ. Eng.*, 17, 55-67.

Liu, J., and Astaneh-Asl, A. (2000). “Cyclic testing of simple connections including effects of slab.” *J. Struct. Eng.*, 126(1), 32-39.

Liu, J., and Astaneh-Asl, A. (2004). “Moment-rotation parameters for composite shear tab connections.” *J. Struct. Eng.*, 130(9), 1371-1380.

Lubliner, J. (2008). *Plasticity Theory.* Dover, Mineola, New York.

Mazzoni, S., McKenna, F., Scott, M.H., and Fenves, G.L. (2009). *Open System for Earthquake Engineering Simulation User Command-Language Manual*. Pacific Earthquake Engineering Research Center, University of California, Berkeley, California.

Nelson, T., Gryniuk, M.C., and Hines E.M. (2006). “Comparison of low-ductility moment resisting frames and chevron braced frames under moderate seismic demands.” *Proceedings, 8th US National Conference on Earthquake Engineering*, April 18-22.

Rai D.C. and Goel S.C. (2003). “Seismic evaluation and upgrading of chevron braced frames.” *J. Const. St. Res.*, 59(8), 971-994.

Richard, J.M. (1986). “Analysis of large bracing connection designs for heavy construction.” *Proceedings, 1986 National Engineering Conference*, June.

Rojahn, C. (1995). *Structural Response Modification Factors*, ATC 19, Redwood City, California.

Ross, A.E. and Mahin, S.H. (1994). “Steel moment resisting frames and the Northridge earthquake.” *Proceedings, 6th U.S. - Japan Workshop on the Improvement of Building Structural Design and Construction Practices,* ATC 15-5, prepared by the Applied Technology Council, August.

Salmon, C.G., Johnson, J.E., and Malhas, F.A. (2009). *Steel Structures: Design and Behavior, 5th Ed.*, Pearson, Upper Saddle River, New Jersey.

Simulia (2011). *Abaqus FEA*, www.simulia.com.

Sorabella, S. (2006). *Ground Motion Selection for Boston, Massachusetts*, Masters Thesis, Department of Civil and Environmental Engineering, Tufts University, Medford, Massachusetts.

Structural Engineers Association of California. (1959). *Recommended Lateral Force Requirements and Commentary*, Sacramento, California.

Thornton, W.A. (1991). “On the analysis and design of bracing connections.” *Proceedings, 1991 National Engineering Conference*, June.

Tremblay, R. and Stiemer, S.F. (1994). “Back-up stiffness for improving the stability of multi-storey braced frames under seismic loading.” *Proceedings, Structural Stability Research Council Technical Sessions*, June 20.

Tremblay, R., Timler, P., Bruneau, M., and Filiatrault, A. (1995). “Performance of steel structures during the 1994 Northridge earthquake.” *Can. J. Civ. Eng.*, 22(2), 338-360.

United States Geological Survey. (2010). *Earthquake Hazards Program*, www.usgs.gov.

Uriz, P. and Mahin, S.A. (2008). “Toward earthquake-resistant design of concentrically braced steel frame structures.” UCB/PEER-2008/08, University of California, Berkeley, California.

Vamvatsikos, D. and Cornell, C.A. (2002). “Incremental dynamic analysis.” *Earthquake Eng. Struct. Dyn.*, 31(3), 491-514.

Whittaker, A.S., Uang, C.M., and Bertero, V.V. (1989). “Experimental behavior of dual steel system.” *J. Struct. Eng.*, 115(1), 183-200.

Youssef, N.F.G., Bonowitz, D., and Gross, J.L. (1995). *A Survey of Steel Moment-Resisting Frame Buildings Affected by the 1994 Northridge Earthquake*, NISTIR 5625, National Institute of Science and Technology, Gaithersburg, Maryland.

APPENDIX A

CASE STUDY BUILDING IDA CURVES

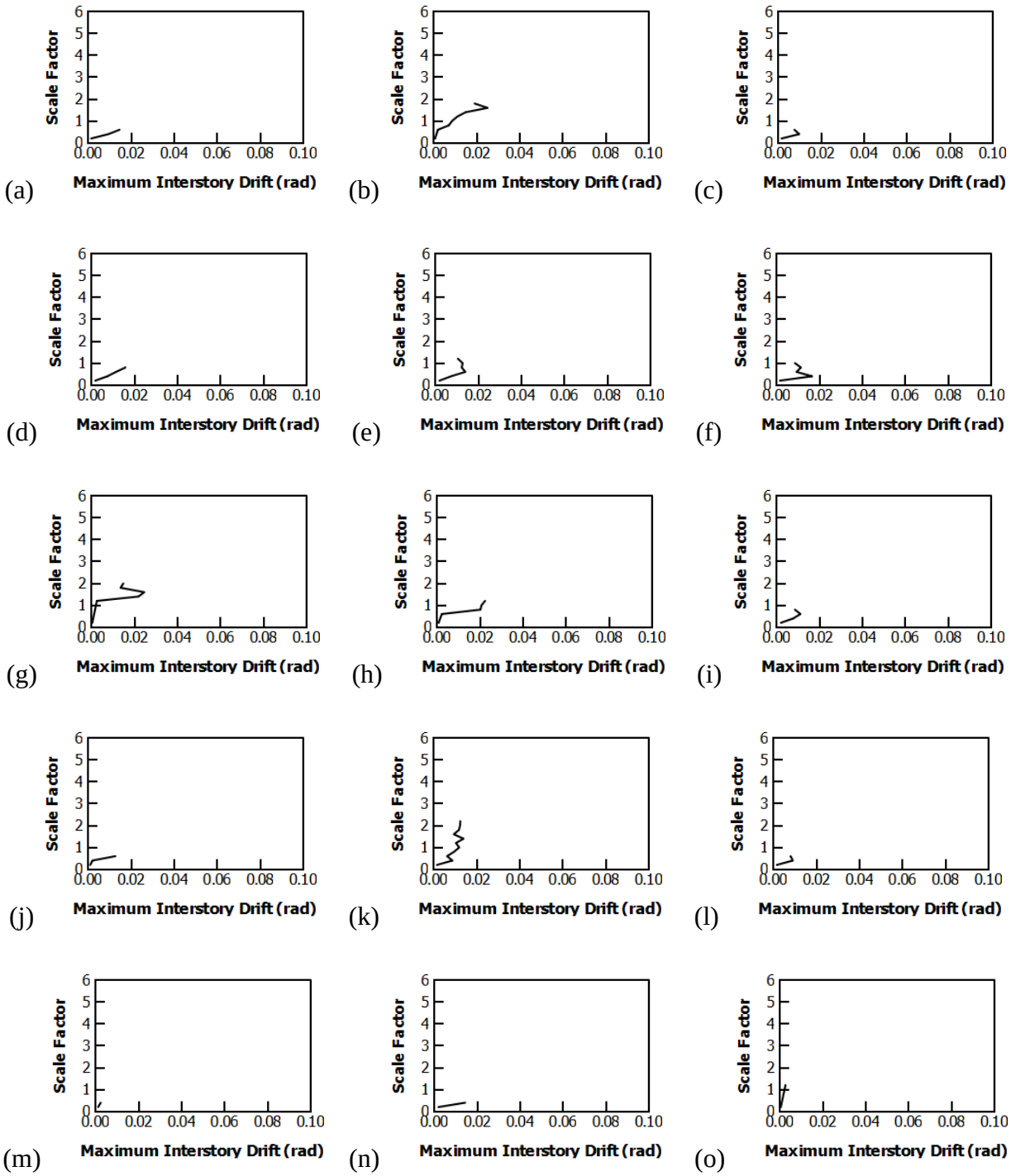

Figure A.1 IDA curves for 3storyR3w14a000: (a) gm1 – (o) gm15.

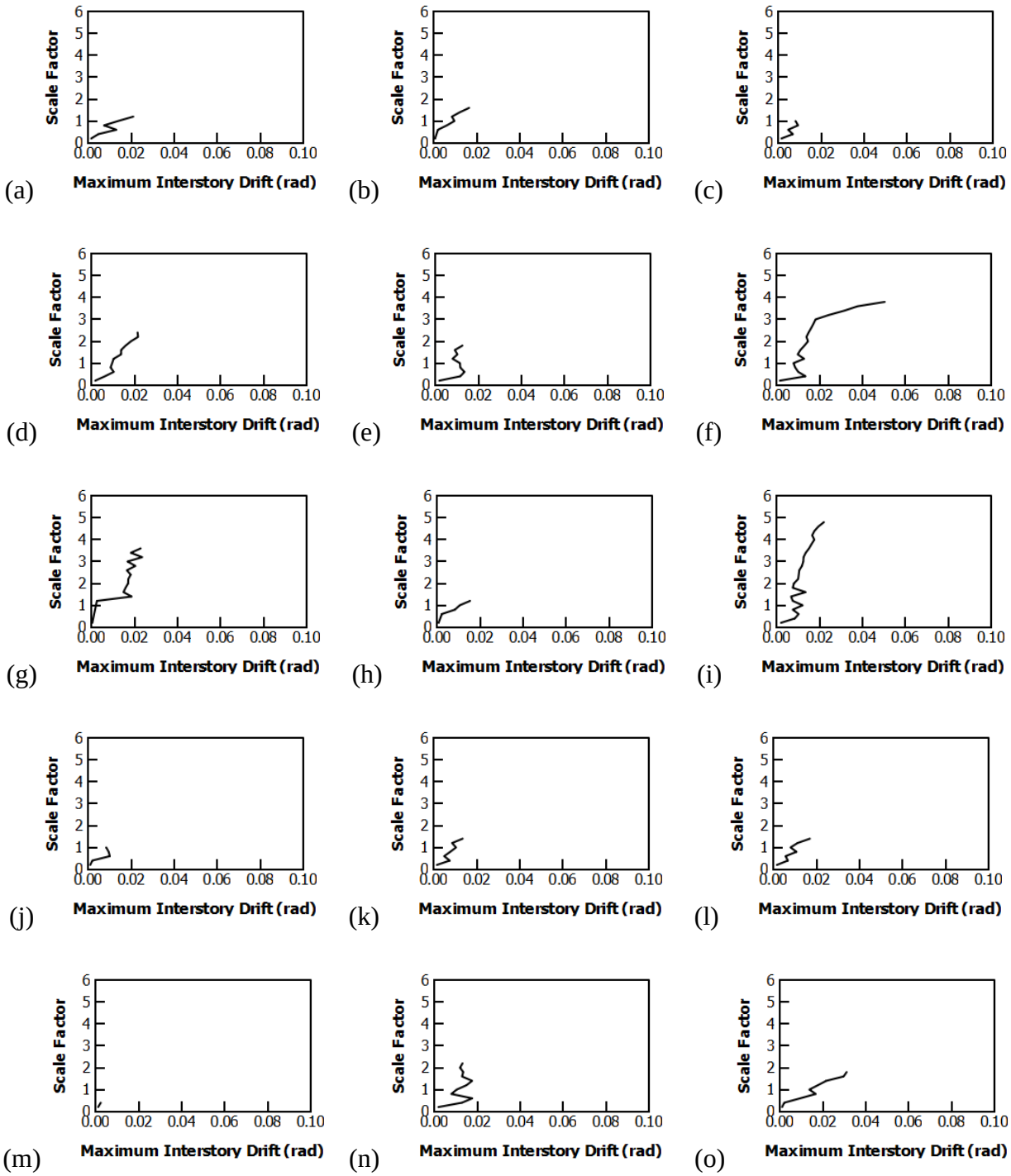

Figure A.2 IDA curves for 3storyR3w14a375: (a) gm1 – (o) gm15.

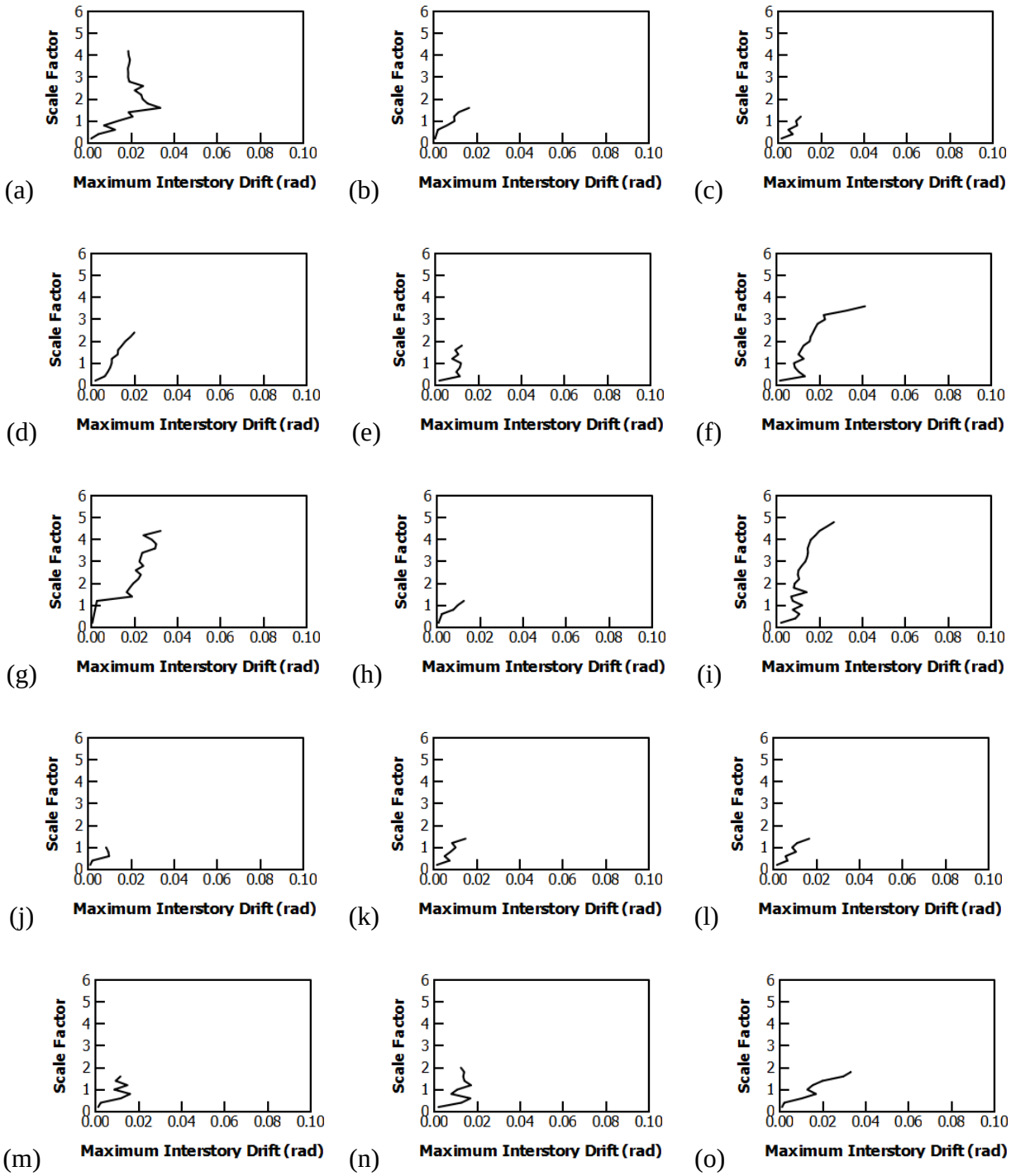

Figure A.3 IDA curves for 3storyR3w14a500: (a) gm1 – (o) gm15.

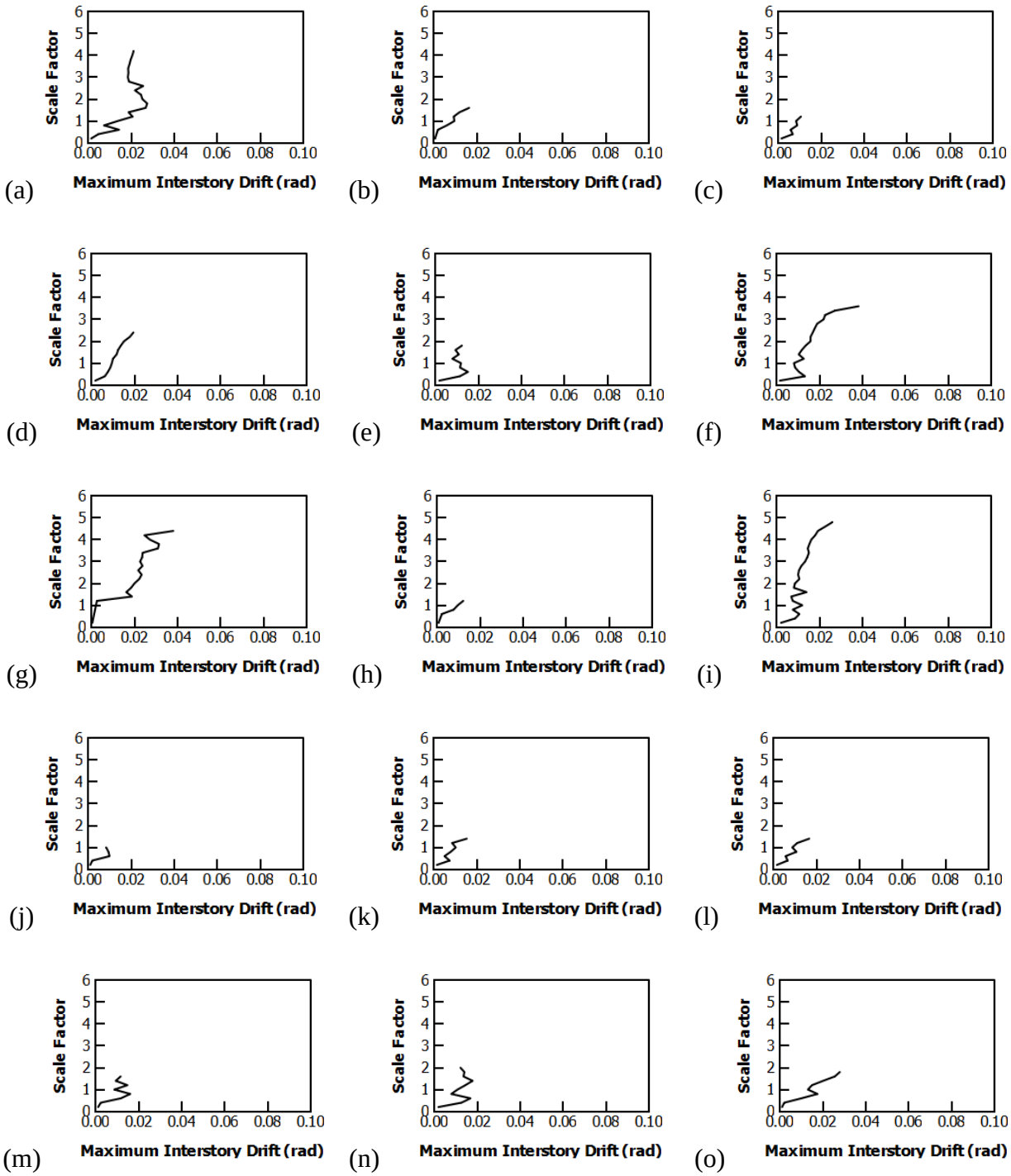

Figure A.4 IDA curves for 3storyR3w14a625: (a) gm1 – (o) gm15.

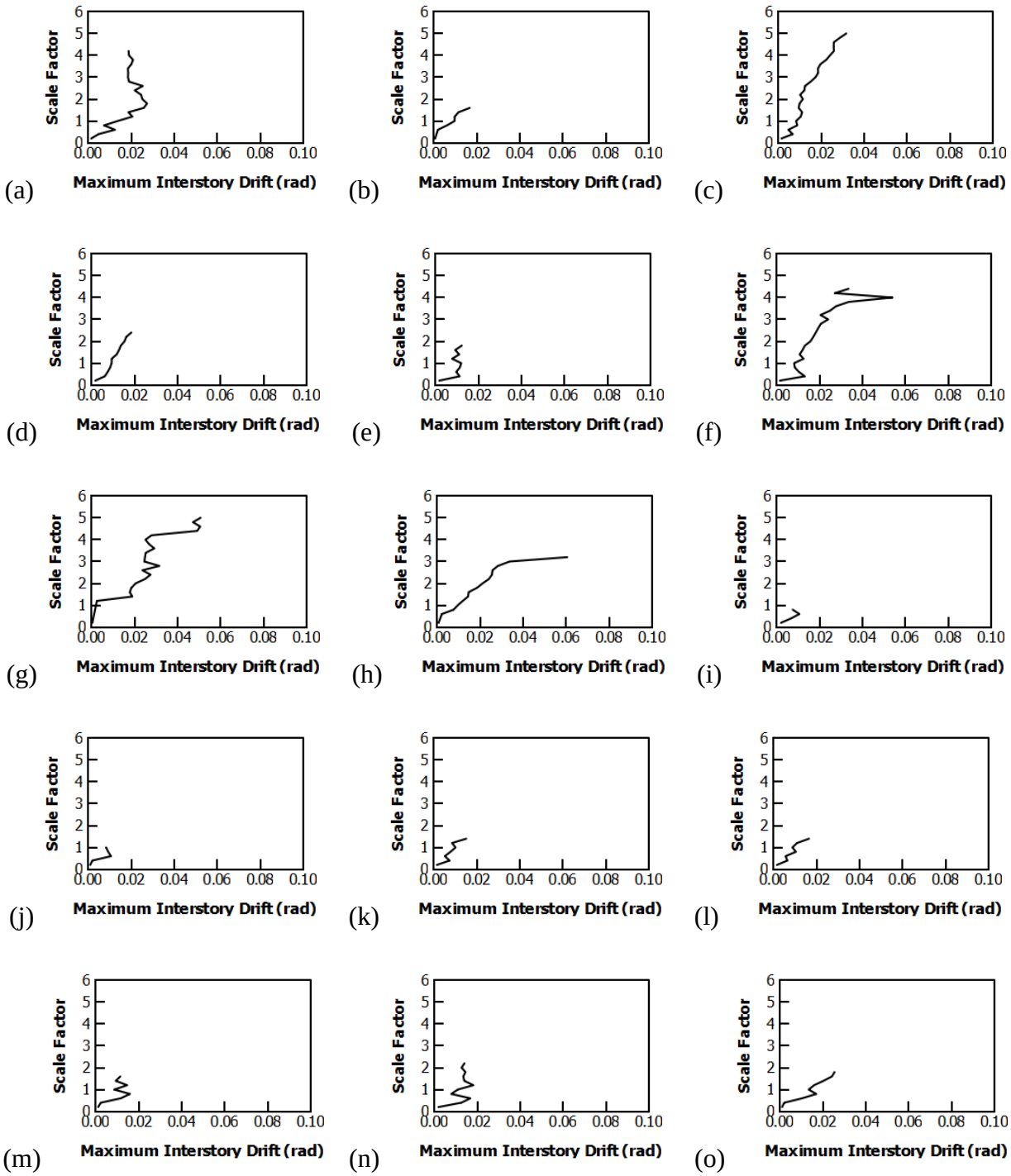

Figure A.5 IDA curves for 3storyR3w14a750: (a) gm1 – (o) gm15.

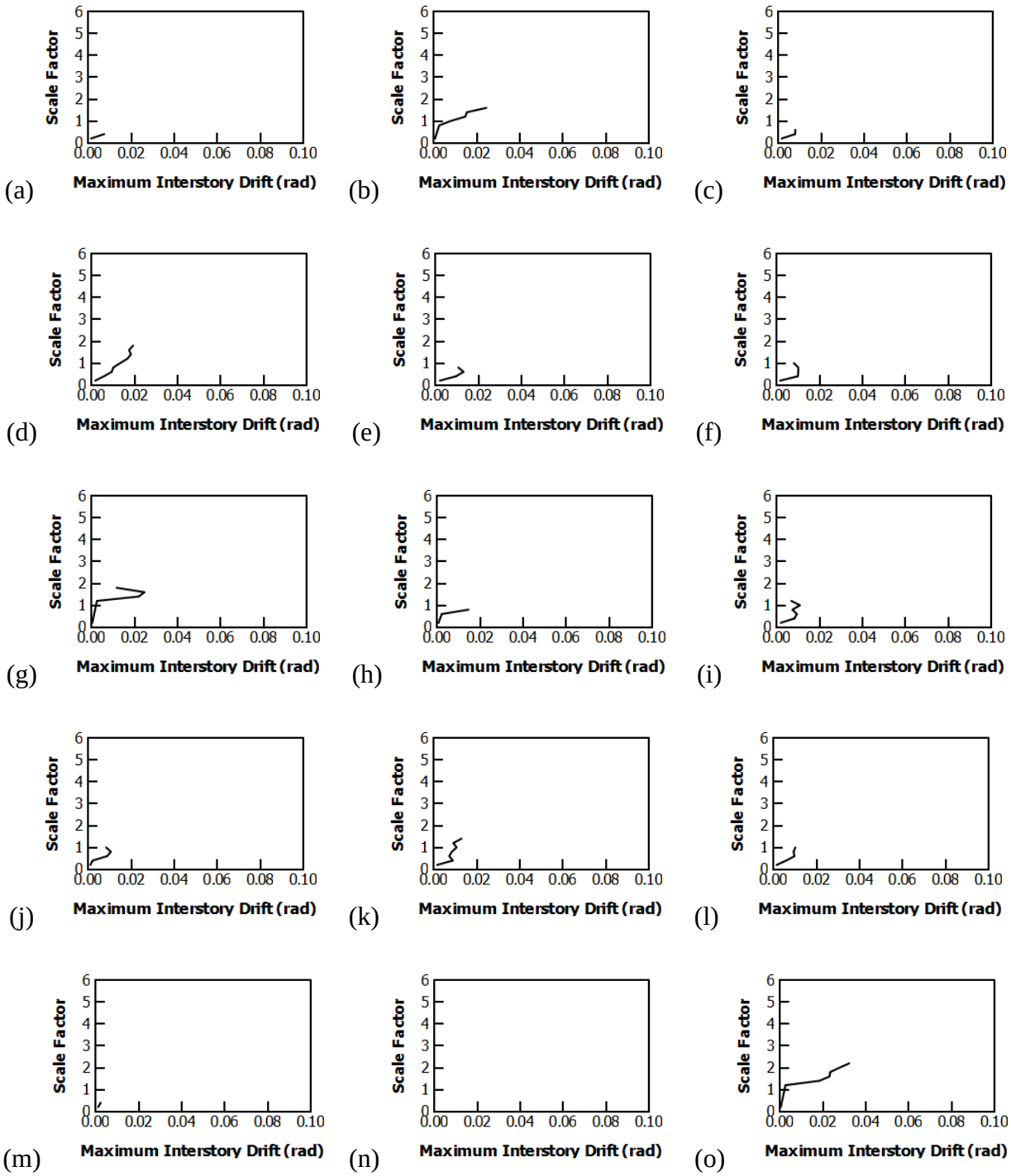

Figure A.6 IDA curves for 3storyR3w18a000: (a) gm1 – (o) gm15.

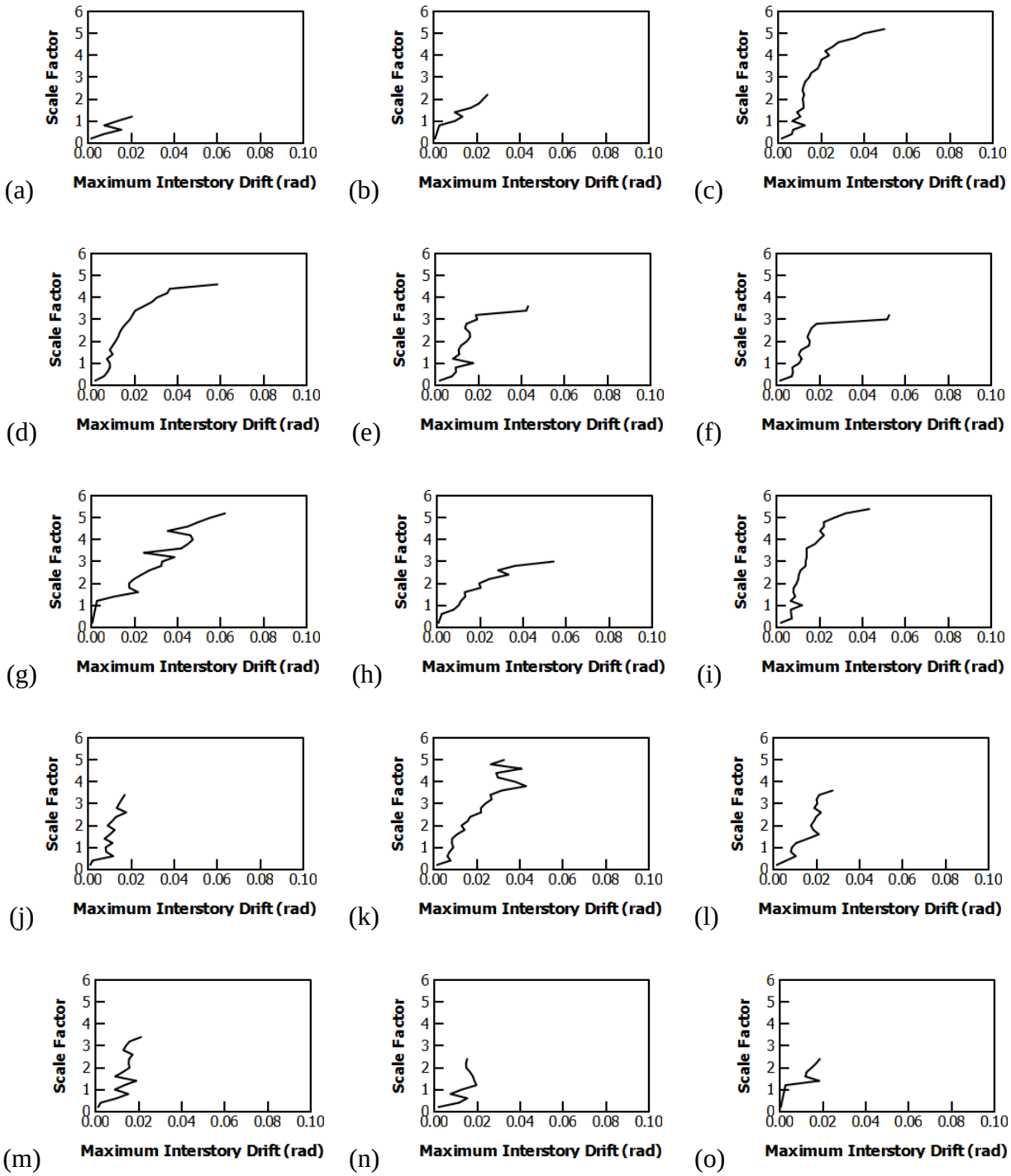

Figure A.7 IDA curves for 3storyR3w18a375: (a) gm1 – (o) gm15.

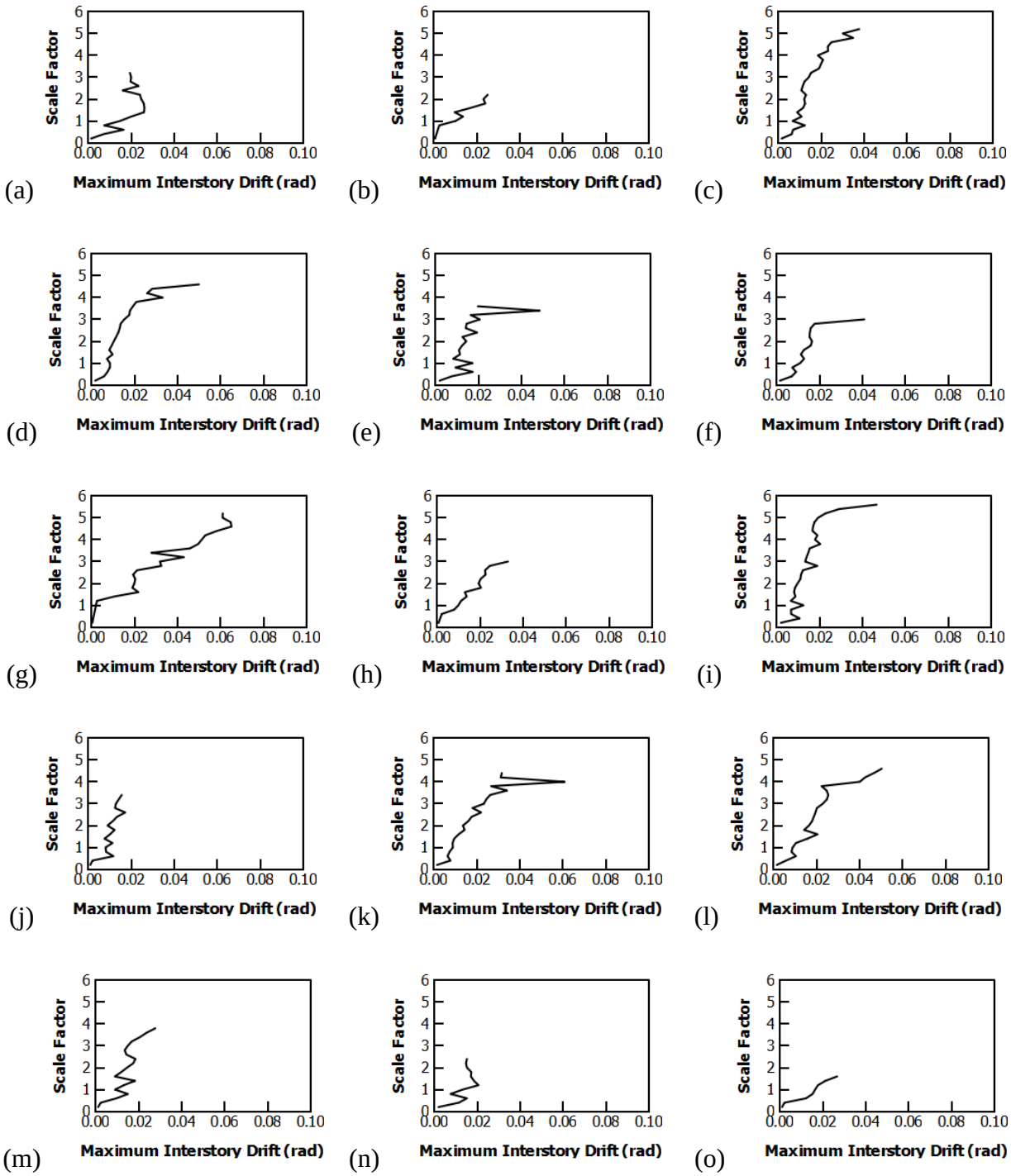

Figure A.8 IDA curves for 3storyR3w18a500: (a) gm1 – (o) gm15.

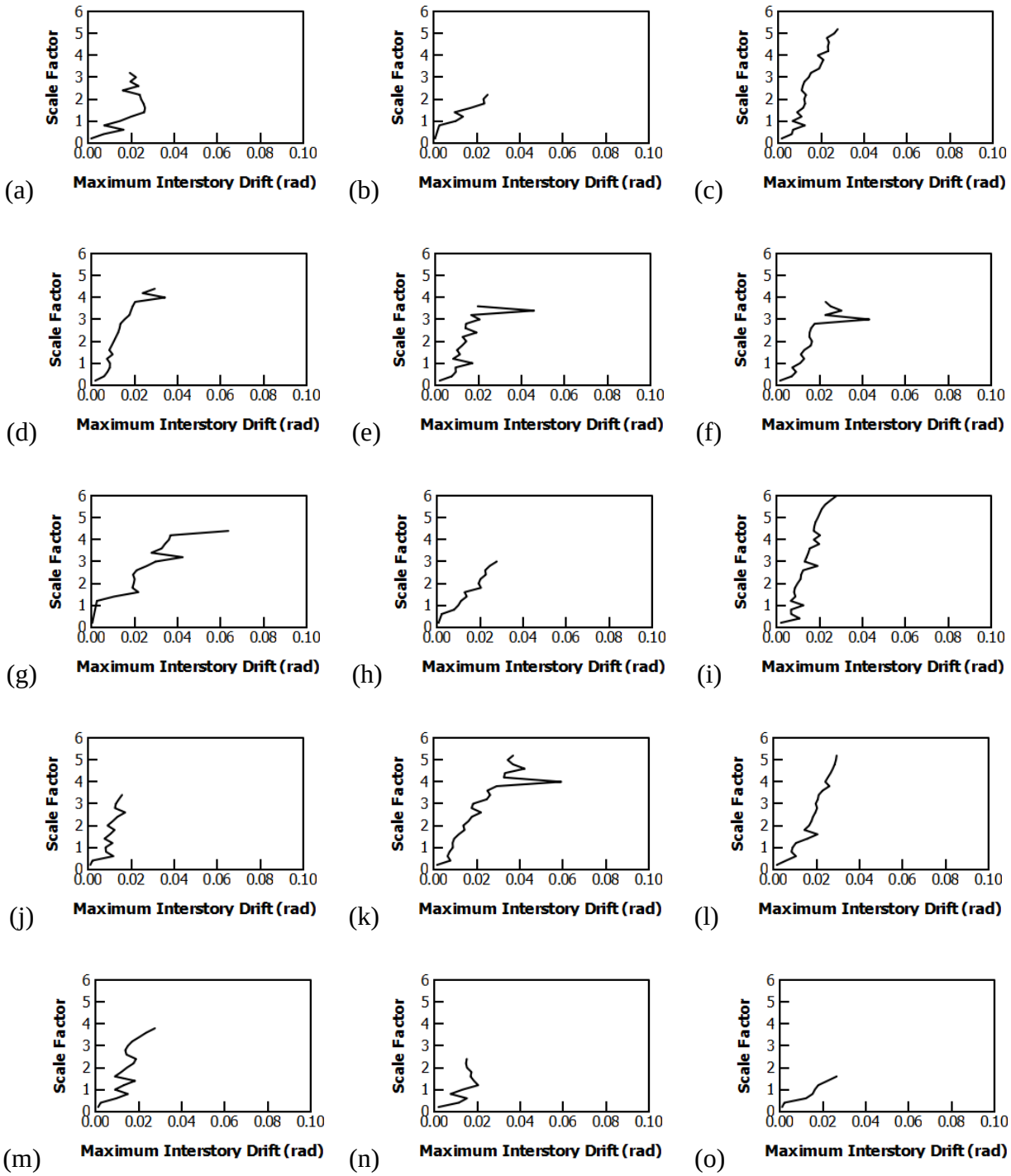

Figure A.9 IDA curves for 3storyR3w18a625: (a) gm1 – (o) gm15.

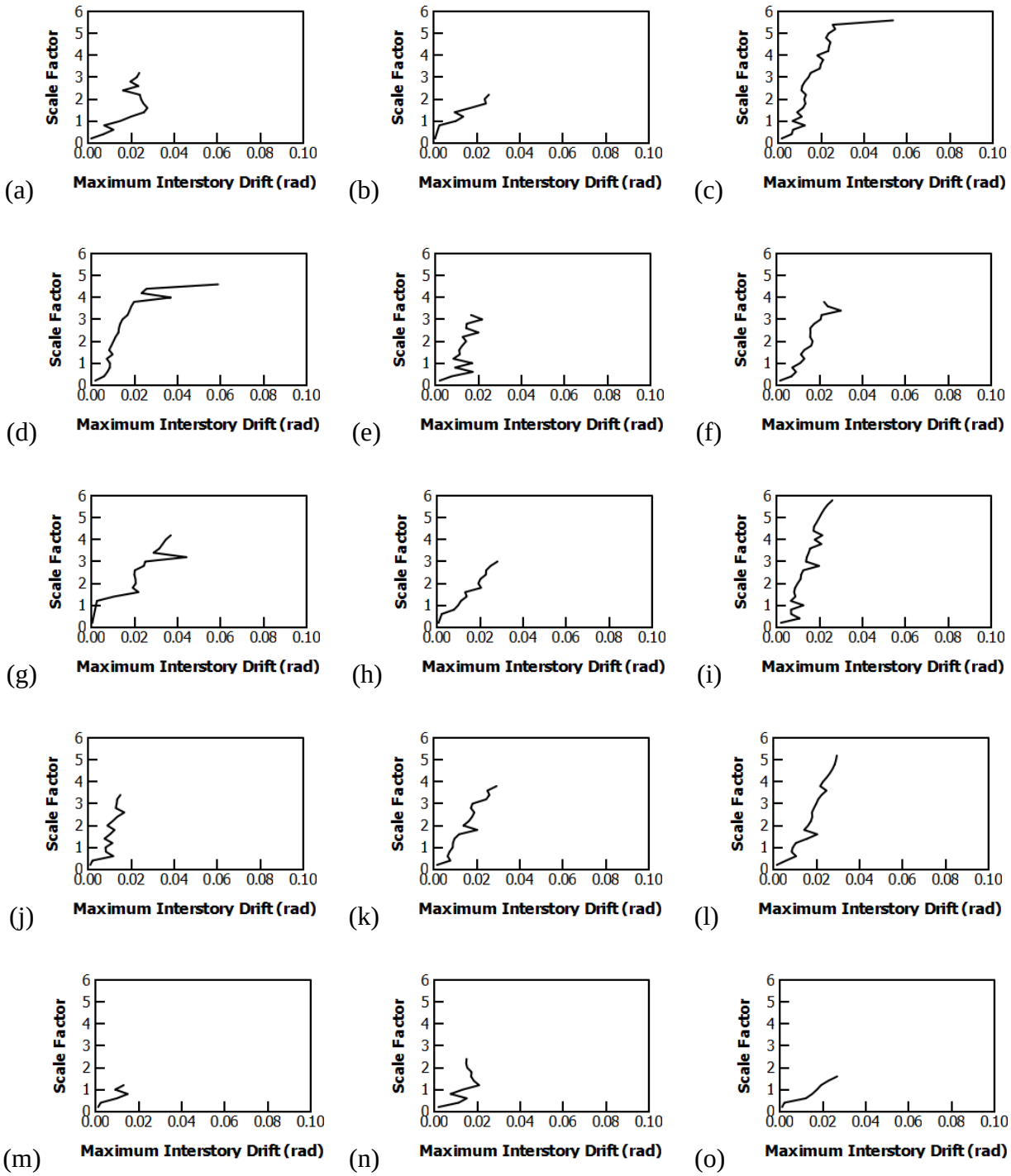

Figure A.10 IDA curves for 3storyR3w18a750: (a) gm1 – (o) gm15.

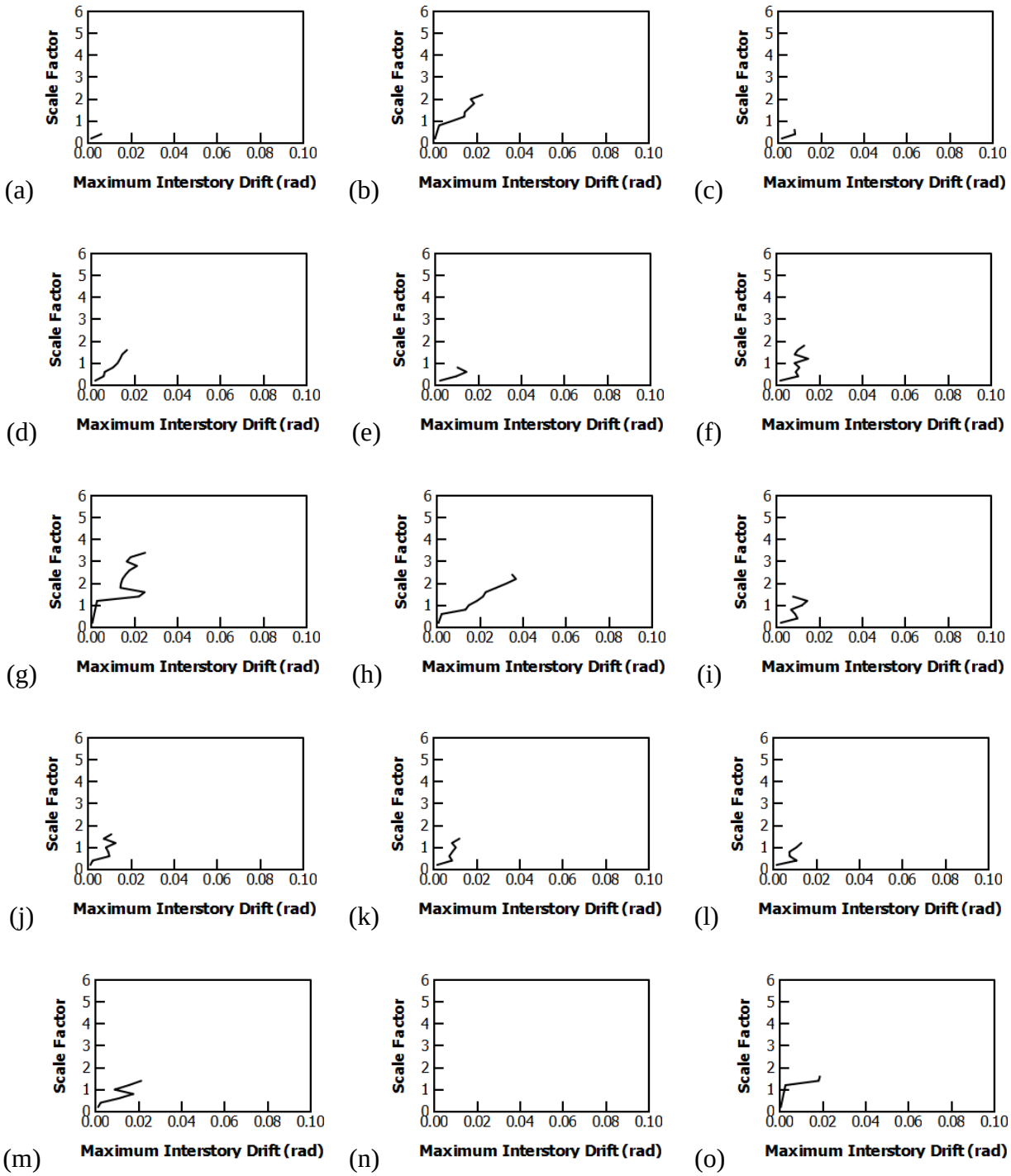

Figure A.11 IDA curves for 3storyR3w21a000: (a) gm1 – (o) gm15.

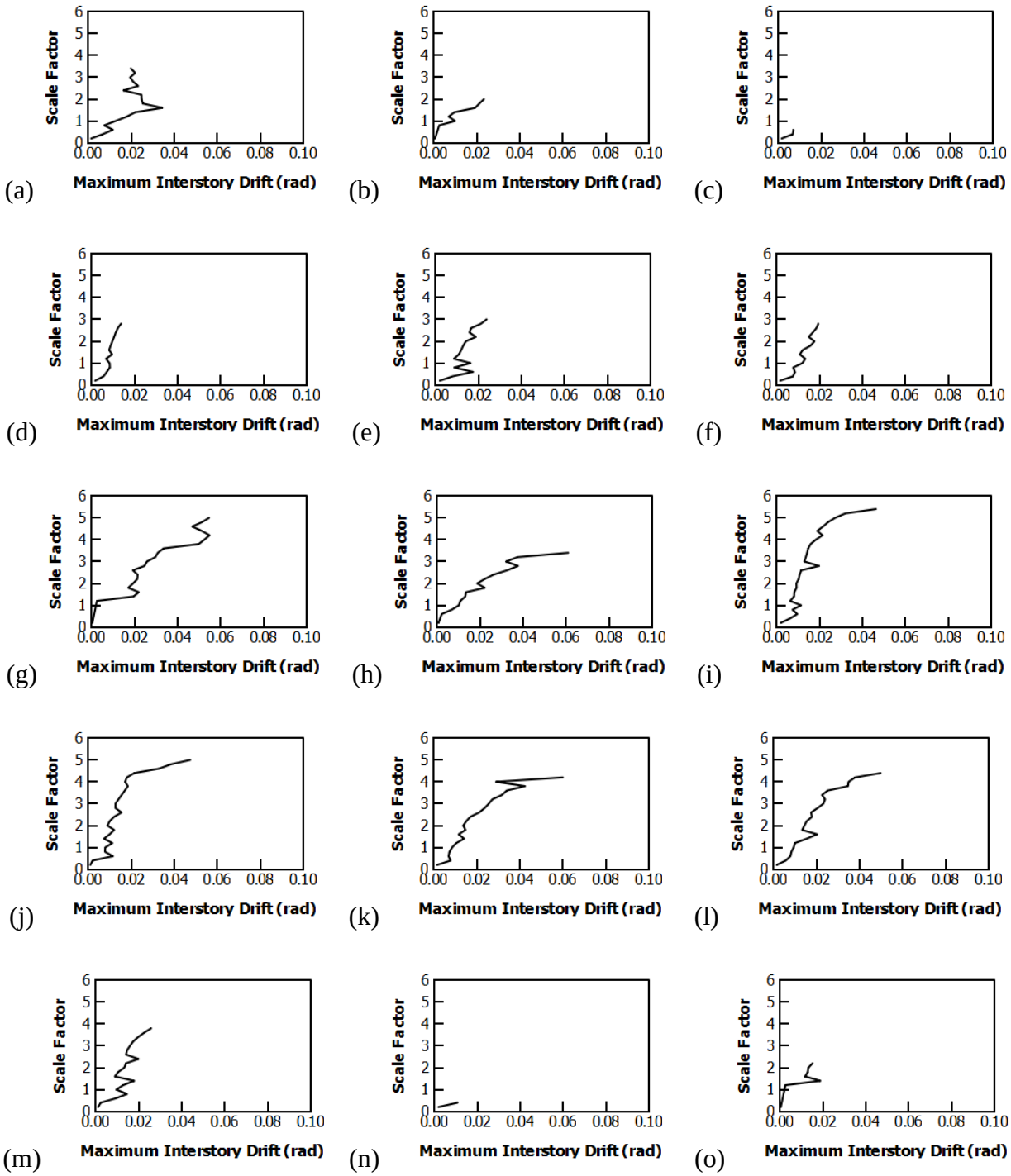

Figure A.12 IDA curves for 3storyR3w21a375: (a) gm1 – (o) gm15.

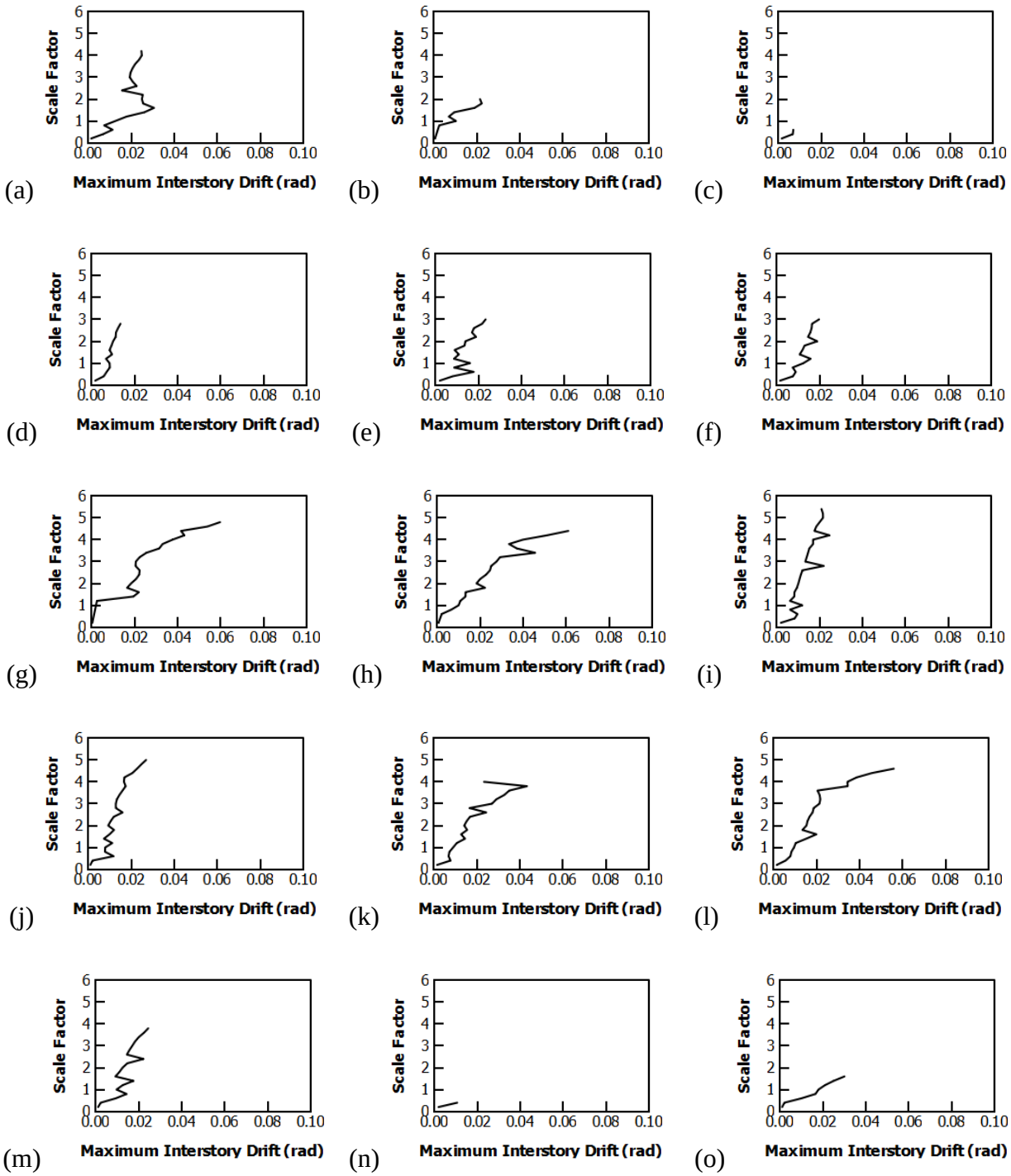

Figure A.13 IDA curves for 3storyR3w21a500: (a) gm1 – (o) gm15.

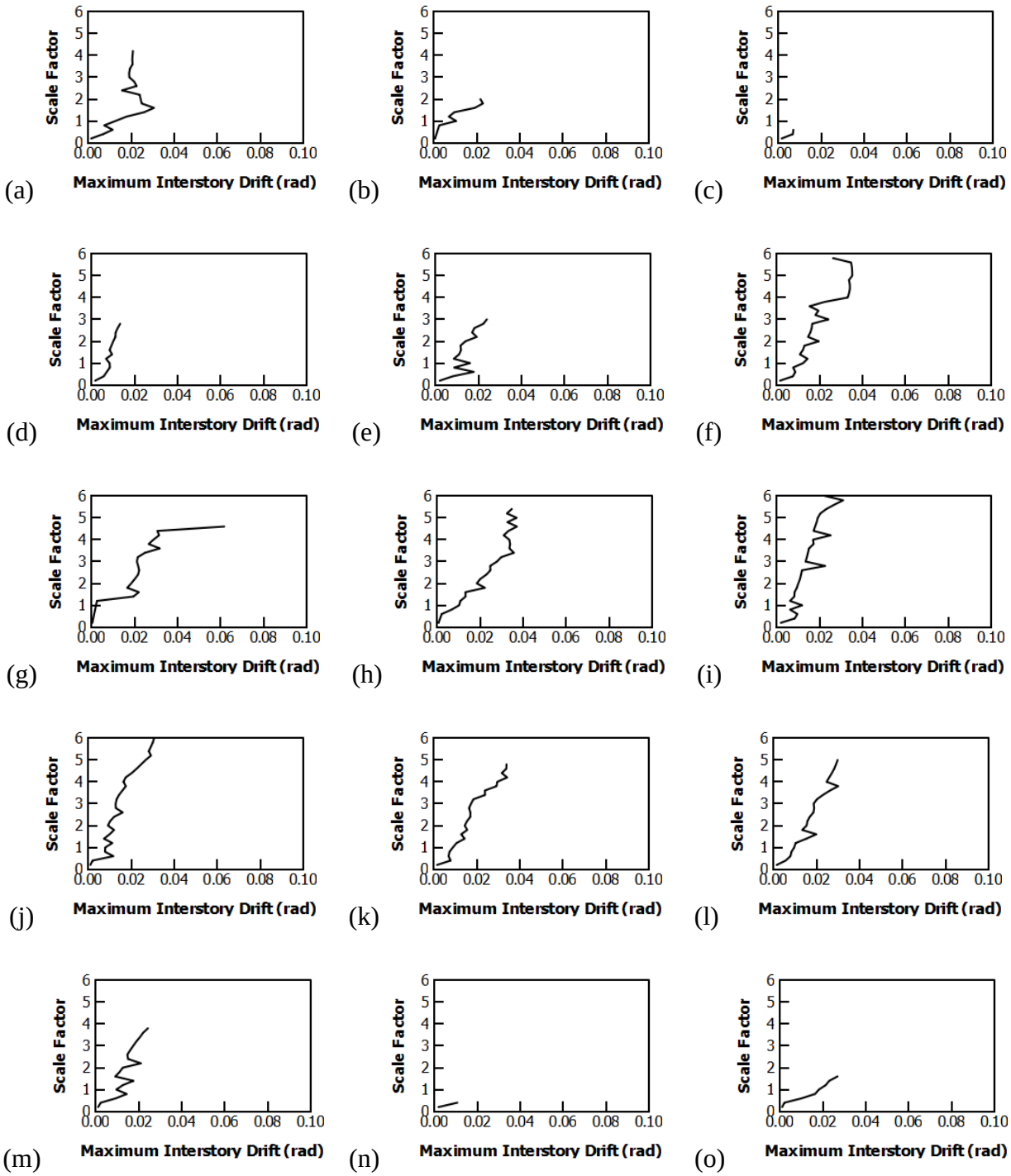

Figure A.14 IDA curves for 3storyR3w21a625: (a) gm1 – (o) gm15.

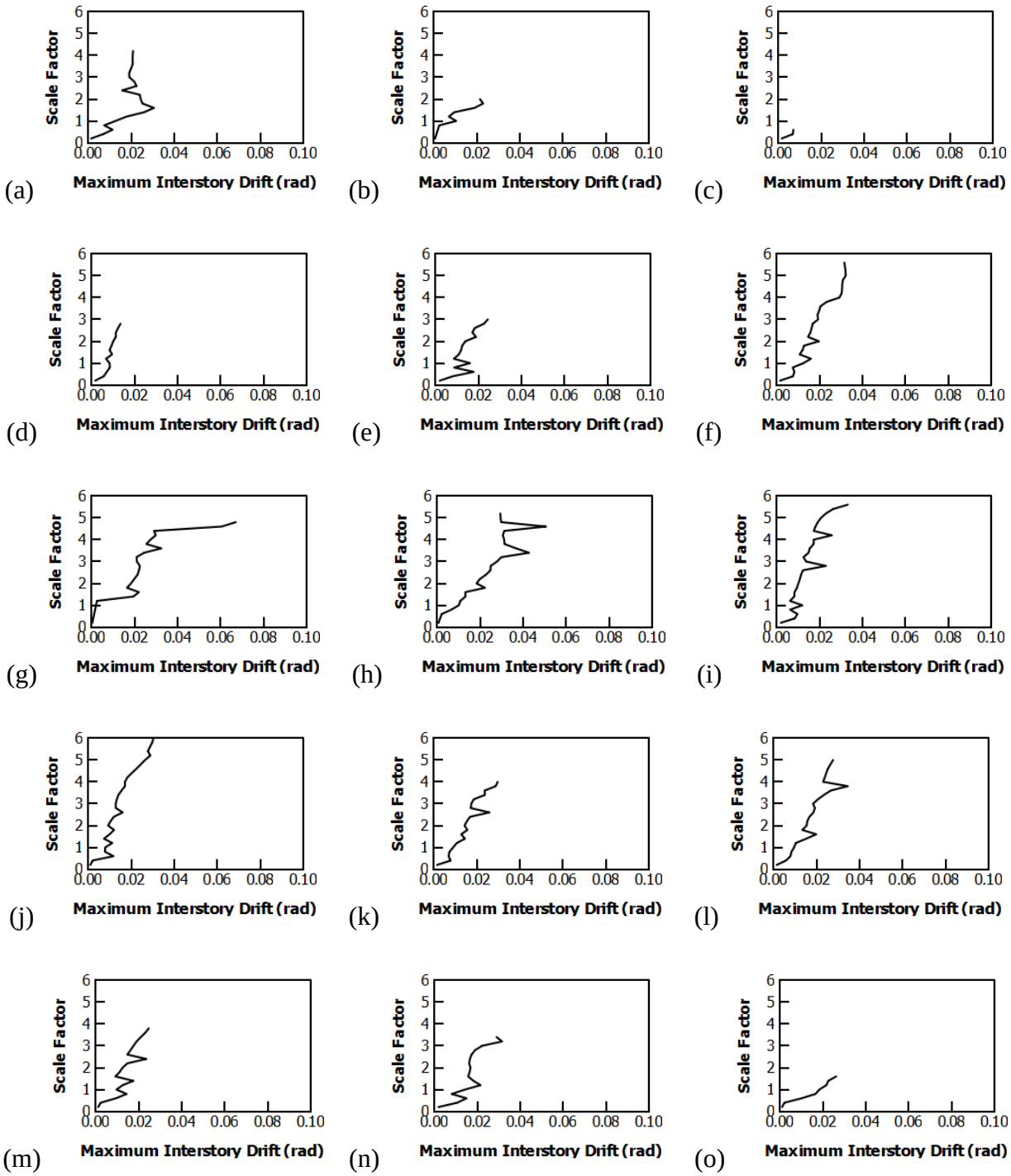

Figure A.15 IDA curves for 3storyR3w21a750: (a) gm1 – (o) gm15.

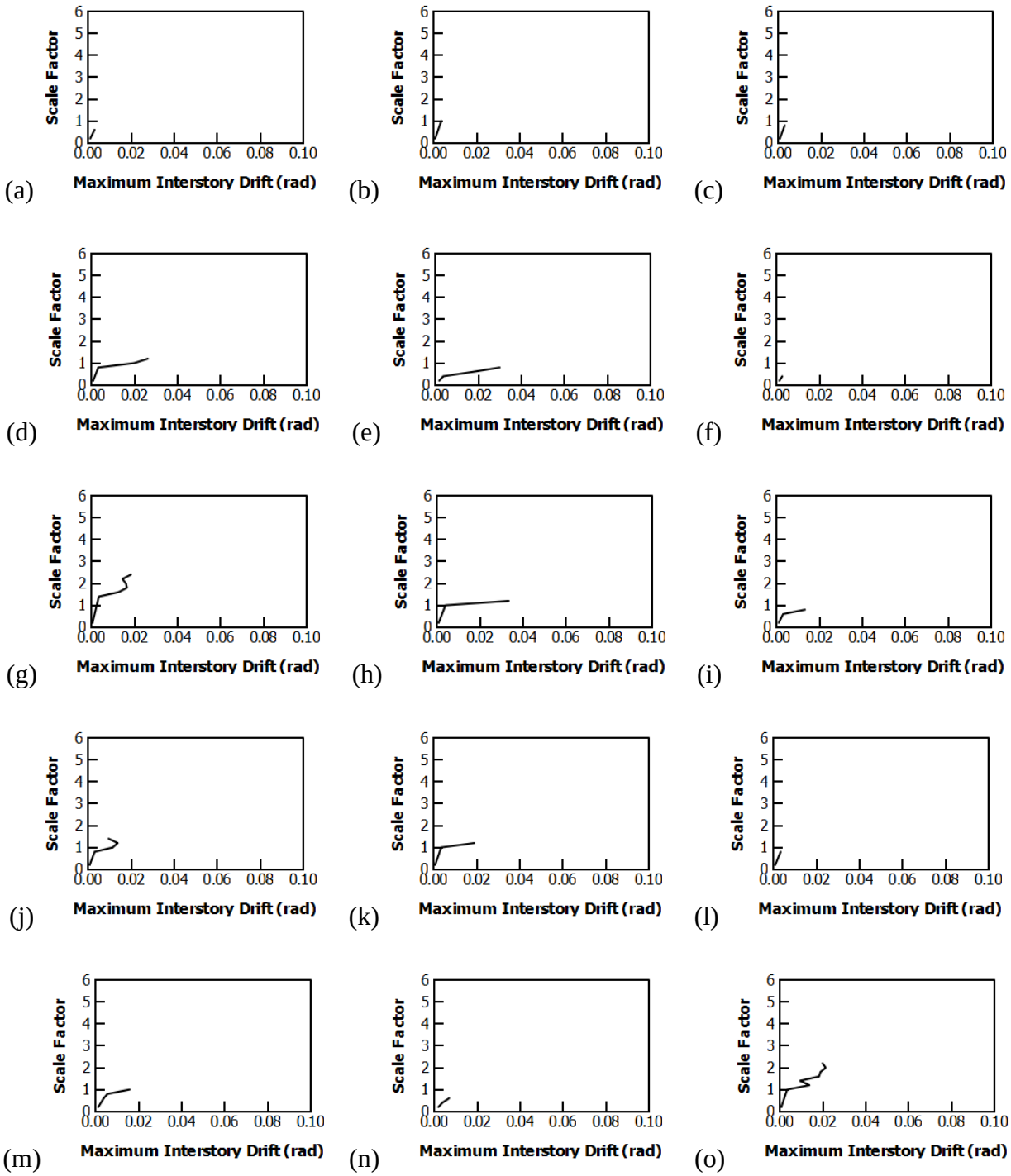

Figure A.16 IDA curves for 6storyR3w14a000: (a) gm1 – (o) gm15.

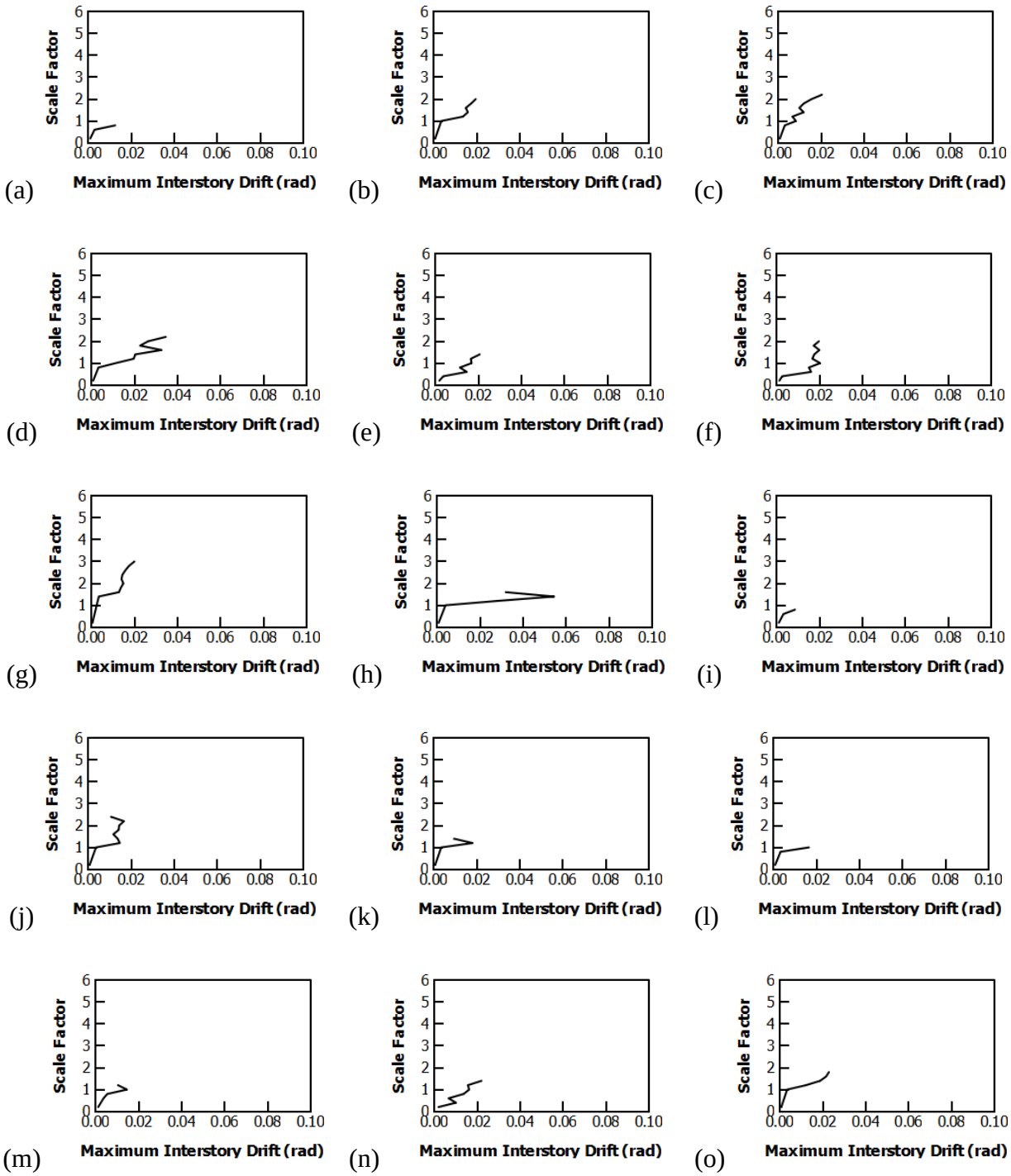

Figure A.17 IDA curves for 6storyR3w14a375: (a) gm1 – (o) gm15.

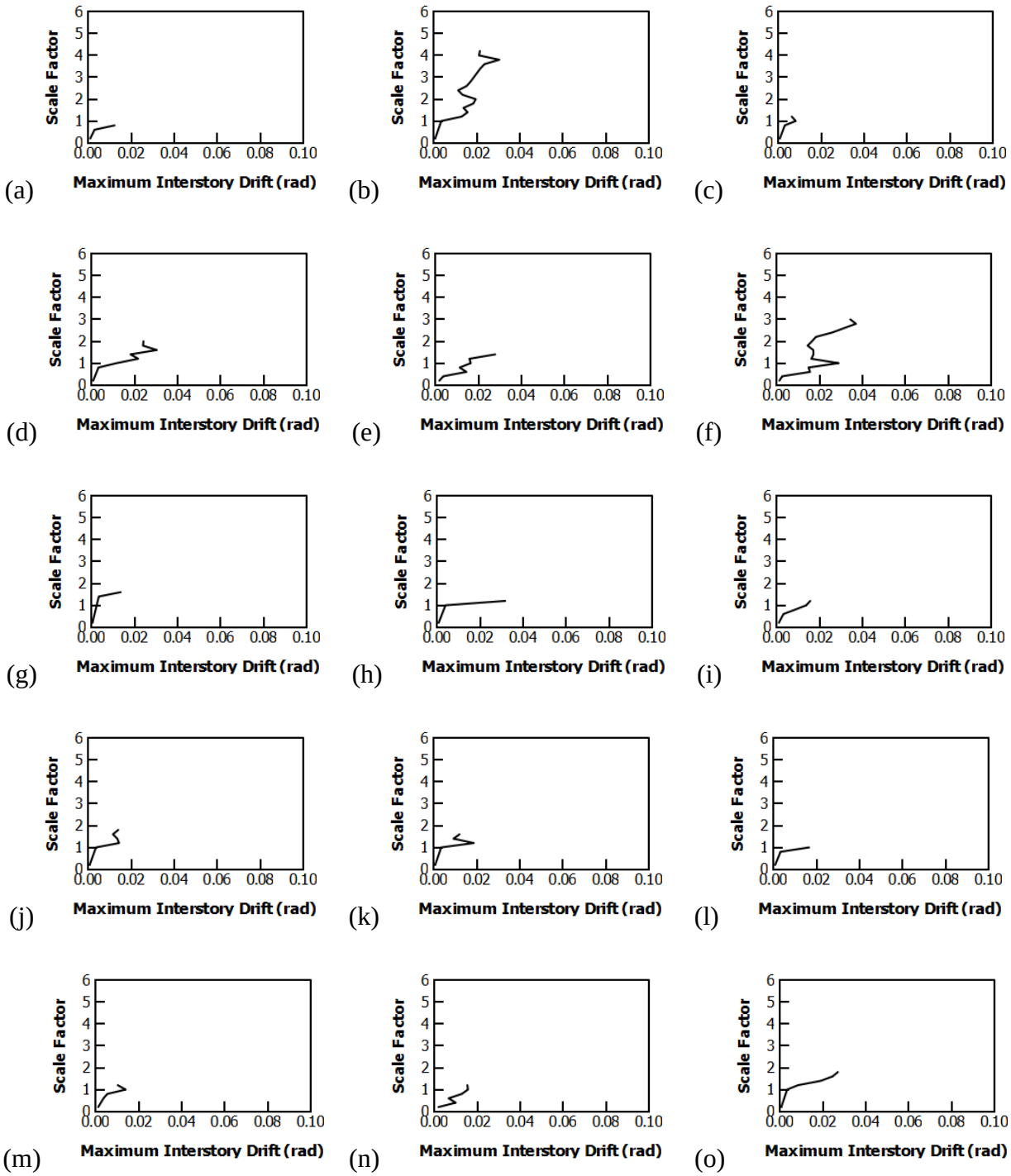

Figure A.18 IDA curves for 6storyR3w14a500: (a) gm1 – (o) gm15.

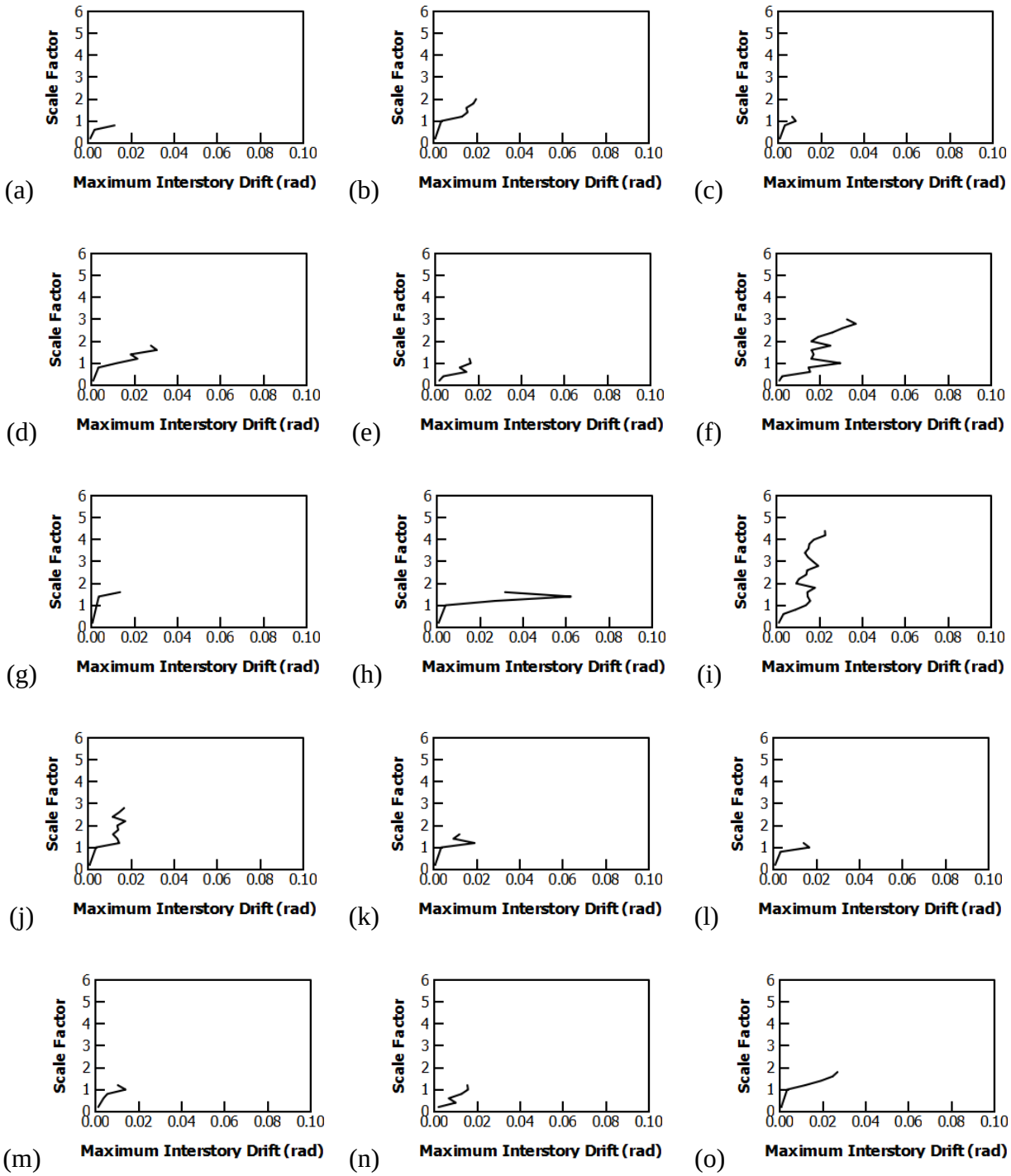

Figure A.19 IDA curves for 6storyR3w14a625: (a) gm1 – (o) gm15.

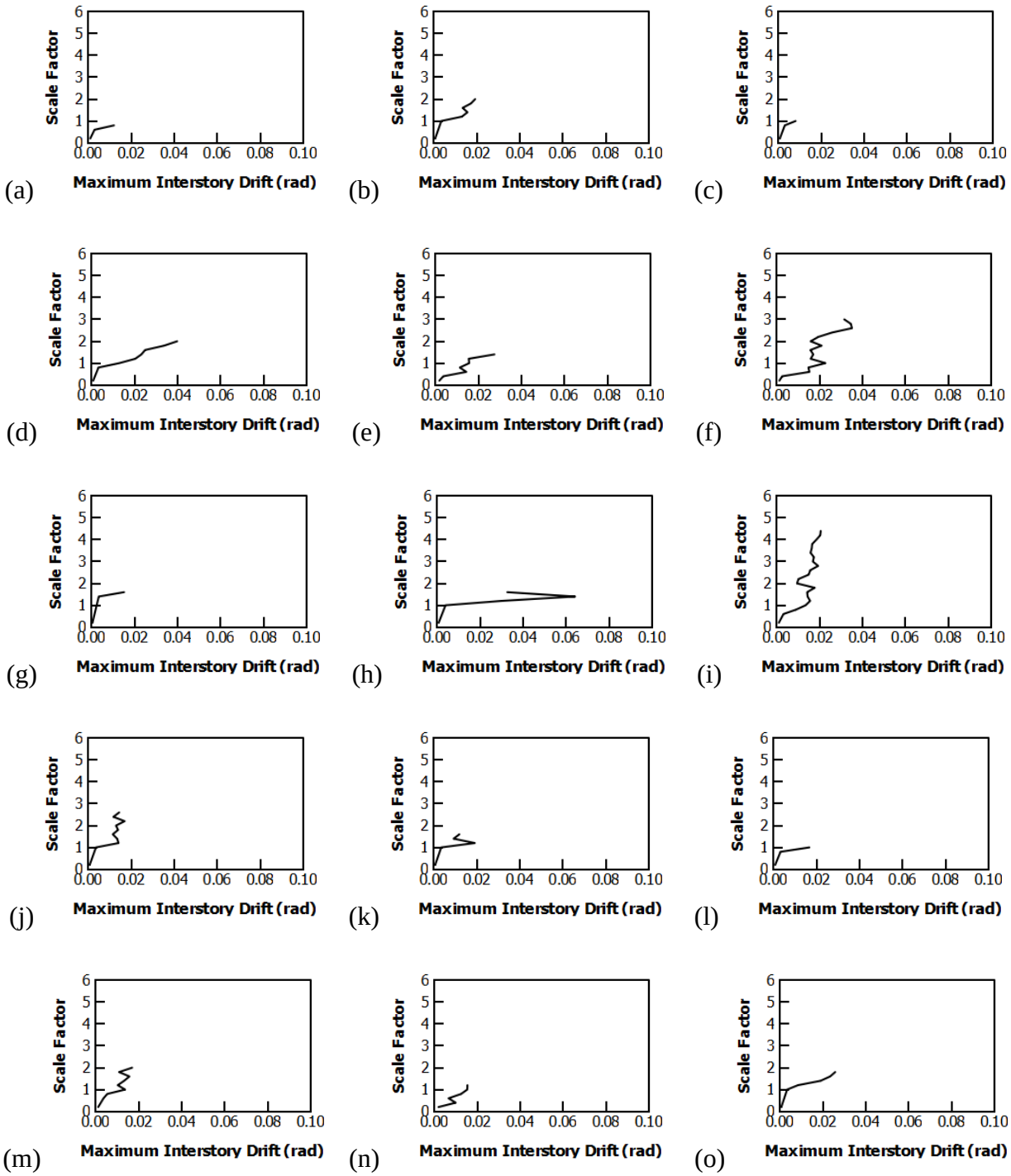

Figure A.20 IDA curves for 6storyR3w14a750: (a) gm1 – (o) gm15.

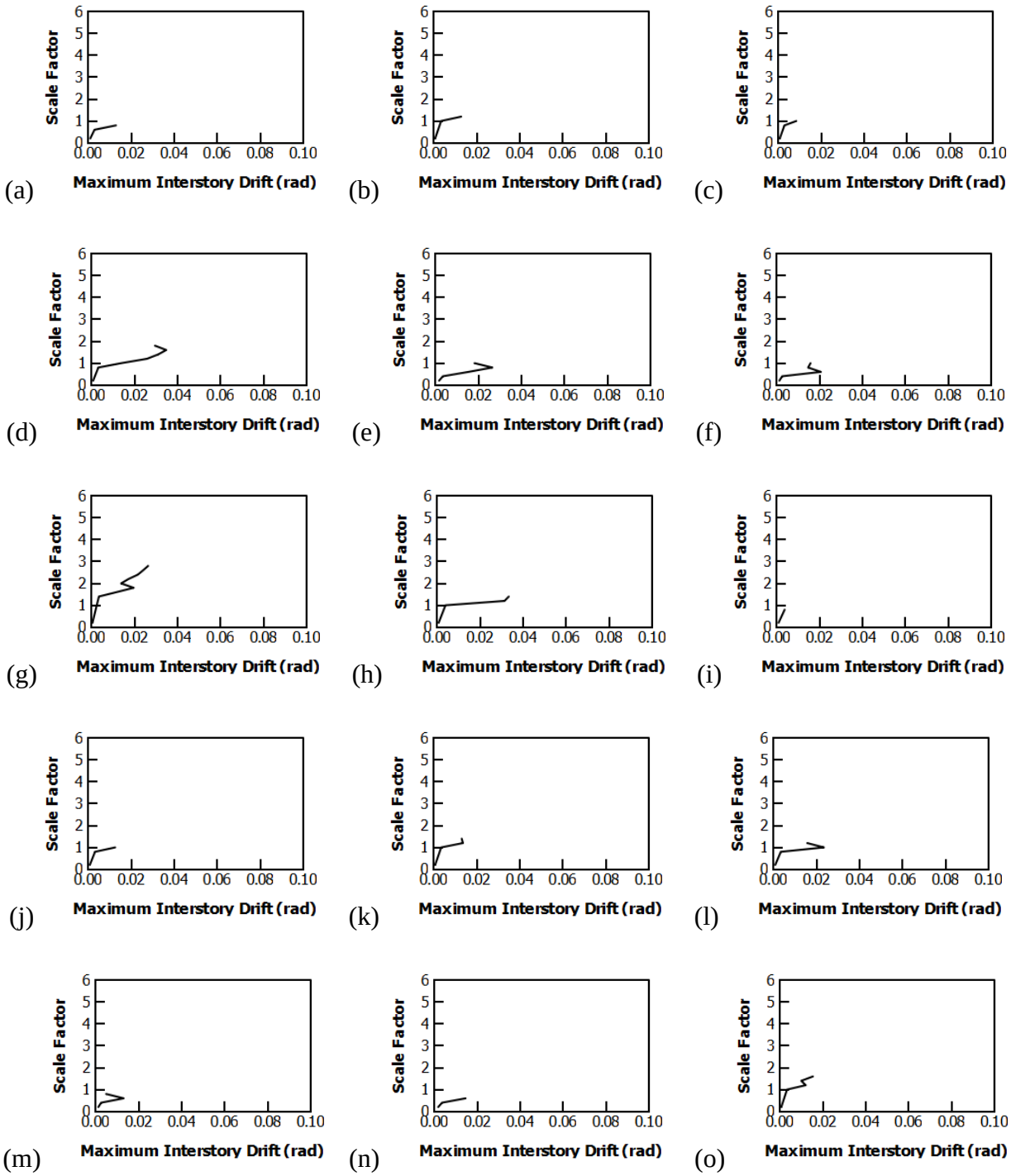

Figure A.21 IDA curves for 6storyR3w18a000: (a) gm1 – (o) gm15.

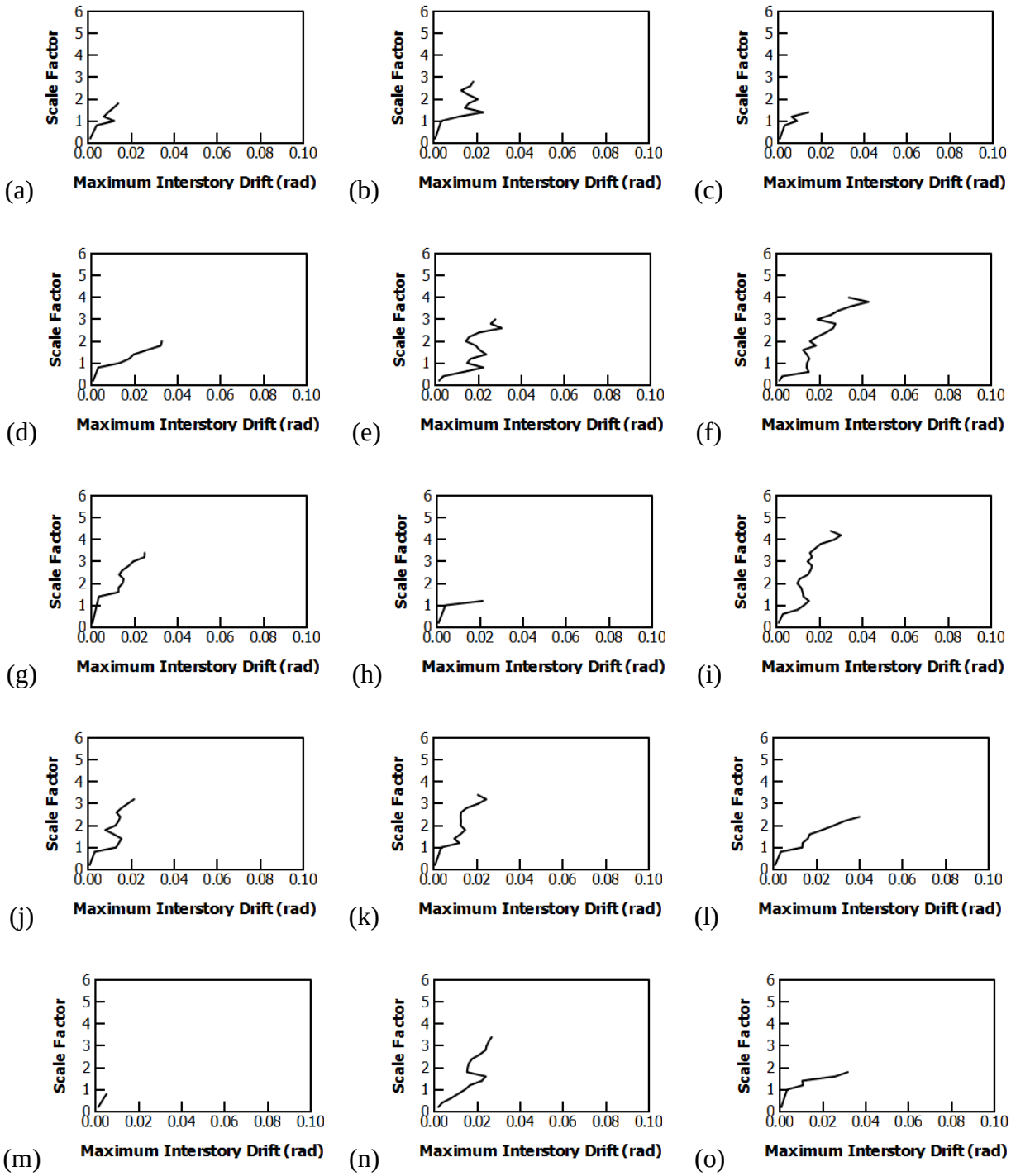

Figure A.22 IDA curves for 6storyR3w18a375: (a) gm1 – (o) gm15.

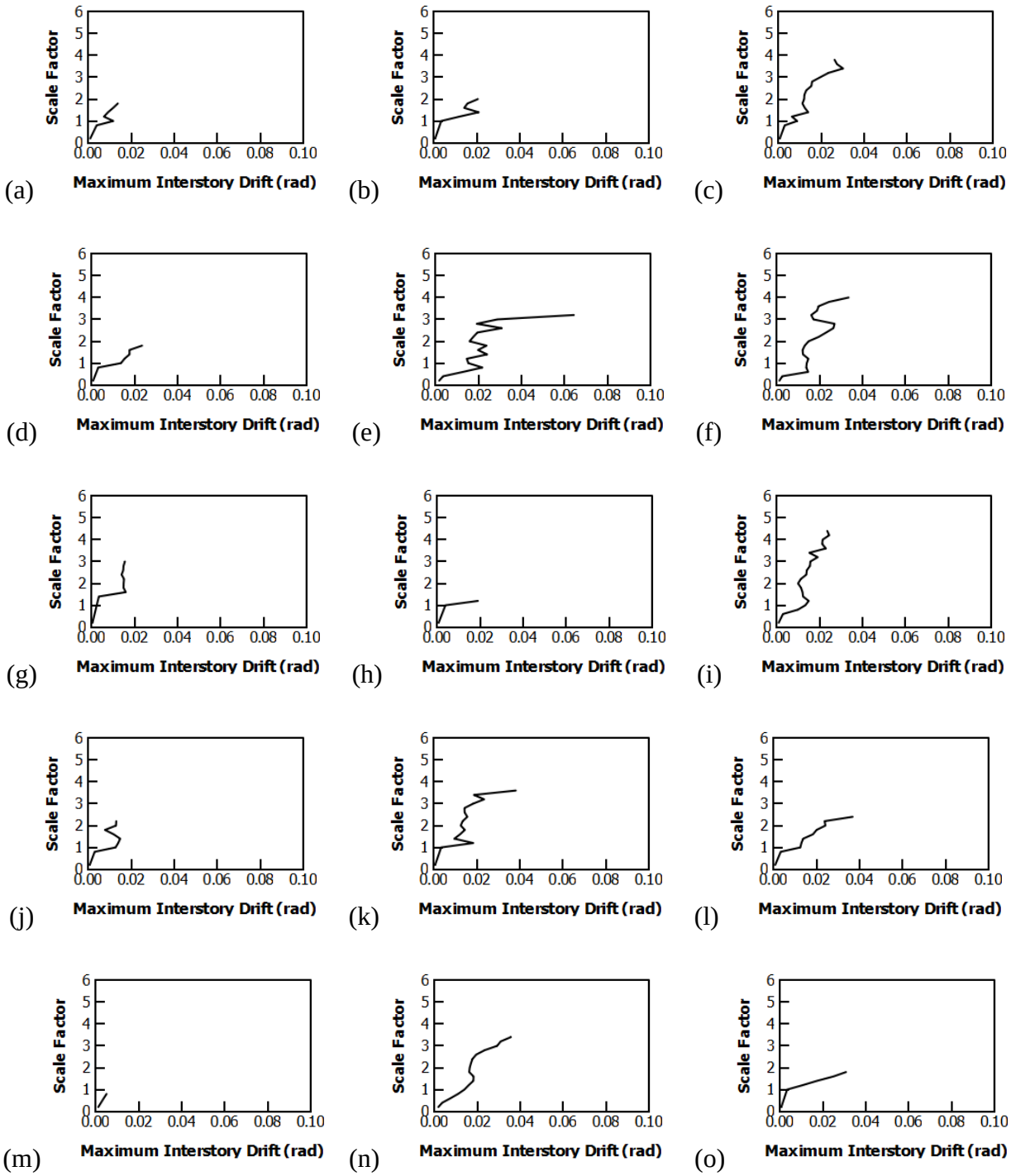

Figure A.23 IDA curves for 6storyR3w18a500: (a) gm1 – (o) gm15.

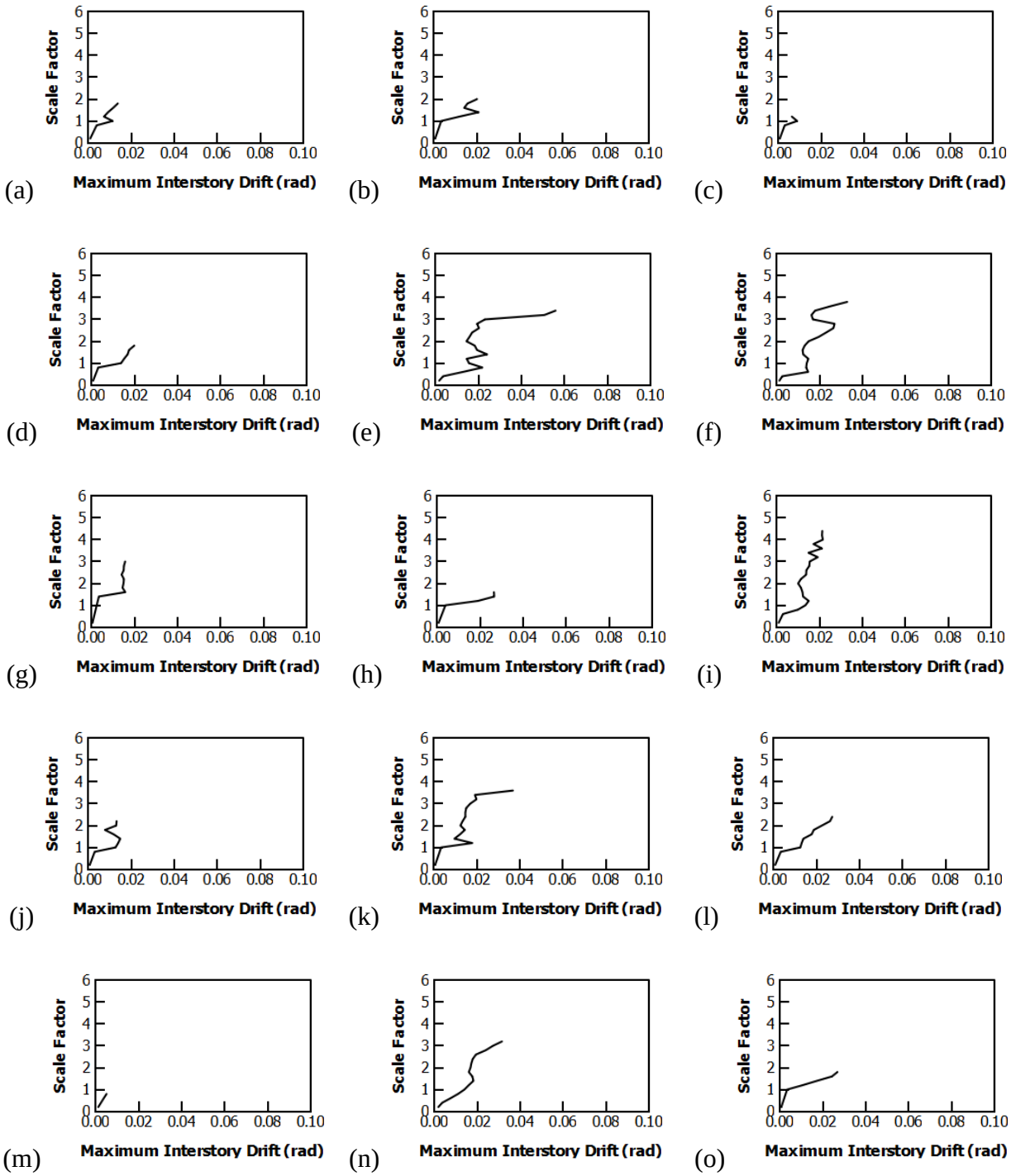

Figure A.24 IDA curves for 6storyR3w18a625: (a) gm1 – (o) gm15.

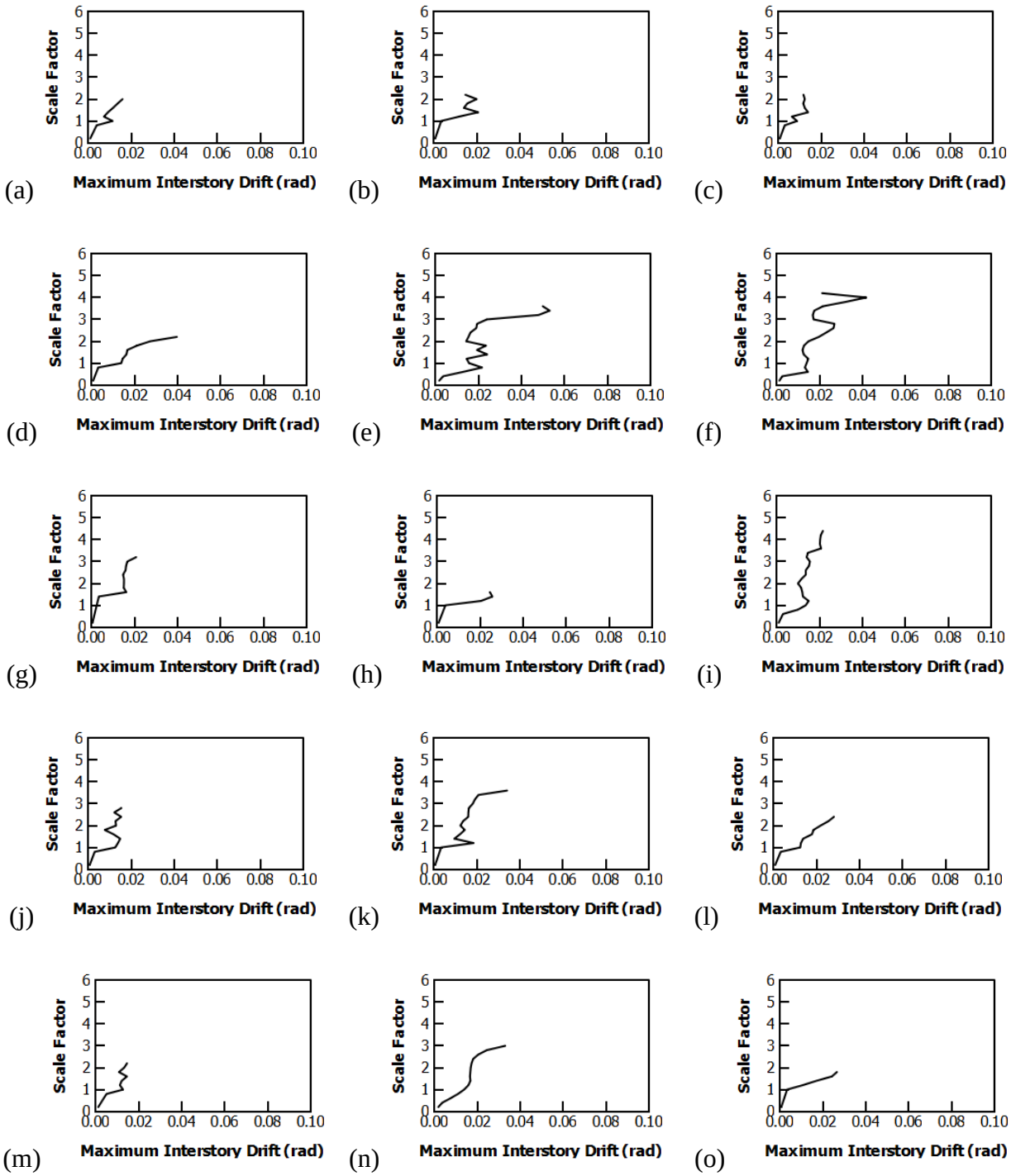

Figure A.25 IDA curves for 6storyR3w18a750: (a) gm1 – (o) gm15.

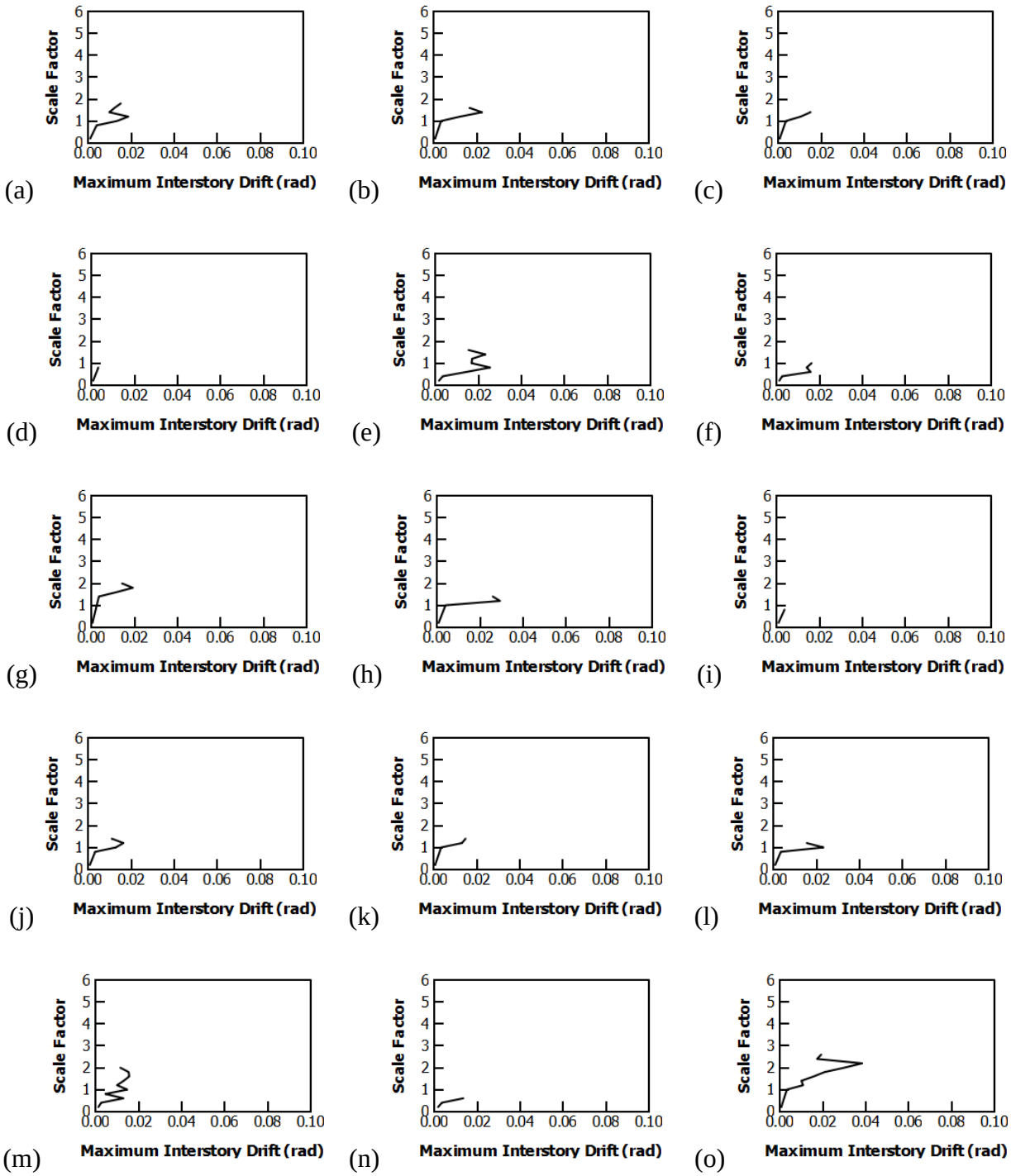

Figure A.26 IDA curves for 6storyR3w21a000: (a) gm1 – (o) gm15.

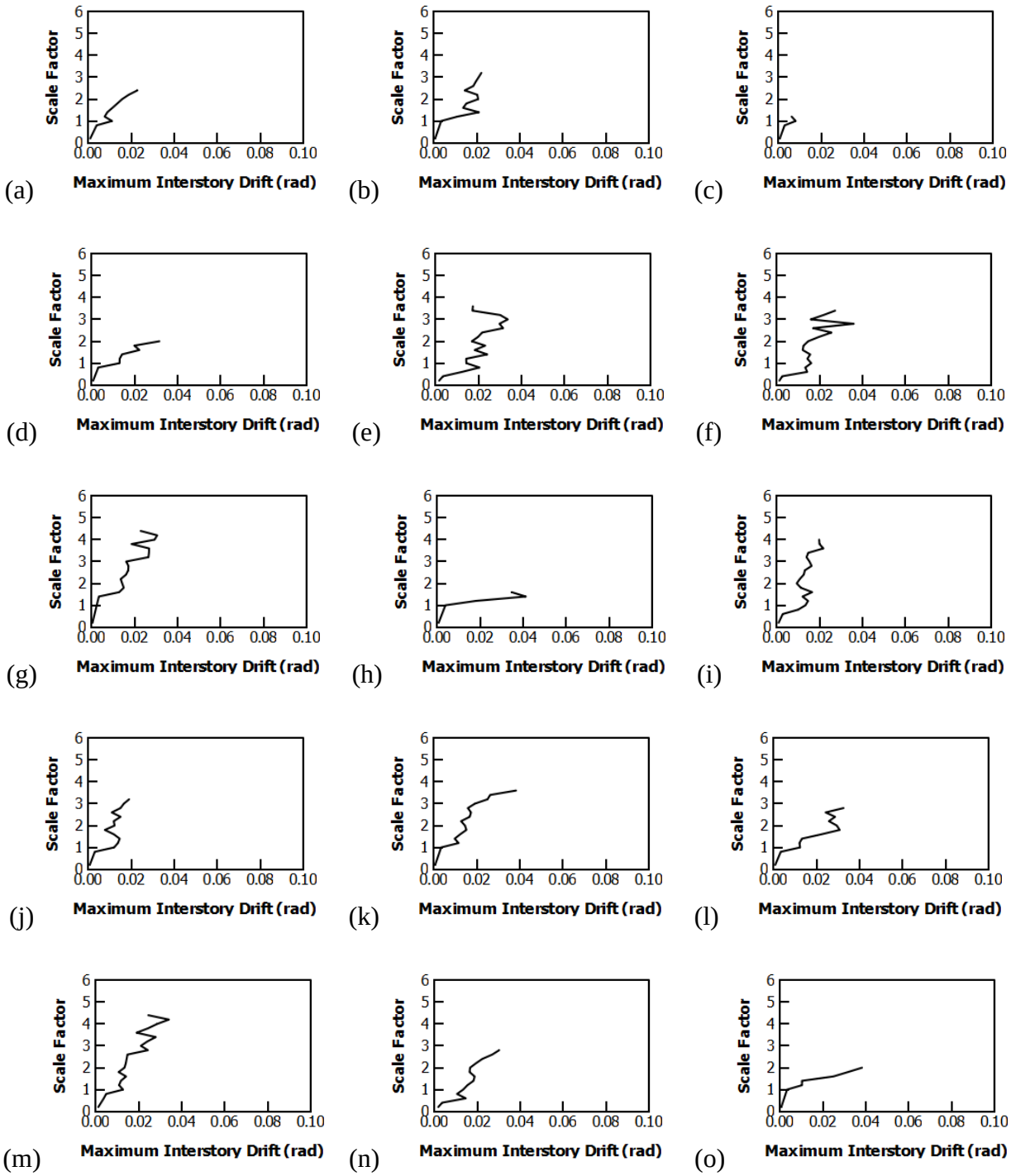

Figure A.27 IDA curves for 6storyR3w21a375: (a) gm1 – (o) gm15.

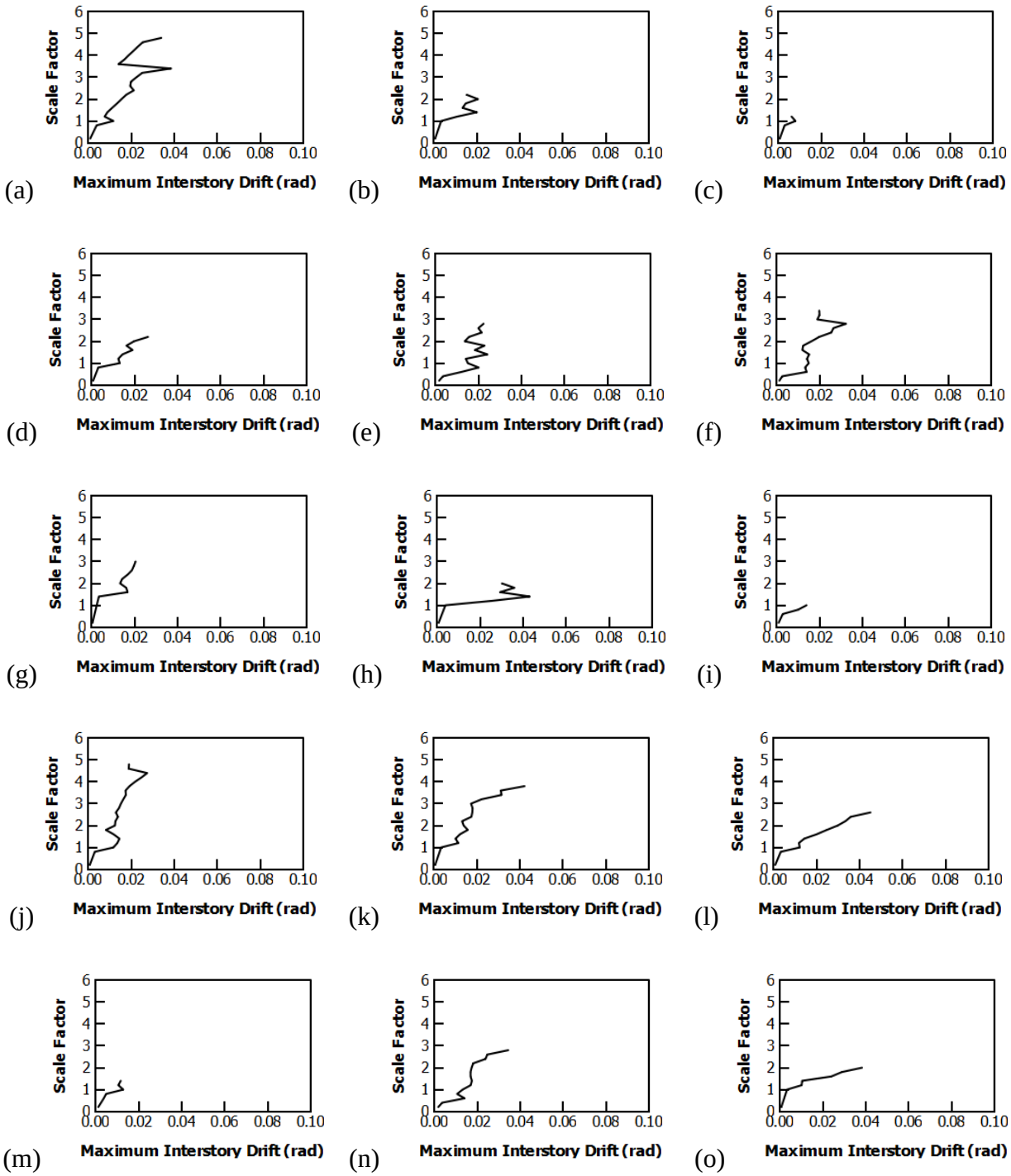

Figure A.28 IDA curves for 6storyR3w21a500: (a) gm1 – (o) gm15.

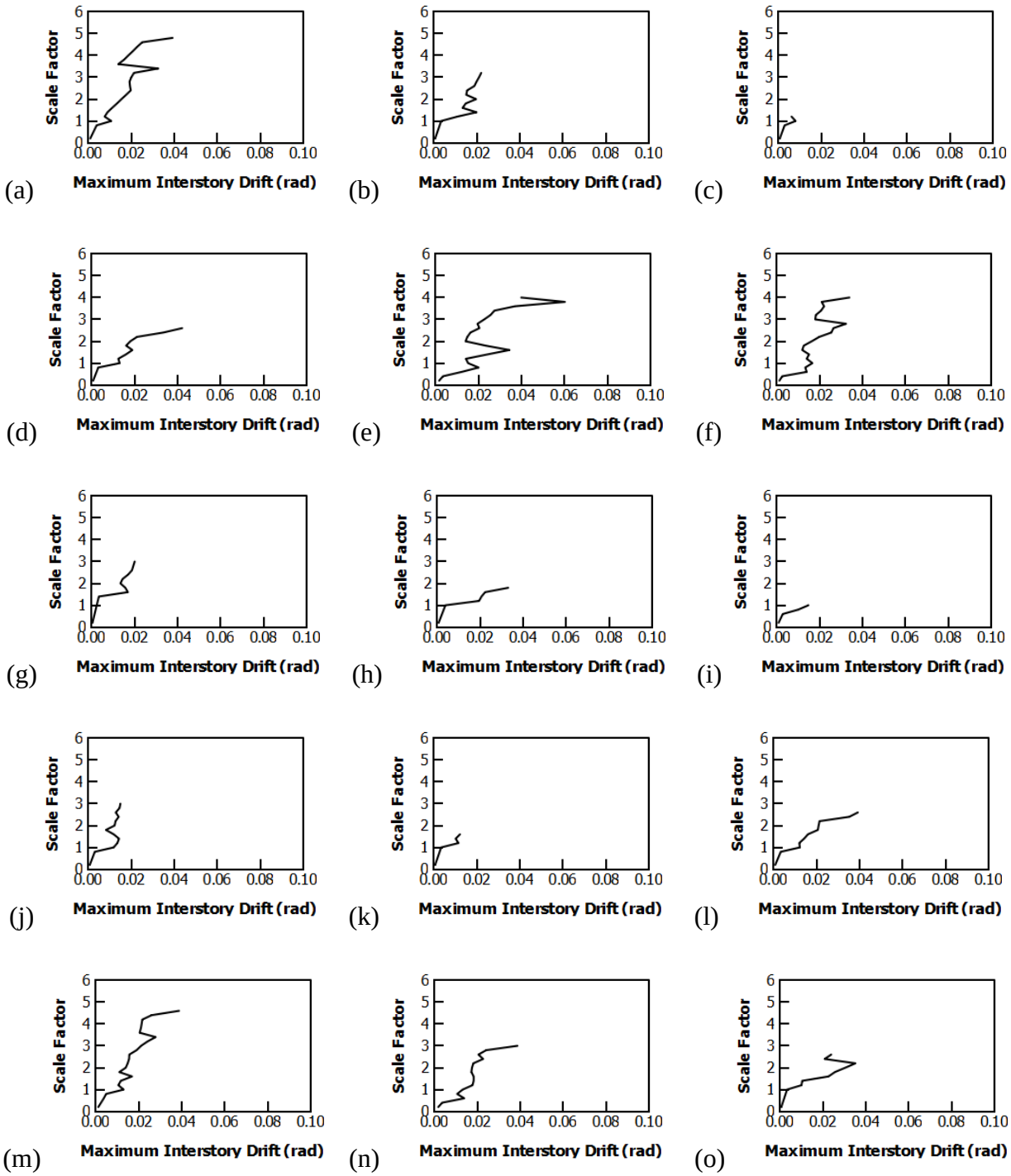

Figure A.29 IDA curves for 6storyR3w21a625: (a) gm1 – (o) gm15.

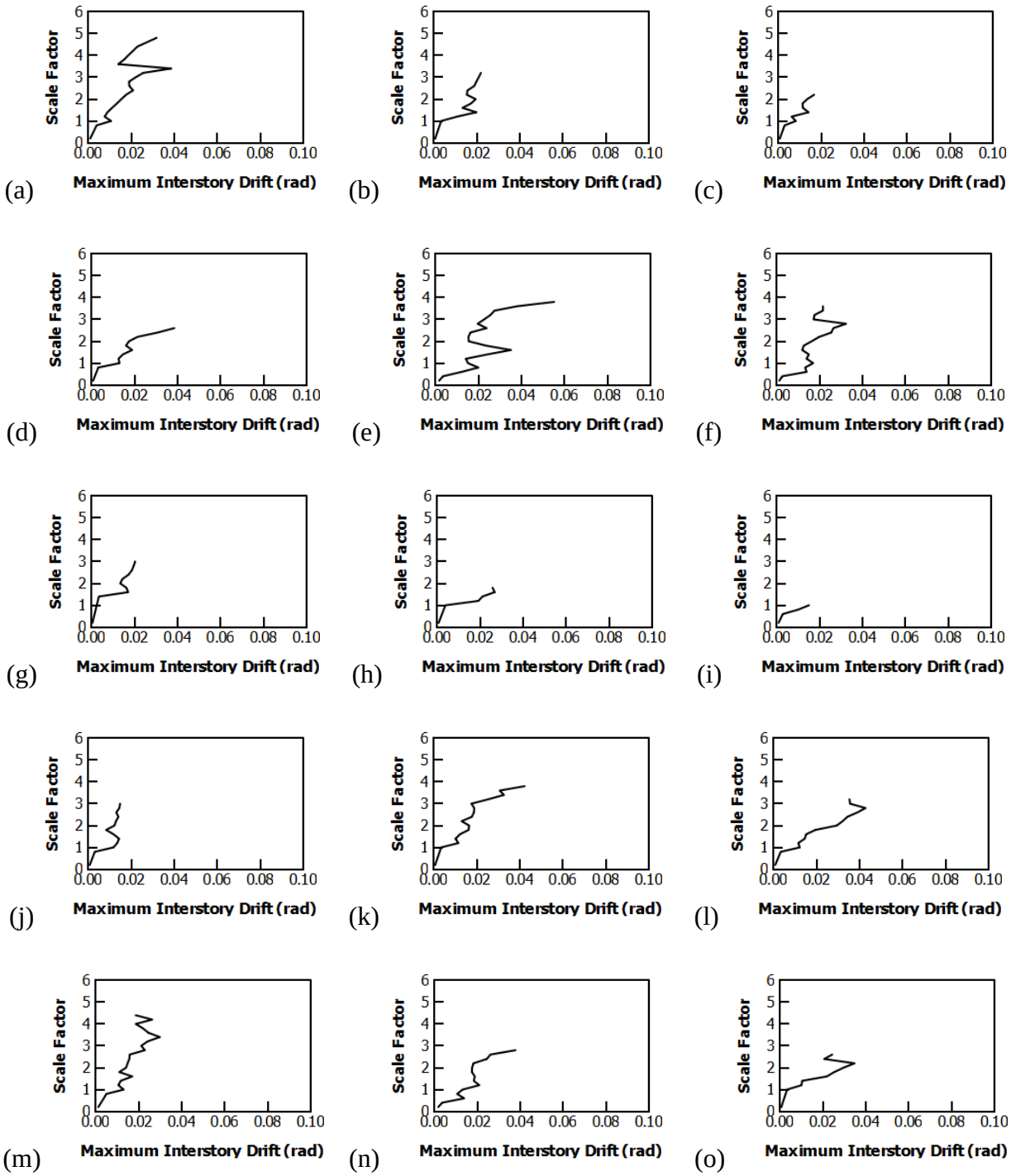

Figure A.30 IDA curves for 6storyR3w21a750: (a) gm1 – (o) gm15.